

**Dissertation**  
**submitted to the**  
**Combined Faculty of Mathematics, Engineering and Natural Sciences**  
**of Heidelberg University, Germany**  
**for the degree of**  
**Doctor of Natural Sciences**

Put forward by

**Henrik Peter Eckhardt**

born in: Karlsruhe (Germany)

Oral examination: **15.10.2025**





# **Automated Measurements of $\delta^{13}\text{C}$ , $\delta^{18}\text{O}$ & $\Delta_{47}$ in Atmospheric $\text{CO}_2$**

— A Study on Atmospheric  $\Delta_{47}$  —

Referees: Prof. Dr. Norbert Frank  
Prof. Dr. Werner Aeschbach



## Abstract

In this work, a automated preparation line was constructed that was coupled to an Isotope-Ratio Mass Spectrometer MAT 253+ for the measurement of  $\delta^{13}\text{C}$ ,  $\delta^{18}\text{O}$ , and  $\Delta_{47}$  in atmospheric  $\text{CO}_2$  samples. Besides  $\text{CO}_2$  from ambient air collected directly through an inlet on the roof of the Institute of Environmental Physics in Heidelberg, gas cylinders and flasks can be connected for preparation. A preparation takes approximately 90 minutes. The external reproducibility over a period of about 10 months was  $\sim 0.005\text{‰}$  for  $\delta^{13}\text{C}$ ,  $\sim 0.01\text{‰}$  for  $\delta^{18}\text{O}$ , and  $\sim 0.011\text{‰}$  for  $\Delta_{47}$ . Furthermore, successful calibration of  $\Delta_{48}$  was demonstrated. Through automation, unprecedented densities of atmospheric  $\Delta_{47}$  measurements were achieved in the second quarter of 2024. During summer months, the data indicate strong dominance of sources having  $\Delta_{47}$  corresponding to air temperatures and/or re-equilibration with water reservoirs linked to air temperatures. Deviations from  $\Delta_{47}$  corresponding to air temperatures were observed in winter. Correction equations for isobaric interference by  $\text{N}_2\text{O}$  were determined for  $\delta^{13}\text{C}$ ,  $\delta^{18}\text{O}$ ,  $\Delta_{47}$ ,  $\Delta_{48}$ , and  $\Delta_{49}$ . An equation was determined to correct non-linear mixing behavior of  $\Delta_{47}$ . After applying it to data from one night in October, 2024, a Keeling plot indicated a likely contribution of combustion sources.

## Kurzfassung

In dieser Arbeit wurde eine automatische Aufbereitungslinie konstruiert, die für die Messung von  $\delta^{13}\text{C}$ ,  $\delta^{18}\text{O}$  und  $\Delta_{47}$  atmosphärischer  $\text{CO}_2$ -Proben an ein Isotopenverhältnis-Massenspektrometer MAT 253+ gekoppelt wurde. Neben atmosphärischem  $\text{CO}_2$ , das direkt über einen Einlass auf dem Dach des Instituts für Umweltphysik in Heidelberg gesammelt wird, können Gasflaschen und Flasks zur Aufbereitung angeschlossen werden. Eine Aufbereitung beträgt in etwa 90 Minuten. Die externe Reproduzierbarkeit betrug über ca. 10 Monat  $\sim 0,005\text{‰}$  für  $\delta^{13}\text{C}$ ,  $\sim 0,01\text{‰}$  für  $\delta^{18}\text{O}$  und  $\sim 0,011\text{‰}$  für  $\Delta_{47}$ . Darüber hinaus wurde eine erfolgreiche Kalibration von  $\Delta_{48}$  nachgewiesen. Durch die Automatisierung konnten im zweiten Quartal 2024 unerreichte Dichten von atmosphärischen  $\Delta_{47}$ -Messungen erreicht werden. Während der Sommermonate wiesen die Daten auf eine starke Dominanz von Quellen mit  $\Delta_{47}$ -Werten bezüglich einer Equilibration bei Außenlufttemperaturen und/oder auf eine Re-Equilibration mit an die Außenlufttemperatur gekoppelten Wasserreservoirs hin. Im Winter wurde eine Abweichung von  $\Delta_{47}$ -Werten entsprechend einer Equilibration bei Außenlufttemperaturen beobachtet. Zur Korrektur der isobaren Interferenz mit  $\text{N}_2\text{O}$  wurden Korrekturgleichungen für  $\delta^{13}\text{C}$ ,  $\delta^{18}\text{O}$ ,  $\Delta_{47}$ ,  $\Delta_{48}$  und  $\Delta_{49}$  bestimmt. Es wurde eine Gleichung zur Korrektur des nichtlinearen Mischungsverhaltens von  $\Delta_{47}$  bestimmt. Nach Anwendung dieser Korrektur auf Daten einer Nacht im Oktober 2024 wies ein Keeling-Plot auf einen wahrscheinlichen Beitrag von Verbrennungsquellen hin.



# Contents

List of Abbreviations . . . . .	xi
Preliminary remarks . . . . .	xv
<b>1. Motivation</b>	<b>1</b>
<b>2. Fundamentals</b>	<b>5</b>
2.1. Carbon-Cycle . . . . .	5
2.2. CO <sub>2</sub> -Isotopes & Applications . . . . .	8
2.3. CO <sub>2</sub> -Isotopologues . . . . .	11
2.3.1. The Stochastic Distribution . . . . .	11
2.3.2. Distribution under Thermodynamic Equilibrium . . . . .	12
2.3.3. The $\Delta$ -Notation . . . . .	15
2.3.4. $\Delta_{47}$ in Atmospheric CO <sub>2</sub> . . . . .	17
2.4. Measurement Site, Weather Station & CRDS . . . . .	19
2.5. Isotope-Ratio Mass Spectrometer . . . . .	21
2.5.1. Physical Measurement Principle . . . . .	21
2.5.2. Dual Inlet Measurement Mode . . . . .	22
2.5.3. Data Storage and Processing . . . . .	23
2.5.4. Measurement Protocol . . . . .	24
2.5.5. Control Parameters . . . . .	25
2.5.6. Practical Calculation of $\delta^{13}\text{C}$ , $\delta^{18}\text{O}$ , $\Delta_{47}^{\text{LF}}$ , $\Delta_{48}^{\text{LF}}$ , and $\Delta_{49}^{\text{LF}}$ . . . . .	26
<b>3. Automatic Preparation Line for Atmospheric CO<sub>2</sub></b>	<b>29</b>
3.1. Conceptual Function and Construction . . . . .	29
3.2. Gas Chromatograph and GC Step . . . . .	35
3.2.1. Structure . . . . .	35
3.2.2. GC step . . . . .	38
3.2.3. Cleaning Procedure . . . . .	43
3.2.4. Comparison With and Without GC Preparation . . . . .	43
3.2.5. Dependency on Sample Quantity . . . . .	45

## Contents

<b>4. N<sub>2</sub>O Correction, Calibration &amp; Reproducibility</b>	<b>47</b>
4.1. Isobaric Interference with N <sub>2</sub> O . . . . .	47
4.1.1. Theoretical N <sub>2</sub> O Correction . . . . .	48
4.1.2. Experimental Determination of C <sub>N<sub>2</sub>O</sub> /C <sub>CO<sub>2</sub></sub> . . . . .	55
4.2. Calibration of $\delta^{13}\text{C}$ , $\delta^{18}\text{O}$ . . . . .	59
4.3. Calibration of $\Delta_{47}$ (and $\Delta_{48}$ , $\Delta_{49}$ ) . . . . .	63
4.3.1. Production of Temperature-Equilibrated CO <sub>2</sub> Standards . . . . .	63
4.3.2. Purity of Standards . . . . .	64
4.3.3. Calibration and Correction on $^{47}\delta$ (and $^{48}\delta$ , $^{49}\delta$ ). . . . .	65
4.3.4. Stability of the produced Standards . . . . .	68
4.3.5. Recommendations . . . . .	70
4.4. Reproducibility . . . . .	71
<b>5. Mixing of <math>\Delta_{47}</math> and Source + Ambient Air Measurements</b>	<b>75</b>
5.1. Nonlinear Mixing of $\Delta_{47}$ . . . . .	75
5.2. Measurements of Human Breath and in a Parking Garage . . . . .	84
5.2.1. Human Breath . . . . .	84
5.2.2. Underground Parking Garage . . . . .	86
5.3. Ambient Air Measurements in Heidelberg . . . . .	93
5.3.1. Overview of Ambient Air Measurements in 2024 . . . . .	94
5.3.2. Seasonal Trend 2024 . . . . .	94
5.3.3. Nighttime Inversion in October 2024 . . . . .	101
5.3.4. Exemplary Periods: May and June – Mean Diurnal Cycle . . . . .	106
<b>6. Conclusion and Prospect</b>	<b>119</b>
<b>Appendices</b>	<b>125</b>
A. Supplementary Material on Chapter 2 . . . . .	125
A.1. Additional Figures and Tables . . . . .	125
A.2. Discussion on Reference Frames for $\Delta_{47}$ . . . . .	128
A.3. Old versus New Measurement Protocol . . . . .	130
A.4. Background Correction . . . . .	132
A.5. Correction for Imbalance on m/z 44 . . . . .	135
B. Supplementary Material on Chapter 3 . . . . .	141
B.1. Tubing & Connection Elements . . . . .	141
B.2. Pneumatically actuated Valves . . . . .	142
B.3. Pumps . . . . .	144

B.4.	Cold Traps . . . . .	145
B.5.	Multifunctional Device . . . . .	147
B.6.	Pressure Sensors . . . . .	148
B.7.	Mass Flow Controller . . . . .	149
B.8.	Silver Wool Trap . . . . .	150
B.9.	Multiposition Valve, Gas Cylinders & Ambient Air Access . . . . .	151
B.10.	Injection via Syringe & External Access to Pump Unit . . . . .	153
B.11.	Valve Blocks for Standards . . . . .	154
B.12.	Programming . . . . .	156
B.13.	Security Features and Error Handling . . . . .	157
B.14.	Operation . . . . .	159
B.15.	Automatic Reference Refill . . . . .	163
B.16.	Determination of actual Bellow Volumes . . . . .	166
B.17.	Drift of $\delta^{13}\text{C}$ & $\delta^{18}\text{O}$ with Number of Reference Refills . . . . .	169
B.18.	Duration of Preparation & Measurement . . . . .	173
B.19.	Experiment on Reusing Reference Gas . . . . .	174
B.20.	Experiment on “Flush Time” in AT step . . . . .	176
B.21.	Test on Ambient Air Intake Line . . . . .	177
B.22.	Additional Figures and Tables . . . . .	178
C.	Supplementary Material on Chapter 4 . . . . .	189
C.1.	Additional $\text{N}_2\text{O}$ Correction Functions . . . . .	189
C.2.	Re-Equilibration of $\text{CO}_2$ with and without Water . . . . .	191
C.3.	Supplementary Material on Calibration . . . . .	192
C.4.	Supplementary Material on Reproducibility . . . . .	201
D.	Supplementary Material on Chapter 5 . . . . .	203
D.1.	Supplementary Material on Nonlinear Mixing of $\Delta_{47}$ . . . . .	203
D.2.	Supplementary Material on Ambient Air Measurements . . . . .	204
<b>List of Figures</b>		<b>213</b>
<b>List of Tables</b>		<b>217</b>
<b>Bibliography - Author-Related Contributions</b>		<b>219</b>
<b>Bibliography</b>		<b>221</b>
<b>Danksagung</b>		<b>239</b>





# Abbreviations

<b>ArdV</b>	Arduino valve
<b>AT</b>	Air Trap
<b>BCE</b>	Before the Common Era
<b>CE</b>	Common Era
<b>cf.</b>	compare ( <i>Latin: confer</i> )
<b>CO</b>	Change Over
<b>corr</b>	correction
<b>CRDS</b>	Cavity Ring-Down Spectrometer
<b>DI</b>	Dual Inlet
<b>dp</b>	diaphragm pump
<b>e.g.</b>	for example ( <i>Latin: exempli gratia</i> )
<b>EGL</b>	equilibrated (and heated) gas line
<b>etc.</b>	and all the rest ( <i>Latin: et cetera</i> )
<b>ETF</b>	empirical transfer function
<b>fvp</b>	fore vacuum pump
<b>GAW</b>	Global Atmospheric Watch
<b>GC</b>	Gas Chromatograph
<b>GUI</b>	graphical user interface
<b>IAEA</b>	International Atomic Energy Agency
<b>ICOS</b>	Integrated Carbon Observation System
<b>IRMS</b>	Isotope-Ratio Mass Spectrometer
<b>ISL</b>	Isodat Script Language
<b>IUP</b>	Institute of Environmental Physics ( <i>German: Institut für Umweltphysik</i> )
<b>LF</b>	laboratory frame
<b>LSCE</b>	Climate and Environment Sciences Laboratory ( <i>French: Laboratoire des sciences du climat et de l'environnement</i> )
<b>m/z</b>	mass-to-charge-ratio
<b>MPI-BGC</b>	Max Planck Institute for Biogeochemistry
<b>MV</b>	manual valve
<b>NOAA</b>	National Oceanic and Atmospheric Administration
<b>norm</b>	normalized
<b>PBL</b>	pressure baseline
<b>RB</b>	reference bellow
<b>ref</b>	reference
<b>RF</b>	reference frame
<b>rvp</b>	rotary vane pump
<b>SB</b>	sample bellow
<b>SD</b>	standard deviation

<b>SEM</b>	standard error of the mean
<b>smp</b>	sample
<b>SMS</b>	Short Message Service
<b>std</b>	standard
<b>stoch</b>	stochastic distribution
<b>turbo</b>	turbo molecular pump
<b>WMO</b>	World Meteorological Organization





# Preliminary Remarks

## Conventions for $\delta$ & $\Delta$

$\delta^{13}\text{C}$  is referred to the VPDB scale and  $\delta^{18}\text{O}$  to the VPDB- $\text{CO}_2$  scale, unless specified otherwise. Furthermore,  $\delta^{13}\text{C}$ ,  $\delta^{18}\text{O}$ ,  $\Delta_{45}$ ,  $\Delta_{46}$ ,  $\Delta_{47}$ ,  $\Delta_{48}$ ,  $\Delta_{49}$  refers to  $\text{CO}_2$  unless otherwise stated. See Table 2.1 for more details.

## Reproducibility & Error for External Comparisons

The achieved reproducibility of calibrated data was  $\sim 0.005\text{‰}$  ( $n = 44$ ) for  $\delta^{13}\text{C}$ ,  $\sim 0.01\text{‰}$  ( $n = 44$ ) for  $\delta^{18}\text{O}$ , and  $\sim 0.011\text{‰}$  ( $n = 57$ ) for  $\Delta_{47}$  (February to November 2024). To account for systematic uncertainties from calibration or corrections, such as the  $\text{N}_2\text{O}$  correction or the dependency of  $\Delta_{47}$  on  $^{47}\delta$ , the error for external comparisons should be chosen at least  $\sim 0.01\text{‰}$  for  $\delta^{13}\text{C}$ ,  $\sim 0.03\text{‰}$  for  $\delta^{18}\text{O}$ , and  $\sim 0.018\text{‰}$  for  $\Delta_{47}$ .

## Measurement Uncertainties

The individual measurement uncertainties or short-term reproducibility values reported in the text and tables may be lower than the long-term reproducibility achieved. These values are used to assess measurement quality and to make short-term relative comparisons. Statistical errors are expressed as standard deviation (SD) (including Bessel's correction):

$$\sigma_{x_i} = \sqrt{\frac{\sum_{i=1}^n (\bar{x} - x_i)^2}{n - 1}} \quad (1)$$

and/or standard error of the mean (SEM):

$$\hat{\sigma}_{\bar{x}} = \frac{\sigma_{x_i}}{\sqrt{n}} = \sqrt{\frac{\sum_{i=1}^n (\bar{x} - x_i)^2}{n(n - 1)}} \quad (2)$$

Note: Some uncertainties are indicated as “total error”, which includes both statistical SEM from measurement and systematic errors from corrections and calibration.

## Nomenclature

The nomenclature for isotope calculations and the underlying quantities are based on the recommendations of *Coplen*, 2011. Additionally, the common abbreviation “m/z”, which stands for “mass-to-charge ratio”, is used. In the context of equations,  $\mathcal{M} \in \{45, 46, 47, 48, 49\}$  and  $\mathcal{M}' \in \{45, 46, 47, 48\}$  are used.







# 1. Motivation

Human activities are now having a profound impact on the Earth's natural systems, causing an unprecedented species extinction [e.g. *De Vos et al.*, 2015]. The scale and geological significance of this impact have led some scientists to propose the term "Anthropocene" [*Crutzen*, 2002]. One key affected area is the atmosphere, which is undergoing significant changes due to rising levels of trace gases. Some of these gases, such as carbon dioxide ( $\text{CO}_2$ ), act as potent greenhouse gases, driving human-induced climate change [*Canadell et al.*, 2021].

To mitigate the effects of anthropogenic climate change, the international community has committed to reducing greenhouse gas emissions [*United Nations*, 2015]. Therefore, investigating the  $\text{CO}_2$  cycle, which plays a crucial role in this process, is not only scientifically important but also socially relevant. In addition to measuring atmospheric  $\text{CO}_2$  concentrations, isotopic tracers have emerged as valuable tools in recent decades. These tracers are based on analyzing isotope ratios such as  $^{13}\text{C}/^{12}\text{C}$ ,  $^{18}\text{O}/^{16}\text{O}$ ,  $^{14}\text{C}/^{12}\text{C}$  and  $^{17}\text{O}/^{16}\text{O}$ . These are referred to as  $\delta^{13}\text{C}$ ,  $\delta^{18}\text{O}$ ,  $\Delta^{14}\text{C}$  and  $\Delta^{17}\text{O}$  when expressed in relation to international standards. Examining these allows the quantification of sources and sinks within the  $\text{CO}_2$  cycle. This is made possible by the fact that physical, chemical, and biological processes influence these isotopic signatures [e.g. *Mook*, 2000; *Affek et al.*, 2014].

Each of these tracers has its own strengths and weaknesses. For example,  $\delta^{13}\text{C}$  is used to determine  $\text{CO}_2$  fluxes from the oceanic and terrestrial biospheres [e.g. *Francey et al.*, 1995; *Ciais et al.*, 1995]. In urban regions, it can also be used to better quantify the influence of natural gas combustion [*Cranton*, 2023]. However, a major disadvantage of this tracer is that it is difficult to distinguish between the combustion of fossil fuels and respiration processes in the biosphere because their isotopic signatures overlap [e.g. *Mook*, 2000, p. 90ff].  $\Delta^{14}\text{C}$  supplements this measurement by enabling the quantification of  $\text{CO}_2$  resulting from the combustion of fossil fuels [e.g. *Levin et al.*, 2003; *Levin et al.*, 2008]. The reason for this is the  $\sim 5730$ -year half-life [*Godwin*, 1962] of the radioactive isotope  $^{14}\text{C}$ , meaning virtually no  $^{14}\text{C}$  is present in fossil fuels. However,  $\Delta^{14}\text{C}$  cannot distinguish between modern sources. Influences from other local sources, such as nuclear power

## 1. Motivation

plants, must be considered [Kuderer et al., 2018].  $\delta^{18}\text{O}$  is used to distinguish between photosynthesis and soil respiration [e.g. Yakir et al., 1996; Ciais et al., 1997].  $\Delta^{17}\text{O}$  can be used to investigate stratospheric influences [e.g. Liang et al., 2015]. However, the exchange of oxygen isotopes with different water reservoirs complicates the interpretation of  $\text{CO}_2$  oxygen isotopes [e.g. Riley et al., 2003].

The  $\text{CO}_2$  cycle is highly complex due to the numerous sinks and sources involved. Additional tracers could help constrain fluxes and reservoirs more effectively. One possibility is the direct analysis of stable  $\text{CO}_2$  isotopologues. Apart from  $^{16}\text{O}^{12}\text{C}^{16}\text{O}$  and the isotopologues with a single rare isotope —  $^{16}\text{O}^{13}\text{C}^{16}\text{O}$ ,  $^{16}\text{O}^{12}\text{C}^{18}\text{O}$ , and  $^{16}\text{O}^{12}\text{C}^{17}\text{O}$  — which make up the majority of the isotopic tracers,  $\delta^{13}\text{C}$ ,  $\delta^{18}\text{O}$ , and  $\Delta^{17}\text{O}$ , further information is offered by eight more stable  $\text{CO}_2$  isotopologues. These isotopologues have more than one rare isotope and are called “multiply-substituted isotopologues” [Eiler et al., 2004] or “clumped isotopes” [Eiler, 2007]. They have enhanced thermodynamic stability [e.g. Eiler, 2007]. The most abundant multiply-substituted isotopologue is  $^{16}\text{O}^{13}\text{C}^{18}\text{O}$ , which accounts for approximately 96 % of isotopologues with a molecular mass of 47 u.

The relative ratio of the actual abundance of isotopologues with a mass of 47 u to their predicted random (stochastic) distribution is called  $\Delta_{47}$  [Wang et al., 2004; Eiler et al., 2004]. Similarly, tracers  $\Delta_{48}$  and  $\Delta_{49}$  can be defined, but they are more difficult to determine due to the lower abundance of the underlying isotopologues [e.g. Bernecker et al., 2023]. A few pioneering studies in the mid 2000s demonstrated the potential applications of  $\Delta_{47}$  [Eiler et al., 2004; Affek et al., 2006; Affek et al., 2007]. Since  $\Delta_{47}$ ,  $\Delta_{48}$ , and  $\Delta_{49}$  are largely independent of isotopic composition [e.g. Cao et al., 2012], they have specific advantages. For example, Eiler et al., 2004 considers  $\Delta_{47}$  a useful constraint when interpreting  $\delta^{18}\text{O}$  because  $\delta^{18}\text{O}$  depends on the isotopic composition and temperature of the interacting water. In contrast,  $\Delta_{47}$  only depends on temperature. Other applications include distinguishing between combustion [e.g. Laskar, Mahata, and Liang, 2016] and non-combustion processes, constraining photosynthetic activities [e.g. Adnew et al., 2021], and possibly intrusion of stratospheric  $\text{CO}_2$  [Yeung et al., 2009; Laskar et al., 2019]. However, since the initial pioneering studies, few publications have appeared on the atmospheric application of  $\Delta_{47}$  [Yeung et al., 2009; Laskar and Liang, 2016; Laskar, Mahata, and Liang, 2016; Laskar et al., 2019; Adnew et al., 2021; Laskar et al., 2021]. Meanwhile,  $\Delta_{47}$  has become an established temperature tracer in paleoclimate research [e.g. Ghosh et al., 2006; Bernasconi et al., 2021].

The small number of publications to date leaves plenty of space for additional studies on multiply-substituted isotopologues in atmospheric  $\text{CO}_2$ . In particular, conflicting results have emerged from the comparison of theory and published data regarding the

influence of photosynthesis [Adnew et al., 2021]. Additionally, there have only been a few diurnal and long-term measurements [Affek et al., 2007; Laskar and Liang, 2016]. To investigate the potential of the tracer, regular, high-density measurements must be carried out.

Since manually preparing CO<sub>2</sub> samples for measurements of multiply-substituted isotopologues is very time-consuming (approx. 2 hours [Eckhardt, 2019]), the aim of this work was to design and test an automatic preparation and sampling system for measuring  $\Delta_{47}$ , using an Isotope-Ratio Mass Spectrometer (IRMS). This system should provide more insight into the potential of  $\Delta_{47}$  as a tracer and allow for additional measurements of  $\Delta_{48}$  and  $\Delta_{49}$ . These measurements are accompanied by high-accuracy  $\delta^{13}\text{C}$  and  $\delta^{18}\text{O}$  measurements. As far as is known, such a system is currently unique worldwide. Without automatic sampling and preparation, measuring CO<sub>2</sub> at night is also only possible to a limited extent. Accurate and reproducible measurements are required to interpret  $\Delta_{47}$  [Adnew et al., 2021]; therefore, the measurement protocol and various effects were investigated.

Following the fundamentals chapter, chapter 3 explains the construction of the automatic preparation line and several tests. Chapter 4 discusses reproducibility, calibration, and the production of standards. It also includes a correction for isobaric interference with N<sub>2</sub>O. Chapter 5 discusses the influence of mixing CO<sub>2</sub> gases with different bulk isotopic compositions and presents the results of ambient air measurements in Heidelberg.



## 2. Fundamentals

This introductory chapter presents the theoretical and conceptual foundations for understanding the carbon cycle, CO<sub>2</sub> isotopes, and CO<sub>2</sub> isotopologues. First, it provides an overview of the carbon cycle, followed by an introduction to CO<sub>2</sub> isotopes and their representation according to international standards. Then, the isotopologues of CO<sub>2</sub> are discussed, including the theoretical calculation of  $\Delta_{47}$ ,  $\Delta_{48}$ , and  $\Delta_{49}$ , their reference scales, and basic knowledge about  $\Delta_{47}$  in ambient air measurements. The chapter concludes with a description of the Isotope-Ratio Mass Spectrometer (IRMS) used and how data is evaluated.

### 2.1. Carbon-Cycle

In principle, the global carbon cycle can be divided into a slow and a fast cycle. These cycles differ greatly in terms of the exchange times of their reservoirs, as well as in their overall comparison. Figure 2.1 shows some reservoirs from both cycles as dots. Thin arrows correspond to natural carbon fluxes, while thick arrows indicate human-induced fluxes (both in PgC/a and averaged from 2014 to 2023).

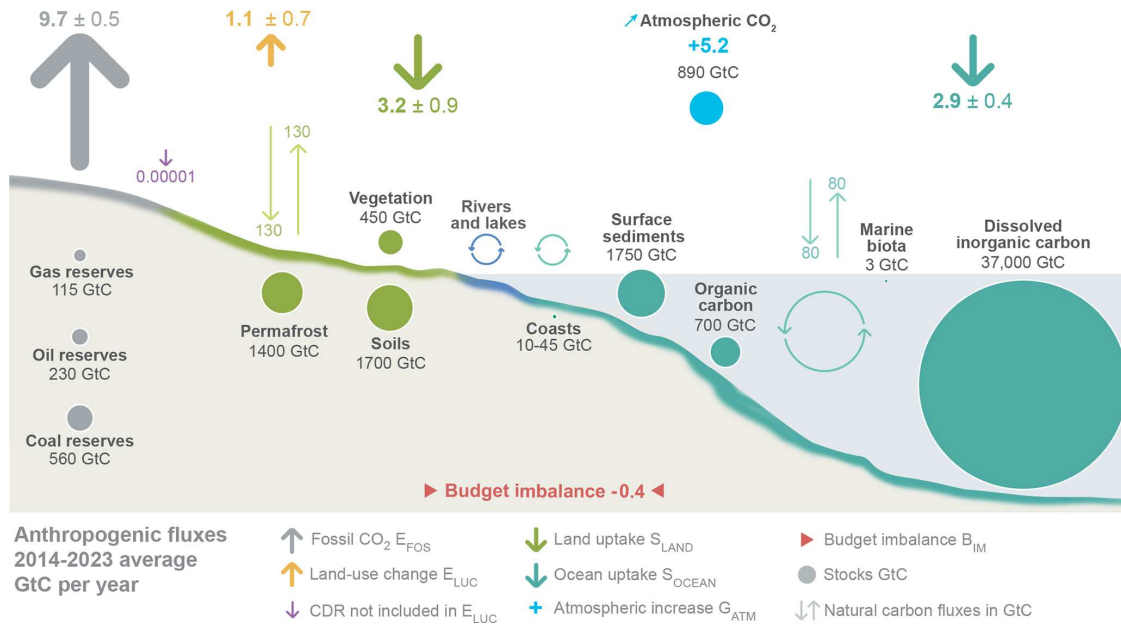
The fast cycle is characterized by large cross reservoir fluxes and short reservoir exchange times. These include the atmosphere, the upper ocean, the fresh water reservoirs, the upper soil and the active biosphere. The major constituents of carbon are CO<sub>2</sub>, HCO<sub>3</sub><sup>-</sup>, CO<sub>3</sub><sup>2-</sup> and organic matter. Exchange times are of the order of ~1-10 years, e.g. for the atmosphere, biosphere, freshwater and surface ocean. Time scales of ~10<sup>3</sup> years are relevant for the deep oceans.

The exchange processes of the slow carbon cycle, on the other hand, take place on geological time scales, including, for example, the large reservoirs in rocks and sediments. The cross-exchange between the two cycles occurs naturally through processes such as volcanism, weathering, erosion and sedimentation. The natural exchange fluxes between the two cycles can be assumed to be almost constant over the last few centuries at <0.3PgC/a [Ciais et al., 2014].

## 2. Fundamentals

Since the beginning of the Industrial Revolution around 1750, atmospheric CO<sub>2</sub> concentrations have risen from  $(278 \pm 5)$  ppm [Ciais et al., 2014] to  $\sim 425.19$  ppm today (as of December 2024 [Lan, P. Tans, et al., 2025]). This increase is primarily attributed to human activities [Canadell et al., 2021], such as burning fossil fuels, which shifts carbon from the slow cycle to the fast cycle.

According to Friedlingstein et al., 2025, the means of the anthropogenic source fluxes for the period 2014 to 2023 are  $E_{\text{FOS}} = (9.7 \pm 0.5)$  PgC/a (fossil fuel combustion and oxidation from all energy and industrial processes, including cement production and carbonation) and  $E_{\text{LUC}} = (1.1 \pm 0.7)$  PgC/a (land-use, land-use change, and forestry), shown by the thick upward arrows in Figure 2.1, respectively. Where  $E_{\text{FOS}}$  has increased by 1.1 PgC/a per decade since 1960, while  $E_{\text{LUC}}$  has decreased slightly since 1999 ( $-0.2$  PgC per decade). These additional emissions are offset by increased carbon uptake by land and ocean sinks, so that the increase in CO<sub>2</sub> in the atmospheric reservoir is significantly lower. The airborne fraction (AF) of CO<sub>2</sub> is the part of anthropogenic emissions that remains in the atmosphere ( $\text{AF} = G_{\text{ATM}} / (E_{\text{FOS}} + E_{\text{LUC}})$ ). According to Friedlingstein et al., 2025, the stability of the airborne fraction over the past 60 years indicates that the land and ocean



**Figure 2.1.:** The schematic by Friedlingstein et al., 2025 (figure created by Nigel Hawtin) shows the anthropogenic perturbation of the global carbon cycle (averaged for 2014 – 2023). The numbers in the background of the active carbon cycle (fluxes as arrows and reservoirs as dots) are taken from Canadell et al., 2021 according to Friedlingstein et al., 2025, with the exception of the coastal carbon reservoir, which the authors say, comes from a literature review of coastal marine sediments [Price et al., 2016]. “CDR” stands for “carbon dioxide removal”. Fluxes are in PgC/a.

carbon sinks have increased with increasing anthropogenic emissions and have absorbed about 56 % of the integrated emissions over this period. However, since the land and ocean sinks depend on the atmospheric CO<sub>2</sub> partial pressure, this also means that they will become sources if the atmospheric reservoir is reduced in the future, counteracting this reduction to some extent and thereby reducing the land and ocean reservoirs [e.g. *Canadell et al.*, 2021].

To constrain these cross-fluxes, measurements of CO<sub>2</sub> and O<sub>2</sub> concentrations, as well as stable and radioactive isotopes, have been used over the past decades [e.g. *P. P. Tans et al.*, 1990; *Francey et al.*, 1995; *R. F. Keeling et al.*, 1996; *Ciais et al.*, 1997; *C. D. Keeling et al.*, 2001; *Levin et al.*, 2003]. However, especially constraining biospheric sinks and sources remains challenging because they are highly sensitive to various environmental parameters, such as temperature and precipitation. In order to improve the understanding of the carbon cycle at the global and local levels, as well as its changes and responses to a changing climate, it is not only crucial to continue measuring concentrations and isotopes, but also to get new insights from further research, including new tracers.

## 2. Fundamentals

### 2.2. CO<sub>2</sub>-Isotopes & Applications

Atoms with varying numbers of neutrons but an equal number of protons are designated as isotopes of an element. The various isotopes of an element have different atomic masses  $u$ . This can result in reversible equilibrium or irreversible kinetic fractionation processes [e.g. *Mook*, 2000 (ch. 3)]. Such processes include diffusion, chemical reactions and biological processes.

CO<sub>2</sub> is composed of one carbon atom and two oxygen atoms. According to *Nier*, 1950 the two stable isotopes, <sup>12</sup>C and <sup>13</sup>C occur naturally with relative abundances of ~98.9% and ~1.1%, respectively. While the three stable oxygen atoms have the following relative abundances: <sup>16</sup>O (~99.76%), <sup>17</sup>O (~0.035%), and <sup>18</sup>O (~0.2%). Consequently, CO<sub>2</sub> occurs in 12 stable combinations of these isotopes with six different masses (44u to 49u), known as “isotopologues”.

The  $\delta$ -notation (isotope delta) is used to express small natural variations in the isotope composition. The isotope ratio  $R(^iE/^jE)$  of a heavier isotope <sup>i</sup>E of an element E to a lighter isotope <sup>j</sup>E of the same element is compared to the corresponding ratio  $R(^iE/^jE)_{\text{std}}$  of an international measurement standard (std) [*Coplen*, 2011]:

$$\delta^iE_{\text{std}} = \frac{R(^iE/^jE)}{R(^iE/^jE)_{\text{std}}} - 1 \quad . \quad (2.1)$$

For carbon, <sup>j</sup>E is equivalent to <sup>12</sup>C, and for oxygen, <sup>j</sup>E is equivalent to <sup>16</sup>O. Therefore, the expressions  $R(^{13}\text{C}/^{12}\text{C})$ ,  $R(^{18}\text{O}/^{16}\text{O})$ ,  $R(^{17}\text{O}/^{16}\text{O})$  are simplified to <sup>13</sup>R, <sup>17</sup>R & <sup>18</sup>R. The carbon and oxygen isotope ratios are referred to as the bulk isotopic composition. It is common practice to express  $\delta$ -values in per mil.

**Table 2.1.:** The table lists the international measurement standards (std) used in this work and recommended by *Daëron* et al., 2016. Note that in the literature, *Chang* et al., 1990 is sometimes cited as *Zhang* et al., 1990.

Isotope Ratio	Value	Comment
<sup>13</sup> R <sub>VPDB</sub>	0.01118	from <i>Chang</i> et al., 1990 (or <i>Zhang</i> et al., 1990; see caption)
<sup>18</sup> R <sub>VSMOW</sub>	0.0020052	from <i>Baertschi</i> , 1976
<sup>17</sup> R <sub>VSMOW</sub>	0.00038475	original value from <i>Assonov</i> et al., 2003 (rescaled by <i>Daëron</i> et al., 2016)
<sup>18</sup> R <sub>VPDB-CO<sub>2</sub></sub>	0.00208839	derived from <sup>18</sup> R <sub>VSMOW</sub>
<sup>17</sup> R <sub>VPDB-CO<sub>2</sub></sub>	0.00039310	original value from <i>Assonov</i> et al., 2003 (rescaled by <i>Daëron</i> et al., 2016)



## 2.2. CO<sub>2</sub>-Isotopes & Applications

To describe the bulk isotopic composition of CO<sub>2</sub> using the  $\delta$ -notation according to Equation (2.1), this thesis employs the  $^iR_{\text{std}}$  values proposed by *Daëron et al., 2016* from various recognized publications (Table 2.1). Unless otherwise stated, oxygen isotopes are expressed relative to the “VPDB-CO<sub>2</sub>” scale. For simplicity,  $\delta^{13}\text{C}_{\text{VPDB}}$  and  $\delta^{18}\text{O}_{\text{VPDB-CO}_2}$  are abbreviated as  $\delta^{13}\text{C}$  and  $\delta^{18}\text{O}$  in the following.

The following relationship between  $^{17}R$  and  $^{18}R$  is referred to in the literature as  $^{17}\text{O}$  correction [*Craig, 1957, Santrock et al., 1985, Brand et al., 2010, Daëron et al., 2016*]:

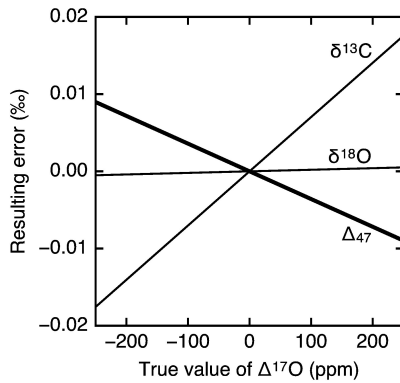
$$^{17}R = K \cdot (^{18}R)^\lambda, \quad (2.2)$$

$$\text{with } K = \frac{^{17}R_{\text{std}}}{(^{18}R_{\text{std}})^\lambda}. \quad (2.3)$$

The phenomenological constant  $\lambda$  describes the mass-dependent fractionation between  $^{17}R$  and  $^{18}R$  [*Brand et al., 2010; Laskar et al., 2019*] and was originally introduced by *Craig, 1957* with a value of 0.5. The value of  $\lambda = 0.528$  [*Barkan et al., 2005*] as recommended by *Daëron et al., 2016* is used in this thesis. VPDB-CO<sub>2</sub> is used as a standard for calculating  $K$ . For a more general consideration, Equation (2.2) is extended to include the variable  $\Delta^{17}\text{O}$  ( $^{17}\text{O}$  anomaly), which describes a non-mass dependent fractionation [*Brand et al., 2010*]. This is defined in logarithmic form as follows [e.g. *Liang et al., 2015; Daëron et al., 2016; Laskar et al., 2019*]:

$$\Delta^{17}\text{O} = \ln \left( \frac{^{17}R}{^{17}R_{\text{std}}} \right) - \lambda \cdot \ln \left( \frac{^{18}R}{^{18}R_{\text{std}}} \right). \quad (2.4)$$

As the value of  $\Delta^{17}\text{O}$  is unknown for the CO<sub>2</sub> gases used in this thesis and  $^{17}R$  cannot be measured independently with the mass spectrometer used,  $\Delta^{17}\text{O} = 0$  is assumed. This is a common assumption in mass-spectrometric analysis [e.g. *Santrock et al., 1985; Brand et al., 2010*]. However, it should be noted that this assumption is not universally valid and



**Figure 2.2.:** Figure from *Daëron et al., 2016*. This figure shows the magnitude of the systematic uncertainties due to the assumption  $\Delta^{17}\text{O} = 0$  for different true  $\Delta^{17}\text{O}$  values. For the definition of  $\Delta_{47}$  see subsection 2.3.3.

## 2. Fundamentals

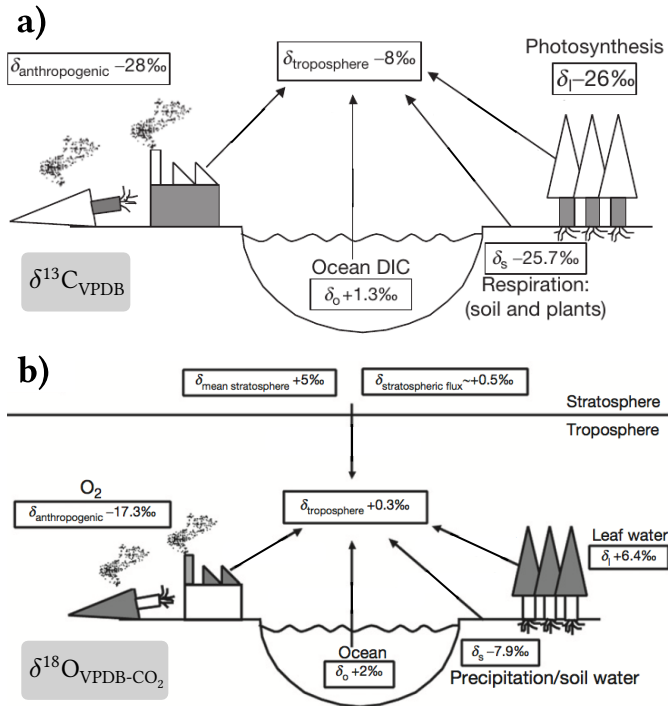
can result in substantial systematic errors if  $\Delta^{17}\text{O}$  deviates significantly from  $\Delta^{17}\text{O} \approx 0$  (see Figure 2.2). An example of this deviation would be a deep stratospheric intrusion [e.g. Liang et al., 2015, Laskar et al., 2019, Carlstad et al., 2023].

### Typical Values for $\delta^{13}\text{C}$ & $\delta^{18}\text{O}$

Typical values for  $\delta^{13}\text{C}$  and  $\delta^{18}\text{O}$  of various reservoirs are presented in Figure 2.3.

C3 plants have a  $\delta^{13}\text{C}$  of approximately  $(-26 \pm 3)\text{‰}$  [Mook, 2000, p. 98]. The  $\delta^{13}\text{C}$  value of petroleum is around  $-26.5\text{‰}$ , while the combustion of coal and lignite yields a value of approximately  $-24\text{‰}$  [P. Tans, 1981]. The trend to depleted  $\delta^{13}\text{C}$  values in the atmosphere (from approx.  $-6.6\text{‰}$  in 1850 to about  $-8.4\text{‰}$  in 2015) serves as evidence for the increase in atmospheric  $\text{CO}_2$  concentration due to fossil fuel combustion and land-use change (Suess effect) [Graven et al., 2020].

It is expected that  $\delta^{18}\text{O}$  from combustion is close to the value of atmospheric  $\text{O}_2$  [Ciais et al., 1997], with  $\delta^{18}\text{O}(\text{O}_2) = -17.3\text{‰}$  [converted from VSMOW; Coplen, 2002]. For other contributions,  $\delta^{18}\text{O}$  is strongly influenced by the  $\delta^{18}\text{O}$  values of the water pools involved [e.g. Peylin et al., 1999] through isotopic exchange during  $\text{CO}_2$  hydration [e.g. Mills et al., 1940]. As stated by Affek et al., 2014, only a little  $\delta^{18}\text{O}$  isotope exchange is expected to occur in the atmosphere due to low liquid water content and non-catalyzed  $\text{CO}_2$  hydration reaction. However, equilibrium is rapidly established in presence of catalysis, particularly in leaves, due to the enzyme carbon anhydrase [e.g. Farquhar et al., 1993].



**Figure 2.3.:** Reproduced from Affek et al., 2014. a) shows typical  $\delta^{13}\text{C}$  values for various carbon reservoirs. b) shows corresponding  $\delta^{18}\text{O}$  values.

## 2.3. CO<sub>2</sub>-Isotopologues

CO<sub>2</sub> has twelve stable naturally occurring isotopologues [e.g. Wang et al., 2004; Huntington et al., 2023]. A list of these isotopologues is provided in Table 2.2. The isotopomers that exhibit rotational symmetry with one another, for instance, <sup>18</sup>O<sup>13</sup>C<sup>16</sup>O and <sup>16</sup>O<sup>13</sup>C<sup>18</sup>O, are enumerated and designated as a single isotopologue.

**Table 2.2.:** The table lists the twelve naturally occurring stable CO<sub>2</sub> isotopologues  $y'$  (column 2), along with their isotopologue fraction  $x(y')_{\text{stoch}}$  in the case of a stochastic distribution (column 3). The corresponding atomic masses  $M$  are given in the first column. The calculations were carried out according to the procedure described in subsection 2.3.1 for a gas with <sup>13</sup>R<sub>VPDB</sub>, <sup>18</sup>R<sub>VPDB-CO<sub>2</sub></sub>, <sup>17</sup>R<sub>VPDB-CO<sub>2</sub></sub>. The last column shows the concentration in air based on 430 ppm CO<sub>2</sub> in air.

atomic mass $M$ [u]	isotopologue $y'$	isotopologue fraction (rounded) $x(y')_{\text{stoch}}$	concentration in air (rounded) based on 430 ppm CO <sub>2</sub> in air
44	<sup>16</sup> O <sup>12</sup> C <sup>16</sup> O	98.41 %	423 ppm
45	<sup>16</sup> O <sup>13</sup> C <sup>16</sup> O	1.10 %	4.73 ppm
	<sup>16</sup> O <sup>12</sup> C <sup>17</sup> O	774 ppm	333 ppb
46	<sup>16</sup> O <sup>12</sup> C <sup>18</sup> O	4.11 ‰	1.77 ppm
	<sup>16</sup> O <sup>13</sup> C <sup>17</sup> O	8.65 ppm	3.72 ppb
	<sup>17</sup> O <sup>12</sup> C <sup>17</sup> O	152 ppb	65.4 ppt
47	<sup>16</sup> O <sup>13</sup> C <sup>18</sup> O	46.0 ppm	19.8 ppb
	<sup>17</sup> O <sup>12</sup> C <sup>18</sup> O	1.62 ppm	695 ppt
	<sup>17</sup> O <sup>13</sup> C <sup>17</sup> O	1.70 ppb	731 ppq
48	<sup>18</sup> O <sup>12</sup> C <sup>18</sup> O	4.29 ppm	1.85 ppb
	<sup>17</sup> O <sup>13</sup> C <sup>18</sup> O	18.1 ppb	7.77 ppt
49	<sup>18</sup> O <sup>13</sup> C <sup>18</sup> O	48.0 ppb	20.6 ppt

### 2.3.1. The Stochastic Distribution

The stochastic distribution (stoch) represents a random distribution of all given isotopes of a gas over all possible isotopologues resulting from them [e.g. Eiler, 2007]. In the context of a stochastic distribution, the isotopologue fraction  $x(y')_{\text{stoch}}$  is determined by the multiplication of the atomic fractions  $x(^i\text{E})$  and  $x(^j\text{E})$ , respectively, from which the respective isotopologue  $y'$  is built<sup>(1)</sup>. For example:

$$x(^{16}\text{O}^{13}\text{C}^{18}\text{O})_{\text{stoch}} = 2 \cdot x(^{16}\text{O}) \cdot x(^{13}\text{C}) \cdot x(^{18}\text{O}) . \quad (2.5)$$

<sup>(1)</sup> The atom/isotopologue fraction corresponds to the proportion of a specific atom/isotopologue in relation to the total number of all (stable) atoms of an element/isotopologues of a substance.

## 2. Fundamentals

The factor of two takes into account the isotopomer that is rotational symmetrical to  $^{16}\text{O}^{13}\text{C}^{18}\text{O}$ . The calculation of the atomic fractions is performed in the following manner:

$$x(^{12}\text{C}) = \frac{1}{1 + ^{13}\text{R}}, \quad x(^{13}\text{C}) = ^{13}\text{R} \cdot x(^{12}\text{C}), \quad (2.6)$$

$$x(^{16}\text{O}) = \frac{1}{1 + ^{17}\text{R} + ^{18}\text{R}}, \quad x(^{17}\text{O}) = ^{17}\text{R} \cdot x(^{16}\text{O}), \quad x(^{18}\text{O}) = ^{18}\text{R} \cdot x(^{16}\text{O}). \quad (2.7)$$

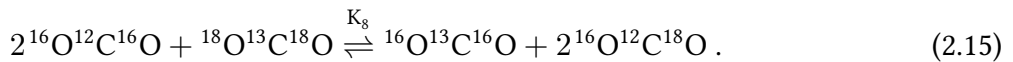
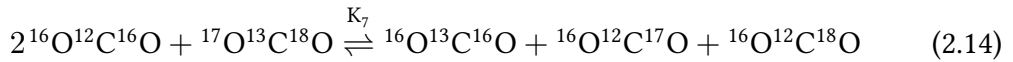
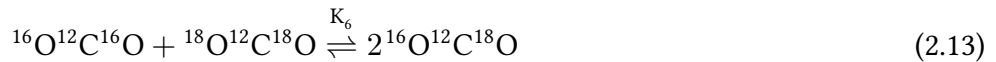
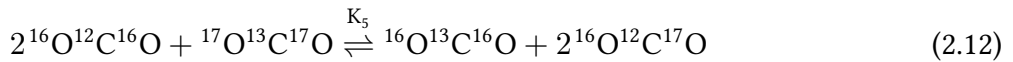
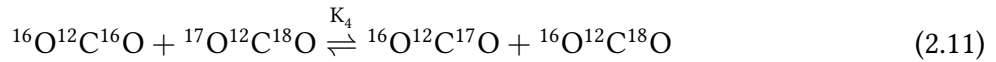
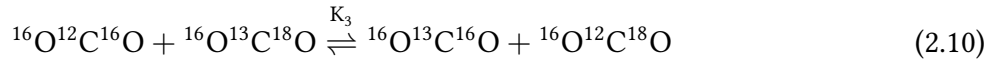
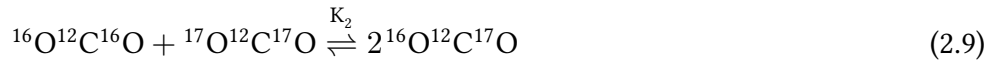
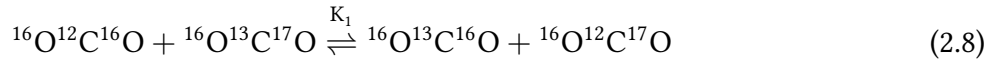
The same logic applies to the isotopologue fraction  $x(y')_{\text{stoch}}$  and the isotopologue ratio  $R(y'/y)$ . Here,  $y$  corresponds to the isotopologue  $^{16}\text{O}^{12}\text{C}^{16}\text{O}$ .

### 2.3.2. Distribution under Thermodynamic Equilibrium

For finite equilibrium temperatures, the isotopologue fractions deviate from the stochastic distribution. This is a consequence of the temperature dependence of the partition functions of the individual isotopologues.

#### Equilibrium Constants

Wang et al., 2004 state eight linearly independent exchange reactions for the twelve stable  $\text{CO}_2$  isotopologues  $y'$  (Table 2.2):



Here,  $K_1$  to  $K_8$  correspond to the equilibrium constants for the respective exchange reaction in thermodynamic equilibrium at a given temperature  $T$ . The equilibrium constants can be calculated from the ratios of the partition sums  $Q_{y'}$  of the individual isotopologues  $y'$  of the respective equilibrium reactions (2.8)-(2.15) [see, for example, Urey, 1947]. For

K<sub>3</sub>, for instance, this results in:

$$K_3 = \frac{Q_{^{16}\text{O}^{13}\text{C}^{16}\text{O}} \cdot Q_{^{16}\text{O}^{12}\text{C}^{18}\text{O}}}{Q_{^{16}\text{O}^{12}\text{C}^{16}\text{O}} \cdot Q_{^{16}\text{O}^{13}\text{C}^{18}\text{O}}} \quad [\text{Wang et al., 2004}]. \quad (2.16)$$

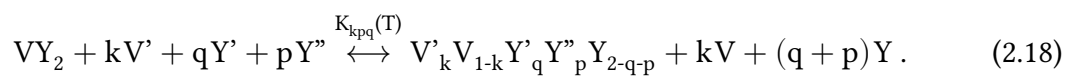
Urey, 1947 presented an approximation for the ratio of two partition functions  $Q_y$ , using the Teller-Redlich product rule. This approximation, which, according to Wang et al., 2004 considers only the vibrational energies and approximates the intermolecular bonds as harmonic oscillators, was adapted by Wang et al., 2004 for the case of a known zero point energies, exemplarily for the case  $\frac{Q_{^{16}\text{O}^{13}\text{C}^{16}\text{O}}}{Q_{^{16}\text{O}^{12}\text{C}^{16}\text{O}}}$ , as follows:

$$\frac{Q_{^{16}\text{O}^{13}\text{C}^{16}\text{O}}}{Q_{^{16}\text{O}^{12}\text{C}^{16}\text{O}}} = \frac{\sigma_{^{16}\text{O}^{12}\text{C}^{16}\text{O}}}{\sigma_{^{16}\text{O}^{13}\text{C}^{16}\text{O}}} e^{-\left(u_0^{^{16}\text{O}^{13}\text{C}^{16}\text{O}} - u_0^{^{16}\text{O}^{12}\text{C}^{16}\text{O}}\right)} \prod_{i=1}^{3n-5} \frac{u_i^{^{16}\text{O}^{13}\text{C}^{16}\text{O}}}{u_i^{^{16}\text{O}^{12}\text{C}^{16}\text{O}}} \frac{1 - e^{-u_i^{^{16}\text{O}^{12}\text{C}^{16}\text{O}}}}{1 - e^{-u_i^{^{16}\text{O}^{13}\text{C}^{16}\text{O}}}}. \quad (2.17)$$

$\sigma_{^{16}\text{O}^{12}\text{C}^{16}\text{O}}$  and  $\sigma_{^{16}\text{O}^{13}\text{C}^{16}\text{O}}$  are symmetry numbers and  $n$  corresponds to the number of atoms in the molecule under consideration ( $n = 3$  for CO<sub>2</sub>). Furthermore,  $u_i = \frac{hc\varpi_i}{kT}$ , where  $\varpi_i$  is the normal vibrational wave number of the respective isotopologue at vibration mode  $i$ ,  $h$  is Planck's constant,  $c$  is the speed of light,  $k$  is Boltzmann's constant and  $T$  is the absolute temperature<sup>(2)</sup>. The symmetry numbers used for the further calculations are listed in Table A.1 on page 125. The  $\varpi_i$  used, which correspond to the values given by Wang et al., 2004 (Table 3), are also listed there. Using equations of the form of (2.16) together with (2.17), the equilibrium constants  $K_1(T)$  to  $K_8(T)$  at given temperatures  $T$  can be calculated. Furthermore, Wang et al., 2004 employed the eight linearly independent exchange reaction Equation (2.8) - (2.15) to set up four coupled equations to calculate the isotopologue fractions of the stable CO<sub>2</sub> isotopologues under thermodynamic equilibrium conditions. Cao et al., 2012 presented an approach that works with one less coupled equation. This approach, which is used for the calculations in this work, is presented in the following section.

### Isotopologues Fractions under Thermodynamic Equilibrium

The theoretical calculations in this section are essentially based on the work of Cao et al., 2012. They introduce the consideration of the reaction of a clumped isotope system with a monatomic ideal gas. According to this approach:



<sup>(2)</sup> In this work,  $c = 299792458 \text{ m/s}$ ,  $k = 1.38064852 \cdot 10^{-23} \text{ J/K}$  and  $h = 6.626070040 \cdot 10^{-34} \text{ Js}$  were used for the calculations.

## 2. Fundamentals

With  $V \triangleq {}^{12}\text{C}$ ,  $V' \triangleq {}^{13}\text{C}$ ,  $Y \triangleq {}^{16}\text{O}$ ,  $Y' \triangleq {}^{17}\text{O}$  and  $Y'' \triangleq {}^{18}\text{O}$ . The numbers of respective isotopes exchanged are expressed by  $k \in \{0, 1\}$ ,  $q \in \{0, 1, 2\}$ ,  $p \in \{x \in \mathbb{N}_0 \mid 0 \leq x \leq 2-q\}$ . The equilibrium constants  $K_{kpq}(T)$  for the reaction (2.18) are obtained for any temperature  $T$  [K] in the sense of Equation (2.17) as follows:

$$K_{kpq}(T) = \frac{Q_{y'}(T)}{Q_y(T)} = \frac{\sigma_y}{\sigma_{y'}} e^{-(u_0^{y'} - u_0^y)} \prod_{i=1}^4 \frac{u_i^{y'}}{u_i^y} \frac{1 - e^{-u_i^y}}{1 - e^{-u_i^{y'}}}, \quad (2.19)$$

with  $y = VY_2$  and  $y' = V'_k V_{1-k} Y'_q Y''_p Y_{2-q-p}$ <sup>(3)</sup>. For the equilibrium isotopologue ratios from Equation (2.18) the following applies:

$$R(y'/y) = K_{kpq}(T) \cdot (y_1)^p (y_2)^q (y_3)^k. \quad (2.20)$$

Here,  $y_1 \triangleq R(Y''/Y)_O$ ,  $y_2 \triangleq R(Y'/Y)_O$ ,  $y_3 \triangleq R(V'/V)_C$  correspond to the isotope ratios of the ideal monatomic materials of O and C in equilibrium with  $\text{CO}_2$ . The bulk isotope ratios  $R(V'/V)_{\text{CO}_2}$ ,  $R(Y'/Y)_{\text{CO}_2}$ ,  $R(Y''/Y)_{\text{CO}_2}$  are calculated from the ratios of the sums of all the respective isotopologues. Using Equation (2.20), the following equations are obtained according to Cao et al., 2012:

$$R(V'/V)_{\text{CO}_2} = \frac{\sum_{p=0}^2 \sum_{q=0}^{2-p} K_{1pq}(T) (y_1)^p (y_2)^q}{\sum_{p=0}^2 \sum_{q=0}^{2-p} K_{0pq}(T) (y_1)^p (y_2)^q} \cdot y_3, \quad (2.21)$$

$$R(Y'/Y)_{\text{CO}_2} = \frac{\sum_{p=0}^2 \sum_{q=0}^{2-p} q (K_{1pq}(T) y_3 + K_{0pq}(T)) (y_1)^p (y_2)^q}{\sum_{p=0}^2 \sum_{q=0}^{2-p} (2-p-q) (K_{1pq}(T) y_3 + K_{0pq}(T)) (y_1)^p (y_2)^q}, \quad (2.22)$$

$$R(Y''/Y)_{\text{CO}_2} = \frac{\sum_{p=0}^2 \sum_{q=0}^{2-p} p (K_{1pq}(T) y_3 + K_{0pq}(T)) (y_1)^p (y_2)^q}{\sum_{p=0}^2 \sum_{q=0}^{2-p} (2-p-q) (K_{1pq}(T) y_3 + K_{0pq}(T)) (y_1)^p (y_2)^q}. \quad (2.23)$$

Given a known bulk isotopic distribution and a temperature  $T$  [K], this system of equations can be solved numerically for  $y_1$ ,  $y_2$  and  $y_3$ . The ratios  $R(y'/y)$  can then be determined for all  $k, q, p$  using Equation (2.20). Then, at the given equilibrium temperature (indicated by subscript  $T$ ), the isotopologue fractions  $x(y')_T$  and  $x(y)_T$  can be calculated using the same logic as in Equation (2.6) and Equation (2.7).

---

<sup>(3)</sup>  $y = y'$  in the case that  $k = 0$ ,  $p = 0$  and  $q = 0$ .

### 2.3.3. The $\Delta$ -Notation

Wang et al., 2004 and Eiler et al., 2004 introduced the  $\Delta$ -notation as a tracer. It is sensitive to the influence of temperature on the isotope distribution on the isotopologues of a gas with a given bulk isotopic composition. The  $\Delta$ -notation for a given isotopologue  $y'$  is defined on the basis of the above nomenclature as follows.

$$\Delta_{y'} = \frac{\frac{x(y')_T}{x(y)_T}}{\frac{x(y')_{\text{stoch}}}{x(y)_{\text{stoch}}}} - 1 . \quad (2.24)$$

Here,  $y'$  corresponds to the respective isotopologue with k, p, q under consideration (cf. Equation (2.18) and Table 2.2). As a reminder,  $y$  is  $y'$  with k = p = q = 0.  $x(y)_{\text{stoch}}$  and  $x(y')_{\text{stoch}}$  are the isotopologue fractions of the respective isotopologues  $y'$  under stochastic distribution. They are calculated as described in subsection 2.3.1. The denominator and numerator refer to the same gas (same bulk isotopic composition). For the stable isotopologues of a given molecular mass  $\mathcal{M} \in \{45, 46, 47, 48, 49\}$ , the following definition applies:

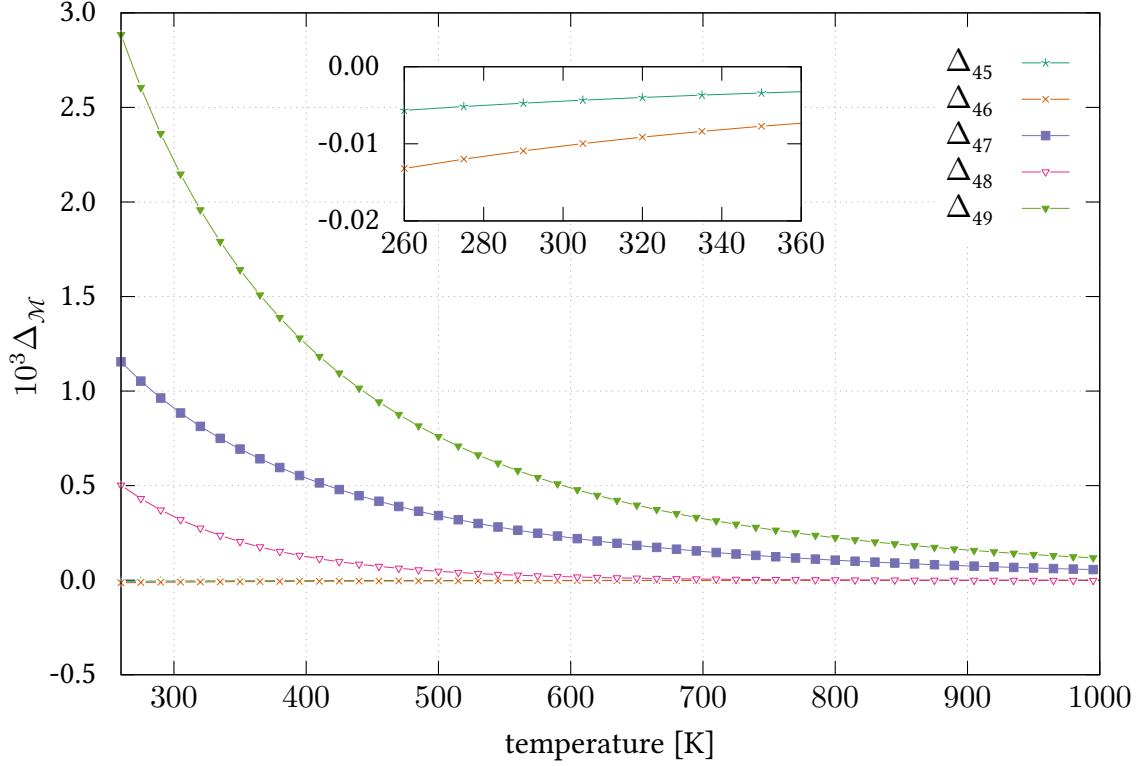
$$\Delta_{\mathcal{M}} = \frac{\frac{\sum_{y' \text{ with } \mathcal{M}} x(y')_T}{x(y)_T}}{\frac{\sum_{y' \text{ with } \mathcal{M}} x(y')_{\text{stoch}}}{x(y)_{\text{stoch}}}} - 1 = \frac{\mathcal{M}R_T}{\mathcal{M}R_{\text{stoch}}} - 1 . \quad (2.25)$$

In this context,  $\sum_{y' \text{ with } \mathcal{M}}$  is the sum of the respective isotopologues  $y'$  with mass  $\mathcal{M}$  (cf. Table 2.2).  $\mathcal{M}R_T$  and  $\mathcal{M}R_{\text{stoch}}$  are the mass ratios at temperature T and in the stochastic case, respectively. As for the  $\delta$ -values, it is common practice to express the  $\Delta$ -values in per mil<sup>(4)</sup>. Determining the abundances of the individual isotopologues is not possible with the mass spectrum used. Therefore, only  $\Delta_{\mathcal{M}}$  is of relevance for this work. Furthermore,  $\mathcal{M}R_T$  is not determined by  $\sum_{y' \text{ with } \mathcal{M}} x(y')_T / x(y)_T$ , but is obtained directly from the measurement. In this case,  $\mathcal{M}R_T$  equals the measured  $\mathcal{M}R$  (see subsection 2.5.6).

As shown in Figure 2.4, the dependencies of  $\Delta_{\mathcal{M}}$  decrease with increasing temperature and converge to zero in the case of an infinitely high temperature. This corresponds to a state of stochastic distribution. In the enlarged section, it can be seen that  $\Delta_{45}$  and  $\Delta_{46}$  show a slight dependence towards negative values. At low temperatures, multiply-substituted isotopologues are favored over the singly-substituted isotopologues. However, this dependence on  $\Delta_{45}$  and  $\Delta_{46}$  cannot be observed in practice, due to an unavoidable

<sup>(4)</sup> The initial definition proposed by Wang et al., 2004 and Eiler et al., 2004 incorporated the factor of 1000. However, the IUPAC guidelines [Coplen, 2011] advocate for a definition that omits this factor. To ensure clarity and consistency with the  $\delta$ -values, the definition is also provided here without the factor of 1000.

## 2. Fundamentals



**Figure 2.4.:** The dependence of the different  $\Delta_{\mathcal{M}}$  on temperature can be seen. The dependence decreases with increasing temperature. For the limiting case of an infinitely high temperature,  $\Delta_{\mathcal{M}}$  converge to zero. This corresponds to a stochastic distribution.

approximation in the calculation (see subsection 2.5.6).

The relative consideration of the stochastic distribution of the same gas makes  $\Delta_{\mathcal{M}}$  almost independent of the bulk isotopic composition. A slight theoretical dependence, as described by *Cao et al., 2012*, exists, as shown in Figure A.1 on page 126 for  $\Delta_{47}$ . In practice, this dependence is neglected or partially compensated by calibration and corrections.

### Reference Frame

An empirical transfer function (ETF) [*Dennis et al., 2011*] is used for calibration, converting measured values from the laboratory frame (LF) to a reference frame (RF). The reference frame values  $\Delta_{47}^{\text{RF}}$  are calculated using the function given by *Dennis et al., 2011*:

$$\begin{aligned} \Delta_{47}^{\text{RF}} = \Delta_{47}^{\text{RF, Dennis et al., 2011}} = & 0.003 \left( \frac{1000}{T} \right)^4 - 0.0438 \left( \frac{1000}{T} \right)^3 \\ & + 0.2553 \left( \frac{1000}{T} \right)^2 - 0.2195 \left( \frac{1000}{T} \right) + 0.0616 . \end{aligned} \quad (2.26)$$

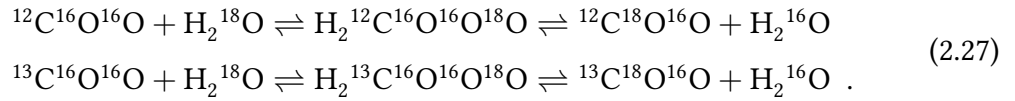


This function is based on a fit to the values given by Wang et al., 2004. Since Dennis et al., 2011 used a zero point of -273 °C, instead of -273.15 °C, when converting between °C and K (see appendix to Dennis et al., 2011), there is a deviation from the values reported by Wang et al., 2004. Nevertheless, for comparison with other published values, Equation (2.26) is used instead of own calculated reference frame values. A more detailed discussion on the reference frame and own calculated values is provided in appendix A.2 on page 128.

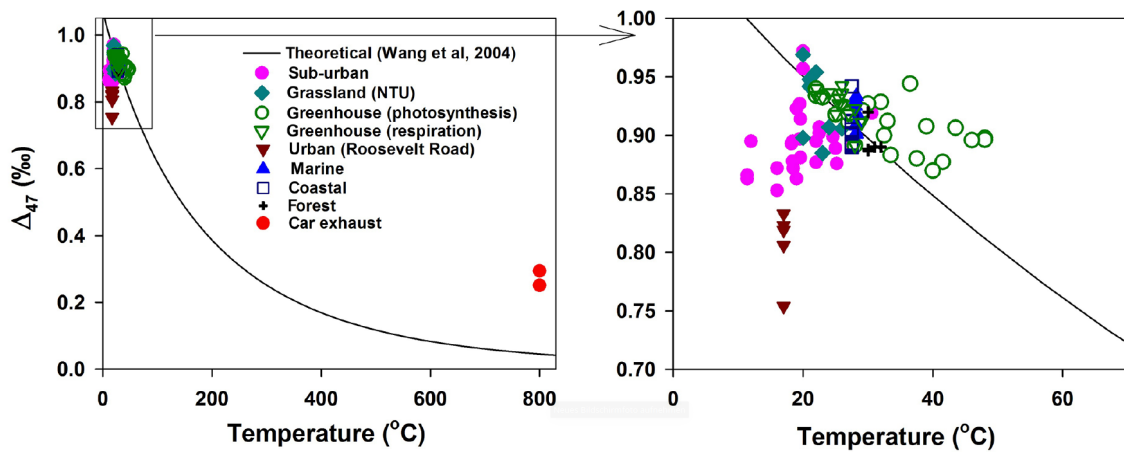
For  $\Delta_{48}$  and  $\Delta_{49}$ , values calculated according to equations in this section are used as reference frame values.

### 2.3.4. $\Delta_{47}$ in Atmospheric CO<sub>2</sub>

At atmospheric temperatures, thermodynamic re-equilibration does not occur according to the exchange reactions in Equations (2.8) - (2.15). In this case, H<sub>2</sub>O acts as a catalyst. For example, the catalytic reaction for Equation (2.10) is written as follows [Affek, 2013]:



Catalytic effects of this type play a crucial role in the equilibration of CO<sub>2</sub> isotopologues, thereby altering  $\Delta_{47}$ . However, according to Affek et al., 2014, the exchange of  $\delta^{18}\text{O}$  with atmospheric water is rather slow. Since the rate constants for the isotope exchange under contact with liquid water seem to be similar (or equal) for  $\delta^{18}\text{O}$  and  $\Delta_{47}$  [Kalb et al., 2020], it is reasonable to assume the same applies on the re-equilibration of  $\Delta_{47}$  only in contact

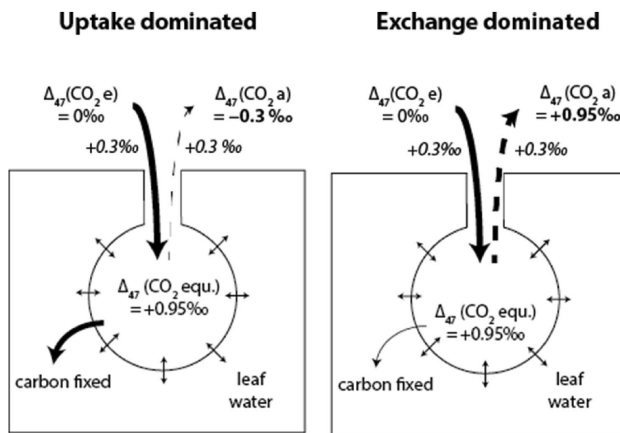


**Figure 2.5.:** This figure from Laskar and Liang, 2016 shows  $\Delta_{47}$  values for different environments and sources compared with thermodynamic equilibrium values (solid line). Note that the photosynthesis results contradict experiments and theoretical calculations by Eiler et al., 2004 and Adnew et al., 2021, which predict lower values than equilibrium.

## 2. Fundamentals

with atmospheric water (vapor). In contrast, as mentioned in section 2.2, equilibrium is nearly instantaneous for catalytic reactions involving the enzyme carbonic anhydrase, especially in leaves. Therefore, it is plausible that catalytic reactions involving carbonic anhydrase could lead to the rapid re-equilibration of  $\Delta_{47}$ , as *Eiler et al., 2004* and *Adnew et al., 2021* assumed for their leaf models.

Results on  $\Delta_{47}$  of *Laskar and Liang, 2016* for different environments and sources are shown in Figure 2.5. Combustion sources have low  $\Delta_{47}$  values [*Eiler et al., 2004; Affek et al., 2006; Laskar, Mahata, and Liang, 2016*]. Influenced samples (Urban; Figure 2.5) are likely to have  $\Delta_{47}$  values lower than expected for the current outside temperature. Environments with strong water interaction, such as marine and coastal environments, show  $\Delta_{47}$  values close to the expected equilibrium value [*Laskar and Liang, 2016*]. The values of *Laskar and Liang, 2016* for the influence of photosynthesis (Figure 2.5) contradict the experiments and calculations of *Eiler et al., 2004* and *Adnew et al., 2021*. *Adnew et al., 2021* states that photosynthesis should lead to  $\Delta_{47}$  values below the equilibrium temperature (“uptake dominated”, Figure 2.6). In cases where no carbon fixation takes place, the  $\Delta_{47}$  of the ambient air should approach the equilibrium temperature in the leaf (“exchange dominated”; Figure 2.6). *Laskar and Liang, 2016* states that respired  $\text{CO}_2$  is close to thermodynamic equilibrium with the water temperature of the source. *Eiler et al., 2004* supports this hypothesis for soil respiration; however, they also note that diffusion through soil could theoretically also lead to elevated  $\Delta_{47}$  values. It contradicts the calculations *Affek et al., 2007*, which yielded lower values for respiration (high uncertainty). Furthermore *Affek et al., 2014* hypothesize that an interaction between gas-phase and dissolved  $\text{CO}_2$  in an incomplete  $\text{CO}_2\text{-H}_2\text{O}$  equilibrium, caused by rapid diffusion or kinetic isotope effects, could also result in higher  $\Delta_{47}$  values. Moreover,



**Figure 2.6.:** Schematic illustration from *Adnew et al., 2021* on  $\Delta_{47}$  alteration during air-leaf exchange. Exemplarily shown for entering  $\Delta_{47}$  with  $0\text{‰}$  and leaf water temperature equivalent to  $\Delta_{47} = 0.95\text{‰}$ .  $\Delta_{47}$  of surrounding air is controlled by  $\text{CO}_2\text{-H}_2\text{O}$  exchange and kinetic fractionation into and out of leaf stomata. In uptake dominated cases,  $\Delta_{47}$  is reduced. In exchange-dominated cases, it is driven to thermodynamic equilibrium, corresponding to the temperature of leaf water.

it was shown that  $\Delta_{47}$  of human respired  $\text{CO}_2$  is slightly lower than expected from thermodynamic equilibrium [Eiler et al., 2004; Affek et al., 2006].

It should be noted that a mixture of  $\text{CO}_2$  from different sources does not behave linearly with respect to  $\Delta_{47}$  [Eiler et al., 2004; Affek et al., 2006; Laskar, Mahata, and Liang, 2016]. The greater the difference in the bulk isotopic composition of the mixed gases, the greater the effect of the non-linearity [Eiler et al., 2004; Defliese et al., 2015]. According to Eiler et al., 2004, however, this could also be used to constrain isotopically different end members.

## 2.4. Measurement Site, Weather Station & CRDS

Ambient air measurements conducted in this work were taken in Heidelberg, a medium-sized city with approximately  $\sim 162,000$  residents (2022) [Amt für Stadtentwicklung und Statistik, 2022] located in the southwestern part of Germany in the county of Baden-Württemberg (Figure 2.7 (a)). In the eastern part of the city, the Odenwald forest is located, which is divided at Heidelberg by the Neckar River (Figure 2.7 (b)). The western part extends into the Rhine Valley. The city's area is  $\sim 109 \text{ km}^2$ , with approximately 30.0 % of the area being urban, 40.5 % forest, and 26.2 % agricultural land (2022) [Amt für Stadtentwicklung und Statistik, 2022]. Heidelberg has a moderate climate. The average temperature in January is  $2.8^\circ\text{C}$ , and in July is  $20.8^\circ\text{C}$ , based on a 30-year average (1990-2020) [Deutscher Wetterdienst (DWD), 2023]. Approximately 436.7 kt of anthropogenic  $\text{CO}_2$  was emitted statistically by the Heidelberg city district in 2022 [Landesanstalt für Umwelt



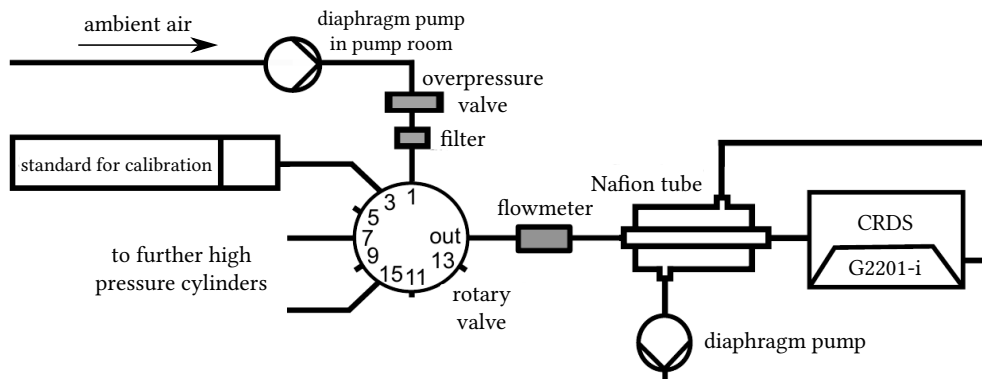
**Figure 2.7.:** Location of Heidelberg, Germany (a). Part of Heidelberg and the location of the Institute of Environmental Physics (IUP) (b). Surrounding area of the Institute of Environmental Physics (IUP) in Heidelberg (c). Sources for background images: (a) Copernicus, 2025 (b) LGL-BW, 2024b (c) LGL-BW, 2024a.

## 2. Fundamentals

*Baden-Württemberg (LUBW), 2022*]. According to *Hoheisel, 2021*, the CO<sub>2</sub> concentration in Heidelberg was on average (19±1 [SEM]) ppm higher than the Marine Boundary Layer (latitude range of 47° to 50° N) for the years 2014 to 2020.

The measurements were conducted at the Institute of Environmental Physics (IUP) (49°25'2" N, 8°40'28" E, 116 m above sea level; see Figure 2.7 (b) and (c)). An inlet for ambient air is located at the southeast corner of institute's roof at approximately 31 m above ground level (see Figure A.2; page 127). The ambient air is pumped into a pump room in the fifth floor of the institute via a diaphragm pump (PM 9967-035.1.2; KNF Neuberger, Freiburg, Germany), from which it is distributed to different laboratories. After the air is dried using a cooling unit set to -37 °C (ETK 50; LAUDA, Lauda-Königshofen, Germany), another diaphragm pump (LABOPORT N86; KNF Neuberger, Freiburg, Germany) pumps the air directly to the automatic preparation line in room 508 (see chapter 3). For this purpose, a ~ 40 m long 1/8" tube (TCC quality; Dockweiler, Neustadt-Glewe, Germany) was installed from the pump room to the laboratory in room 508 as part of this thesis.

In a similar way air is pumped to a different laboratory room, where a cavity ring-down spectrometer (CRDS) model G2201-i (Picarro, Santa Clara (CA), U.S.) is located. This instrument (continuously) measures the CO<sub>2</sub> concentration and  $\delta^{13}\text{C}$  of the ambient air. These data complement the results of the IRMS ambient air measurements ( $\delta^{13}\text{C}$ ,  $\delta^{18}\text{O}$ , and  $\Delta_{47}$ ) by providing the absolute CO<sub>2</sub> concentration, which cannot be determined using the IRMS. The air flowing into the CRDS is dried using a Nafion tube instead of the mentioned cooling unit. In 2022, an Allan variance analysis of raw data yielded a 10-minute precision of 0.012 ppm for the CO<sub>2</sub> concentration and 0.08 ‰ for  $\delta^{13}\text{C}$  [*Grandke, 2022*]. The raw data are calibrated at regular intervals of a few hours using single-point



**Figure 2.8.:** Setup for cavity ring-down spectrometer (CRDS) ambient air measurements. The air is pumped from the roof of the IUP to a pump room by a diaphragm pump and then to the laboratory with the CRDS by another diaphragm pump. For calibration, a rotary valve switches the air between the ambient air and air from a gas cylinder (calibration standard). The air is dried using a Nafion tube. [reproduced from *Cranton, 2023*]

calibrations, by switching to a high-pressure gas cylinder (calibration standard) via a 16-port rotary valve (see sketch Figure 2.8). Concentration measurements are calibrated with respect to the World Meteorological Organization X2007 scale [Zhao et al., 2006], and  $\delta^{13}\text{C}$  measurements are calibrated with respect to the VPDB scale. Further details on the calibration, data processing, measurement accuracy, and the CRDS setup (changed to Nafion tube in July 2022) can be found in Dinger, 2014; Hoheisel et al., 2019; Hoheisel, 2021; Grandke, 2022 and Cranton, 2023.

A weather station is located on a mast on the south side of the roof of the IUP. Temperature (Pt-1000 sensor) and humidity is measured at approximately 32 m above ground level. Wind (ultrasonic anemometer) and global radiation (CM11, Kipp & Zonen; Delft; Netherlands) are measured at approximately 37 m above ground level.

## 2.5. Isotope-Ratio Mass Spectrometer

An Isotope-Ratio Mass Spectrometer (IRMS) (MAT253+; Thermo Fisher Scientific, Waltham, Massachusetts, U.S.) is used to determine  $\delta^{13}\text{C}$ ,  $\delta^{18}\text{O}$ ,  $\Delta_{47}$ ,  $\Delta_{48}$ , and  $\Delta_{49}$  (Figure 2.9). Using the IRMS, the ionized molecules or atoms of a gas sample can be measured via seven Faraday cups at mass-to-charge ratios ( $m/z$ ):  $m/z$  44,  $m/z$  45,  $m/z$  46,  $m/z$  47,  $m/z$  47.5,  $m/z$  48, and  $m/z$  49. The Faraday cups are connected to high-impedance amplifier resistors, which have a resistance of  $10^{13}\ \Omega$  for  $m/z$  47-49. The additional Faraday cup at  $m/z$  47.5 is intended to allow monitoring of the background signal during the measurement process [e.g. Müller et al., 2017, Fiebig et al., 2019].

### 2.5.1. Physical Measurement Principle

This subsection refers in part to information from the user manual *Thermo Fisher Scientific*, 2016. The analyzer block (Figure 2.10 [1]) contains a cathode (filament) which ionizes the incoming molecules by the impact of the electrons produced. Subsequent to ionization, the molecules, which are no longer electromagnetically neutral, are accelerated and focused by a metal lens optic to which different potentials (up to 10 kV) are applied. A 0.75 T [*Thermo Fisher Scientific*, 2016] magnet (Figure 2.10 [2]) deflects and spreads out the ionized molecules. This occurs according to the ratio of the mass  $m$  and the charge  $z$  of the ionized molecules. Which is a consequence of the equivalence of the Lorentz force with the centripetal force:

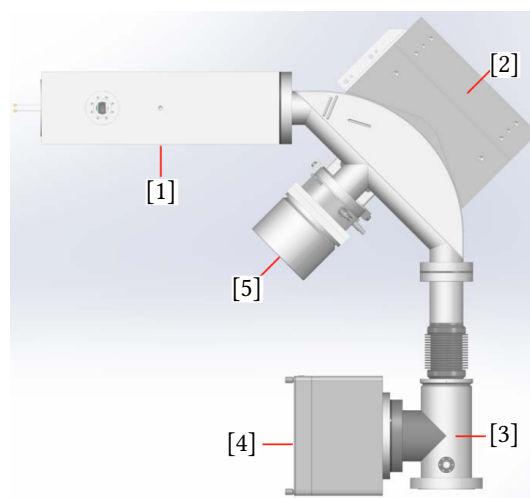
$$\frac{m}{z} = \frac{r^2 \cdot H^2}{2 \cdot U} \quad (2.28)$$

## 2. Fundamentals

The constant nominal radius  $r$  of the ion path is 23 cm [Thermo Fisher Scientific, 2016]. The magnetic field strength  $H$  and the accelerating voltage  $U$  can be adjusted to allow the desired ionized molecules to enter the Faraday cups, which are located in the analyzer housing (Figure 2.10 [3]). The resulting signal can subsequently be measured as a potential at the high-impedance amplifier resistors located within the amplifier housing (Figure 2.10 [4]).



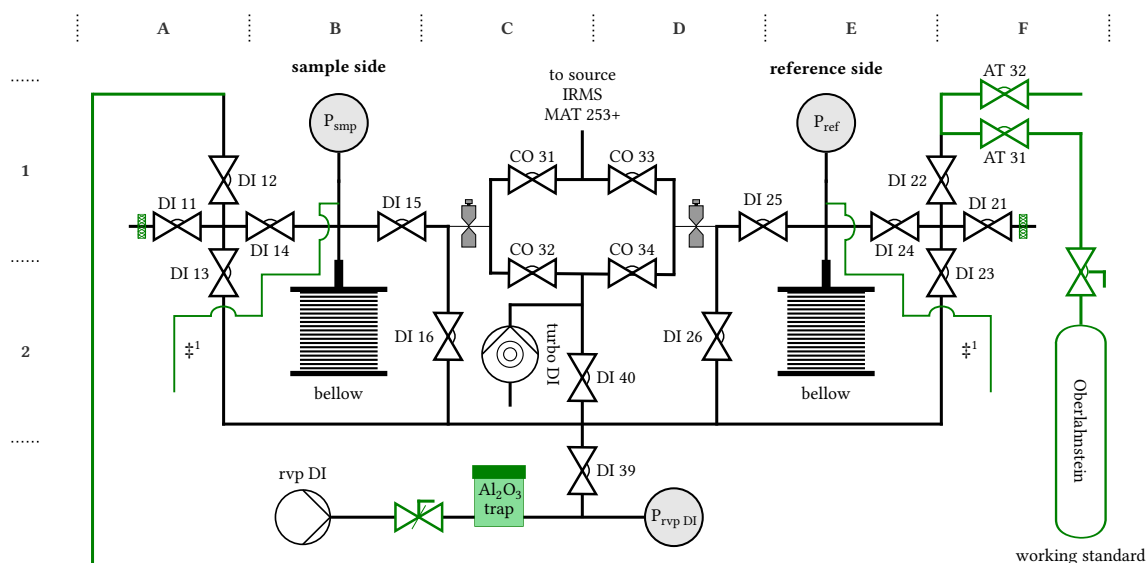
**Figure 2.9.:** The figure shows the MAT 253+ Isotope-Ratio Mass Spectrometer (IRMS) used. [Image: Thermo Fisher Scientific, 2016]



**Figure 2.10.:** [1]  $\hat{=}$  analyzer block, [2]  $\hat{=}$  magnet, [3]  $\hat{=}$  analyzer housing, [4]  $\hat{=}$  amplifier housing, [5]  $\hat{=}$  amplifier housing (hydrogen isotopes). [Image (edited): Thermo Fisher Scientific, 2016]

### 2.5.2. Dual Inlet Measurement Mode

The IRMS is used in the Dual Inlet (DI) mode. This setup consists of a sample side and a reference side, each of which is equipped with a bellow (see Figure 2.11). The sample bellow contains an unknown sample gas that is measured against a reference gas, known as the “working standard”. The working standard used here is called “Oberlahnstein”. It was originally obtained by dissolving marine limestone from Oberlahnstein, Germany [Neubert, 1998]. Its bulk isotopic composition is set to  $\delta^{13}\text{C} = -4.42 \text{ ‰}$  and  $\delta^{18}\text{O} = -9.79 \text{ ‰}$ . This gas has been used at the IUP for decades as a working standard and in many interlaboratory comparisons [e.g. Neubert, 1998; Worthy et al., 2023]. It has been measured against International Atomic Energy Agency (IAEA) standards and in intercomparisons with the Max Planck Institute for Biogeochemistry (MPI-BGC) in Jena multiple times [Ghosh et al., 2005; World Meteorological Organization, 2014].



**Figure 2.11.:** The figure shows a schematic of the Dual Inlet setup used. The sample side is on the left, and the reference side is on the right, along with the corresponding bellows. The green color indicates components that were added to the original system during the work. This includes two 1/8" single-sided welded stainless steel tubes that serve as traps  $\ddagger^1$  and are directly connected to the bellows volumes (see chapter 3).

During the measurement process, gases flow from the bellows through capillaries to the changeover valves. These valves alternate between measuring the sample gas and the working standard. Both signals are measured over a specified “integration time”. This is preceded by an “idle time”, during which no data is recorded and the signal stabilizes as the gas in the source is replaced. The transition from reference to sample to reference is called a “cycle”. A measurement consists of one or more “acquisitions”, each of which consists of several cycles. An acquisition begins and ends with a working standard measurement. At the start of an acquisition, the bellows are usually adjusted to produce a similar signal at  $m/z$  44. Each acquisition begins with a “peak center” on Faraday cup 2. For the first acquisition, a background noise measurement is conducted without gas.

### 2.5.3. Data Storage and Processing

The IRMS MAT253+ is controlled by the software “Isodat” (Version 3; Thermo Fisher Scientific, Waltham, Massachusetts, U.S.). As part of the software adjustments conducted in this work, in addition to the intensities measured at  $m/z$  44 to 49, further metadata is now stored in the output files from Isodat (format: .did). This includes information about preparation, timestamps, and pressure in the analyzer. An R script that incorporates code from the GitHub repository “Isoread” (<https://github.com/sebkopf/isoread>) is used to read these files. The script is used in combination with gnuplot for data evaluation.



## 2. Fundamentals

### 2.5.4. Measurement Protocol

Initially, the measurement protocol consisted of eight acquisitions with ten cycles each. The integration time was 26 seconds, and the idle time 15 seconds. Between each acquisition, the bellows were adjusted to an intensity of 6 V at m/z 44 [see e.g. *Kalb et al., 2020; Weise et al., 2020*].

To increase the cumulative integration time, the measurement protocol was modified at the end of January/beginning of February 2024. The bellow adjustment was modified to yield 8 V at m/z 44. The integration time increased to 200 seconds, while the number of cycles and acquisitions decreased to minimize time lost adjusting the bellows and during idle time. In the final setup, one acquisition with 20 cycles was used. The integration time has been divided into two-second slices. Forming intensity ratios of m/z 45 to 49 and m/z 44 on this smaller timescale reduced dependence on intensity decay and simultaneous signal fluctuations. This also enabled filtering the data using a median absolute deviation filter. The mean values obtained were used for further data processing.

Appendix A.3 (page 130) provides an overview of the differences between the measurement protocols and how the data was transferred from the old protocol to the new one for joint calibration.

### Differences in Reproducibility between Measurement Protocols

Repeated measurements of the “Pic\_8\_1” gas cylinder were used to compare the two measurement protocols. The total measurement time was 2 hours and 35 minutes using the old protocol and 2 hours and 32 minutes (17 cycles) using the new one. These times included pressure adjustments, determining the peak center, and measuring the background noise and control masses at m/z 18, 40, and 30 (see below). The total integration time for the sample increased from 2,080 to 3,400 seconds. The external reproducibility, calculated using the standard deviation (SD) of 18 measurements conducted between 19 and 27 January 2024 using the old protocol, yielded the following results in the laboratory frame (LF):  $\Delta_{47}^{LF} \approx 0.017 \text{ ‰}$ ,  $\Delta_{48}^{LF} \approx 0.046 \text{ ‰}$  and  $\Delta_{49}^{LF} \approx 0.67 \text{ ‰}$ . Seven measurements taken between 2 and 10 February using the new protocol yielded the following results:  $\Delta_{47}^{LF} \approx 0.011 \text{ ‰}$ ,  $\Delta_{48}^{LF} \approx 0.031 \text{ ‰}$  and  $\Delta_{49}^{LF} \approx 0.45 \text{ ‰}$ . The  $\Delta_{48}^{LF}$  and  $\Delta_{49}^{LF}$  data were corrected for the dependence of the m/z 44 intensity difference between the sample gas and the working standard (see appendix A.5 on page 135). The reproducibility of  $\delta^{13}\text{C}$  and  $\delta^{18}\text{O}$  remained unchanged. When using such long measurement times to determine them, external factors influence the results more than measurement statistics do.



### 2.5.5. Control Parameters

To evaluate the purity of the sample and apply an  $N_2O$  correction (see section 4.1), if necessary, the intensities at  $m/z$  18, 40, and 30 were measured. In the new protocol, this occurs at the beginning of the first acquisition; in the old protocol, it occurs at the end. Additionally, the new protocol includes measuring  $m/z$  30 for the working gas. These measurements are performed at the beginning to evaluate the quality of the processing performed by the automatic preparation line described in chapter 3. Furthermore, time was saved by eliminating the need to switch between the working standard and the sample by including the measurement just after the respective bellow was adjusted. The following description is only about the new measurement protocol.

In addition to  $m/z$  18, which corresponds to the mass of water, and  $m/z$  40, which corresponds to argon and indicates air impurities,  $m/z$  49 is assessed. If the signals are above specific benchmarks, the measurement does not begin, and the system enters a secure state. The expected intensity at  $m/z$  49 for prepared  $CO_2$  for clumped isotope measurements is below 0 mV.

To make the measured intensities  $I$  of the control parameters more comparable across different measurements, the following ratios were formed to minimize their dependence on the amount of gas flowing into the ion source:

$$^{18}R = \frac{I_{18}}{I_{44}} , \quad ^{40}R = \frac{I_{40}}{I_{44}} , \quad ^{30}R = \frac{I_{30}}{I_{44}} . \quad (2.29)$$

$I_{44}$  is the mean obtained from a short measurement at  $m/z$  44, taken before and after measuring the control parameters. The additional measurement at  $m/z$  30 for the working gas enables the formation of the following expression:

$$^{30}\Lambda = \frac{^{30}R}{^{30}R_{\text{reference}}} = \frac{I_{30}/I_{44}}{I_{30, \text{reference}}/I_{44, \text{reference}}} . \quad (2.30)$$

In comparison to  $^{30}R$ , the advantage is a more stable value over time (see section 4.1).

## 2. Fundamentals

### 2.5.6. Practical Calculation of $\delta^{13}\text{C}$ , $\delta^{18}\text{O}$ , $\Delta_{47}^{\text{LF}}$ , $\Delta_{48}^{\text{LF}}$ , and $\Delta_{49}^{\text{LF}}$

For simplicity, the practical calculation of  $\delta^{13}\text{C}$ ,  $\delta^{18}\text{O}$ ,  $\Delta_{47}^{\text{LF}}$ ,  $\Delta_{48}^{\text{LF}}$ , and  $\Delta_{49}^{\text{LF}}$  is explained without considering slice levels and cycles, calculating mean values and uncertainties, filtering data, or applying other corrections.

The first step in evaluating the data is a background correction, which is referred to in the literature as pressure baseline (PBL) correction [He et al., 2012]. This correction is applied to the intensities measured at m/z 44 to 49 as a function of the intensity measured at m/z 47.5 (see appendix A.4 on page 132 for further details).

Next, the background-corrected intensities at m/z 45 to 49 are divided by the intensity measured at m/z 44 to form the following ratios:

$$^{45}R_{\text{mv}} = \frac{I_{45}}{I_{44}}, \quad ^{46}R_{\text{mv}} = \frac{I_{46}}{I_{44}}, \quad ^{47}R_{\text{mv}} = \frac{I_{47}}{I_{44}}, \quad ^{48}R_{\text{mv}} = \frac{I_{48}}{I_{44}}, \quad ^{49}R_{\text{mv}} = \frac{I_{49}}{I_{44}}. \quad (2.31)$$

The subscript “mv” indicates that this is the ratio of ions collected at m/z 45 to 49 to those collected at m/z 44. This differs from the abundance ratio of molecules with these masses [see e.g. Brand et al., 2010]. These ratios Equation (2.31) are calculated for both the sample and the working (reference) gas. The reference gas is measured twice per cycle: once before (reference before) and once after the sample gas (reference after). The following relative deviations are then calculated using bracketing:

$$^{45}\delta = \frac{^{45}R_{\text{mv}}}{(^{45}R_{\text{mv, reference before}} + ^{45}R_{\text{mv, reference after}})/2} - 1, \quad (2.32)$$

$$^{46}\delta = \frac{^{46}R_{\text{mv}}}{(^{46}R_{\text{mv, reference before}} + ^{46}R_{\text{mv, reference after}})/2} - 1, \quad (2.33)$$

$$^{47}\delta = \frac{^{47}R_{\text{mv}}}{(^{47}R_{\text{mv, reference before}} + ^{47}R_{\text{mv, reference after}})/2} - 1, \quad (2.34)$$

$$^{48}\delta = \frac{^{48}R_{\text{mv}}}{(^{48}R_{\text{mv, reference before}} + ^{48}R_{\text{mv, reference after}})/2} - 1, \quad (2.35)$$

$$^{49}\delta = \frac{^{49}R_{\text{mv}}}{(^{49}R_{\text{mv, reference before}} + ^{49}R_{\text{mv, reference after}})/2} - 1. \quad (2.36)$$

This step cancels out the mass spectrometric sensitivity factors that are valid for both the sample and the reference [see e.g. Brand et al., 2010]. Therefore,  $^{45}\delta$  to  $^{49}\delta$  in equations (2.32) to (2.36) equals the relative deviation in abundance ratio between the sample and the reference at a given mass:

$$^{45}\delta = \frac{^{45}R}{^{45}R_{\text{reference}}} - 1, \quad (2.37)$$

$$^{46}\delta = \frac{^{46}R}{^{46}R_{\text{reference}}} - 1 , \quad (2.38)$$

$$^{47}\delta = \frac{^{47}R}{^{47}R_{\text{reference}}} - 1 , \quad (2.39)$$

$$^{48}\delta = \frac{^{48}R}{^{48}R_{\text{reference}}} - 1 , \quad (2.40)$$

$$^{49}\delta = \frac{^{49}R}{^{49}R_{\text{reference}}} - 1 . \quad (2.41)$$

However, it is probably only possible to completely eliminate all mass spectrometric effects in equations (2.32) to (2.36) if, in particular, the signal measured at  $m/z$  44 is identical for the sample and the reference. This assumption is based on a observed dependence of  $^{45}\delta$  to  $^{49}\delta$  on the imbalance at  $m/z$  44 between the sample and the reference (cf. Figure A.8; page 140). Additionally, a further term was identified for  $^{46}\delta$  at least. This appears to depend on the absolute value of  $^{46}\delta$  in combination with the signal height at  $m/z$  44 (cf. Figure A.6; page 138). This suggests that significant differences in bulk isotopic composition between sample and reference result in an additional effect that is not fully canceled out, particularly for  $^{46}\delta$ . *Fiebig et al., 2016* for  $\Delta_{47}$  and *Bernecker et al., 2023* for  $\Delta_{47}$  and  $\Delta_{48}$  have demonstrated that the PBL correction almost completely eliminates dependence on imbalances at  $m/z$  44. Therefore, based on these and own observations, effects dependent on this imbalance can probably be eliminated, or at least partially compensated for, by an optimized PBL correction. The observed dependence on the imbalance and the corrections made in the context of the evaluation are discussed in more detail in appendix A.5 on page 135. Nevertheless, it is at least a very good approximation to assume that mass spectrometric effects cancel out in equations (2.32) to (2.36), resulting in equivalence with equations (2.37) to (2.41).

Therefore, adding one to  $^{45}\delta$  to  $^{49}\delta$  (obtained from Equations (2.32) to (2.36)), then multiplying  $^{45}R_{\text{reference}}$  to  $^{49}R_{\text{reference}}$ , results in  $^{45}R$  to  $^{49}R$ , respectively.  $^{45}R_{\text{reference}}$  to  $^{49}R_{\text{reference}}$  are calculated from the known isotopic values of the working gas (assuming  $\Delta^{17}\text{O} = 0$ ) using following equations [see *Sanrock et al., 1985*]:

$$^{45}R_{\text{stoch}} = ^{13}R + 2 \cdot ^{17}R , \quad (2.42)$$

$$^{46}R_{\text{stoch}} = 2 \cdot ^{18}R + 2 \cdot ^{13}R \cdot ^{17}R + (^{17}R)^2 , \quad (2.43)$$

$$^{47}R_{\text{stoch}} = ^{13}R \cdot (^{17}R)^2 + 2 \cdot ^{13}R \cdot ^{18}R + 2 \cdot ^{17}R \cdot ^{18}R , \quad (2.44)$$

$$^{48}R_{\text{stoch}} = (^{18}R)^2 + 2 \cdot ^{13}R \cdot ^{17}R \cdot ^{18}R , \quad (2.45)$$

$$^{49}R_{\text{stoch}} = ^{13}R \cdot (^{18}R)^2 . \quad (2.46)$$

## 2. Fundamentals

However, this is only an approximation because the working gas is not under a stochastic distribution. For masses 45 and 46, though, it is a good approximation, as demonstrated in Figure 2.4 on page 16. For masses  $\geq 47$ , however, it is grossly wrong, as shown in the same figure. This causes an offset in  $\Delta_{47}^{\text{LF}}$  to  $\Delta_{49}^{\text{LF}}$ . However, the calibration described in section 4.3 compensates for that.

Now, applying  $^{45}\text{R}$  and  $^{46}\text{R}$  to Equations (2.42) and (2.43), along with Equation (2.2) from page 9, enables the calculation of  $^{13}\text{R}$ ,  $^{17}\text{R}$ , and  $^{18}\text{R}$ .  $\Delta^{17}\text{O}$  is assumed to be zero [see e.g. *Santrock et al.*, 1985; *Brand et al.*, 2010]. As for the reference, the sample is typically not distributed stochastically. The same argument applies, however, and using these equations is an acceptable approximation for masses 45 and 46. This system of equations is solved analytically using a second-order Taylor polynomial, as proposed by *Daëron et al.*, 2016. The calculation of  $\delta^{13}\text{C}$  and  $\delta^{18}\text{O}$  is then performed using Equation (2.1) from page 8. According to *Daëron et al.*, 2016, this analytical approach enables the determination of  $\delta^{13}\text{C}$ ,  $\delta^{18}\text{O}$ , and  $\Delta_{47}^{\text{LF}}$  with an accuracy better than 0.02 ppm. This is well below the achieved reproducibility of about 0.005 ‰ for  $\delta^{13}\text{C}$ , 0.01 ‰ for  $\delta^{18}\text{O}$ , and 0.009 ‰ for  $\Delta_{47}^{\text{LF}}$  (see section 4.4).

Finally,  $\Delta_{45}^{\text{LF}}$  to  $\Delta_{49}^{\text{LF}}$  are calculated using Equation (2.25) from page 15. Equations (2.42) to (2.46) are applied to calculate  $^{45}\text{R}_{\text{stoch}}$  to  $^{49}\text{R}_{\text{stoch}}$  using the just-determined  $\delta^{13}\text{C}$  and  $\delta^{18}\text{O}$  of the sample gas. Equation (2.2) from page 9 is used again, and  $\Delta^{17}\text{O}$  is assumed to be zero.  $^{45}\text{R}$  to  $^{49}\text{R}$  obtained from  $^{45}\delta$  to  $^{49}\delta$  are used in the numerator of Equation (2.25). Since  $^{45}\text{R}$  and  $^{46}\text{R}$  were also used to determine  $\delta^{13}\text{C}$  and  $\delta^{18}\text{O}$ ,  $\Delta_{45}^{\text{LF}}$  and  $\Delta_{46}^{\text{LF}}$  are constrained to mathematically equal zero. Because this step was unavoidable, this type of mass spectrometer is unable to determine the temperature dependency of  $\Delta_{45}$  and  $\Delta_{46}$ . Alternative definitions of  $\Delta_{47}$ ,  $\Delta_{48}$ , and  $\Delta_{49}$ , which are widely used, include terms containing  $\Delta_{45}$  and  $\Delta_{46}$  [e.g. *Affek et al.*, 2006; *Huntington et al.*, 2009; *Dennis et al.*, 2011; *Fiebig et al.*, 2019; *Swart et al.*, 2021]. Consequently, as *Daëron et al.*, 2016 also pointed out, these must be zero. As *Olack et al.*, 2019 and *Saenger et al.*, 2021 noted that deviations from zero occur when mixed sets of parameters are used. For example, this occurs when  $\delta^{13}\text{C}$  and  $\delta^{18}\text{O}$  are reported by mass spectrometric software that uses different international standard reference values than those used in subsequent evaluations.

The final reported values of  $\delta^{13}\text{C}$ ,  $\delta^{18}\text{O}$ ,  $\Delta_{47}^{\text{LF}}$ ,  $\Delta_{48}^{\text{LF}}$ , and  $\Delta_{49}^{\text{LF}}$  in this thesis are given as weighted means, along with their respective weighted standard errors (SEM), calculated over all cycles and acquisitions of a measurement. A median absolute deviation filter was applied beforehand to exclude outliers. The uncertainties used for weighting were propagated throughout the entire calculation using Gaussian error propagation.

## 3. Automatic Preparation Line for Atmospheric CO<sub>2</sub>

This chapter describes and characterizes the automatic CO<sub>2</sub> preparation line built in this thesis, which is referred as Air Trap (AT). The aim was to build a fully automated system to process ambient air samples to enable high-reproducible  $\delta^{13}\text{C}$ ,  $\delta^{18}\text{O}$ , and  $\Delta_{47}$  measurements. Figure 3.2 shows pictures of the Air Trap, including the IRMS MAT 253+. A technical drawing of the entire structure, including the Dual Inlet system of the IRMS MAT253+, is given in Figure 3.3. Coordinates [A1] to [F8] given in the following text and appendix B always refer to this graphic.

### 3.1. Conceptual Function and Construction

The concept for the construction of the Air Trap is based on several published approaches, a visit to the Max Planck Institute for Biogeochemistry (MPI-BGC) and the Flask and Calibration Laboratory in Jena, as well as a visit to Utrecht University [e.g. *Werner et al.*, 2001; *Eiler et al.*, 2004 & *Affek et al.*, 2006; *Kalb*, 2015; *Eckhardt*, 2019; *Adnew et al.*, 2021].

The Air Trap's underlying construction is based on the system described in *Werner et al.*, 2001, which was initially installed at Climate and Environment Sciences Laboratory (*Laboratoire des sciences du climat et de l'environnement*, LSCE) in 2005 through a collaborative effort between the MPI-BGC in Jena and the LSCE in Saclay. In 2019, it was transferred to the IUP, where it underwent an upgrade to enable automated preparation of  $\Delta_{47}$  from atmospheric CO<sub>2</sub> samples.

In the following, the preparation of an ambient air sample is conceptually described using Figure 3.1, which illustrates the final concept of the Air Trap. This graphic is to be read from left to right, beginning at “Start”.

The first processing step, referred to as the “AT step”, essentially follows the concept of *Werner et al.*, 2001. In this step, a flow controller regulates the ambient air that enters the processing line. The air then passes through the so-called “H<sub>2</sub>O trap”, which is immersed in a mixture of ethanol and dry ice (−72 °C) to freeze out water vapor. Next, the air flows

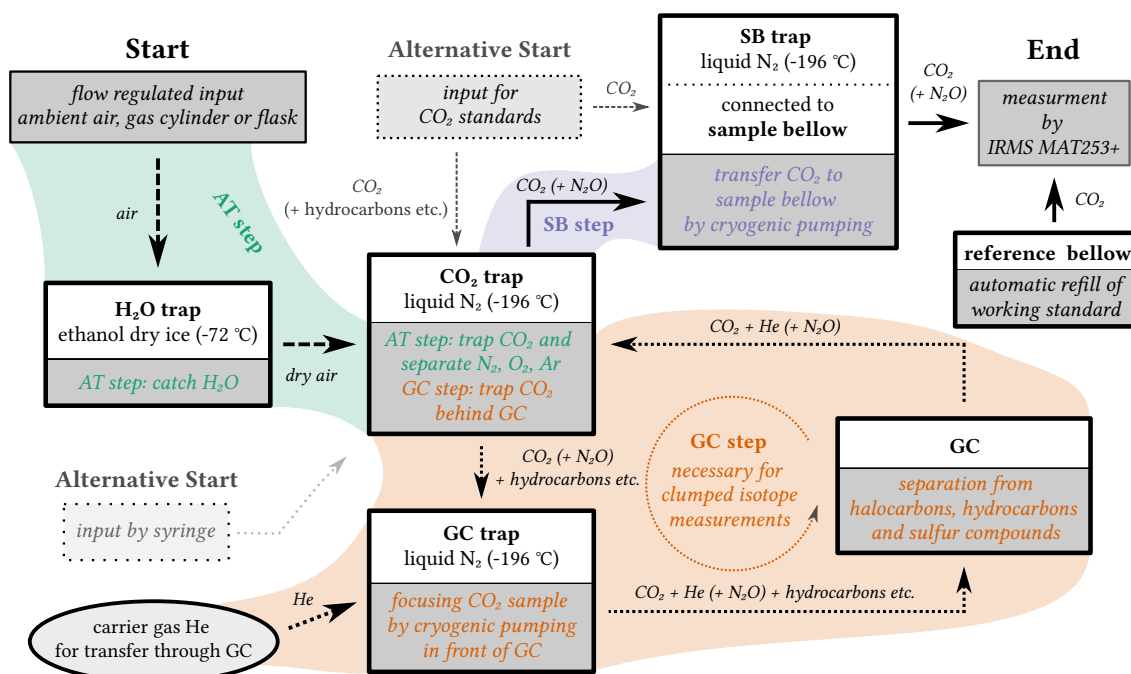
### 3. Automatic Preparation Line for Atmospheric CO<sub>2</sub>

through the so-called “CO<sub>2</sub> trap”, which is cooled with liquid nitrogen (–196 °C). In this trap, CO<sub>2</sub>, N<sub>2</sub>O, as well as some hydrocarbons, halocarbons, and sulfur compounds freeze. O<sub>2</sub>, N<sub>2</sub>, and Ar pass through the trap and are pumped out. At this stage, the processed CO<sub>2</sub> could be transferred directly to the IRMS for measurement of  $\delta^{13}\text{C}$  and  $\delta^{18}\text{O}$ .

However, clumped isotopes analysis requires additional separation of halocarbons, hydrocarbons and sulfur compounds [e.g. *Eiler et al.*, 2004]. To achieve this, in the next step, which is referred to as the “GC step”, a gas chromatograph (GC) equipped with a glass capillary filled with a porous divinylbenzene polymer is employed. First, the sample is cryogenically pumped into the so-called “GC trap”, which is used to focus the sample in front of the GC column. After passing through the GC using helium as a carrier gas, the sample is trapped again by the “CO<sub>2</sub> trap”, while the carrier gas is pumped out.

In the final “SB step”, the sample is cryogenically pumped into the sample bellow of the Dual Inlet System of the IRMS MAT253+ using the “SB trap”. After sublimation and automated filling of the reference bellow with the working standard “Oberlahnstein”, the measurement process starts.

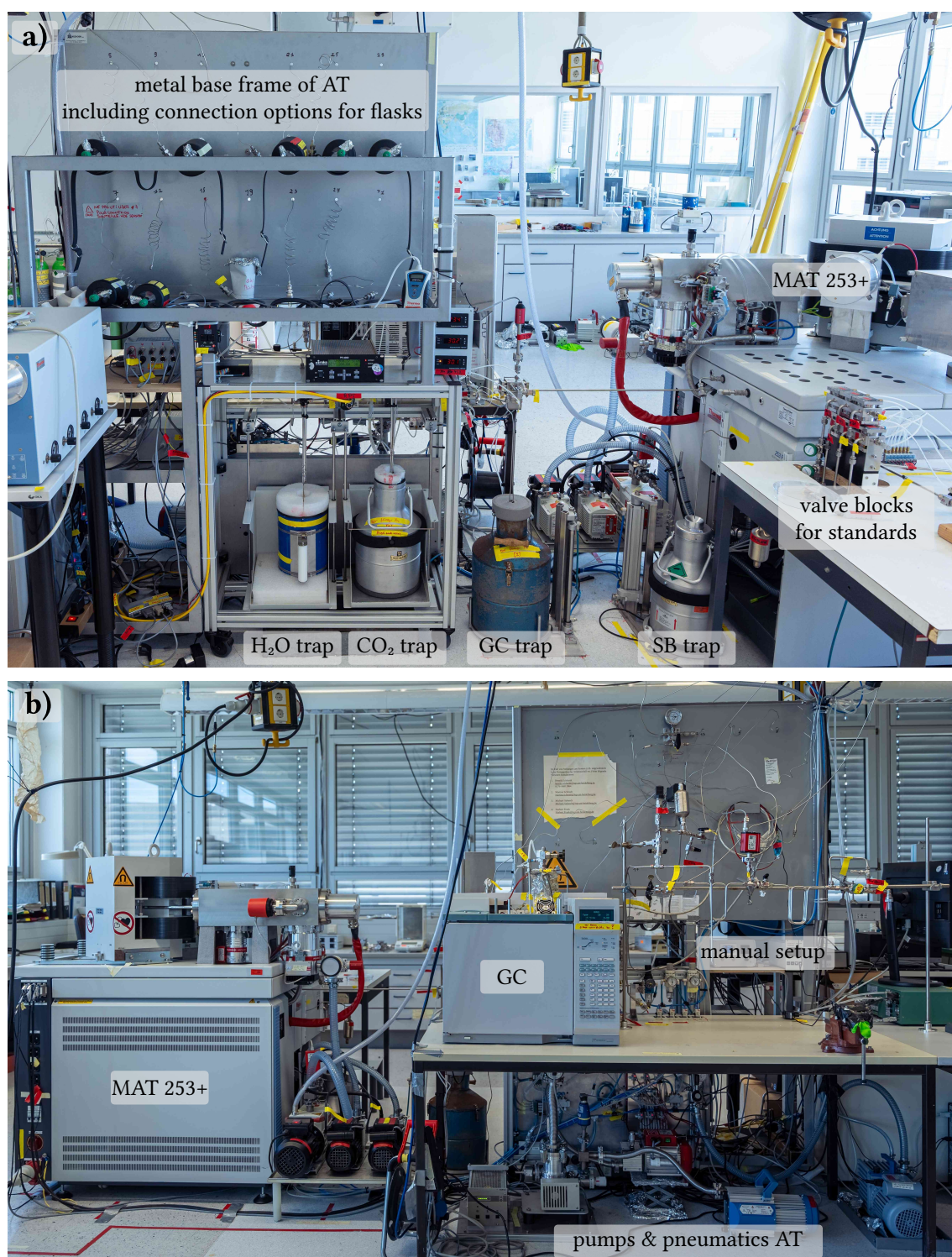
In addition, there is an optional access via a syringe as well as valve blocks for the direct connection of temperature-equilibrated CO<sub>2</sub> standards.



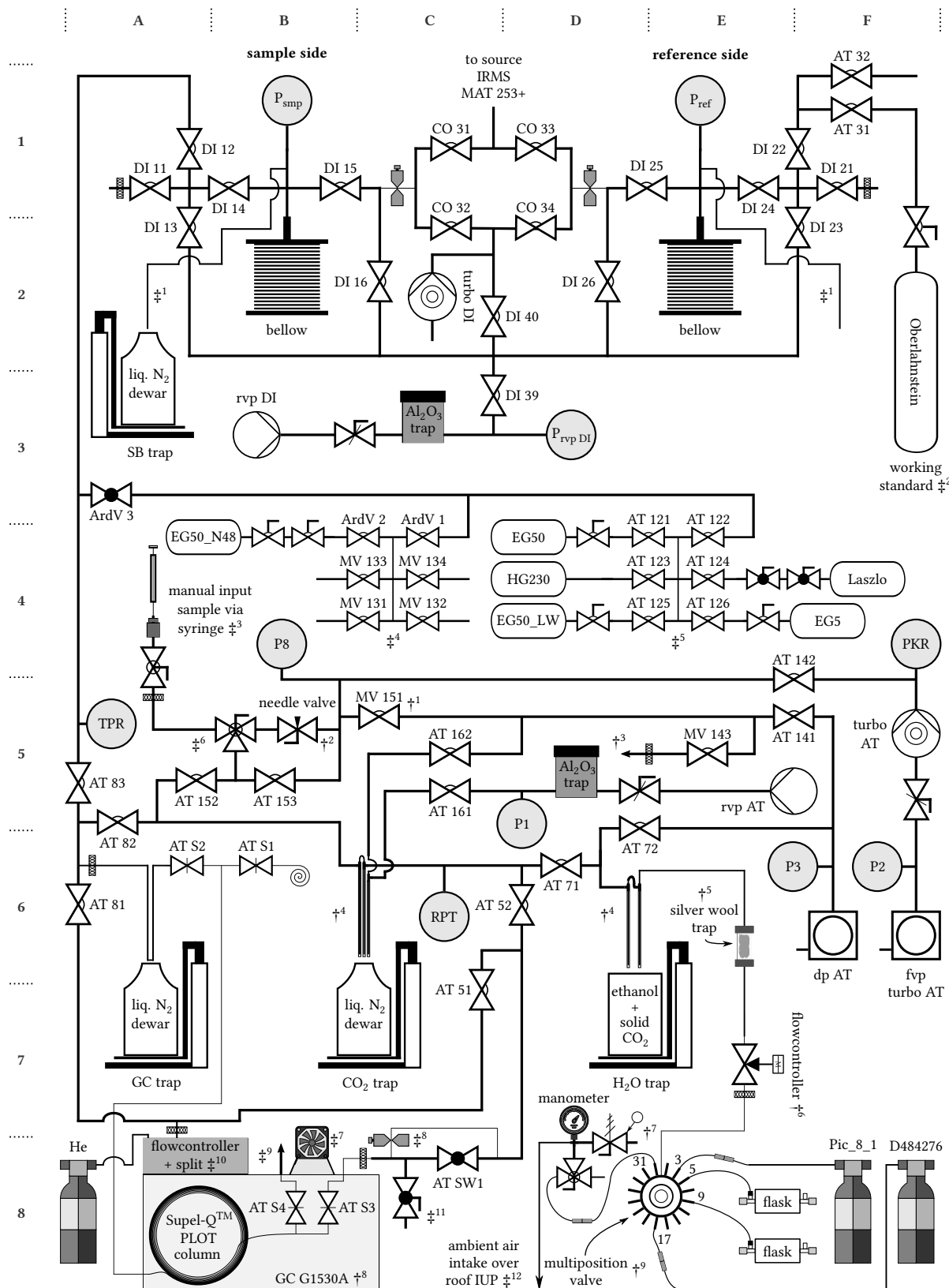
**Figure 3.1.:** The diagram shows the final concept for the construction of the Air Trap (AT) and should be read from left to right. The GC step is required for the measurement of clumped isotopes and can be omitted for the pure measurement of  $\delta^{13}\text{C}$  and  $\delta^{18}\text{O}$ .



### 3.1. Conceptual Function and Construction




















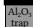

**Figure 3.2.:** The images show the overall structure of the Air Trap (AT), including the IRMS MAT 253+. Image (a) shows the traps, the connection options for flasks and the valve blocks for connecting temperature-equilibrated CO<sub>2</sub> standards. Image (b) shows the GC, the pneumatic control and the pumps of the Air Trap as well as a manual setup, which was used for preparation of temperature-equilibrated CO<sub>2</sub> standards.



**Figure 3.3.:** A legend and the caption can be found on the next page. Further information with reference to † can be found in the legend and occasionally in the text. ‡ refers to further information only in the text.




### Legend and further information on Figure 3.3.

Valves		diaphragm valve (pneumatically actuated valves that have gold stamps and gold seals)		needle valve [B5]
		globe valve	$\dagger^2$	<i>This valve is set manually so that a pressure of ~100 mbar is maintained in the CO<sub>2</sub> trap during the AT step.</i>
		ball valve		pressure relief valve [E7-8]
		butterfly valve	$\dagger^7$	<i>This valve is set using the manometer next to it so that there is an overpressure of 1 bar at port 31.</i>
		MOVP valve [A6,B6,B8]		
		Valves with this symbol  are operated directly by hand. All other valves are pneumatically actuated.		
		With exception of valves: ArdV3, AT SW1, AT S1 - AT S4, all pneumatically actuated valves are normally open.		
Pumps		rotary vane pump (rvp)		diaphragm pump (dp)
		turbo molecular pump (turbo)		
Further Symbols		pressure gauge		filter
		crimp		stainless steel sample container
		Al <sub>2</sub> O <sub>3</sub> trap to catch gases flowing back from rotary vane pump		10 µm filter screen
Additional Information	$\dagger^1$	The pneumatic head of MV 151 is not connected to a solenoid valve and is always open - installed due to an earlier design approach.		
	$\dagger^3$	Manual access for evacuating flasks or a manual setup.		
	$\dagger^4$	The freezing fingers consist of an outer 1/4" stainless steel tube with an inner 1/8" stainless steel tube (design according to Werner et al., 2001). The freezing finger on the right of the CO <sub>2</sub> trap only connects AT 161 with AT 162 and is used to retain vapor residues when pumping with the rvp AT.		
	$\dagger^5$	This trap containing silver wool is used to trap elemental S and H <sub>2</sub> S (appendix B.8; p. 150).		
	$\dagger^6$	This flow controller (MKS, Andover, Massachusetts, U.S.) is set to 100 ml/min and, in addition to the needle valve $\dagger^2$ , should guarantee a constant pressure of ~100 mbar in the CO <sub>2</sub> trap during the AT step (appendix B.7; 149).		
	$\dagger^8$	This GC (G1530A, Agilent, Santa Clara, CA, U.S.) is equipped with a fused silica capillary (L × I.D. 30 m × 0.53 mm, Supel-Q™PLOT, Sigma-Aldrich, Burlington, Massachusetts, U.S.) and is used to separate trace substances such as SO <sub>2</sub> and hydrocarbons from CO <sub>2</sub> (section 3.2).		
	$\dagger^9$	This is a 32 port multiposition valve (VICI, Schenkon, Switzerland), whereby every second port is blind and serves as an intermediate step. This allows samples to be introduced into the AT via flasks, gas cylinders or ambient air over a line to the roof of the IUP $\dagger^{12}$ .		
	Dual Inlet (DI)	Change Over (CO)	Air Trap (AT)	
	sample bellow (SB)	reference bellow (RB)	fore vacuum pump (fvp)	

**Figure 3.3.:** (Previous page.) This figure shows a schematic representation of the automatic preparation line built in this work for the measurement of  $\delta^{13}\text{C}$ ,  $\delta^{18}\text{O}$  and  $\Delta_{47}$  from ambient air samples. The lower part of the technical drawing essentially shows the preparation line including pneumatic traps, the GC, pumps and the inlet via a multiposition valve. The middle part of the diagram shows valve blocks to which temperature-equilibrated CO<sub>2</sub> standards in stainless steel sample vessels have been connected. In the upper part of the picture the Dual Inlet system of the MAT253+ IRMS is shown.

### 3. Automatic Preparation Line for Atmospheric CO<sub>2</sub>

The system was set up between June 2019 and June 2024 on the fifth floor of the IUP. It was built upon the existing preparation line from LSCE, with some reused components such as the metal base frame, multiposition valve, and flow controller (see Figure B.20 on page 178 for initial setup). A comparison with the classic Dual Inlet setup, which was available prior to the thesis, is accessible via the interactive panel  in Figure 3.3 and shown in Figure B.21 on page 179.

The following section provides a more detailed description of the gas chromatograph (GC) used. Further details on other components, along with information on programming, operation, and more, can be found in appendix B.

#### Components:

- Tubing & Connection Elements (appendix B.1; page 141)
- Pneumatically actuated Valves (appendix B.2; page 142)
- Pumps (appendix B.3; page 144)
- Cold Traps (appendix B.4; page 145)
- Multifunctional Device (appendix B.5; page 147)  
*monitors pressure sensors and laboratory parameters, and fulfills safety-related functions*
- Pressure Sensors (appendix B.6; page 148)
- Mass Flow Controller (appendix B.7; page 149)
- Silver Wool Trap (appendix B.8; page 150)
- Multiposition Valve, Gas Cylinders & Ambient Air Access (appendix B.9; page 151)
- Injection via Syringe & External Access to Pump Unit (appendix B.10; page 153)
- Valve Blocks for Standards (appendix B.11; page 154)  
*includes Table B.1, which lists  $\delta^{13}\text{C}$ ,  $\delta^{18}\text{O}$ , and  $\Delta_{47}$  of temperature-equilibrated standards and gas cylinders “Pic\_8\_1” and “D484276”*

#### Other topics:

- Programming (appendix B.12; page 156)
- Security Features and Error Handling (appendix B.13; page 157)
- Operation (appendix B.14; page 159)
- Automatic Reference Refill (appendix B.15; page 163)
- Determination of actual Bellow Volumes (appendix B.16; page 166)  
*correction of incorrect readout by mass spectrometer software*
- Drift of  $\delta^{13}\text{C}$  &  $\delta^{18}\text{O}$  with Number of Reference Refills (appendix B.17; page 169)
- Duration of Preparation & Measurement (appendix B.18; page 173)
- Experiment on Reusing Reference Gas (appendix B.19; page 174)
- Experiment on “Flush Time” in AT step (appendix B.20; page 176)
- Test on Ambient Air Intake Line (appendix B.21; page 177)

## 3.2. Gas Chromatograph and GC Step

Nowadays, many laboratories that measure clumped isotopes in CO<sub>2</sub> (mostly from carbonates) use either static Porapak™Q traps or gas chromatographs (GC's) equipped with Porapak™Q meshes or suitable capillary columns to separate halocarbons, hydrocarbons, and sulfur compounds from CO<sub>2</sub> samples. For this purpose, these setups are usually cooled below 0 °C during this cleaning step [see *Petersen et al.*, 2016 (Table 1)]. However, *Eiler et al.*, 2004 had already shown that this is possible at room temperature in principle.

The setup used here employs a GC G1530A (Agilent Technologies, Santa Clara, CA, USA; see Figure 3.4). It is equipped with the same fused silica capillary filled with a porous divinylbenzene polymer that *Affek et al.*, 2006 selected for their setup (L×I.D.30m×0.53mm, Supel-Q™PLOT, Sigma-Aldrich, Burlington, Massachusetts, U.S.).

The manufacturer stated that this column effectively dissolves carbon dioxide and C1-C4 hydrocarbons above room temperature and pointed out the possible separation of SO<sub>2</sub>. The latter could affect measurements of m/z 48 and 49 over the fragment SO.

In the final setup, this processing step was successfully performed at 30 °C.

### 3.2.1. Structure

The integration of the GC into the preparation line is illustrated in Figure 3.4. In b), an exhaust air stack is visible at the exit. This was added on April 25, 2024, with the objective of preventing the outgoing warm air from blowing at the height of the detector electronics of the IRMS MAT253+. Since the original GC was designed for injection with a syringe, the three-part outlet of the flow controller  $\frac{1}{4}$ "<sup>10</sup> used for the carrier gas helium (ALPHAGAZ™ 2, 99,9999% He; Air Liquide Deutschland, Düsseldorf, Germany) had to be modified and is now routed as a joined outlet to valves AT 81 [A6] and AT 51 [C6/7].

Figure 3.5 shows the inside of the GC oven with the installed fused silica capillary. On the right side of the image, the valves AT S3 and AT S4 [B8] are shown, which were placed directly into the GC to minimize dead volume and facilitate effective separation directly after the column (see Figure B.24 on page 182 for a close-up). The output of AT S3 is connected to a CO<sub>2</sub>/H<sub>2</sub>O analyzer (LI-7000; Li-COR, Lincoln, NE, U.S.), henceforth referred to as Li7000 (see Figure B.25 a) on page 183).

Figure 3.6 shows a close-up of the structure on the GC. The image depicts the 1/16" tube coming from AT S3 within the GC, which is linked to the subsequent system through a crimp and/or via AT SW1. During the GC step, the crimp  $\frac{1}{4}$ "<sup>8</sup> maintains a slight pressure above atmospheric levels downstream of the column when AT SW1 is closed and the sample flows from the column toward the CO<sub>2</sub> trap to be caught. Having a vacuum at the

### 3. Automatic Preparation Line for Atmospheric CO<sub>2</sub>

end of the column could allow atmospheric air to enter. The crimp was adjusted so that, at a setting of 243 mbar above atmospheric pressure upstream of the column, resulting in a flow rate of ~3.6 ml/min (He), a pressure of ~1030 mbar is maintained downstream of the column. For adjustment, a PAA-23SY absolute pressure sensor (0...4bar abs; KELLER, Winterthur, Switzerland) was temporarily affixed above the manual valve  $\ddagger^{11}$ .

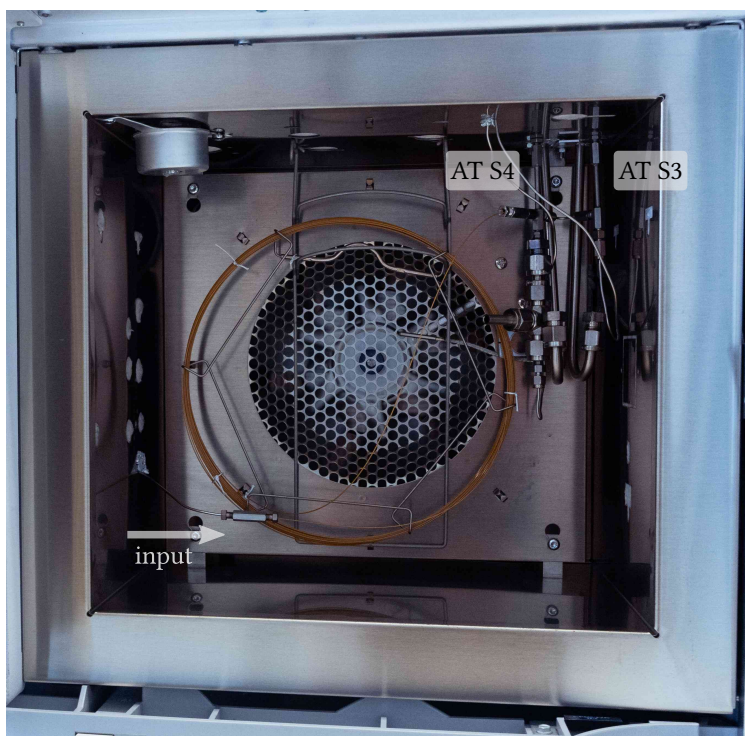
The GC is connected to the IRMS computer via RS232. A Python script continuously records various data, such as pressure, flow, and temperature, and establishes communication with the mass spectrometer software.



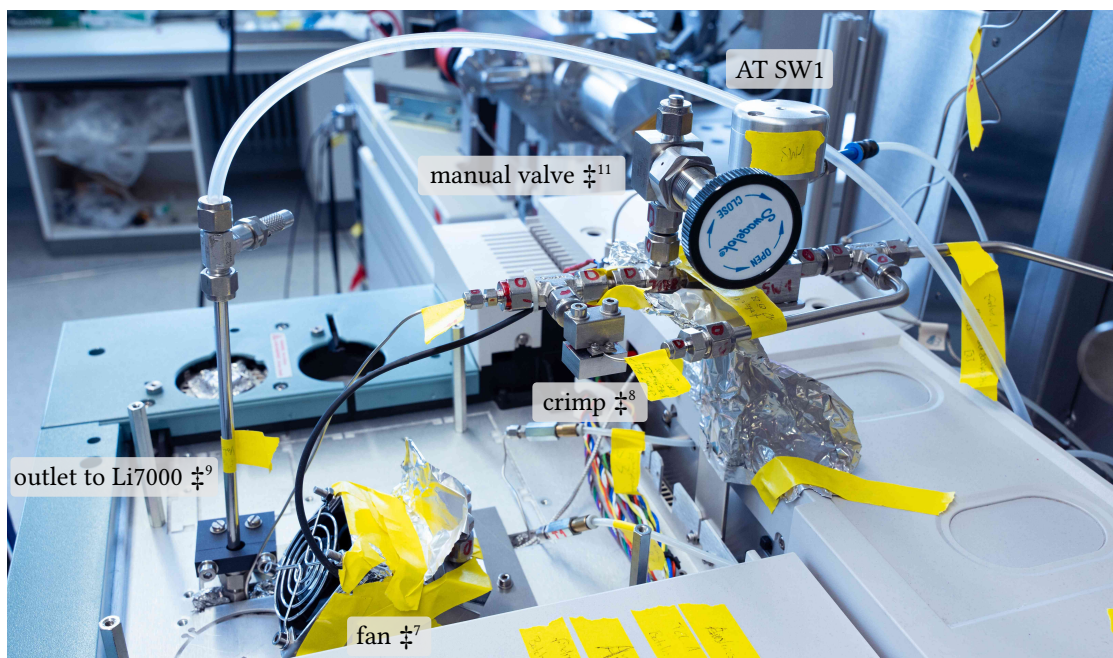
**Figure 3.4.:** The images show the GC (G1530A, Agilent, Santa Clara, CA, U.S.) a) from the front and b) from the side. In b), the exhaust chimney installed at the end of April 2024 can be seen on the left.



### 3.2. Gas Chromatograph and GC Step



**Figure 3.5.:** The image depicts the interior of the GC oven [A8 - B8]. The silica capillary column is positioned at the center. The valves AT S3 and AT S4 are located on the right. The sample inlet side of the column is positioned at the bottom left. The 1/4" tubes behind AT S3 and AT S4 are no longer utilized and were installed as part of an earlier design approach.



**Figure 3.6.:** The image depicts the outlet area of the GC [B7 - C8]. A crimp  $\ddagger^8$  was installed and adjusted to prevent a vacuum from forming downstream of the column at the GC step. The fan  $\ddagger^7$  is used to cool the pneumatic control heads of AT S3 and AT S4. Additionally, an outlet  $\ddagger^9$  with a needle valve is visible on the left side of the picture. This is connected to AT S4 and leads to the Li7000 CO<sub>2</sub>/H<sub>2</sub>O analyzer (see text).

### 3. Automatic Preparation Line for Atmospheric CO<sub>2</sub>

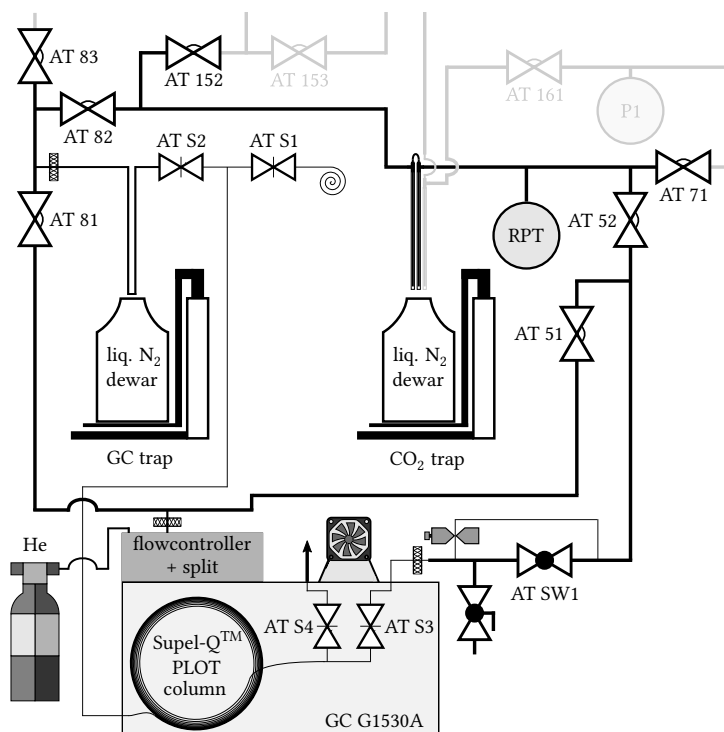
#### 3.2.2. GC step

In order to determine an optimal procedure for the GC step, a series of experiments were conducted. The part of the Air Trap scheme relevant for the GC step is shown in Figure 3.7. For the tests, the CO<sub>2</sub>/H<sub>2</sub>O analyzer Li7000 was used.

##### Idle Mode

The initial scenario for the tests was, and the GC step is the “Idle Mode”, where:

- valves AT S2, AT S4, AT 52, and AT 81 are closed,
- valves AT S1, AT S3, AT 51, and AT SW1 are open,
- the oven temperature is set to 30 °C,
- the upstream pressure is set to 216 mbar above atmosphere, resulting in a flow of ~4 ml/min,
- the GC flow controller is set to “splitless mode”.



**Figure 3.7.:** The figure illustrates the section [A6-C8] of the Air Trap schematic Figure 3.3 that is relevant for the GC step. In order to conduct a series of tests, a pressure sensor was affixed to the manual valve situated behind the GC. The output of AT S4 is directed to the CO<sub>2</sub>/H<sub>2</sub>O analyzer Li7000.

### Experiments to Determine the Final Scenario

At the beginning of the GC step, the column is stabilized at a pressure slightly above atmospheric. Then, the valves on both sides of the column close. Simultaneously, the sample is cryogenically pumped into the GC trap, and the non-condensable gases are evacuated (see appendix B.4 on 145). Two extreme approaches are then possible, which are explained below before the final scenario is discussed. Figure 3.8 a) and b) show the results of the two tests and the final scenario, respectively. The y-axis shows the CO<sub>2</sub> concentration measured by the Li7000 downstream of the column. The x-axis shows the time elapsed since the carrier gas was introduced to the GC trap.

**“CO<sub>2</sub> frozen” (—)** In this approach, the GC trap lifting platform initially remains raised so that the sample remains frozen. The carrier gas (He) is introduced to flush the GC trap and column. Once the desired flow rate is reached and after a brief stabilization period, the lifting platform is lowered, allowing the sample to sublime.

**“CO<sub>2</sub> gas phase” (—)** Unlike the previous approach, the lifting platform is lowered first to allow for the complete sublimation of the sample before the carrier gas is introduced. Then, similar to the other approach, the carrier gas enters and the flow rate through the capillary increases.

Upon examining Figure 3.8 a), several observations can be made for the two tests.

In the “CO<sub>2</sub> frozen” approach, a small leading peak can be seen. This is probably caused by a partial removal of the frozen CO<sub>2</sub> from the GC trap due to a pressure pulse when the carrier gas is admitted. This hypothesis is supported by the fact that this leading peak occurs at the same time as the first peak in the “CO<sub>2</sub> gas phase” approach. The main peak of this approach occurs some time after the lifting platform is lowered and the sample is sublimated.

In the “CO<sub>2</sub> gas phase” approach, a second peak appears after the first. This phenomenon is not observed in the other approach, so it is assumed that the second peak occurs because the sample can fully expand in the GC trap, allowing it to expand into the dead volume between valves AT 81 to AT 83.

Since both an additional leading peak or a delayed second peak could result in fractionation and overlap with the molecules to be separated, a single-peak approach was sought.

### *3. Automatic Preparation Line for Atmospheric CO<sub>2</sub>*

#### **Final Scenario**

The final scenario resulted from combining the two approaches. It begins with the trap being lowered, as in the “CO<sub>2</sub> gas phase” approach. However, twenty seconds after the trap is lowered, before the sample sublimates but after the trap has clearly warmed up, valve AT 81 is opened for 180 milliseconds. This floods the volume of the trap surrounding the frozen sample with helium. The purpose of this procedure is to circumvent the occurrence of a second retarded peak, by filling the dead volume with helium rather than with the sample. Nevertheless, to prevent pressure exceeding atmospheric pressure within the trap, filling is initiated only after the trap has warmed up slightly. After an 83-second equilibration phase and simultaneous gradual adjustment of the carrier gas pressure to 120 mbar above atmosphere the valves on both sides of the column open. Four seconds later, the carrier gas pressure is gradually adjusted to 243 mbar above atmospheric pressure.

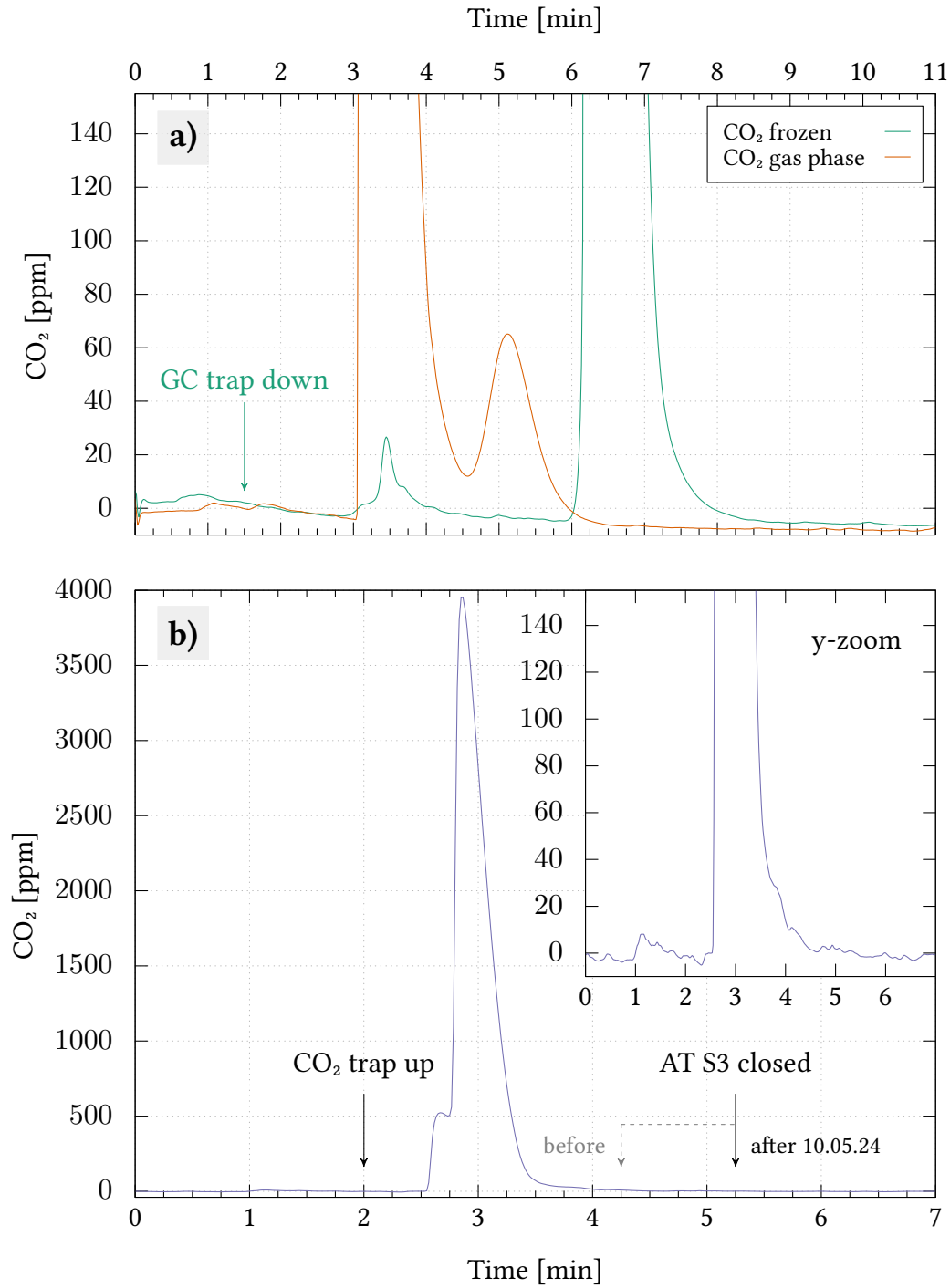
As can be seen in Figure 3.8 b), the occurrence of a delayed second peak is prevented in comparison to the “CO<sub>2</sub> gas phase” approach. Additionally, the leading peak from the “CO<sub>2</sub> frozen” approach is observed to be higher, but merges into the main peak. It is assumed that this is caused by the slight warming of the trap, which allows for a greater release of the frozen sample by the pressure pulse, which is then placed in front of the closed valve AT S2.

#### **Downstream Sampling**

In the case of the Air Trap preparation, the carrier gas and sample are passed via AT S3, through the crimp and AT 52 to the CO<sub>2</sub> trap. AT SW1 is closed. Two minutes after the initial opening of valve AT S2, the lifting platform of the CO<sub>2</sub> trap is elevated to collect the sample (“CO<sub>2</sub> trap up” in Figure 3.8 b)). After a further 3.25 min, AT S3 is closed, thus ending the flow through the column (“AT S3 closed” in Figure 3.8 b)). AT SW 1 remains closed for an additional four minutes to prevent a pressure surge that could potentially dislodge sample material from the CO<sub>2</sub> trap. Once the remaining gases have been pumped up to valve AT S1 and the trap has been evacuated, the valves surrounding the trap are closed and the trap’s lifting platform is lowered to sublime the sample



### 3.2. Gas Chromatograph and GC Step

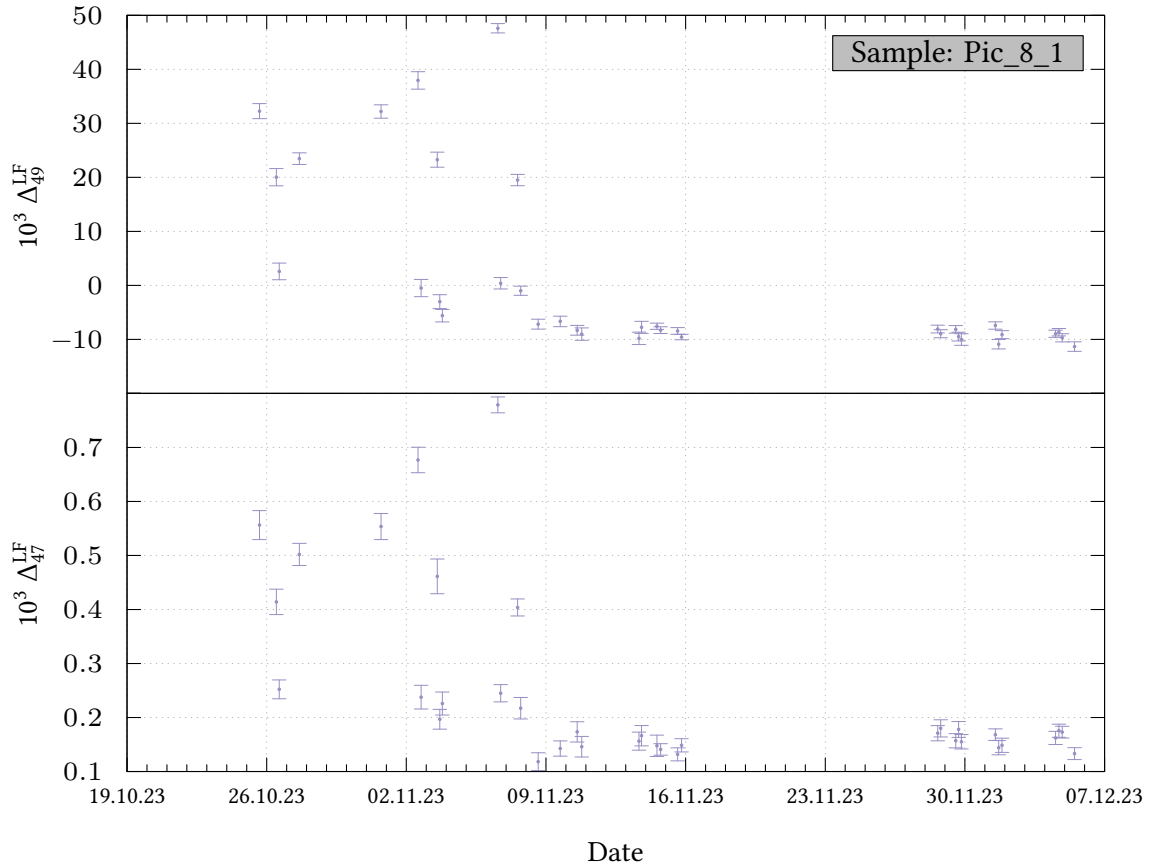


**Figure 3.8.:** The figures illustrate the results of preliminary tests conducted to identify the optimal method and settings for the GC step. The CO<sub>2</sub> concentrations plotted on the y-axes (background subtracted) were measured with the CO<sub>2</sub>/H<sub>2</sub>O analyzer Li7000. In figure a), the label “CO<sub>2</sub> frozen” indicates a test in which the sample in the GC trap was frozen and the carrier gas He was admitted to the frozen sample. At the point in time marked “GC trap down”, the platform with the liquid N<sub>2</sub> Dewar was lowered. In contrast, the data labeled “CO<sub>2</sub> gas phase” indicate a test in which the CO<sub>2</sub> in the GC trap was in a completely gaseous state prior to the introduction of the carrier gas. Figure b) illustrates the final course of the GC step. The times for initiating sampling with the CO<sub>2</sub> trap “CO<sub>2</sub> trap open” and for terminating the flow through the GC column “AT S3 closed” are indicated. Before May 10, 2024, the valve closed one minute earlier. This was changed to counteract the possibility of slight fractionation. However, long-term comparisons revealed no significant difference in results.

### 3. Automatic Preparation Line for Atmospheric CO<sub>2</sub>

#### Additional Evacuation Step

The preparation was only partially successful using the described procedure. Measurements for  $\Delta_{47}$ ,  $\Delta_{48}$ , and  $\Delta_{49}$  showed higher-than-expected values, indicating contamination [e.g. *Eiler et al.*, 2004]. Meaningful results were obtained after evacuating the area between valves AT S3, AT 51, and AT 52 prior to the GC step. Consequently, an additional evacuation step was incorporated on November 9, 2023. This step is performed immediately after closing valves AT S1 and AT S3 and stabilizing the pressure in the column. Following evacuation to approximately  $6 \cdot 10^{-3}$  mbar, the area is filled with fresh helium to a pressure of  $\sim 20$  mbar above atmosphere. Then, the procedure described under “Final Scenario” is initiated. The measurements of  $\Delta_{47}^{\text{LF}}$  and  $\Delta_{49}^{\text{LF}}$  for the gas cylinder “Pic\_8\_1” in Figure 3.9 demonstrate a clear improvement before and after November 9, 2023.



**Figure 3.9.:** The figure shows  $\Delta_{47}^{\text{LF}}$  and  $\Delta_{49}^{\text{LF}}$  of measurements of the gas cylinder “Pic\_8\_1”. All measurements were processed via the GC. There are clear outliers before November 9, 2023, towards high  $\Delta_{47}^{\text{LF}}$  and  $\Delta_{49}^{\text{LF}}$ , indicating contamination. After incorporating an additional evacuation step from this date, the results were reproducible and corresponded to the expected magnitude. The data are given uncalibrated in the laboratory frame (LF).

One possible explanation for this necessary step is that a small leak allows impurities to enter the area over time while it is flushed with the carrier gas between preparations. However, based on numerous evacuation tests, the leak must be very small. Another possible explanation is the presence of impurities in the 99.9999 % helium or in the components through which it passes on its way to the described area (e.g., the GC's flow controller). These impurities might accumulate due to the GC column's taper. Ultimately, the reason for this could not be conclusively determined within the scope of this work. Nevertheless, reproducible and meaningful results are obtained with the additional evacuation step.

#### 3.2.3. Cleaning Procedure

As soon as the CO<sub>2</sub> trap's platform is lowered to sublime the sample, the column is cleaned to remove any remaining contaminants. To accomplish this, the system switches to flush the column in the opposite direction. Then, the oven is heated to 230 °C at a rate of 16 °C/min after the pressure is adjusted to 216 mbar above atmosphere (4 ml/min; see "Idle Mod"). To prevent backflow, the GC is programmed to increase the pressure as the temperature rises, maintaining a constant flow rate ["Constant Flow" mode; see *Agilent Technologies*, 2000]. The oven maintains this temperature for one hour. Then, a "Post Run" of one hour at 180 °C is initiated. Afterwards, the GC returns to "Idle Mode".

The manufacturer's specifications for conditioning were used as a guide [*Merck KGaA (Sigma-Aldrich)*, 2020]. The values chosen here are rather conservative compared to those found in the literature (see Table B.2 on page 184). However, it was found that a longer baking of six hours at 220 °C every 24 hours, as performed by *Huntington et al.*, 2009, is not necessary. During the course of the work, it could not be clarified whether this is due to the slightly higher temperature chosen.

Individual tests suggest that the "Post Run" at 180 °C is unnecessary and can likely be omitted in the future. Nevertheless, to ensure the reproducibility of the measurements in case of an unexpected influence, this modification was not implemented.

#### 3.2.4. Comparison With and Without GC Preparation

To demonstrate the effect of the GC step on measurement of  $\Delta_{47}^{LF}$ ,  $\Delta_{48}^{LF}$ ,  $\Delta_{49}^{LF}$ , Table 3.1 compares the measurement of these with and without GC preparation for the gas cylinders "Pic\_8\_1" and "D484276", respectively. It is evident that without this processing step, a meaningful measurement of  $\Delta_{47}^{LF}$ ,  $\Delta_{48}^{LF}$ ,  $\Delta_{49}^{LF}$  is not possible. Additionally, the  $I_{18}/I_{44}$  ratio decreases, indicating that the samples become drier. This finding aligns with the analysis

### 3. Automatic Preparation Line for Atmospheric CO<sub>2</sub>

**Table 3.1.:** Effects on  $\Delta_{47}^{LF}$ ,  $\Delta_{48}^{LF}$ ,  $\Delta_{49}^{LF}$ , and  $I_{18}/I_{44}$  for the preparation of samples from “Pic\_8\_1” and “D484276” with and without GC (red, upper rows). The data are given in the laboratory frame (LF). Since this is a qualitative comparison, no uncertainties are provided. Regarding  $I_{18}/I_{44}$ , the mean of 14 samples processed using the GC within  $\pm 2$  weeks of these measurements was  $(0.049 \pm 0.004 \text{ [SD]}) \text{ ‰}$ .

sample	date/time [UTC]	$10^3 \Delta_{47}^{LF}$	$10^3 \Delta_{48}^{LF}$	$10^3 \Delta_{49}^{LF}$	$I_{18}/I_{44}$
Pic_8_1	17.07.24 14:07	5.163	13.3	461.4	0.118
	17.07.24 18:47	0.147	0.4	-6.3	0.053
D484276	18.07.24 13:33	7.380	71.7	620.1	0.068
	11.07.24 22:03	0.002	0.3	0.9	0.051

diagrams provided by the manufacturer [e.g. *Merck KGaA (Sigma-Aldrich)*, 2025], which illustrate that H<sub>2</sub>O travels through the column after CO<sub>2</sub> with a time delay. Furthermore, these results suggest that the current drying process using the H<sub>2</sub>O trap may need improvement.

#### Effects on the N<sub>2</sub>O/CO<sub>2</sub> Concentration Ratio

No significant change in the N<sub>2</sub>O/CO<sub>2</sub> concentration ratio, was observed for “Pic\_8\_1” measurements (contains N<sub>2</sub>O), with and without GC step. Additionally, no significant change occurred when the GC’s step sample time was increased by one minute permanently on May 10, 2024, from 2.25 minutes (see Figure 3.8 b)). The mean  $^{30}\Lambda$  (see subsection 2.5.5) for eight “Pic\_8\_1” measurements (2.25 minutes) from April 4 to May 1, 2024, was  $(1800.8 \pm 3.8 \text{ [SD]}) \text{ ‰}$ , while the mean  $^{30}\Lambda$  for eight measurements (3.25 minutes) from April 29 to May 13, 2024, was  $(1797.1 \pm 1.9 \text{ [SD]}) \text{ ‰}$ . For comparison, the expected value for “Pic\_8\_1” from April 4 to May 13, 2024, without N<sub>2</sub>O, would have been  $(1001.1 \pm 0.4 \text{ [SD]}) \text{ ‰}$  ( $n = 20$ ). The mean  $^{30}\Lambda$  for two measurements on April 30 and May 2, 2024, with a longer sample period of 4.25 minutes, was  $(1798.8 \pm 1.7 \text{ [SD]}) \text{ ‰}$ . One measurement on April 28, with sampling starting 30 seconds earlier for a total of 2.75 minutes, yielded  $^{30}\Lambda \approx 1797.0 \text{ ‰}$ . Therefore, it can be concluded that N<sub>2</sub>O is not separated from CO<sub>2</sub> and that the ratio remains constant under the selected settings.

However, a measurement taken on May 2, 2024 with a shorter sample period of 1.75 minutes showed a significant change, yielding  $^{30}\Lambda \approx 1759.8 \text{ ‰}$ . This reduced value suggests that the N<sub>2</sub>O peak passes through the column slightly offset from the CO<sub>2</sub> peak. Additionally, significant isotopic enrichment was observed:  $\Delta(\delta^{13}\text{C}) \approx +0.093 \text{ ‰}$  and  $\Delta(\delta^{18}\text{O}) \approx +0.067 \text{ ‰}$ , compared to a mean of 18 measurements between April 4, 2024, and May 13, 2024, of  $\delta^{13}\text{C} = (-10.312 \pm 0.003 \text{ [SD]}) \text{ ‰}$  and  $\delta^{18}\text{O} = (-2.398 \pm 0.007 \text{ [SD]}) \text{ ‰}$ .  $\Delta_{47}$  was  $\sim 0.020 \text{ ‰}$  lower than the mean of these 18 measurements, which was  $(0.9749 \pm 0.0092$

[SD]) ‰. However, this is still within three sigma. These 18 measurements include all other special preparation cases mentioned.

The  $I_{18}/I_{44}$  ratio did not change within the limits of measurement uncertainty for these experiments.

#### 3.2.5. Dependency on Sample Quantity

An experiment involving different freeze times in the AT step revealed a slight dependence of  $\delta^{13}\text{C}$  and  $\delta^{18}\text{O}$  on sample quantity. Although this was not investigated without a GC step, it is plausible that the GC step caused this dependence. Thirteen measurements of “Pic\_8\_1” were taken between May 11 and May 21, 2024. Freezing times in the AT step ranged from 10 to 16 minutes. This resulted in pressures ranging from approximately 10.1 to 19.9 mbar at the end of the GC step after sublimation in the  $\text{CO}_2$  trap. For the 11 samples with freezing times up to 14 minutes ( $\sim 17.5$  mbar), no significant deviation was observed, with means of  $\delta^{13}\text{C} = (-10.498 \pm 0.002 \text{ [SD]}) \text{ ‰}$  and  $\delta^{18}\text{O} = (-2.565 \pm 0.005 \text{ [SD]}) \text{ ‰}$  (not  $\text{N}_2\text{O}$ -corrected or calibrated). In contrast, the samples with freezing times of 15 and 16 minutes ( $\sim 18.8$  and  $\sim 19.9$  mbar, respectively) showed enrichments of  $\Delta(\delta^{13}\text{C}) = +0.008 \text{ ‰}$  and  $+0.010 \text{ ‰}$ , as well as  $\Delta(\delta^{18}\text{O}) = +0.022 \text{ ‰}$  and  $+0.030 \text{ ‰}$ , respectively. A slight, significant dependence was also observed for  $^{47}\delta$ . No significant changes were observed for  $\Delta_{47}^{\text{LF}}$  to  $\Delta_{49}^{\text{LF}}$ . No change was observed for  $^{30}\Lambda$  that could explain this effect. Results on this experiment are shown in Figure B.28 (page 187) for  $\delta^{13}\text{C}$ ,  $\delta^{18}\text{O}$ , and  $\Delta_{47}^{\text{LF}}$ .

Since 89.8 % of the 540 samples prepared between August 30, 2023, and December 20, 2024, using the GC step yielded pressures  $\lesssim 17.5$  mbar, and 99.3 % yielded pressures  $\lesssim 18.8$  mbar, no correction is applied for the samples measured in this work.

However, the observed dependence was demonstrated by only two samples. Therefore, more thorough investigations and confirmations through repeated experiments are needed. To investigate a potential dependence on isotopic values, these experiments should involve samples with different bulk isotopic compositions. Nevertheless, it is recommended to avoid sample quantities that yield pressures greater than  $\sim 17$  mbar in the  $\text{CO}_2$  trap after the GC step.



## 4. N<sub>2</sub>O Correction, Calibration & Reproducibility

The first section of this chapter discusses the influence of N<sub>2</sub>O on IRMS measurements and presents correction functions. The next two sections focus on calibrating  $\delta^{13}\text{C}$ ,  $\delta^{18}\text{O}$ ,  $\Delta_{47}$ ,  $\Delta_{48}$ , and  $\Delta_{49}$ . Topics include producing temperature-equilibrated CO<sub>2</sub> standards and correcting for the dependence of  $^{47}\delta$  on  $\Delta_{47}$ ,  $^{48}\delta$  on  $\Delta_{48}$ , and  $^{49}\delta$  on  $\Delta_{49}$ . The final section addresses the reproducibility of  $\delta^{13}\text{C}$ ,  $\delta^{18}\text{O}$ , and  $\Delta_{47}$  as determined by regularly measurements of the gas cylinders “Pic\_8\_1” and “D484276”.

### 4.1. Isobaric Interference with N<sub>2</sub>O

In addition to CO<sub>2</sub>, the trace gas nitrous oxide (N<sub>2</sub>O) is present in the atmosphere at a concentration of approximately 338.42 ppb (global monthly mean for January 2025; [Lan, Thoning, et al., 2025]). When measured by IRMS, this gas has stable isotopologues with mass-to-charge ratios  $m/z$  44 to  $m/z$  48. This is illustrated in Table 4.1, which compares the stable N<sub>2</sub>O isotopologues with the stable CO<sub>2</sub> isotopologues.

Since the mass-to-charge ratios of the isotopologues of both molecules overlap, isobaric interferences occur during IRMS measurements, and the results of the CO<sub>2</sub> measurements will be altered if N<sub>2</sub>O is present [e.g. Craig et al., 1963, Ghosh et al., 2004, Eiler et al., 2004]. As mentioned in subsection 3.2.4, N<sub>2</sub>O could not be separated from CO<sub>2</sub> using the Air Trap to prepare ambient air samples. Therefore, a correction is necessary for these samples. For this purpose, WMO/IAEA, 2016 recommend the approaches of Ghosh et al., 2004 and Assonov et al., 2006 to correct  $\delta^{13}\text{C}$  and  $\delta^{18}\text{O}$  measurements. To the best of current knowledge, for the N<sub>2</sub>O correction of  $\Delta_{47}$ ,  $\Delta_{48}$ , and  $\Delta_{49}$ , only a spreadsheet by Fiebig et al., 2024 exists, from which automatic data evaluation is not straightforward.

The following subsection addresses the theoretical N<sub>2</sub>O correction. First, the ionization efficiency between N<sub>2</sub>O and CO<sub>2</sub> is examined. Subsequently, self-calculated corrections for  $\delta^{13}\text{C}$ ,  $\delta^{18}\text{O}$ ,  $\Delta_{47}$ ,  $\Delta_{48}$  and  $\Delta_{49}$  are elucidated. Then, the self-calculated corrections for  $\delta^{13}\text{C}$  and  $\delta^{18}\text{O}$  are compared to those presented by Ghosh et al., 2004. The next subsection

#### 4. N<sub>2</sub>O Correction, Calibration & Reproducibility

describes how the N<sub>2</sub>O/CO<sub>2</sub> concentration ratio was determined for the measurements in this thesis.

**Table 4.1.:** The table lists the stable isotopologues  $y'$  of CO<sub>2</sub> compared to the stable isotopologues  $n'$  of N<sub>2</sub>O.

atomic mass M [u]	CO <sub>2</sub> isotopologue $y'$	N <sub>2</sub> O isotopologue $n'$
44	<sup>16</sup> O <sup>12</sup> C <sup>16</sup> O	<sup>14</sup> N <sup>14</sup> N <sup>16</sup> O
45	<sup>16</sup> O <sup>13</sup> C <sup>16</sup> O	<sup>14</sup> N <sup>15</sup> N <sup>16</sup> O
	<sup>16</sup> O <sup>12</sup> C <sup>17</sup> O	<sup>15</sup> N <sup>14</sup> N <sup>16</sup> O
		<sup>14</sup> N <sup>14</sup> N <sup>17</sup> O
46	<sup>16</sup> O <sup>12</sup> C <sup>18</sup> O	<sup>15</sup> N <sup>15</sup> N <sup>16</sup> O
	<sup>16</sup> O <sup>13</sup> C <sup>17</sup> O	<sup>14</sup> N <sup>15</sup> N <sup>17</sup> O
	<sup>17</sup> O <sup>12</sup> C <sup>17</sup> O	<sup>15</sup> N <sup>14</sup> N <sup>17</sup> O
		<sup>14</sup> N <sup>14</sup> N <sup>18</sup> O
47	<sup>16</sup> O <sup>13</sup> C <sup>18</sup> O	<sup>15</sup> N <sup>15</sup> N <sup>17</sup> O
	<sup>17</sup> O <sup>12</sup> C <sup>18</sup> O	<sup>14</sup> N <sup>15</sup> N <sup>18</sup> O
	<sup>17</sup> O <sup>13</sup> C <sup>17</sup> O	<sup>15</sup> N <sup>14</sup> N <sup>18</sup> O
48	<sup>18</sup> O <sup>12</sup> C <sup>18</sup> O	<sup>15</sup> N <sup>15</sup> N <sup>18</sup> O
	<sup>17</sup> O <sup>13</sup> C <sup>18</sup> O	
49	<sup>18</sup> O <sup>13</sup> C <sup>18</sup> O	

##### 4.1.1. Theoretical N<sub>2</sub>O Correction

###### Ionization Efficiency $E$ between N<sub>2</sub>O & CO<sub>2</sub>

In addition to the N<sub>2</sub>O/CO<sub>2</sub> concentration ratio, corrections like the proposed by *Ghosh et al., 2004* also depend on the ionization efficiency  $E$  between N<sub>2</sub>O and CO<sub>2</sub> [e.g. *Mook et al., 1983; Friedli et al., 1988*].  $E$  is defined by the ratio of the measured ion currents of N<sub>2</sub>O and CO<sub>2</sub> for the respective partial pressures  $p_{\text{N}_2\text{O}}^{\text{I}}$  and  $p_{\text{CO}_2}^{\text{I}}$  in the ion source [e.g. *Friedli et al., 1988; Neubert, 1998; Ghosh et al., 2004; Assonov et al., 2006*]:

$$E = \frac{I_{44, \text{N}_2\text{O}} \cdot p_{\text{CO}_2}^{\text{I}}}{I_{44, \text{CO}_2} \cdot p_{\text{N}_2\text{O}}^{\text{I}}} . \quad (4.1)$$

Here, the intensities  $I_{44, \text{N}_2\text{O}}$  and  $I_{44, \text{CO}_2}$ , measured for N<sub>2</sub>O and CO<sub>2</sub>, respectively, are used instead of the ion currents. This is possible because the proportionality constant between the measured intensities and the ion currents cancels out when using the same Faraday cup for both gases.



$E$  must be determined for each mass spectrometer individually. If the bulk isotopic composition is similar to that of typical ambient air CO<sub>2</sub> samples, it usually ranges from 0.68 to 0.75 [see Assonov et al., 2006]. Several studies have shown that  $E$  depends on the amount of gas introduced into the ion source [e.g. Ghosh et al., 2004; Sirignano et al., 2004; Assonov et al., 2006]. In addition, Ghosh et al., 2004 have shown that the parameter has a slight dependence on the electron energy set on the IRMS. Furthermore, the value obtained by mixing N<sub>2</sub>O and CO<sub>2</sub> appears to differ slightly from that obtained by determining it using pure gases [Ghosh et al., 2004; Assonov et al., 2006]. Ghosh et al., 2004 found a slightly lower  $E \approx 0.68$ -0.72 compared to the pure gas measurement  $E \approx 0.715$ -0.740 (under variations in the amounts of gas introduced). However, they state that the effect does not appear to be significant and is negligible for the isotope deltas determined. Assonov et al., 2006 used an indirect approach and obtained a value of  $E \approx 0.687$ , which is also lower than their value of  $E \approx 0.725$  obtained with pure gases. To avoid certain dependencies on  $E$ , this indirect approach by Assonov et al., 2006 is based on measuring the intensity at  $m/z$  30 ( $I_{30}$ ). However, it requires other parameters to be determined, which may also be subject to change and must be determined individually for each mass spectrometer [e.g. Assonov et al., 2006; Bauska et al., 2014]. A direct comparison with this approach, which uses a correction based on the relationship between  $^{30}R = I_{30}/I_{44}$  and  $^{45}R$  and  $^{46}R$  [see Assonov et al., 2006], could not be made within the scope of this work.

In this work,  $E = (0.70 \pm 0.02$  [3 SD]) is used as determined by Eckhardt, 2019 on 10.10.2018 for the IRMS used here. This was determined using pure gases. The variation of  $E$  with pressure was comparatively small for the determined range. About 13 to 32 mbar were applied for N<sub>2</sub>O and 8 to 29 mbar for CO<sub>2</sub> (pressure in bellow). Using the functions fitted by Eckhardt, 2019 to these data,  $E$  changes in the order of  $\sim 10^{-2}$  per 10 mbar.  $E$  in 2018 was determined when the electron energy was adjusted to 94.127 eV. The setting for the 2024 measurements was 90.391 eV. At least in the tests of Ghosh et al., 2004 using a MAT 252 IRMS this range was quite stable. Since the electron energy is nearly the same and the pressure dependence was quite small, it seems reasonable to use the mentioned value. Nevertheless, this should be re-evaluated in the future, also by mixing tests.

#### Self-Calculated Correction Functions

As part of the work, correction functions were determined for  $\delta^{13}\text{C}$ ,  $\delta^{18}\text{O}$ ,  $\Delta_{47}$ ,  $\Delta_{48}$ ,  $\Delta_{49}$  and  $^{45}\delta$  to  $^{49}\delta$ . A classical approach, similar to that of Ghosh et al., 2004, which depends on  $E$ , is chosen. The functions were calculated according to the currently

#### 4. N<sub>2</sub>O Correction, Calibration & Reproducibility

recommended international measurement standards for CO<sub>2</sub> (see Table 2.1) and take into account dependencies on the isotope deltas of CO<sub>2</sub>.

Different isotope deltas of N<sub>2</sub>O were not taken into account. For this purpose, the average tropospheric isotope deltas determined by *Kaiser et al., 2003* were used:

$\delta^{18}\text{O}_{\text{VSMOW}}(\text{N}_2\text{O}) \approx 44.62 \text{ ‰}$ ,  $\Delta^{17}\text{O}_{\text{VSMOW}}(\text{N}_2\text{O}) \approx 0.9 \text{ ‰}$  and  $^1\delta^{15}\text{N}_{\text{air N}_2} \approx -15.8 \text{ ‰}$ ,  $^2\delta^{15}\text{N}_{\text{air N}_2} \approx 29.2 \text{ ‰}$ .  $^1\delta^{15}\text{N}$  corresponds to the terminal N atom and  $^2\delta^{15}\text{N}_{\text{air N}_2}$  corresponds to the central N atom. As an international standard, *Kaiser et al., 2003* refer to the use of atmospheric N<sub>2</sub> for  $^{15}\text{N}$ . Here  $^{15}R_{\text{air N}_2} = 1/272$  [*Junk et al., 1958*] was used. According to *Kaiser et al., 2003* oxygen isotope deltas were expressed using  $^{18}R_{\text{VSMOW}}(\text{N}_2\text{O}) = 2.0052 \cdot 10^{-3}$  [*Baertschi, 1976*],  $^{17}R_{\text{VSMOW}}(\text{N}_2\text{O}) = 3.799 \cdot 10^{-4}$  [*Li, 1988*] and  $\lambda = 0.516$  [*Kaiser, 2002*].

Furthermore,  $E$  was assumed to be the ionization effectivity of all N<sub>2</sub>O to CO<sub>2</sub> isotopologues. In addition, the gases were considered in the stochastic case for the calculation. As shown by *Eckhardt, 2019*, a deviation from the stochastic case has no significant effect on the correction functions within the limits of measurement accuracy. Nevertheless, the case of an equilibrium temperature of 300 K for CO<sub>2</sub> has been derived for  $\Delta_{47}$  as an example, which is compared to the stochastic derivation (see below). However, this will not be considered in the following mathematical description.

To derive the correction functions, the mass ratios  $^{45}R_{\text{altered by N}_2\text{O}}$  to  $^{49}R_{\text{altered by N}_2\text{O}}$  altered by N<sub>2</sub>O were calculated as follows (subscript “stoch” is omitted here;  $\mathcal{M}' \in \{45, 46, 47, 48\}$ ):

$$\begin{aligned} \mathcal{M}'R_{\text{altered by N}_2\text{O}} &= \frac{\frac{1}{1+f} \cdot \sum_{y' \text{ with } \mathcal{M}'} x(y')_{\text{CO}_2} + \frac{f}{1+f} \cdot \sum_{n' \text{ with } \mathcal{M}'} x(n')_{\text{N}_2\text{O}}}{\frac{1}{1+f} \cdot x(^{16}\text{O}^{12}\text{C}^{16}\text{O})_{\text{CO}_2} + \frac{f}{1+f} \cdot x(^{14}\text{N}^{14}\text{N}^{16}\text{O})_{\text{N}_2\text{O}}} , \\ ^{49}R_{\text{altered by N}_2\text{O}} &= \frac{x(^{18}\text{O}^{13}\text{C}^{18}\text{O})_{\text{CO}_2}}{\frac{1}{1+f} \cdot x(^{16}\text{O}^{12}\text{C}^{16}\text{O})_{\text{CO}_2} + \frac{f}{1+f} \cdot x(^{14}\text{N}^{14}\text{N}^{16}\text{O})_{\text{N}_2\text{O}}} , \quad (4.2) \\ \text{with } f &= E \cdot \rho \quad \text{and} \quad \rho = \frac{C_{\text{N}_2\text{O}}}{C_{\text{CO}_2}} . \end{aligned}$$

The nomenclature is based on subsection 2.3.3. Accordingly,  $x(y')_{\text{CO}_2}$  is the isotopologue fraction of isotopologue  $y'$  of mass  $\mathcal{M}'$  from CO<sub>2</sub> and  $x(n')_{\text{N}_2\text{O}}$  is the isotopologue fraction of isotopologue  $n'$  of mass  $\mathcal{M}'$  from N<sub>2</sub>O (see Table 4.1). The calculation for  $\delta^{13}\text{C}_{\text{altered by N}_2\text{O}}$ ,  $\delta^{18}\text{O}_{\text{altered by N}_2\text{O}}$ ,  $\Delta_{47}^{\text{altered by N}_2\text{O}}$ ,  $\Delta_{48}^{\text{altered by N}_2\text{O}}$  and  $\Delta_{49}^{\text{altered by N}_2\text{O}}$  altered by N<sub>2</sub>O is then performed as described for the experimental case in subsection 2.5.6. To determine the correction value (superscript “N<sub>2</sub>O corr”) under the use of a specific bulk isotopic composition of CO<sub>2</sub> and under the use of a specific  $f = E \cdot \frac{C_{\text{N}_2\text{O}}}{C_{\text{CO}_2}}$ , the unaffected

#### 4.1. Isobaric Interference with N<sub>2</sub>O

values are subtracted from the values altered by N<sub>2</sub>O. Using  $\delta^{13}\text{C}$  as an example, this is done as follows:

$$\delta^{13}\text{C}^{\text{N}_2\text{O corr}} = \delta^{13}\text{C}^{\text{altered by N}_2\text{O}} - \delta^{13}\text{C} . \quad (4.3)$$

These corrections were determined for  $f \in \{0.1, 0.15, \dots, 1.15\}$  and for the combinations of all  $\delta^{13}\text{C} \in \{-50, -49, \dots, 0\}$  and  $\delta^{18}\text{O} \in \{-50, -49, \dots, 10\}$ . Each correction function is therefore based on 71553 data points. These were used to determine the correction functions using a combination of Python and gnuplot along with the nonlinear least-squares Marquardt-Levenberg algorithm.

For easier handling of the concentration ratio between N<sub>2</sub>O and CO<sub>2</sub>,  $\xi$  is defined as follows for the correction functions:

$$\xi = E \cdot 10^3 \cdot \rho = E \cdot \frac{10^3 \cdot C_{\text{N}_2\text{O}}}{C_{\text{CO}_2}} . \quad (4.4)$$

The following correction functions were determined for use with the international measurement standards VPDB for  $\delta^{13}\text{C}$  and VPDB-CO<sub>2</sub> for  $\delta^{18}\text{O}$ :

$$10^3 \delta^{13}\text{C}^{\text{N}_2\text{O corr}} = - (10089 \pm 7) 10^{-7} \cdot 10^3 \delta^{13}\text{C} \cdot \xi - (1017 \pm 5) 10^{-8} \cdot 10^3 \delta^{18}\text{O} \cdot \xi - (3570 \pm 4) 10^{-4} \cdot \xi , \quad (4.5)$$

$$10^3 \delta^{18}\text{O}^{\text{N}_2\text{O corr}} = - (475 \pm 2) 10^{-8} \cdot 10^3 \delta^{13}\text{C} \cdot \xi - (10067 \pm 4) 10^{-7} \cdot 10^3 \delta^{18}\text{O} \cdot \xi - (4980 \pm 4) 10^{-4} \cdot \xi , \quad (4.6)$$

$$10^3 \Delta_{47}^{\text{N}_2\text{O corr}} = (329 \pm 2) 10^{-6} \cdot 10^3 \delta^{13}\text{C} \cdot \xi + (194 \pm 8) 10^{-6} \cdot 10^3 \delta^{18}\text{O} \cdot \xi + (169 \pm 2) 10^{-3} \cdot \xi , \quad (4.7)$$

$$10^3 \Delta_{48}^{\text{N}_2\text{O corr}} = (19 \pm 2) 10^{-7} \cdot 10^3 \delta^{13}\text{C} \cdot \xi + (1040 \pm 6) 10^{-6} \cdot 10^3 \delta^{18}\text{O} \cdot \xi - (217 \pm 9) 10^{-5} \cdot \xi - (235 \pm 7) 10^{-6} \cdot \xi^2 , \quad (4.8)$$

$$10^3 \Delta_{49}^{\text{N}_2\text{O corr}} = (6855 \pm 9) 10^{-7} \cdot 10^3 \delta^{13}\text{C} \cdot \xi + (107 \pm 10) 10^{-5} \cdot 10^3 \delta^{18}\text{O} \cdot \xi + (135 \pm 3) 10^{-2} \cdot \xi . \quad (4.9)$$

For correction functions using VSMOW as the international standard for oxygen isotopes in CO<sub>2</sub>, see appendix subsection C.1 on page 189. In addition, this appendix contains correction functions for  $^{45}\delta$  through  $^{49}\delta$  relative to the working standard “Oberlahnstein” using  $\delta^{13}\text{C}_{\text{VPDB}}$  and  $\delta^{18}\text{O}_{\text{VPDB-CO}_2}$ , as well as relative to virtual working standards with the carbon isotope corresponding to VPDB and the oxygen isotopes corresponding to VPDB-CO<sub>2</sub> or VSMOW.

#### 4. N<sub>2</sub>O Correction, Calibration & Reproducibility

**Table 4.2.:** Correction values calculated using the equations (4.5) to (4.9) are listed. The second column lists the total correction values. Columns three and four list the values within the total correction values that depend on  $\delta^{13}\text{C}$  and  $\delta^{18}\text{O}$ , respectively. For calculation  $\delta^{13}\text{C} = -11 \text{ ‰}$ ,  $\delta^{18}\text{O} = -2 \text{ ‰}$ ,  $C_{\text{CO}_2} = 480 \text{ ppm}$ ,  $C_{\text{N}_2\text{O}} = 339 \text{ ppb}$  and  $E = 0.7$  were assumed.

N <sub>2</sub> O correction	total [‰]	$\delta^{13}\text{C}$ dependent [‰]	$\delta^{18}\text{O}$ dependent [‰]
$\delta^{13}\text{C}^{\text{N}_2\text{O corr}}$	-0.171	0.005	$9 \cdot 10^{-6}$
$\delta^{18}\text{O}^{\text{N}_2\text{O corr}}$	-0.245	$3 \cdot 10^{-5}$	$9 \cdot 10^{-4}$
$\Delta_{47}^{\text{N}_2\text{O corr}}$	0.082	-0.002	$-2 \cdot 10^{-4}$
$\Delta_{48}^{\text{N}_2\text{O corr}}$	-0.002	$-1 \cdot 10^{-5}$	$-9 \cdot 10^{-4}$
$\Delta_{49}^{\text{N}_2\text{O corr}}$	0.662	-0.004	$-9 \cdot 10^{-4}$

The actual N<sub>2</sub>O corrections are then performed as shown here for  $\delta^{13}\text{C}$ :

$$\delta^{13}\text{C} = \delta^{13}\text{C}^{\text{observed}} - \delta^{13}\text{C}^{\text{N}_2\text{O corr}} . \quad (4.10)$$

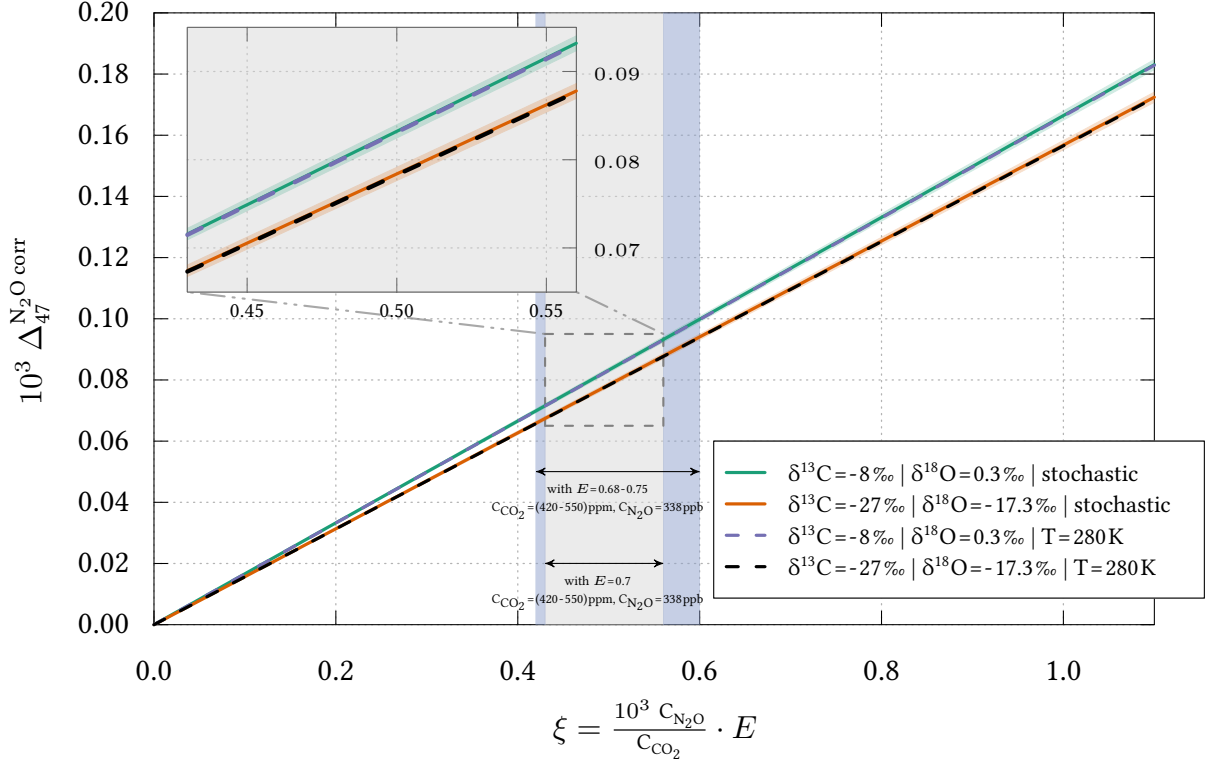
Here  $\delta^{13}\text{C}^{\text{observed}}$  corresponds to the measurement result that is affected by N<sub>2</sub>O.

The corrections themselves are slightly dependent on the unaffected  $\delta^{13}\text{C}$  and  $\delta^{18}\text{O}$ . Since the unaffected isotope deltas are not known, the corrections were applied using three iterations within this work. However, for  $E = 0.7$  and typical atmospheric samples with  $C_{\text{CO}_2} \geq 420 \text{ ppm}$  and  $C_{\text{N}_2\text{O}} = 339 \text{ ppb}$ , the difference from the second iteration to the first is  $< +0.0002 \text{ ‰}$  for both isotope deltas and  $< +0.0001 \text{ ‰}$  for  $\Delta_{47}$ . Therefore, using the observed isotope deltas directly as input variables would suffice within the limits of the achieved reproducibility of  $\sim 0.005 \text{ ‰}$  for  $\delta^{13}\text{C}$ ,  $\sim 0.01 \text{ ‰}$  for  $\delta^{18}\text{O}$ , and  $\sim 0.011 \text{ ‰}$  for  $\Delta_{47}$  (see section 4.4).

For a typical atmospheric measurement in winter in Heidelberg (see section 5.3) with  $\delta^{13}\text{C} = -11 \text{ ‰}$ ,  $\delta^{18}\text{O} = -2 \text{ ‰}$ ,  $C_{\text{CO}_2} = 480 \text{ ppm}$ ,  $C_{\text{N}_2\text{O}} = 339 \text{ ppb}$ , using  $E = 0.7$  and equations (4.5) to (4.9), the correction values listed in Table 4.2 would result. It can be seen that the dependence on  $\delta^{13}\text{C}$  should be taken into account for  $\delta^{13}\text{C}^{\text{N}_2\text{O corr}}$ . This value corresponds to the rounded value that would be obtained using the correction by Ghosh et al., 2004. For  $\delta^{18}\text{O}$  and  $\Delta_{47}$  at least for these exemplary isotope deltas, the influence of  $\delta^{13}\text{C}$  and  $\delta^{18}\text{O}$  on the correction would be negligible compared to the achieved reproducibility (see section 4.4).

For comparison, the corrections were calculated using a spreadsheet provided by Fiebig et al., 2024, with the input values taken from the example just discussed (Table 4.2) and the N<sub>2</sub>O isotope values taken from Kaiser et al., 2003. The following correction values were obtained:  $\delta^{13}\text{C}^{\text{N}_2\text{O corr}} \approx -0.171 \text{ ‰}$ ,  $\delta^{18}\text{O}^{\text{N}_2\text{O corr}} \approx -0.245 \text{ ‰}$ ,  $\Delta_{47}^{\text{N}_2\text{O corr}} \approx 0.081 \text{ ‰}$ ,

#### 4.1. Isobaric Interference with $N_2O$



**Figure 4.1.:** The solid lines represent the correction value with  $\xi$  as given by Equation (4.7). Two different bulk isotopic compositions are chosen as examples (see legend). The transparent regions with the same color as the respective line represent its uncertainty according to Equation (4.7) (see zoom). For both bulk isotopic compositions a calculation under thermodynamic equilibration of  $T_{eq} = 280$  K in  $CO_2$  is shown for comparison (dotted line). It can be clearly seen that the equilibration temperature has no significant effect on the correction. Also shown are representative ranges for common  $\xi$ .

and  $\Delta_{48}^{N_2O\ corr} \approx -0.002$  ‰. These results are identical to those in Table 4.2, except for  $\Delta_{47}$ , which differs by 0.001 ‰. This difference is negligible, but it could be due to setting  $\Delta^{17}O(N_2O) = 0$  in the spreadsheet and using  $\delta^{15}N \approx 6.72$  ‰ [Kaiser et al., 2003] instead of central and terminal N.

Figure 4.1 shows the  $N_2O$  correction for  $\Delta_{47}$  according to Equation (4.7) versus  $\xi$ . Two different bulk isotopic compositions are chosen to show the effect of the bulk isotopic composition on the correction (see legend). The bulk isotopic composition with  $\delta^{13}C = -8$  ‰ [Affek et al., 2014] and  $\delta^{18}O = 0.3$  ‰ [Affek et al., 2014] refers to typical mean tropospheric background signal. Whereas  $\delta^{13}C = -27$  ‰ [Mook, 2000] and  $\delta^{18}O = -17.3$  ‰ [Affek et al., 2014] corresponds to an average anthropogenic fossil fuel source. The shaded region with the same color of each solid line corresponds to its uncertainty with respect to Equation (4.7). The superimposed dotted lines are calculated with the same bulk isotopic compositions, but for a thermodynamic equilibration temperature of  $T_{eq} = 280$  K for  $CO_2$ .

#### 4. N<sub>2</sub>O Correction, Calibration & Reproducibility

(N<sub>2</sub>O still stochastic). In the zoom it can be clearly seen that the equilibration temperature has no significant effect on the correction value. To show typical ranges for the correction with respect to  $\xi$ , two colored areas are shown. For both, N<sub>2</sub>O was assumed to be 338 ppb and CO<sub>2</sub> was assumed to be in the range of 420 to 550 ppm. The gray color indicates the range where a correction using an ionization efficiency of  $E = 0.7$  is expected (as for the IRMS used). The blue area (longer arrow) shows the range when  $E$  is between 0.68 and 0.75.

#### Comparison with Correction Functions provided by Ghosh et al., 2004

Ghosh et al., 2004 provided the following correction functions for  $\delta^{13}\text{C}$  and  $\delta^{18}\text{O}$

$$\begin{aligned} 10^3 \delta^{13}\text{C}^{\text{true}} &= 10^3 \delta^{13}\text{C}^{\text{observed}} \cdot [1 + E \cdot \rho] + 345.4 \cdot E \cdot \rho \\ &= 10^3 \delta^{13}\text{C}^{\text{observed}} + 10^3 \delta^{13}\text{C}^{\text{observed}} \cdot E \cdot \rho + 345.4 \cdot E \cdot \rho \quad (4.11) \\ &= 10^3 \delta^{13}\text{C}^{\text{observed}} + 10^{-3} \cdot 10^3 \delta^{13}\text{C}^{\text{observed}} \cdot \xi + 0.3454 \cdot \xi \end{aligned}$$

$$\begin{aligned} 10^3 \delta^{18}\text{O}^{\text{true}} &= 10^3 \delta^{18}\text{O}^{\text{observed}} \cdot [1 + E \cdot \rho] + 500 \cdot E \cdot \rho \\ &= 10^3 \delta^{18}\text{O}^{\text{observed}} + 10^3 \delta^{18}\text{O}^{\text{observed}} \cdot E \cdot \rho + 500 \cdot E \cdot \rho \quad (4.12) \\ &= 10^3 \delta^{18}\text{O}^{\text{observed}} + 10^{-3} \cdot 10^3 \delta^{18}\text{O}^{\text{observed}} \cdot \xi + 0.500 \cdot \xi \end{aligned}$$

It follows that:

$$10^3 \delta^{13}\text{C}_{\text{Ghosh et al., 2004}}^{\text{N}_2\text{O corr}} = -10000 \cdot 10^{-7} \cdot 10^3 \delta^{13}\text{C}^{\text{observed}} \cdot \xi - 3454 \cdot 10^{-4} \cdot \xi, \quad (4.13)$$

$$10^3 \delta^{18}\text{O}_{\text{Ghosh et al., 2004}}^{\text{N}_2\text{O corr}} = -10000 \cdot 10^{-7} \cdot 10^3 \delta^{18}\text{O}^{\text{observed}} \cdot \xi - 5000 \cdot 10^{-4} \cdot \xi. \quad (4.14)$$

A direct comparison with the equations (4.5) and (4.6) shows slight deviations. For a better comparison it is necessary to use the same international measurement standards and isotope deltas for N<sub>2</sub>O as Ghosh et al., 2004. However, the exact values used by Ghosh et al., 2004 are unclear. They only state that they used VPDB and air-N<sub>2</sub> for  $\delta^{13}\text{C}$  and identical oxygen values for  $\delta^{18}\text{O}$ . For a comparative calculation,  $^{13}R_{\text{VPDB}}$  given in Table 2.1 was used for CO<sub>2</sub>. For the oxygen isotopes of both CO<sub>2</sub> and N<sub>2</sub>O,  $^{17}R_{\text{VPDB-CO}_2}$ ,  $^{18}R_{\text{VPDB-CO}_2}$ , and  $\lambda$  given in Table 2.1 were used.  $\Delta^{17}\text{O}$  (N<sub>2</sub>O) was set to 0. In addition, no distinction was made between central and terminal atoms for  $\delta^{15}\text{N}$ . The best agreement was obtained using  $^{15}R = 0.00376$  provided by Mook et al., 1983. Given that they cited Mook et al., 1983 at the beginning of their paper when presenting the format of previous correction formulas, it seems reasonable to assume that they used this value. The correction formulas

#### 4.1. Isobaric Interference with N<sub>2</sub>O

obtained using these values are:

$$10^3 \delta^{13}C_{\text{VPDB}}^{\text{N}_2\text{O corr compare}} = - (10087 \pm 7) 10^{-7} \cdot 10^3 \delta^{13}C_{\text{VPDB}} \cdot \xi \\ - (1014 \pm 5) 10^{-8} \cdot 10^3 \delta^{18}O_{\text{VPDB-CO}_2} \cdot \xi - (3460 \pm 3) 10^{-4} \cdot \xi, \quad (4.15)$$

$$10^3 \delta^{18}O_{\text{VPDB-CO}_2}^{\text{N}_2\text{O corr compare}} = - (476 \pm 2) 10^{-8} \cdot 10^3 \delta^{13}C_{\text{VPDB}} \cdot \xi \\ - (10066 \pm 4) 10^{-7} \cdot 10^3 \delta^{18}O_{\text{VPDB-CO}_2} \cdot \xi - (4994 \pm 4) 10^{-4} \cdot \xi. \quad (4.16)$$

A direct comparison of the last factors between the equations (4.13) and (4.15), as well as (4.14) and (4.16) shows a comparatively good agreement. It should be noted that the difference between the factors  $\sim 3460 \cdot 10^{-4}$  (Equation (4.15)) and  $\sim 3570 \cdot 10^{-4}$  (Equation (4.5)) is almost entirely due to the different nitrogen isotopic composition considered.  $^{15}R = 0.00376$  in respect to  $^{15}R_{\text{air N}_2} = 1/272$  yields  $\delta^{15}\text{N} \approx 22.72 \text{ ‰}$ . This differs from  $\delta^{15}\text{N} \approx 6.72 \text{ ‰}$ , which is the mean tropospheric background according to *Kaiser et al., 2003*. Assuming  $C_{\text{N}_2\text{O}} = 338 \text{ ppb}$ ,  $C_{\text{CO}_2} = 425 \text{ ppm}$ , and  $E = 0.7$ , this results in a  $\Delta(\delta^{13}\text{C}) \approx +0.006 \text{ ‰}$  enrichment for a corrected  $\delta^{13}\text{C}$  calculated by Equation (4.5) than calculated by Equation (4.15). Therefore it seems reasonable to use the bulk isotopic composition of N<sub>2</sub>O determined by *Kaiser et al., 2003*.

##### 4.1.2. Experimental Determination of C<sub>N<sub>2</sub>O</sub>/C<sub>CO<sub>2</sub></sub>

The intensity measured at  $m/z$  30 is formed by the fragment  $^{14}\text{N}^{16}\text{O}^+$  from N<sub>2</sub>O and  $^{12}\text{C}^{18}\text{O}^+$  and  $^{13}\text{C}^{17}\text{O}^+$  from CO<sub>2</sub> [*Assonov et al., 2006*]. Therefore, the signal at  $m/z$  30 is a tracer for samples altered by N<sub>2</sub>O and can be used to determine the ratio of N<sub>2</sub>O to CO<sub>2</sub> [*Moore, 1974, Neubert, 1998, Assonov et al., 2006*]. As described in subsection 2.5.5,  $^{30}R$  is calculated as the ratio of the intensity of a sample measured at  $m/z$  30 to the intensity at  $m/z$  44. As mentioned there, using the new measurement protocol, this ratio was also determined for the reference gas, and  $^{30}\Lambda = ^{30}R / ^{30}R_{\text{reference}}$  was calculated.

To obtain a direct tracer for N<sub>2</sub>O impurities that is less dependent on CO<sub>2</sub> fragments, the relative difference between  $^{30}R^{\text{CO}_2 + \text{N}_2\text{O}}$  altered by N<sub>2</sub>O and  $^{30}R^{\text{CO}_2}$  for pure CO<sub>2</sub> is calculated for a given sample [see *Neubert, 1998*]. This is denoted as [*Neubert, 1998*]:

$$\delta 30 = \frac{^{30}R^{\text{CO}_2 + \text{N}_2\text{O}}}{^{30}R^{\text{CO}_2}} - 1. \quad (4.17)$$

The same is done for  $^{30}\Lambda$ , which cancels out the contribution of the reference, so in

#### 4. N<sub>2</sub>O Correction, Calibration & Reproducibility

principle the same value is formed:

$$\delta 30 = \frac{{}^{30}\Lambda^{\text{CO}_2 + \text{N}_2\text{O}}}{{}^{30}\Lambda^{\text{CO}_2}} - 1 = \frac{{}^{30}R^{\text{CO}_2 + \text{N}_2\text{O}} / \cancel{{}^{30}R_{\text{reference}}^{\text{CO}_2}}}{{}^{30}R^{\text{CO}_2} / \cancel{{}^{30}R_{\text{reference}}^{\text{CO}_2}}} - 1 \quad (4.18)$$

Since intensity at m/z 30 of pure CO<sub>2</sub> is mainly formed by <sup>12</sup>C<sup>18</sup>O<sup>+</sup> (<sup>13</sup>C<sup>17</sup>O<sup>+</sup> can be ignored), there is a small dependence of <sup>30</sup>R<sup>CO<sub>2</sub></sup> respectively <sup>30</sup>Λ<sup>CO<sub>2</sub></sup> on δ<sup>18</sup>O. Figure 4.2 shows this dependence on δ<sup>18</sup>O using the results of 113 (pure) CO<sub>2</sub> samples measured between March and December of 2024. As can be seen, <sup>30</sup>R<sup>CO<sub>2</sub></sup> (upper plot) shows much more noise than <sup>30</sup>Λ<sup>CO<sub>2</sub></sup> (lower plot). As *Eckhardt, 2019* demonstrated, the noise is caused by drifting over time. The comparatively stable <sup>30</sup>Λ<sup>CO<sub>2</sub></sup> underscores the benefit of measuring <sup>30</sup>R<sub>reference</sub> in addition. In principle, it would be possible to calculate <sup>30</sup>Λ<sup>CO<sub>2</sub></sup> as a function of δ<sup>18</sup>O directly from a linear fit. However, a small time dependence was also found, which was taken into account. The following function was determined for the time period March to December 2024 to calculate <sup>30</sup>Λ<sup>CO<sub>2</sub></sup> in dependence of δ<sup>18</sup>O and time (in [s] since 01.12.2024):

$$\begin{aligned} 10^3 {}^{30}\Lambda^{\text{CO}_2} = & (60.0 \pm 5.5) 10^{-8} \cdot \text{time}_{\text{since 01.12.24}} - (12.1 \pm 1.4) 10^{-15} \cdot (\text{time}_{\text{since 01.12.24}})^2 \\ & + (960.0 \pm 7.8) 10^{-3} \cdot 10^3 \delta^{18}\text{O} + (9983.2 \pm 4.4) 10^{-1} \end{aligned} \quad (4.19)$$

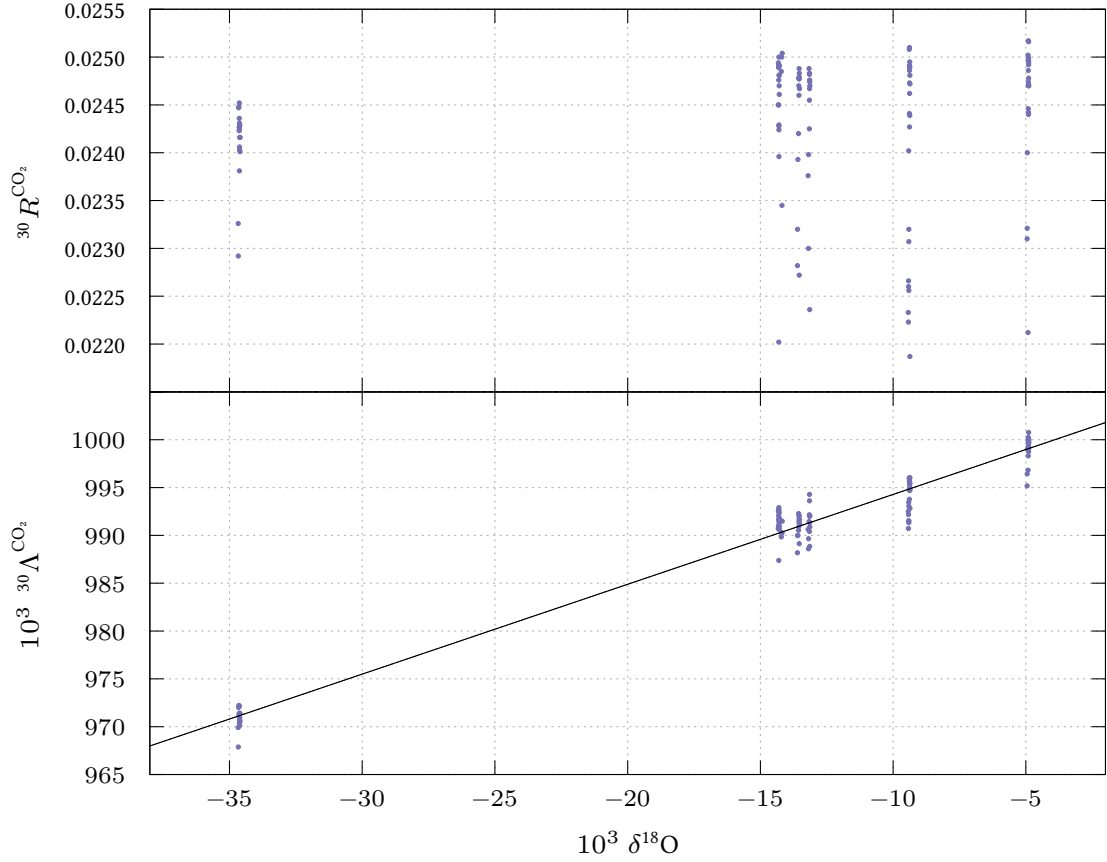
Similar functions for <sup>30</sup>R<sup>CO<sub>2</sub></sup> for measurements conducted in January and February 2024 using the old measurement protocol were determined. For simplicity's sake, these are not provided here. Further discussion will only be based on measurements having <sup>30</sup>Λ.

To determine δ30 of a sample contaminated by N<sub>2</sub>O, <sup>30</sup>Λ<sup>CO<sub>2</sub></sup> was calculated using Equation (4.19), in addition to the measured <sup>30</sup>Λ<sup>CO<sub>2</sub> + N<sub>2</sub>O</sup>. An iterative approach was chosen to calculate <sup>30</sup>Λ<sup>CO<sub>2</sub></sup> in order to account for the effect of N<sub>2</sub>O on δ<sup>18</sup>O. Using the altered δ<sup>18</sup>O in Equation (4.19) would introduce a systematic deviation of +0.0005 in the subsequently calculated (10<sup>3</sup> C<sub>N<sub>2</sub>O</sub>)/C<sub>CO<sub>2</sub></sub> for typical ambient air samples. Regarding the correction of the isotopic delta values and Δ<sub>47</sub>, this systematic deviation would lead to a systematic deviations of < -0.0002 ‰ for the isotopic deltas and < +0.0001 ‰ for Δ<sub>47</sub> for typical ambient air measurements.

The correction equations (4.5) to (4.9) require  $\frac{10^3 C_{\text{N}_2\text{O}}}{C_{\text{CO}_2}}$ , not δ30. As shown by *Neubert, 1998* and *Eckhardt, 2019*, there is a linear relationship between δ30 and  $\frac{10^3 C_{\text{N}_2\text{O}}}{C_{\text{CO}_2}}$ . According to Equation (4.18), δ30 must be zero for a sample without N<sub>2</sub>O. This is because <sup>30</sup>Λ<sup>CO<sub>2</sub> + N<sub>2</sub>O</sup> equals <sup>30</sup>Λ<sup>CO<sub>2</sub></sup> in this case. Therefore, determining  $\frac{10^3 C_{\text{N}_2\text{O}}}{C_{\text{CO}_2}}$  for one repeatedly measured sample containing N<sub>2</sub>O is suitable for calculating the slope between  $\frac{10^3 C_{\text{N}_2\text{O}}}{C_{\text{CO}_2}}$  and δ30 and its temporal development. For this purpose, the “Pic\_8\_1” gas cylinder was used. It was



#### 4.1. Isobaric Interference with N<sub>2</sub>O



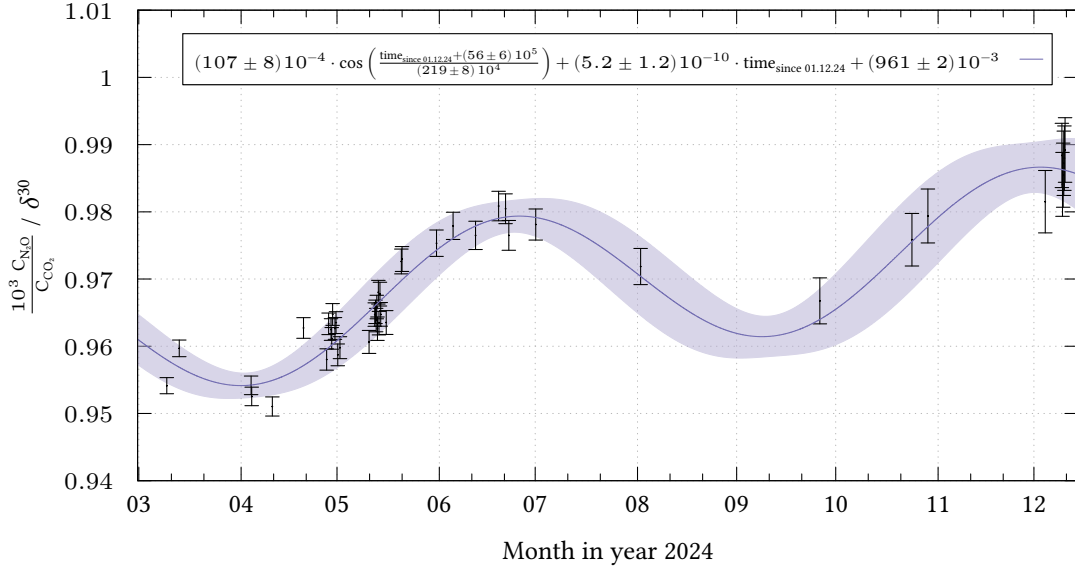
**Figure 4.2.:** This plot compares  $^{30}R^{CO_2}$  (top plot) with  $^{30}\Lambda^{CO_2}$  (bottom plot) for 113 (pure) CO<sub>2</sub> samples with different  $\delta^{18}O$  measured between March and December of 2024. The top and bottom plots show the same 113 measurements. For  $^{30}\Lambda^{CO_2}$  there is a clear dependence on  $\delta^{18}O$ , as expected. For  $^{30}R^{CO_2}$  there is more noise due to a drift with time. The noise is also visible for  $^{30}\Lambda^{CO_2}$ , but much less. So  $^{30}\Lambda^{CO_2}$  is more stable over time than  $^{30}R^{CO_2}$ .

measured ~90 times in 2024. *Eckhardt*, 2019 determined  $C_{CO_2} = (419.012 \pm 0.006)$  ppm. On May 23, 2024, a Fourier-transform infrared spectrometer was used to determine  $C_{N_2O} = (320.975 \pm 0.060)$  ppb. This yielded  $\frac{10^3 C_{N_2O}}{C_{CO_2}} = (0.76603 \pm 0.00015)$  for “Pic\_8\_1”. The temporal development of the slope  $\frac{10^3 C_{N_2O}}{C_{CO_2}}/\delta 30$  was calculated using this value along with the repeatedly determined  $\delta 30$  of “Pic\_8\_1” (see Figure 4.2). For comparison, *Eckhardt*, 2019 determined  $\frac{10^3 C_{N_2O}}{C_{CO_2}}/\delta 30 = (0.9278 \pm 0.0064)$  using the same IRMS in an experiment involving six different N<sub>2</sub>O/CO<sub>2</sub> concentration ratios. This value is slightly lower than the values shown in Figure 4.2. However, as the figure shows, the value is not expected to be constant.

Finally, to determine  $\frac{10^3 C_{N_2O}}{C_{CO_2}}$  for an ambient air sample, the function presented in Figure 4.2 was used to first calculate  $\frac{10^3 C_{N_2O}}{C_{CO_2}}/\delta 30$  at the time of measurement. Next,  $\delta 30$  of the sample was multiplied by the resulting slope.

The mean N<sub>2</sub>O concentration of 149 ambient air samples collected between April 1 and

#### 4. N<sub>2</sub>O Correction, Calibration & Reproducibility



**Figure 4.3.:** The shown temporal development of  $\frac{10^3 C_{N_2O}}{C_{CO_2}} / \delta^{30}$  is determined using  $\delta^{30}$  from Pic\_8\_1 measurements along with a known  $\frac{10^3 C_{N_2O}}{C_{CO_2}}$ . The function presented is used to calculate  $\frac{10^3 C_{N_2O}}{C_{CO_2}} / \delta^{30}$  for an ambient air sample at a given measurement time (in [s] since 01.12.2024). Then,  $\frac{10^3 C_{N_2O}}{C_{CO_2}}$  is calculated by multiplying the respective  $\delta^{30}$ . The shown uncertainty are fitting errors from the Levenberg-Marquardt algorithm implemented in Gnuplot.

November 1, 2024, was  $(338.6 \pm 2.0)$  ppm. This value was determined using the individual calculated  $\frac{10^3 C_{N_2O}}{C_{CO_2}}$  and the CO<sub>2</sub> concentrations measured with the CRDS (see section 2.4). For comparison, the mean N<sub>2</sub>O concentration of the available data<sup>(1)</sup> from April 1 to November 1, 2024, at the ICOS station KIT Karlsruhe (49.0915° N, 8.4249° E, 30 m above ground level) is  $(340.5 \pm 1.5)$  ppm [data: *Kubistin et al.*, 2025]. This value falls within the 1-sigma range of the value determined here, indicating that the determination of  $\frac{10^3 C_{N_2O}}{C_{CO_2}}$  is reliable.

<sup>(1)</sup> No data are available between approximately June 12 and October 16, 2024.

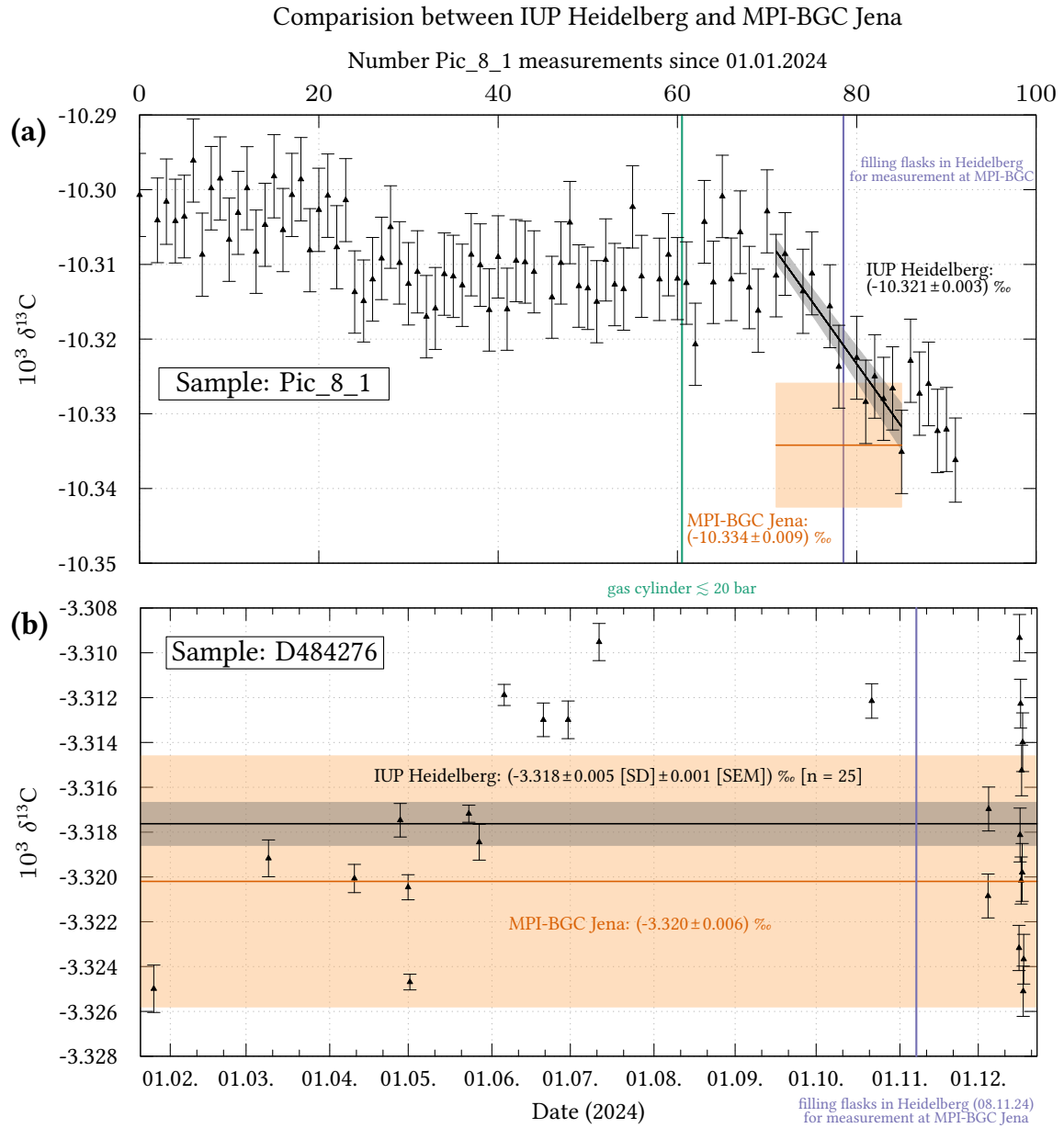
## 4.2. Calibration of $\delta^{13}\text{C}$ , $\delta^{18}\text{O}$

In Dual-Inlet mode, the working standard “Oberlahnstein” is used for a single-point calibration of  $\delta^{13}\text{C}$  and  $\delta^{18}\text{O}$ . As mentioned, this standard has been used at the IUP for many years and was employed in interlaboratory calibrations [e.g. *Neubert*, 1998; *Worthy et al.*, 2023]. However, several years have passed since these intercalibrations, and the previous preparation and measurement system is no longer used. To address potential alterations due to preparation with the Air Trap, slight alterations to the working standard (e.g., when filling the sample vessel to enable automatic refill), as well as to correct potential systematic deviations due to single-point calibration, comparison samples were sent to the Max Planck Institute for Biogeochemistry (MPI-BGC) in Jena. There, the samples were measured against the VPDB ( $\delta^{13}\text{C}$ ) and VPDB- $\text{CO}_2$  ( $\delta^{18}\text{O}$ ) scales [*Ghosh et al.*, 2005; *World Meteorological Organization*, 2014]. On November 8, 2024, two flasks were filled from gas cylinders “Pic\_8\_1” and “D484276”, respectively, for this purpose. The mean of the measurements in Jena yielded  $\delta^{13}\text{C} = (-10.334 \pm 0.009) \text{‰}$  and  $\delta^{18}\text{O} = (-2.476 \pm 0.011) \text{‰}$  for “Pic\_8\_1” and  $\delta^{13}\text{C} = (-3.320 \pm 0.006) \text{‰}$  and  $\delta^{18}\text{O} = (-14.341 \pm 0.012) \text{‰}$  for “D484276”.

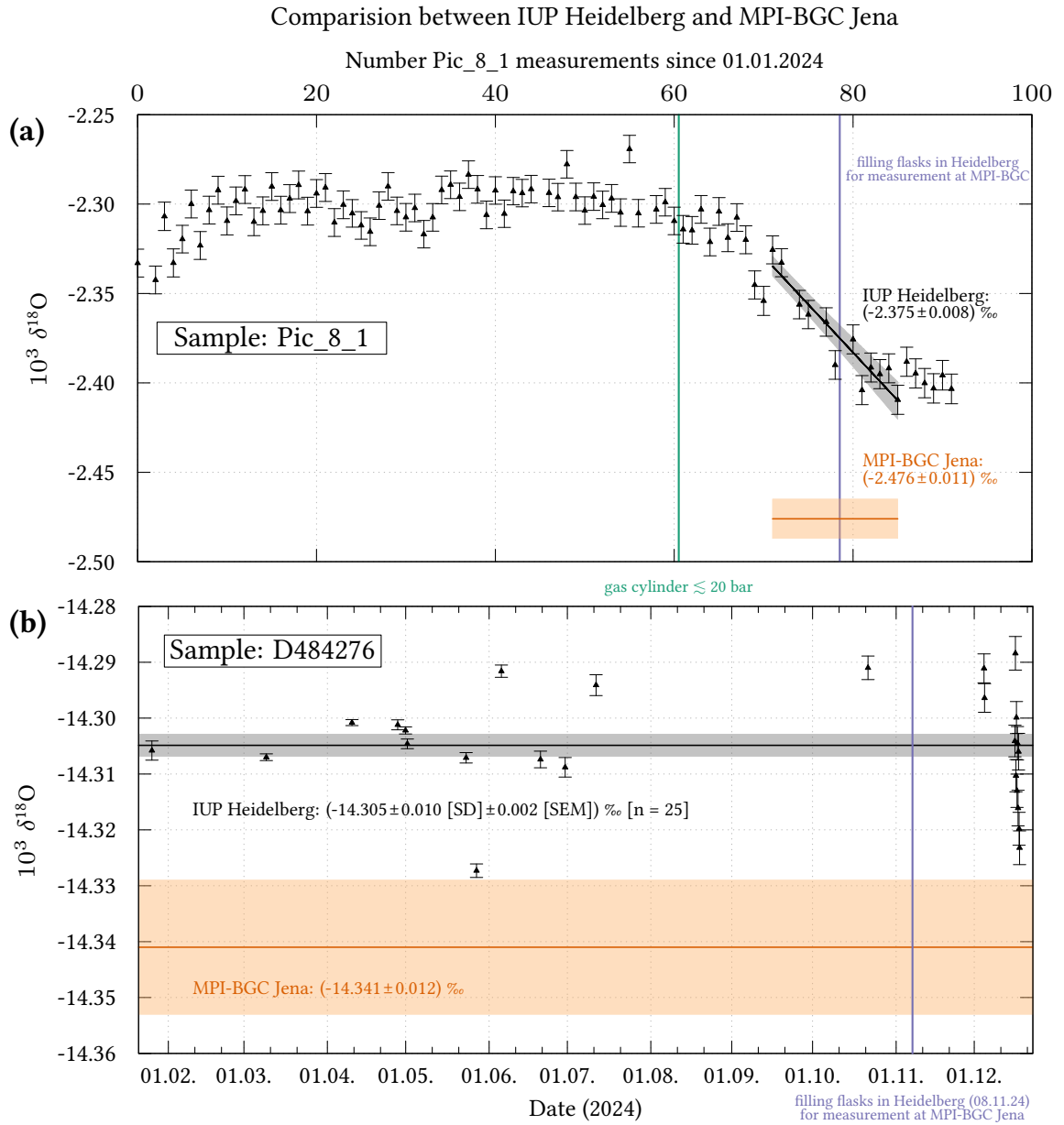
Figure 4.4 displays the  $\delta^{13}\text{C}$  measurements of “Pic\_8\_1” (a) and “D484276” (b) from 2024 in black. Figure 4.5 shows the corresponding image for  $\delta^{18}\text{O}$ . The mean values and measurement uncertainties at the MPI-BGC Jena are plotted in orange. The data from “Pic\_8\_1” are  $\text{N}_2\text{O}$ -corrected.

**Pic\_8\_1:** Results are plotted not against time, but against the number of measurements taken since January 1, 2024. This representation was chosen because “Pic\_8\_1” was undergoing a change at the time of sampling for the measurements in Jena (purple vertical line; between 78th and 79th) that did not depend on time, but on the gas cylinder pressure. The latter correlates better with the number of measurements. On May 23, 2024, the pressure in the gas cylinder decreased from ~35 bar to ~20 bar during the determination of the  $\text{N}_2\text{O}$  concentration with the Fourier-transform infrared spectrometer. It is known that the  $\text{CO}_2$  concentration in a gas cylinder can change as the pressure decreases [e.g. *Leuenberger et al.*, 2015; *Schibig et al.*, 2018; *Aoki et al.*, 2022]. This is potentially due to the desorption of  $\text{CO}_2$  molecules that were previously adsorbed onto surfaces [see *Leuenberger et al.*, 2015]. It is likely that this also influences the isotopy, causing the observed effect. To determine suitable isotope deltas at the time of flask sampling, a linear fit was applied to the data from the 71st to the 85th measurement. The results are  $\delta^{13}\text{C} = (-10.321 \pm 0.003) \text{‰}$  and  $\delta^{18}\text{O} = (-2.375 \pm 0.008) \text{‰}$  at the 78.5 measurement point.

#### 4. N<sub>2</sub>O Correction, Calibration & Reproducibility



**Figure 4.4.:** Comparison of  $\delta^{13}\text{C}$  results from Heidelberg (black line) and MPI-BGC Jena (orange line) for gas cylinders “Pic\_8\_1” (a) and “D484276” (b). Heidelberg measurements are drift-corrected, as described in appendix B.17 (page 169ff) and N<sub>2</sub>O-corrected (for “Pic\_8\_1”) using Equation (4.5). The purple line indicates when flasks from gas cylinders were filled for measurement in Jena. Since “Pic\_8\_1” measurements are subject to drift, presumably due to the gas cylinder emptying, they were plotted against the number of measurements since January 1, 2024 (cf. green line). A linear fit was used to determine the Heidelberg value at the time the flasks for Jena were filled. The results from Heidelberg and Jena are not significantly different. Therefore, a single-point calibration via “Oberlahnstein” is sufficient for  $\delta^{13}\text{C}$ .



**Figure 4.5.:** Comparison of  $\delta^{18}\text{O}$  results from Heidelberg (black line) and MPI-BGC Jena (orange line) for gas cylinders “Pic\_8\_1” (a) and “D484276” (b). Heidelberg measurements are drift-corrected, as described in appendix B.17 (page 169ff) and  $\text{N}_2\text{O}$ -corrected (for “Pic\_8\_1”) using Equation (4.6). The purple line indicates when flasks from gas cylinders were filled for measurement in Jena. Since “Pic\_8\_1” measurements are subject to drift, presumably due to the gas cylinder emptying, they were plotted against the number of measurements since January 1, 2024 (cf. green line). A linear fit was used to determine the Heidelberg value at the time the flasks for Jena were filled. The difference between the Heidelberg and Jena measurements is approximately  $10 \sigma$  for “Pic\_8\_1” and  $3 \sigma$  for “D484276” (Jena uncertainty). A transfer function was obtained using a linear fit (Equation (4.20)) to convert Heidelberg results to Jena VPDB- $\text{CO}_2$  scale.

#### 4. N<sub>2</sub>O Correction, Calibration & Reproducibility

**D484276:** The slight parabolic change in Figure 4.4 (b) between June and December is likely due to an insufficient correction of the drift discussed in appendix B.17 on page 169ff. This was attributed to the presumed decrease in pressure of the working standard. The decrease in working standard pressure probably also caused the greater dispersion observed in December for both  $\delta^{13}\text{C}$  and  $\delta^{18}\text{O}$ . Nevertheless, the mean values of  $\delta^{13}\text{C}$  and  $\delta^{18}\text{O}$  were determined using all available data (black horizontal lines). The results are  $\delta^{13}\text{C} = (-3.318 \pm 0.005 \text{ [SD]} \pm 0.001 \text{ [SEM]}) \text{ ‰}$  and  $\delta^{18}\text{O} = (-14.305 \pm 0.010 \text{ [SD]} \pm 0.002 \text{ [SEM]}) \text{ ‰}$ .

#### Calibration

As can be seen in Figure 4.4, the deviations between the  $\delta^{13}\text{C}$  values determined in Heidelberg and Jena are not significant for either “Pic\_8\_1” (a) or “D484276” (b). Therefore, no additional calibration function is assumed for  $\delta^{13}\text{C}$ , and the values from the single-point calibration are used.

However, significant deviations between the Jena and Heidelberg measurements are observed for  $\delta^{18}\text{O}$ . The more pronounced deviation in “Pic\_8\_1” of approximately  $10 \sigma$  compared to the smaller deviation of approximately  $3 \sigma$  in “D484276” also indicates a slight dependence on isotopy. To express  $\delta^{18}\text{O}$  relative to the VPDB-CO<sub>2</sub> scale according to the measurements in Jena,  $\delta^{18}\text{O}^{\text{LF}}$  measurements in the Heidelberg laboratory frame (LF) are calibrated as follows:

$$\delta^{18}\text{O} = (0.99451 \pm 0.00092) \cdot 10^3 \delta^{18}\text{O}^{\text{LF}} - (0.1144 \pm 0.0057) \quad (4.20)$$

However, this comparison indirectly suggests that processing with the Air Trap does not result in pronounced fractionation, particularly with respect to  $\delta^{13}\text{C}$ . Without further calibration, the World Meteorological Organization (WMO) / Global Atmospheric Watch (GAW) Network Compatibility Goal of 0.01 ‰ is met for  $\delta^{13}\text{C}$  in “D484276”, but narrowly missed in “Pic\_8\_1” [see WMO/IAEA, 2016 (Table 1) for compatibility goals]. The difference in “Pic\_8\_1” could be due to inaccuracies in N<sub>2</sub>O correction. As discussed in subsection 4.1.1, the value determined here could be enriched by approximately 0.006 ‰ in  $\delta^{13}\text{C}$  compared to the value determined in Jena, as Jena presumably uses the function by Ghosh et al., 2004 [see Worthy et al., 2023 (Table 5)]. For  $\delta^{18}\text{O}$ , the WMO/GAW Network Compatibility Goal of 0.05 ‰ is achieved for “D484276” without calibration using Equation (4.20) but the WMO/GAW Extended Compatibility Goal of 0.1 ‰ is narrowly missed for “Pic\_8\_1”.

### 4.3. Calibration of $\Delta_{47}$ (and $\Delta_{48}$ , $\Delta_{49}$ )

To transfer  $\Delta_{47}$  determined in the laboratory frame (LF) to the reference frame (RF) according to *Dennis et al., 2011*, it is necessary to produce suitable calibration standards with different equilibration temperatures. Since  $\Delta_{47}$  also exhibits a dependence on  $^{47}\delta$  related to the mass spectrometer, standards with the same equilibration temperature and varying  $^{47}\delta$  values are also required [see e.g. *Dennis et al., 2011*]. The same applies to  $\Delta_{48}$  and  $\Delta_{49}$ , which depend on  $^{48}\delta$  and  $^{49}\delta$ , respectively. Five standards were produced in total. Three of these standards were equilibrated at  $\sim 50$  °C with varying  $^{47}\delta$  values. These standards are designated “EG50”, “E50\_N48”, and “EG50\_LW”. The other two standards were equilibrated at  $\sim 230$  °C (“HG230”) and  $\sim 5$  °C (“EG5”). To enable regular automated measurement of the standards, an attempt was made to produce them in larger quantities.

#### 4.3.1. Production of Temperature-Equilibrated CO<sub>2</sub> Standards

“EG5”, “EG50”, and “HG230” are based on Oberlahnstein ( $\delta^{13}\text{C} \approx -4.42$  ‰,  $\delta^{18}\text{O} \approx -9.79$  ‰). “EG50\_N48” and “EG50\_LW” are based on high-purity CO<sub>2</sub> from a commercial gas cylinder (N48 | purity  $\geq 99.998$  %; Air Liquide Deutschland GmbH, Düsseldorf, Germany) with  $\delta^{13}\text{C} \approx -35.8$  ‰ and  $\delta^{18}\text{O} \approx -24.7$  ‰.

To prepare “HG230”, Oberlahnstein from a gas cylinder was filled ( $> 1$  bar) into a 150 ml stainless steel vessel (4L-SC18-DN4-150-F2; FITOK, Offenbach am Main, Germany). The lower end of the vessel was welded shut. The upper end was closed with two valves (SS-4H; Swagelok, Solon, Ohio, U.S.) connected in series to the vessel using a 1/8" tube. For equilibration, the vessel was placed in an oven (UT 6; Kendro Laboratory Products, Hanau, Germany) at  $(233.8 \pm 3.0)$  °C for about five days with the valves kept outside. Using Equation (C.23) determined by *Eobaldt, 2019* for the temperature-dependent reaction rate constant, a new equilibrium should be reached within 24 hours at these temperatures when starting from room temperature (see appendix C.2; page 191).

On the other hand, “EG5”, “EG0”, “EG50\_N48”, and “EG50\_LW” were equilibrated using water [see *Dennis et al., 2011*; *Affek, 2013*; *Kalb et al., 2020*]. Using the reaction rate function determined by *Kalb et al., 2020* (see appendix C.2; page 191), starting from room temperature ( $\sim 24$  °C) high-purity CO<sub>2</sub> equilibrates with water in approximately one day at 5 °C and approximately 8 hours at 50 °C (deviation from expected equilibrium  $\lesssim 0.001$  ‰). About 15 ml de-ionized water ( $\delta^{18}\text{O}_{\text{VSMOW}} \approx -8.7$  ‰) was used to equilibrate “EG5”, “EG50”, and “EG50\_N48”. Approximately 10 ml isotopically light water ( $\delta^{18}\text{O}_{\text{VSMOW}} \approx -35$  ‰) from North Greenland was used to equilibrate “EG50\_LW”. A  $\sim 190$  ml glass cylinder with a closing valve (Normag, Ilmenau, Germany) was used as a re-equilibration vessel (see

#### 4. $N_2O$ Correction, Calibration & Reproducibility

Figure C.1; page 192). To minimize potential contamination, the vessel was flushed with synthetic air and high-purity  $CO_2$  after being filled with water. After each flushing, the water was frozen to evacuate the gases. Then, the evacuated container was refilled with  $CO_2$  for re-equilibration. To re-equilibrate “EG5”, the glass vessel was placed in a water-filled container (to dampen temperature fluctuations) inside a refrigerator at  $(4.6 \pm 0.2)^\circ C$  for about five days. The vessel was gently swirled at regular intervals to improve re-equilibration by wetting the inner surface. To equilibrate the “EG50”, “EG50\_N48”, and “EG50\_LW” standards, the glass vessel was placed in a temperature-controlled water bath (F3/S; Haake Fisons) at  $(49.8 \pm 0.3)^\circ C$ , for more than three days, respectively (see Figure C.1; page 192). The vessel was swirled regularly, and the water bath was refilled with preheated water as needed. In all cases, temperatures were recorded using a custom-designed Arduino-based temperature-measuring device with an SD memory function and two Pt-1000 temperature sensors (otom, Bräunlingen, Germany): one heat-resistant for the oven and one waterproof sensor for the water bath.

After re-equilibration in the glass vessel, the water was frozen briefly using liquid  $N_2$ , followed by an ethanol-dry ice mixture. The vessel was then placed in a dry ice-filled container and connected to a manual preparation line (see Figure C.2; page 193). The equilibration vessel in the oven was connected directly to this line.  $CO_2$  was introduced into the line via a needle valve and frozen by cryogenic pumping into a trap immersed in liquid  $N_2$ . Before reaching this trap, the  $CO_2$  passed through four stainless steel coils immersed in an ethanol-dry ice mixture to freeze remaining water molecules. Non-condensed molecules were removed by using the vacuum pumps of the Air Trap. Finally, the  $CO_2$  was transferred by cryogenic pumping into an evacuated stainless steel vessel (FITOK, Offenbach am Main, Germany) immersed in liquid  $N_2$ , while the former trap was cooled using an ethanol-dry ice mixture. After freezing, the valve (SS-4H; Swagelok, Solon, Ohio, U.S.) on the vessel was closed and the vessel was disconnected from the manual line. This was done for each standard, and the vessels were connected to the valve blocks of the Air Trap (see Figure B.13; page 154).

##### 4.3.2. Purity of Standards

In measurements of with and without GC preparation, the standards “EG50\_N48” and “EG50\_LW”, which are based on high-purity  $CO_2$  from the commercial  $CO_2$  gas cylinder, showed no significant differences in  $\Delta_{47}$ ,  $\Delta_{48}$ , and  $\Delta_{49}$ . Therefore, they are presumably largely free of isobarically interacting impurities. Regardless of this, for comparability with other samples, they were nevertheless always prepared using the GC.

There were also no significant deviations in  $\Delta_{47}$  for “EG5” and “EG50” when processed



### 4.3. Calibration of $\Delta_{47}$ (and $\Delta_{48}$ , $\Delta_{49}$ )

with or without GC. However, slight deviations were measured for these standards in  $\Delta_{48}$  and  $\Delta_{49}$ :  $\Delta(\Delta_{48}^{\text{LF}}) \approx +0.2\text{‰}$  and  $+0.5\text{‰}$ , respectively, and  $\Delta(\Delta_{49}^{\text{LF}}) \approx +27\text{‰}$  and  $+18\text{‰}$ , respectively. On the other hand, “HG230” also showed a significant difference for  $\Delta_{47}$ , with  $\Delta(\Delta_{47}^{\text{LF}}) \approx +0.37\text{‰}$ . Large deviations were observed for  $\Delta_{48}$  and  $\Delta_{49}$ , with  $\Delta(\Delta_{48}^{\text{LF}}) \approx +2.1\text{‰}$  and  $\Delta(\Delta_{49}^{\text{LF}}) \approx +246\text{‰}$ .

However, the deviations of “EG5”, “EG50”, and “HG230” may not be fully explained by using “Oberlahnstein” as the basis for these standards. An experiment measuring “Oberlahnstein” prepared with and without GC showed no significant differences in  $\Delta_{48}$  and only slight differences in  $\Delta_{49}$ , with  $\Delta(\Delta_{49}^{\text{LF}}) \approx +5\text{‰}$ . The order in which the preparations were carried out could also be a factor: 1. “HG230”, 2. “EG5”, 3. “EG50”, 4. “EG50\_N48”, 5. “EG50\_LW”. A better routine may have resulted in less contamination. Alternatively, the manual line and glass container (except “HG230”) could have become increasingly free of contamination.

One possible explanation for the significant deviations in “HG230” is that compounds decomposed during heating, which, in their undecomposed state, normally desublimates during ethanol-dry ice cooling or do not cause (large) isobaric interference during measurement. Another possibility is that the compounds detached from the inner surface of the metal cylinder, which may have become in addition contaminated during the welding process. As an alternative explanation, the impurities in the other water-containing preparations may have been retained more effectively due to heterogeneous nucleation on the ice crystals.

#### 4.3.3. Calibration and Correction on $^{47}\delta$ (and $^{48}\delta$ , $^{49}\delta$ ).

Unfortunately, the produced standards exhibited drift (see Figure C.6; page 198). Additionally, superimposed device drifts were detected for  $\Delta_{48}^{\text{LF}}$  and  $\Delta_{49}^{\text{LF}}$ . For this reason, only the initial measurements from  $\Delta_{47}^{\text{LF}}$ ,  $\Delta_{48}^{\text{LF}}$ , and  $\Delta_{49}^{\text{LF}}$  are used for calibrations and corrections on  $^{47}\delta$ ,  $^{48}\delta$  and  $^{49}\delta$ , respectively. The data determined in the laboratory frame (LF) can be found in Table C.2 on page 194. Values calculated according to *Dennis et al., 2011* in the reference frame (RF) are in Table C.1 on the same page.

Several studies have reported a dependency of  $\Delta_{47}$  on  $^{47}\delta$  [e.g. *Huntington et al., 2009; Dennis et al., 2011; He et al., 2012; Bernasconi et al., 2013; Fiebig et al., 2016; Laskar, Mahata, and Liang, 2016*]. The reason for this dependency is likely the influence of secondary electrons [*Bernasconi et al., 2013; Fiebig et al., 2016*]. In Figure 4.6 (a), the means of  $\Delta_{47}^{\text{LF}}$  are plotted against  $^{47}\delta$  for “EG50”, “EG50\_N48”, and “EG50\_LW”. A linear function called the equilibrated (and heated) gas line (EGL) is fitted [*Huntington et al., 2009; Dennis et al., 2011*]. The slope of the EGL in Figure 4.6 (a) is lower than that reported by *Dennis et al.,*

#### 4. N<sub>2</sub>O Correction, Calibration & Reproducibility

2011. This difference may be due to the minimized influence of secondary electrons in the MAT253+, which has shielded collectors, compared to the MAT253 [Müller et al., 2017; Swart et al., 2021], as well as the use of a pressure baseline (PBL) correction [e.g. He et al., 2012; Meckler et al., 2014; Fiebig et al., 2016]. The remaining dependence compared to Bernecker et al., 2023 is likely due to an imperfect PBL correction. The positive slope compared to the values in Dennis et al., 2011 suggests that the chosen PBL correction overestimates the background (see argumentation on  $\Delta_{48}$  in Fiebig et al., 2019). Since several studies found no significant difference in slope depending on the equilibration temperatures of the standards [e.g. Dennis et al., 2011; He et al., 2012; Laskar, Mahata, and Liang, 2016], the slope determined here is assumed to be applicable to other equilibration temperatures as well. This slope is used to correct  $\Delta_{47}^{\text{LF}}$  with regard to  $^{47}\delta$ , ensuring that they uniformly correspond to  $^{47}\delta = 0$  [Dennis et al., 2011]:

$$\begin{aligned} 10^3 \Delta_{47}^{\text{LF} (^{47}\delta = 0)} &= 10^3 \Delta_{47}^{\text{LF}} - 10^3 ^{47}\delta \times \text{Slope}_{\text{EGL}} \\ &= 10^3 \Delta_{47}^{\text{LF}} + 10^3 ^{47}\delta \times (10.4 \pm 2.3) 10^{-4} \end{aligned} \quad (4.21)$$

The correction of  $\Delta_{48}^{\text{LF}}$  and  $\Delta_{49}^{\text{LF}}$  relative to  $^{48}\delta$  and  $^{49}\delta$ , respectively, follows the same principle. Figures C.3 (a) on page 195 and C.4 (a) on page 196 show the corresponding graphs. The dependencies of  $\Delta_{48}^{\text{LF}}$  on  $^{48}\delta$  and of  $\Delta_{49}^{\text{LF}}$  on  $^{49}\delta$  are relatively large. They fall within the expected reference scale of  $\Delta_{48}$  and exceed it for  $\Delta_{49}$  (cf. Figure 2.4; page 16). Fiebig et al., 2019 and Swart et al., 2021 also observed this strong dependency on  $^{48}\delta$  for  $\Delta_{48}^{\text{LF}}$ . As for  $\Delta_{47}^{\text{LF}}$ , an optimized PBL correction could eliminate the dependencies on  $^{48}\delta$  and  $^{49}\delta$ , respectively [see Bernecker et al., 2023]. This could not be implemented within the scope of this work, but it should be addressed in the future.

An empirical transfer function (ETF) [Dennis et al., 2011] was determined to convert  $\Delta_{47}^{\text{LF} (^{47}\delta = 0)}$  into the reference frame (RF) according to Dennis et al., 2011. For this purpose,  $\Delta_{47}^{\text{RF}}$  calculated according to Equation (2.26) for the respective equilibration temperature were plotted against the corresponding  $\Delta_{47}^{\text{LF} (^{47}\delta = 0)}$ , as shown in Figure 4.6 (b).  $\Delta_{47}^{\text{LF} (^{47}\delta = 0)}$  of “EG50”, “EG50\_N48”, and “EG50\_LW” were weighted averaged. The ETF was determined using a linear fit, which was then used for calibration as follows:

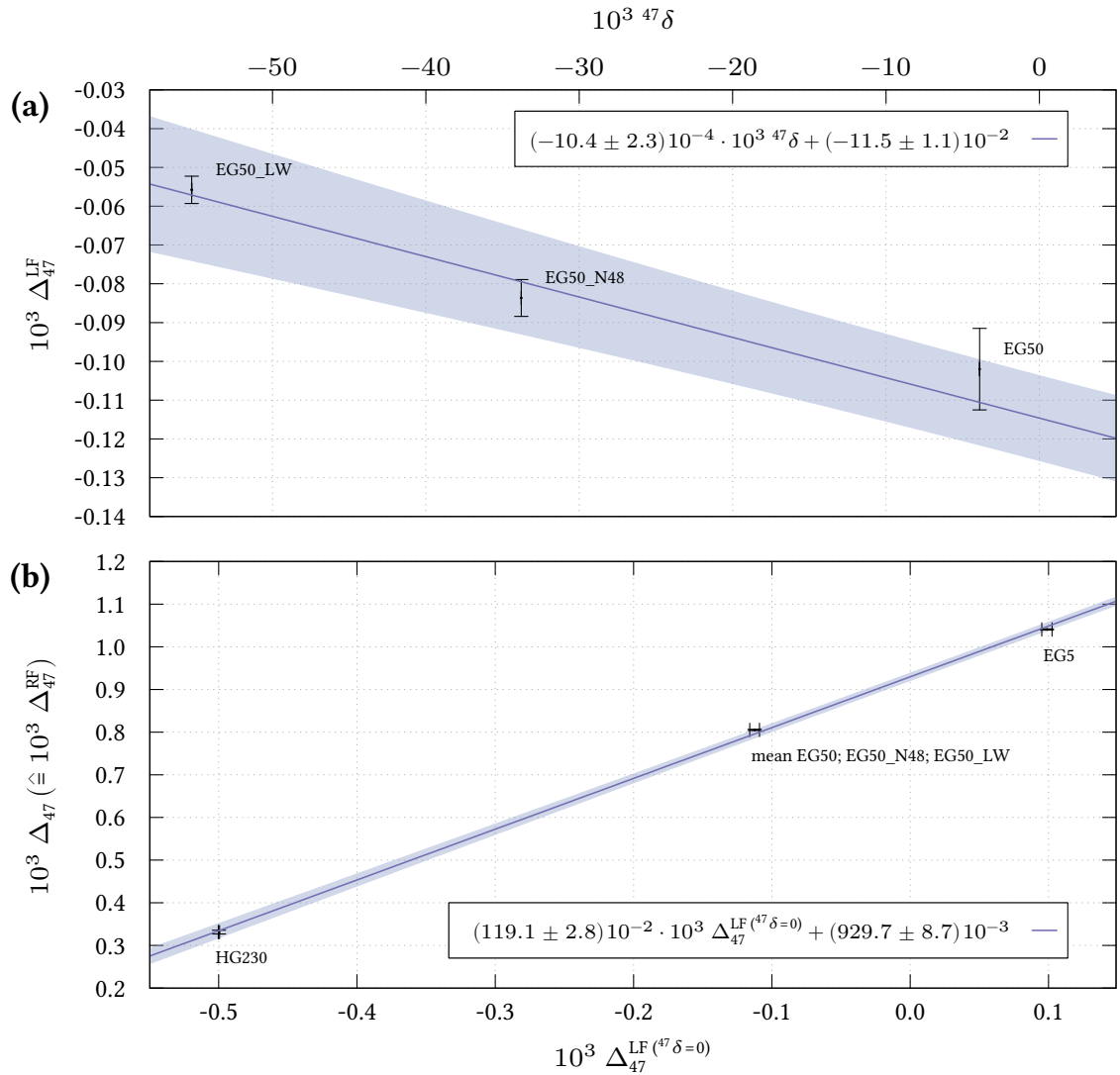
$$10^3 \Delta_{47} = (1.191 \pm 0.028) \cdot 10^3 \Delta_{47}^{\text{LF} (^{47}\delta = 0)} + (929.7 \pm 8.7) 10^{-3} \quad (4.22)$$

Since the long-term measurements of “Pic\_8\_1” and “D484276”, presented in Figure C.5 on page 197, do not show a prominent trend over time, it was concluded that the calibration remained stable. However, based solely on the “D484276” measurements, a slight trend cannot be entirely ruled out. This could result in deviations of up to +0.02 ‰ for

#### 4.3. Calibration of $\Delta_{47}$ (and $\Delta_{48}$ , $\Delta_{49}$ )

measurements taken from January through early March. Additionally, this graph shows no significant differences between the new and old measurement protocols. The latter is corrected as described in appendix A.3 on page 130ff.

Figures C.3 (b) on page 195 and C.4 (b) on page 196 show the corresponding plots and ETFs for  $\Delta_{48}$  and  $\Delta_{49}$ , respectively. Since only a few  $\Delta_{48}$  calibrations have been published [e.g. *Fiebig et al., 2019; Swart et al., 2021; Bernecker et al., 2023; Lucarelli et al.,*



**Figure 4.6.:**  $\Delta_{47}^{LF}$  in the laboratory frame (LF) plotted against  ${}^{47}\delta$  for “EG50”, “EG50\_N48”, and “EG50\_LW”, which have the same equilibration temperature of  $\sim 49.8$  °C (a). An empirical linear function was fitted, which is referred as the equilibrated (and heated) gas line (EGL). The slope of the EGL is used to adjust the value of  $\Delta_{47}^{LF}$  as if  ${}^{47}\delta$  were equal to zero (see Equation (4.21)). (b) shows  $\Delta_{47}^{RF}$  for the corresponding equilibration temperatures calculated according to Equation (2.26) in the reference frame (RF) provided by *Dennis et al., 2011* plotted against the correspondingly corrected  $\Delta_{47}^{LF ({}^{47}\delta=0)}$ .  $\Delta_{47}^{LF ({}^{47}\delta=0)}$  of “EG50”, “EG50\_N48”, and “EG50\_LW” was weighted averaged. The linearly determined function is used for calibration.

#### 4. $N_2O$ Correction, Calibration & Reproducibility

2023], the successful calibration indicates the quality of the preparation and the selected measurement method. However, as previously mentioned, a superimposed drift was present for  $\Delta_{48}$ , so this calibration was only applicable for a short period of time. The ETF of  $\Delta_{49}$  exhibits a high degree of uncertainty. Without drift of the standards and the superimposed drift, a more reliable ETF might have been possible with a higher number of repeated standard measurements.

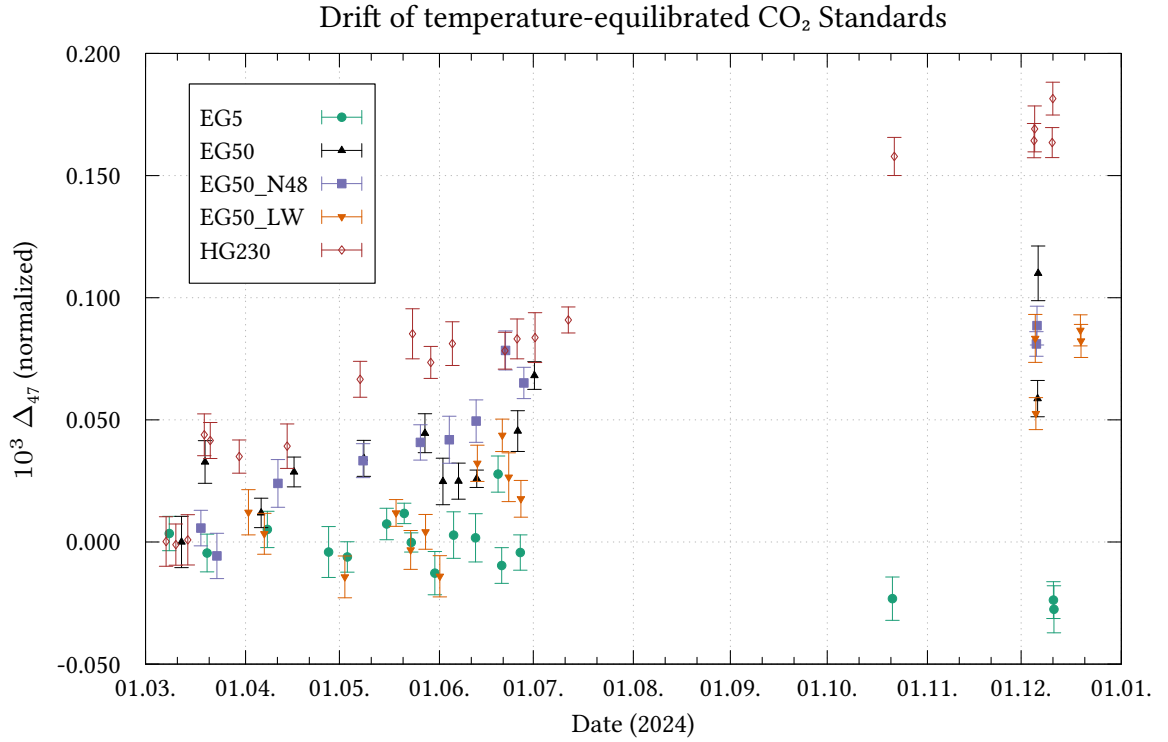
##### $\Delta_{47}$ of “Pic\_8\_1” and “D484276”

When the calibration of  $\Delta_{47}$  is applied to the “Pic\_8\_1” and “D484276” measurements conducted from February 1 to November 1, 2024, the results are  $\Delta_{47} = (0.974 \pm 0.010$  [SD]  $\pm 0.002$  [SEM]) ‰ [n = 45] and  $\Delta_{47} = (0.946 \pm 0.012$  [SD]  $\pm 0.004$  [SEM]) ‰ [n = 12], respectively. These correspond to equilibration temperatures of  $(15.9 \pm 1.8$  [SD]  $\pm 0.4$  [SEM]) °C and  $(21.0 \pm 2.3$  [SD]  $\pm 0.8$  [SEM]) °C, respectively. In 2019, *Eckhardt*, 2019 determined  $\Delta_{47} = (0.958 \pm 0.022)$  ‰ for one “Pic\_8\_1” measurement and  $\Delta_{47} = (0.937 \pm 0.024)$  ‰ and  $(0.899 \pm 0.022)$  ‰ for two “D484276” measurements. Considering the reported measurement uncertainties, the “Pic\_8\_1” measurement falls within one  $\sigma$ , while the “D484276” measurements fall within one and three  $\sigma$ , respectively. *Eckhardt*, 2019 performed his preparations using a manual preparation line [see e.g. *Kalb*, 2015; *Eckhardt*, 2019; *Kalb et al.*, 2020; *Weise et al.*, 2020], which uses a packed Porapak™ Q trap held at -35 °C to remove potentially interfering molecules, such as hydrocarbons. Compliance with this established manual preparation method is an indication of successful preparation using the Air Trap built in this thesis.

#### 4.3.4. Stability of the produced Standards

As previously mentioned, the produced standards exhibited a drift. Figure 4.7 shows the normalized  $\Delta_{47}$  values of the various standards over time. To normalize the data, the mean of the initial measurement results after preparing the standards was subtracted from each value. The laboratory’s room temperature was determined using 116 daily mean values between March 1 and July 2, 2024, yielding a mean of  $(24.4 \pm 0.8)$  °C. As can be seen in Figure 4.7, “EG5”, which was equilibrated below room temperature, takes on increasingly lower values and thus drifts toward a higher temperature. The opposite is true for the other standards, which drift toward higher values and thus toward a lower temperature. The drift is most pronounced in “EG230”, which was equilibrated farthest from room temperature. Based on the good stability of “Pic\_8\_1” and “D484276” measurement results shown in Figure C.5 on page 197, a true alteration of the calibration

### 4.3. Calibration of $\Delta_{47}$ (and $\Delta_{48}$ , $\Delta_{49}$ )



**Figure 4.7.:** The observed drift of the equilibrated CO<sub>2</sub> standards is shown (errors: SEM). The data have been normalized by subtracting the mean of the initial measurements taken after preparing the standards. Standard “EG5”, equilibrated at ~4.6 °C, is drifting toward a lower Δ<sub>47</sub> (higher temperatures). The other standards, equilibrated at ~49.8 °C and ~233.8 °C, are drifting toward higher Δ<sub>47</sub> (lower temperatures). This suggests drift toward room temperature, which was approximately 24 °C. Due to this drift, only the initial measurements of these standards could be used for calibration

of Δ<sub>47</sub> can be ruled out. Therefore, it can be assumed that the standards are drifting toward room temperature.

Laskar et al., 2019 measured middle tropospheric CO<sub>2</sub> samples that had been collected and prepared several years earlier [see Assonov et al., 2009]. These samples still exhibited Δ<sub>47</sub>, which does not correspond to Δ<sub>47</sub> at room temperature. Therefore, if the samples were stored at temperatures close to room temperatures, the Δ<sub>47</sub> value of (pure) CO<sub>2</sub> should be more stable, as was observed here. Additionally, a stabilizing trend in δ<sup>18</sup>O was observed (see Figure C.7 on page 199). The absence of this trend in δ<sup>13</sup>C (see Figure C.8 on page 200) suggests the potential involvement of oxygen atom exchange. This could indicate the presence of trace amounts of water. However, other effects, such as interaction with the inner surface of the sample vessels, might also be a factor. Regardless, future measurements of the standards produced here could reveal whether they converge to a Δ<sub>47</sub> value corresponding to room temperature. A change in storage temperature that may induces a shift in δ<sup>18</sup>O could indicate water’s influence, as the fractionation of δ<sup>18</sup>O

#### 4. $N_2O$ Correction, Calibration & Reproducibility

during water- $CO_2$  exchange depends on temperature [see *Brenninkmeijer et al.*, 1983].

##### 4.3.5. Recommendations

Due to the observed drift, which may be caused by water traces, the preparation process of the temperature-equilibrated standards should include more extensive steps to remove water, for example using  $P_2O_5$ , as used by *Assonov et al.*, 2009. Regardless, at least three standards could be equilibrated at room temperature to correct for dependence on  $^{47}\delta$ ,  $^{48}\delta$ , and  $^{49}\delta$ , respectively. To ensure similar drift, these should be stored connected under a good heat conduction and, to minimize temperature fluctuations, surrounded by a medium with high heat capacity. It is advisable to store standards that are equilibrated at temperatures other than room temperature at temperatures as low as possible, for example, in a freezer or cold storage room. This greatly reduces re-equilibration with water vapor and might slow other potential effects that induce re-equilibration.

## 4.4. Reproducibility

To determine the reproducibility, results of regular measurements of the gas cylinders “Pic\_8\_1” and “D484276” from February 1 to November 1, 2025, were considered. Measurements taken after November 1, 2025, were not considered because no relevant tests or ambient air measurements were conducted after that date, and the reproducibility of measurements after that date was compromised likely due to the increasing exhaustion of the working standard (see appendix B.17; page 169ff). Additionally, measurements outside the standard procedure for measurement or preparation were not considered. Figure 4.8 shows the normalized data of the final calibrated and corrected measurement results for  $\delta^{13}\text{C}$  (a),  $\delta^{18}\text{O}$  (b), and  $\Delta_{47}$  (c). The mean values of the “Pic\_8\_1” and “D484276” measurement results were subtracted from the individual results for normalization.  $\delta^{13}\text{C}$  and  $\delta^{18}\text{O}$  of “Pic\_8\_1” were not considered after May 23, 2024, due to drift induced by the emptying gas cylinder (see section 4.2). Note that this drift did not significantly impact  $\Delta_{47}$ ; compare Figures 4.4 (a) and 4.5 (a) on page 60f for  $\delta^{13}\text{C}$  and  $\delta^{18}\text{O}$  (November 1, 2024 corresponds to “Pic\_8\_1” measurement 78.5 in these figures). The relatively higher values for “D484276” after June 1 in Figure 4.8 (a) are likely due to the suboptimal drift correction discussed in appendix B.17 (page 169ff). The conservatively rounded reproducibility based on the SD of the normalized “Pic\_8\_1” and “D484276” results is  $\sim 0.005\text{‰}$  ( $n = 44$ ) for  $\delta^{13}\text{C}$ ,  $\sim 0.01\text{‰}$  ( $n = 44$ ) for  $\delta^{18}\text{O}$ , and  $\sim 0.011\text{‰}$  ( $n = 57$ ) for  $\Delta_{47}$ . Figure C.9 on page 201 resembles Figure 4.8, but it uses uncalibrated data that has not been corrected for the effects of  $\text{N}_2\text{O}$  and  $^{47}\delta$  on  $\Delta_{47}$ . The reproducibility of  $\delta^{13}\text{C}$  and  $\delta^{18}\text{O}$  is comparable to that obtained in Figure 4.8. However, better reproducibility of  $\sim 0.009$  is achieved for  $\Delta_{47}^{\text{LF}}$ . The higher value in Figure 4.8 is due to calibration.

Slightly better reproducibility values can probably be achieved for  $\delta^{13}\text{C}$  and  $\delta^{18}\text{O}$ , and possibly for  $\Delta_{47}$ , provided that additional effects due to drift caused by an emptying working standard and refilling the working standard from the intermediate volume only occur once (see appendix B.17; page 169ff). Furthermore, prolonged non-use of the IRMS initially leads to slightly different results, which are probably partly due to a differently conditioned ion source. For instance, considering only measurements with a single refill from the intermediate volume during the period from April 1 to May 20, 2024, with regular IRMS use, the normalized, calibrated, and corrected data from “Pic\_8\_1” and “D484276” ( $n = 25$ ) yield an SD of approximately  $0.0025\text{‰}$  for  $\delta^{13}\text{C}$ ,  $0.0060\text{‰}$  for  $\delta^{18}\text{O}$ , and  $0.0091\text{‰}$  for  $\Delta_{47}$ .

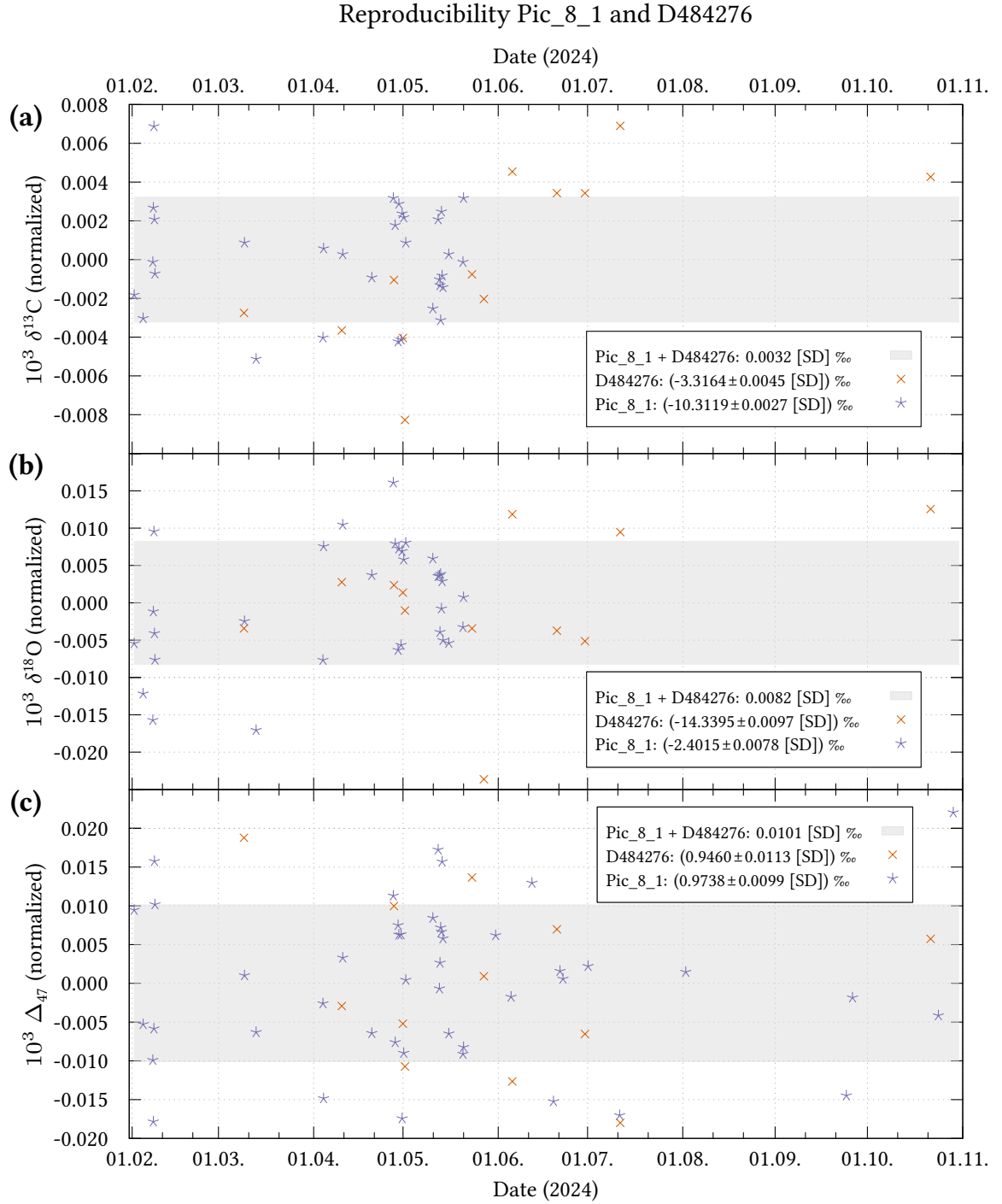
For comparison, Affek et al., 2006 achieved an external reproducibility of  $0.1\text{‰}$  for  $\delta^{13}\text{C}$ ,  $0.3\text{‰}$  for  $\delta^{18}\text{O}$ , and  $0.07\text{‰}$  for  $\Delta_{47}$ . Laskar, Yui, et al., 2016 achieved a reproducibility of  $0.01\text{‰}$  for  $\delta^{13}\text{C}$ ,  $0.05\text{‰}$  for  $\delta^{18}\text{O}$ , and  $0.014\text{‰}$  for  $\Delta_{47}$  ( $n = 15$ ) over a period of six

#### 4. $N_2O$ Correction, Calibration & Reproducibility

months. *Fiebig et al.*, 2019 achieved an external reproducibility of approximately 0.01 ‰ for  $\Delta_{47}$  [*Fiebig et al.*, 2021] over a period of about one and a half months. *Werner et al.*, 2001 achieved a long term (> 9 months) single sample precision for  $\delta^{13}C$  and  $\delta^{18}O$  of 0.013 ‰ and 0.019 ‰, respectively. Excluding a period of approximately two months during which the values were systematically offset, possibly due to a leak, they achieved 0.008 ‰ and 0.013 ‰, respectively.

Compared to *Affek et al.*, 2006 and *Laskar, Yui, et al.*, 2016, who also measured  $\Delta_{47}$  from ambient air  $CO_2$  in other studies [cf. *Affek et al.*, 2007; *Laskar and Liang*, 2016], significantly better external reproducibility has been achieved for  $\delta^{13}C$  and  $\delta^{18}O$ . The reproducibility of  $\Delta_{47}$  is comparable to the one reported by *Fiebig et al.*, 2019. However, it is worth noting that *Fiebig et al.*, 2019 used 16 V and *Laskar, Yui, et al.*, 2016 used 12 V, but here, only 8 V was used at the beginning of an acquisition. The voltage was not increased in this study to ensure comparability. A higher voltage may result in better reproducibility because the expected shot-noise limit would be lower [see *Merritt et al.*, 1994]. However, handling effects, such as the intensity difference on  $m/z$  44 between the working standard and the sample (see appendix A.5; page 135ff), would be potentially more difficult at higher intensities (i.e., higher sample flows) (cf. *Fiebig et al.*, 2016). Nevertheless, achieving reproducibility comparable to *Fiebig et al.*, 2019 at half the voltage and with less sample loss demonstrates the quality of the newly developed measurement procedure, which uses an extended integration time with fewer cycles but slices while integrating.





**Figure 4.8.:** Reproducibility of finally corrected and calibrated  $\delta^{13}\text{C}$  (a),  $\delta^{18}\text{O}$  (b), and  $\Delta_{47}^{\text{LF}}$  (c) measurements from gas tanks “Pic\_8\_1” and “D484276” over the period of February 1 - November 1, 2024, expressed as SD. Measurement values were normalized to their respective means (see legend).  $\delta^{13}\text{C}$  and  $\delta^{18}\text{O}$  were excluded for “Pic\_8\_1” results after May 23, 2024, due to gas tank depletion and related superimposed drift (see appendix B.17; page 169ff) . For the 44 considered measurements the SD for  $\delta^{13}\text{C}$  and  $\delta^{18}\text{O}$  are conservatively rounded to  $\sim 0.005$  ‰ and  $0.01$  ‰, respectively. The SD for the 57  $\Delta_{47}$  results is  $\sim 0.011$  ‰.



## 5. Mixing of $\Delta_{47}$ and Source + Ambient Air Measurements

The first section of this chapter investigates the nonlinearity of  $\Delta_{47}$  under various mixing conditions. The second section presents the results of measurements of human breath and in a parking garage. The final section discusses ambient air measurements in Heidelberg. Errors declared as “total error” include statistical errors of measurement, as well as systematic errors from calibration and corrections.

### 5.1. Nonlinear Mixing of $\Delta_{47}$

$\Delta_{47}$  does not follow a conservative mixing as already shown by *Eiler et al., 2004; Affek et al., 2006; Defliese et al., 2015* and *Laskar, Mahata, and Liang, 2016*. A thorough understanding of  $\Delta_{47}$  under mixing conditions is essential for the interpretation of  $\Delta_{47}$  in ambient air. Applying a linear Keeling plot [*C. D. Keeling, 1958*], as known from analyses of  $\delta^{13}\text{C}$  or  $\delta^{18}\text{O}$ , can lead to incorrect results for the  $\Delta_{47}$  end member. In principle, nonlinear functions can be fitted, if sufficient data on diverse mixing fractions is available. *Laskar, Mahata, and Liang, 2016* and *Laskar et al., 2021* demonstrated this for measurements in a tunnel by using a second order polynomial fit. However, when a mean source mixes with a local background and contributes only a few percent to the total mixture, the nonlinear behavior is often not measurable and cannot be handled in this way. This is typically the case when measuring ambient air at a rural or semi-urban station like Heidelberg (see section 2.4).

The nonlinear behavior of  $\Delta_{47}$  is a consequence of the procedure for calculating the stochastic distribution of a mixed gas under practical measurement conditions. In practice,  $\delta^{13}\text{C}$  and  $\delta^{18}\text{O}$  from the measurement are used to calculate the stochastic  $^{47}R_{\text{stoch}}$ . In a mixture, this  $^{47}R_{\text{stoch}}$  corresponds to a hypothetical unmixed gas with the isotopic composition of the mixture. However, mixtures take place on the level of isotopologues, not isotopes, making this  $^{47}R_{\text{stoch}}$  incorrect (see in addition Figure 5.1). Demonstrated exemplarily for isotopologue  $^{16}\text{O}^{13}\text{C}^{18}\text{O}$  under a two-component mixture of “gas 1”

## 5. Mixing of $\Delta_{47}$ and Source + Ambient Air Measurements

(mixing fraction  $f_{\text{gas } 1}$ ) and “gas 2”, the “correct” stochastic isotopologue fraction would be calculated as follows (cf. Equation (2.5)):

$$\begin{aligned}
 x(^{16}\text{O}^{13}\text{C}^{18}\text{O})_{\text{stoch (mix)}}^{\text{correct}} &= f_{\text{gas } 1} \cdot 2 \cdot x(^{16}\text{O})_{\text{gas } 1} \cdot x(^{13}\text{C})_{\text{gas } 1} \cdot x(^{18}\text{O})_{\text{gas } 1} \\
 &\quad + (1 - f_{\text{gas } 1}) \cdot 2 \cdot x(^{16}\text{O})_{\text{gas } 2} \cdot x(^{13}\text{C})_{\text{gas } 2} \cdot x(^{18}\text{O})_{\text{gas } 2} \\
 &= \underbrace{f_{\text{gas } 1} \cdot x(^{16}\text{O}^{13}\text{C}^{18}\text{O})_{\text{stoch (gas } 1)} + (1 - f_{\text{gas } 1}) \cdot x(^{16}\text{O}^{13}\text{C}^{18}\text{O})_{\text{stoch (gas } 2)}}_{\text{level isotopologues}}.
 \end{aligned} \tag{5.1}$$

Yet, under practical measurement conditions, the mixed atomic fractions are determined instead of the individual atomic fractions. These fractions are treated as if they were those of an unmixed gas. The calculation according to Equation (2.5) is as follows:

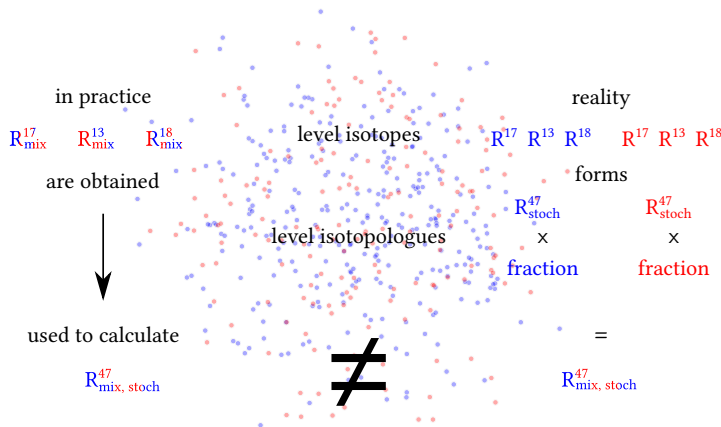
$$x(^{16}\text{O}^{13}\text{C}^{18}\text{O})_{\text{stoch (mix)}}^{\text{incorrect}} = 2 \cdot x(^{16}\text{O})_{\text{mix}} \cdot x(^{13}\text{C})_{\text{mix}} \cdot x(^{18}\text{O})_{\text{mix}}. \tag{5.2}$$

Theoretically, this practical mixed case can be calculated from theoretically known individual atomic fractions as follows:

$$\begin{aligned}
 x(^{16}\text{O}^{13}\text{C}^{18}\text{O})_{\text{stoch (mix)}}^{\text{incorrect}} &= 2 \cdot \left[ f_{\text{gas } 1} \cdot x(^{16}\text{O})_{\text{gas } 1} + (1 - f_{\text{gas } 1}) \cdot x(^{16}\text{O})_{\text{gas } 2} \right] \\
 &\quad \cdot \left[ f_{\text{gas } 1} \cdot x(^{13}\text{C})_{\text{gas } 1} + (1 - f_{\text{gas } 1}) \cdot x(^{13}\text{C})_{\text{gas } 2} \right] \\
 &\quad \cdot \underbrace{\left[ f_{\text{gas } 1} \cdot x(^{18}\text{O})_{\text{gas } 1} + (1 - f_{\text{gas } 1}) \cdot x(^{18}\text{O})_{\text{gas } 2} \right]}_{\text{level isotopes}}.
 \end{aligned} \tag{5.3}$$

Equations (5.1) and (5.3) are unequal. Under practical conditions, this results in nonlinearity in  $\Delta_{47}$  under mixing because equations of type (5.2) – which theoretical correspond to equations of type (5.3) – are used to calculate the stochastic  $^{47}R_{\text{stoch}}$ .

As mentioned, it is usually not possible to perform a polynomial fit for ambient air measurements with slight  $\text{CO}_2$  enhancements, corresponding to a low fraction of a



**Figure 5.1.:** When mixing gases with different bulk isotopic compositions, the calculation method used in mass spectrometric practice can lead to incorrect stochastic  $^{47}R_{\text{stoch}}$  values (left). In reality, mixing occurs at the level of isotopologues (right), not isotopes.

mean source gas mixed into a background gas. To account for nonlinearity and enable a conventional linear Keeling plot, a correction function is derived here. Theoretical calculations for  $\Delta_{47}$  were performed under different mixing conditions using equations from section 2.3.  $^{47}R_{\text{stoch}}$  was calculated both “correctly” and “incorrectly” using equations of type (5.1) and (5.3), respectively. The difference between the “correct” and “incorrect”  $\Delta_{47}$  calculations was analyzed to determine the dependencies on isotope deltas and mixing fraction. Fitting this theoretical difference resulted in a correction for a two-component mixture. This correction depends on the relative fraction of a local “background” gas  $f_{\text{background}}$  in mixture with a mean “source” gas, as well as differences in isotope deltas of these mixing gases, which are analogous to “gas 1” and “gas 2”, respectively:

$$\begin{aligned}
 10^3 \Delta_{47}^{\text{mix corr.}} \approx & \left\{ (9.51 \pm 0.01) \cdot 10^{-4} (0.5 - f_{\text{background}})^2 - (2.378 \pm 0.045) \cdot 10^{-4} \right\} \cdot 10^3 \Delta\delta^{18}\text{O} \cdot 10^3 \Delta\delta^{13}\text{C} \\
 & + \left\{ (1.563 \pm 0.002) \cdot 10^{-5} (0.5 - f_{\text{background}})^2 - (3.908 \pm 0.060) \cdot 10^{-6} \right\} \cdot (10^3 \Delta\delta^{18}\text{O})^2, \quad (5.4) \\
 \text{with} \quad 10^3 \Delta\delta^{13}\text{C} = & 10^3 \delta^{13}\text{C}_{\text{background}} - 10^3 \delta^{13}\text{C}_{\text{source}} \\
 \& \quad 10^3 \Delta\delta^{18}\text{O} = & 10^3 \delta^{18}\text{O}_{\text{background}} - 10^3 \delta^{18}\text{O}_{\text{source}}.
 \end{aligned}$$

The calculation was based on the international measurement standard “VPDB- $\text{CO}_2$ ” for the oxygen isotopes. Dependencies on equilibration temperature are negligible and mostly covered in the uncertainties of the correction term. Note that it does not matter which gas is “gas 1”, e.g., “background”, and which gas is “gas 2”, e.g., “source”. The correction for the uncorrected  $\Delta_{47}^{\text{mix}}$  is applied as follows:

$$10^3 \Delta_{47}^{\text{mix-corrected}} = 10^3 \Delta_{47}^{\text{mix}} + 10^3 \Delta_{47}^{\text{mix corr.}}. \quad (5.5)$$

As shown in visualization Figure 5.2 of the correction Equation (5.4), anti-correlated differences in carbon and oxygen isotopic compositions between background and source gas exhibit a nonlinear change to lower values and vice versa. Under ambient air conditions, this correction could be applied if: (1) e.g. isotope fractions  $f_{\text{background}}$  are determined using  $\text{CO}_2$  concentrations; (2) isotope deltas from local background are known or determined by measurement; and (3) corresponding source values are determined using a Keeling plot, for example. This is exemplified in section 5.3, under the heading “Nighttime Inversion in October 2024”.

Since real-world ambient air samples usually involve multicomponent mixing, it is important to study  $\Delta_{47}$  under multimixing conditions. Figure 5.3 illustrates a theoretical example of a three-component mixture and the effect of applying the correction Equa-

## 5. Mixing of $\Delta_{47}$ and Source + Ambient Air Measurements

tion (5.4). It is shown, that a three-component mixture can be reduced to a two-component mixture of a background gas and a mean source gas.

In this example, a background gas is mixed with two source gases 75:25 (for parameters such as isotope deltas, see “Parameters of gases” in Figure 5.3). The main plot of Figure 5.3 shows the nonlinear mixing  $\Delta_{47}^{\text{mix}}$  ( $\text{---}\blacklozenge\text{---}$ ) and a hypothetical linear mixing behavior  $\Delta_{47}^{\text{mix-linear}}$  ( $\text{---}\blacktriangleleft\text{---}$ ) between all gases, with  $f_{\text{background}}$  varying (source gases held constant in a 75:25 mixture). In the enlargement, the nonlinear mixing  $\Delta_{47}^{\text{mix source gases}}$  ( $\text{---}\blacktriangleleft\text{---}$ ) and hypothetical linear mixing  $\Delta_{47}^{\text{mix-linear source gases}}$  ( $\text{---}\blacktriangleleft\text{---}$ ) of the two source gases is shown over the mixing-fraction  $f_{\text{source 1}}$  on the x2 axis. When  $f_{\text{background}} = 0$ , the  $\Delta_{47}$  values of the three-gas mixture are equal to those of the two-component source gas mixture for  $f_{\text{source 1}} = 0.75$ . This is at  $\Delta_{47} \approx 0.298 \text{ ‰}$  and  $\Delta_{47} \approx 0.308 \text{ ‰}$  for linear and nonlinear mixing, respectively.

To demonstrate that a three-component mixture can be reduced to a two-component mixture,  $\Delta_{47}^{\text{mix background \& mean source}}$  ( $\text{---}\circ\text{---}$ ) was calculated. It represents a hypothetical nonlinear two-component mixture of the background gas and a mean source gas.  $T_{\text{mean source}} \approx 523.58 \text{ K}$  was used, corresponding to  $\Delta_{47} \approx 0.308 \text{ ‰}$  at  $f_{\text{background}} = 0$  for nonlinear mixing. In addition  $\delta^{13}\text{C}_{\text{mean source}} = -22.75 \text{ ‰}$  and  $\delta^{18}\text{O}_{\text{mean source}} = -16.475 \text{ ‰}$  were utilized, calculated assuming conservative mixing:

$$10^3 \delta^{13}\text{C}_{\text{mean source}} = f_{\text{source 1}} \cdot 10^3 \delta^{13}\text{C}_{\text{source 1}} + (1 - f_{\text{source 1}}) \cdot 10^3 \delta^{13}\text{C}_{\text{source 2}} \quad (5.6)$$

$$10^3 \delta^{18}\text{O}_{\text{mean source}} = f_{\text{source 1}} \cdot 10^3 \delta^{18}\text{O}_{\text{source 1}} + (1 - f_{\text{source 1}}) \cdot 10^3 \delta^{18}\text{O}_{\text{source 2}} \quad (5.7)$$

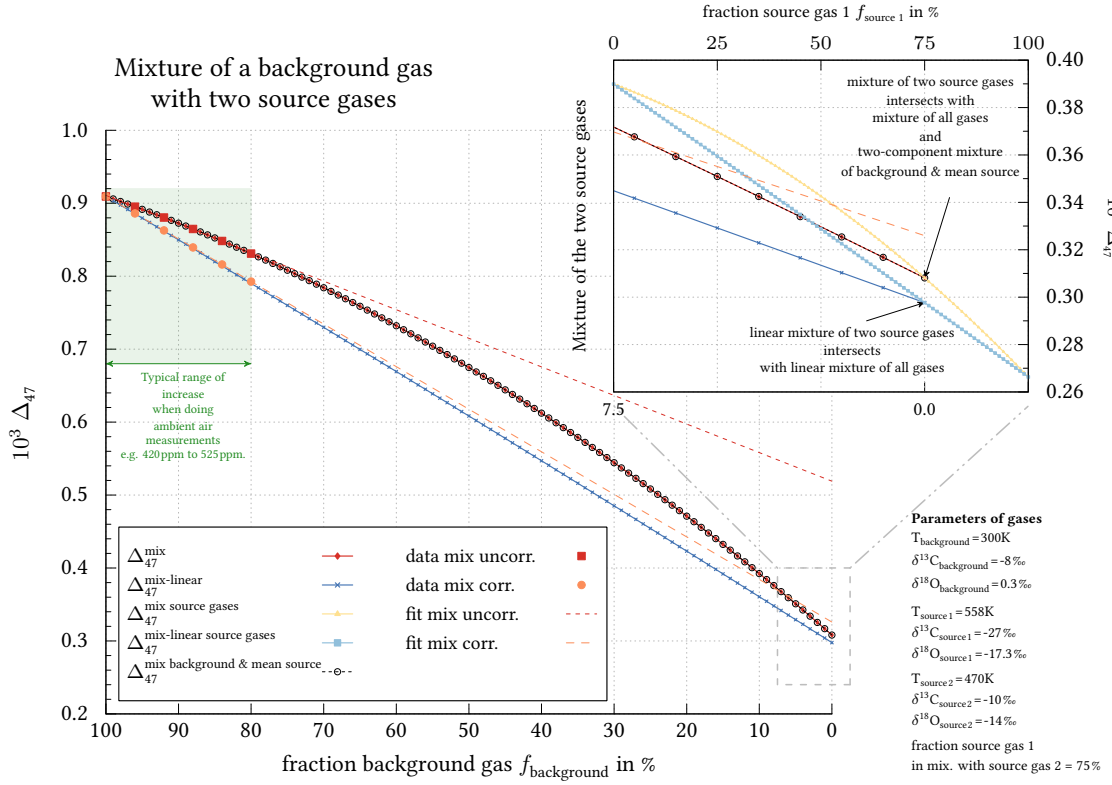
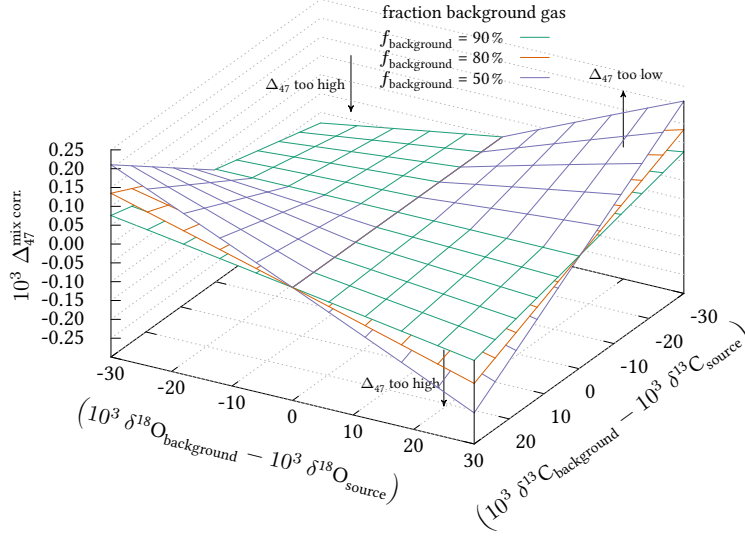
These  $\delta^{13}\text{C}_{\text{mean source}}$  and  $\delta^{18}\text{O}_{\text{mean source}}$  correspond to the best possible results that would be obtained using a Keeling plot under ambient air conditions. As can be seen,  $\Delta_{47}^{\text{mix background \& mean source}}$  ( $\text{---}\circ\text{---}$ ) follows  $\Delta_{47}^{\text{mix}}$  ( $\text{---}\blacklozenge\text{---}$ ) without any apparent deviations. This suggests that reducing the mixture from three components to two is valid. This should be a consequence of the conservative mixing of  $\delta^{13}\text{C}$  and  $\delta^{18}\text{O}$ . Mathematically, this can be understood considering Equation (5.3), adapted for the three-component mixing case between a background (b) and two source gases (s 1 & s 2, respectively):

$$\begin{aligned} x(^{16}\text{O}^{13}\text{C}^{18}\text{O})_{\text{stoch (mix)}}^{\text{incorrect}} = & 2 \cdot \left[ f_b \cdot x(^{16}\text{O})_b + (1 - f_b) \cdot (f_{s1} \cdot x(^{16}\text{O})_{s1} + (1 - f_{s1}) \cdot x(^{16}\text{O})_{s2}) \right] \\ & \cdot \left[ f_b \cdot x(^{13}\text{C})_b + (1 - f_b) \cdot (f_{s1} \cdot x(^{13}\text{C})_{s1} + (1 - f_{s1}) \cdot x(^{13}\text{C})_{s2}) \right] \\ & \cdot \left[ f_b \cdot x(^{18}\text{O})_b + (1 - f_b) \cdot (f_{s1} \cdot x(^{18}\text{O})_{s1} + (1 - f_{s1}) \cdot x(^{18}\text{O})_{s2}) \right] \end{aligned} \quad (5.8)$$

Since the mixing fraction  $f_{s1}$  between the source gases remains constant, the reduced two-component mixing case between the background and a mean source can be written

### 5.1. Nonlinear Mixing of $\Delta_{47}$

**Figure 5.2.:** Visualization of the correction Equation (5.4) for two-component mixtures using three distinct  $f_{\text{background}}$ . For correlated differences in carbon and oxygen isotopic compositions between background and source gas, the correction is negative, indicating that the uncorrected  $\Delta_{47}^{\text{mix}}$  is overestimated, and vice versa.



**Figure 5.3.:** Example of a three-component mixture, reduced to a two-component mixture between a background gas and two source gases 75:25 (see “Parameters of gases”). At  $f_{\text{background}} = 0$ ,  $\Delta_{47}$  of the nonlinear mixture of all gases is  $\sim 0.308\text{‰}$ , which corresponds to the nonlinear mixing value for a 75:25 mixture of the two source gases. Fits using uncorrected and corrected (Equation (5.4)) hypothetical data points yield for the mean source  $\Delta_{47} \approx 0.519\text{‰}$  and  $0.326\text{‰}$ , respectively. This demonstrates the potential of the correction by showing that the mixture’s superimposed nonlinearity can be corrected. However, this is a first-order correction that may not apply to all situations, such as changes in the source mixture over time or re-equilibration of the background gas.

## 5. Mixing of $\Delta_{47}$ and Source + Ambient Air Measurements

as follows:

$$\begin{aligned}
 x(^{16}\text{O}^{13}\text{C}^{18}\text{O})_{\text{stoch (mix)}}^{\text{incorrect}} = 2 \cdot & \overbrace{\left[ \begin{aligned} & f_{\text{background}} \cdot x(^{16}\text{O})_{\text{background}} + (1 - f_{\text{background}}) \cdot x(^{16}\text{O})_{\text{mean source}} \\ & \cdot \left[ f_{\text{background}} \cdot x(^{13}\text{C})_{\text{background}} + (1 - f_{\text{background}}) \cdot x(^{13}\text{C})_{\text{mean source}} \right] \\ & \cdot \left[ f_{\text{background}} \cdot x(^{18}\text{O})_{\text{background}} + (1 - f_{\text{background}}) \cdot x(^{18}\text{O})_{\text{mean source}} \right] \end{aligned} \right]}^{\text{reduced two-component mixture between background and mean source}} \cdot \underbrace{\phantom{\left[ f_{\text{background}} \cdot x(^{18}\text{O})_{\text{background}} + (1 - f_{\text{background}}) \cdot x(^{18}\text{O})_{\text{mean source}} \right]}}_{\text{nonlinearity mixture source gases persists}}. \quad (5.9)
 \end{aligned}$$

This shows the virtual reduced two-component mixing which could be corrected using Equation (5.4). However, the nonlinearity between the source gases persists and cannot be corrected as long as information on the source gases is unavailable.

Yet, under realistic ambient air conditions, mixtures typically contain more than three gases. To demonstrate the validity of these statements for more than three gases, the presented logical argument is expanded. The general case of mixing multiple components of  $n \in \mathbb{N}_{\neq 0}$  background and  $m \in \mathbb{N}_{\neq 0}$  source gases for an adapted Equation (5.3) can be expressed as follows:

$$\begin{aligned}
 x(^{16}\text{O}^{13}\text{C}^{18}\text{O})_{\text{stoch (mix)}}^{\text{incorrect}} = 2 \cdot & \left[ \sum_{i=1}^n f_{\text{background } i} \cdot x(^{16}\text{O})_{\text{background } i} + \sum_{j=1}^m f_{\text{source } j} \cdot x(^{16}\text{O})_{\text{source } j} \right] \\
 & \cdot \left[ \sum_{i=1}^n f_{\text{background } i} \cdot x(^{13}\text{C})_{\text{background } i} + \sum_{j=1}^m f_{\text{source } j} \cdot x(^{13}\text{C})_{\text{source } j} \right] \\
 & \cdot \left[ \sum_{i=1}^n f_{\text{background } i} \cdot x(^{18}\text{O})_{\text{background } i} + \sum_{j=1}^m f_{\text{source } j} \cdot x(^{18}\text{O})_{\text{source } j} \right], \quad (5.10) \\
 & \text{with } \sum_{i=1}^n f_{\text{background } i} + \sum_{j=1}^m f_{\text{source } j} = 1.
 \end{aligned}$$

As long as the mixing distributions within the background and source gases do not change and their bulk isotopic distributions remain constant, this can be simplified to a



two-component mixture between a mean background and mean source gas:

$$x(^{16}\text{O}^{13}\text{C}^{18}\text{O})_{\text{stoch (mix)}}^{\text{incorrect}} = 2 \cdot \left[ f_{\text{mean background}} \cdot x(^{16}\text{O})_{\text{mean background}} + (1 - f_{\text{mean background}}) \cdot x(^{16}\text{O})_{\text{mean source}} \right] \\ \cdot \left[ f_{\text{mean background}} \cdot x(^{13}\text{C})_{\text{mean background}} + (1 - f_{\text{mean background}}) \cdot x(^{13}\text{C})_{\text{mean source}} \right] \\ \cdot \left[ f_{\text{mean background}} \cdot x(^{18}\text{O})_{\text{mean background}} + (1 - f_{\text{mean background}}) \cdot x(^{18}\text{O})_{\text{mean source}} \right], \quad (5.11)$$

$$\text{with } f_{\text{mean background}} \cdot \sum_{i=1}^n f_{\text{background } i} + (1 - f_{\text{mean background}}) \cdot \sum_{j=1}^m f_{\text{source } j} = 1$$

$$\text{and } \sum_{i=1}^n f_{\text{background } i} = \sum_{j=1}^m f_{\text{source } j} = 1 \quad \text{for the submixtures of background and source gases.}$$

Note, “mean background” and “mean source” are only examples of arbitrary mean gases consisting of several gases in a constant mixing composition. Therefore, in principle, Equation (5.4) could be used to correct the nonlinearity between two arbitrary mean gases (submixtures) in a multicomponent mixture if the submixture mixing compositions remain unchanged.

To investigate the potential determination of a mean  $\Delta_{47}$  source value for ambient air measurements at a station like Heidelberg (see section 2.4), Keeling plots are simulated in Figure 5.3. In this context, the green area in the main diagram represents the range of mixing fractions that would result from realistic measurable  $\text{CO}_2$  enhancements. Six hypothetical data points within this range are shown for uncorrected  $\Delta_{47}$  (■) and for under use of Equations (5.4) & (5.5) corrected  $\Delta_{47}$  (■). For the correction  $\delta^{13}\text{C}_{\text{mean source}}$  and  $\delta^{18}\text{O}_{\text{mean source}}$  (see above) are used. Linear fits through these data points, as in a Keeling plot, are shown by --- and - -, respectively. The value at the intersection for nonlinear mixing (0.308 ‰) represents the best possible result achievable under this reduced two-component mixing consideration. The mean source values (at  $f_{\text{background}} = 0$ ) determined for the uncorrected and corrected data are 0.519 ‰ and 0.326 ‰, respectively. The source value for the uncorrected data deviates by approximately 0.211 ‰ from the best possible result. In contrast, the value determined using mixing-corrected data differs by only 0.018 ‰. About 0.003 ‰ of this deviation can be explained by an imperfect correction Equation (5.4). The residual deviation of 0.015 ‰ is likely due to a “true” nonlinearity in  $\Delta_{47}$  under mixing conditions, and slight dependencies on equilibration temperatures, which are not accounted for in Equation (5.4). The “true” nonlinearity was examined by *Eckhardt, 2019* (Figure 3.9) and likely originates from the slight dependence of  $\Delta_{47}$  on the bulk isotopic composition (cf. Figure A.1; page 126). Although these effects are small, they can significantly impact the outcome of linear extrapolation in a Keeling plot when only low source mixing fractions are present. However, when comparing the outcomes using uncorrected and corrected data, the necessity and potential of the correction becomes

## 5. Mixing of $\Delta_{47}$ and Source + Ambient Air Measurements

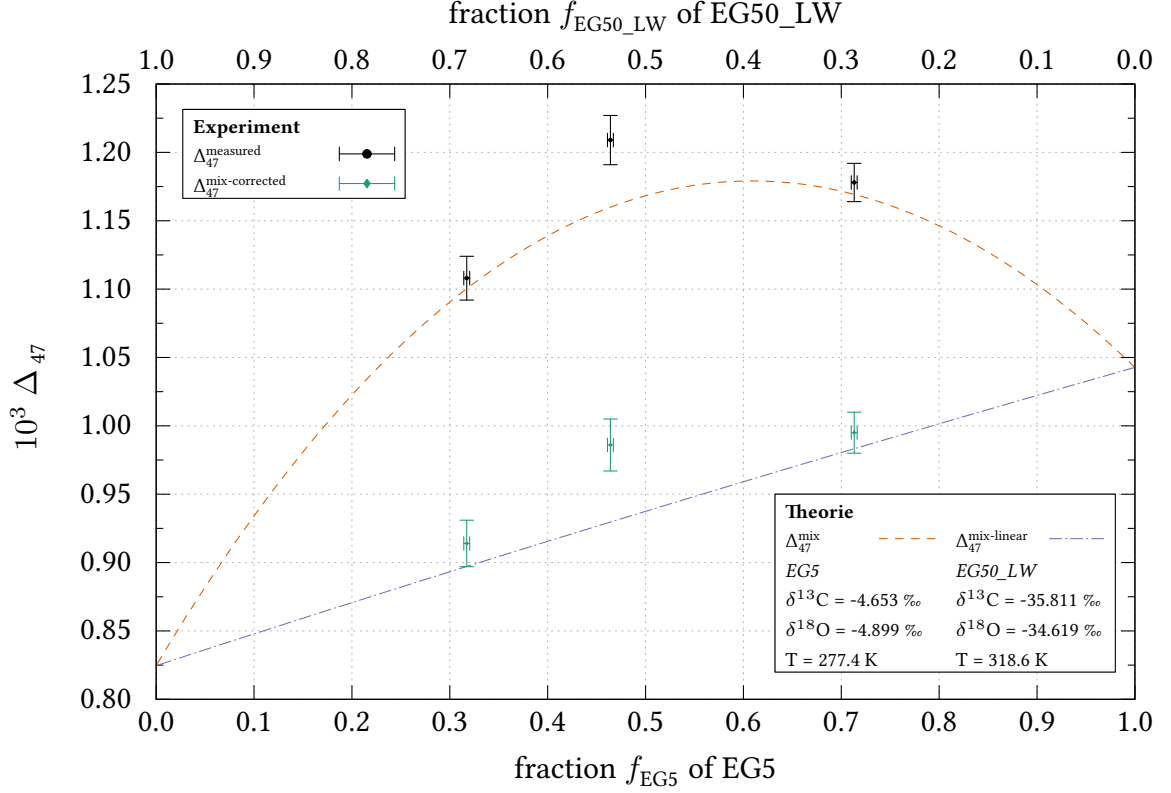
apparent. Nevertheless, this is a special case (first-order correction) that may not apply to all situations. In reality, the mixing ratios of the source or background gases may change during the mixing process. Additionally, re-equilibration during mixing could result in formerly distinct gases becoming partially uniform. However, some of such effects should be visible as deviations from linearity in conventional Keeling plots of  $\delta^{13}\text{C}$  and  $\delta^{18}\text{O}$  values.

*Schmid, 2023* studied  $\Delta_{47}$  mixtures in his bachelor's thesis and obtained comparable results using a machine learning approach. He also corrected the tunnel data of *Laskar, Mahata, and Liang, 2016* using Equation (5.4) and found a mean source value of  $\Delta_{47} = (0.286 \pm 0.050) \text{‰}$  by applying a linear fit. This is within one  $\sigma$  of  $\Delta_{47} = (0.267 \pm 0.036) \text{‰}$  derived by *Laskar, Mahata, and Liang, 2016* using a polynomial approach and confirms the correction Equation (5.4). However, further investigation is needed to determine whether alternative correction terms can be developed that improve the accuracy of the correction (e.g., by disregarding the true nonlinearity).

### Experiments on $\Delta_{47}$ under Mixture

Two experiments were conducted in June 2024 to investigate the mixing effect. In the first experiment the temperature-equilibrated  $\text{CO}_2$  standards, “EG5” and “EG50\_LW” were mixed, while in the second experiment, “EG5”, “EG50\_N48” and “HG230” were mixed. The mixing fractions  $f$  were determined based on pressure sensor readings taken while preparing the mixtures. Values of these standards from measurements some days before and after the experiments are presented in Table D.1 on page 203. The results of the mixing experiments are summarized in Table D.2 on the same page.

In the first experiment, the two gases were mixed in three different ratios. The corresponding mixing fractions are shown in Figure 5.4 – on the top x-axis for “EG50\_LW” and on the bottom x-axis for “EG5”. The data points with  $f_{\text{EG5}} \approx 0.317$  and  $f_{\text{EG5}} \approx 0.713$  fit well to the expected theoretical curve. This curve and the curve for linear mixing were calculated using the parameters from temperature-equilibrated gases (legend Figure 5.4 and Table D.1 (page 203)). Since the calibration of measurements is with respect to the reference frame proposed by *Dennis et al., 2011*, the theoretical data was slightly shifted ( $< 0.01 \text{‰}$ ) using the transfer function Equation (A.1) (see appendix A.2 on page 128). The measured data point at  $f_{\text{EG5}} \approx 0.464$  with  $\Delta_{47} = (1.209 \pm 0.018 \text{ [total error]}) \text{‰}$  is slightly increased, but still within three  $\sigma$  from the theoretically expected value  $\Delta_{47}^{\text{mix}} \approx 1.160 \text{‰}$ . However, this measurement showed a higher statistical SEM of  $0.010 \text{‰}$ ; the others had errors of  $0.007 \text{‰}$ . The raw data from the measurement performed directly before showed a large jump at  $m/z$  48, and the actual measurement showed an exceptionally high fluctu-



**Figure 5.4.:** Experiment on two-component mixture using temperature-equilibrated CO<sub>2</sub> standards "EG5" and "EG50\_LW". Theoretical lines were calculated using the parameters in the legend. The data points  $\Delta_{47}^{mix-corrected}$  are derived by applying the mix correction Equation (5.4) to the measured  $\Delta_{47}^{measured}$ . Uncertainties are total errors, which include systematic errors from calibration and corrections. Apart from the data point at  $f_{EG5} \approx 0.464$ , there is good agreement with the theoretical expectations.

ation in  $\Delta_{47}$  at the beginning. Both could be indicating that e.g. some impurity at the source of the IRMS was released. The data points  $\Delta_{47}^{mix-corrected}$  are calculated using the correction Equation (5.4). The function corrects for nonlinearity, but cannot account for the increase seen for  $f_{EG5} \approx 0.464$  compared to the theoretically nonlinear mixing curve. Considering this, a good agreement is achieved with the hypothetical linear mixing, confirming the correction Equation (5.4).

In the second experiment, the measured  $\Delta_{47} = (0.890 \pm 0.013 \text{ [total error]}) \text{ ‰}$  is within two  $\sigma$  from the theoretical expected value  $\Delta_{47}^{mix} \approx 0.870 \text{ ‰}$ .

Notably, all experimental values were higher than the expected theoretical values (experiments 1 & 2). Using the expected results from linear mixing of  $\delta^{13}C$  and  $\delta^{18}O$  to calculate the mixing fractions did not significantly change the fractions, and therefore only slightly changed the theoretical expectations. Therefore, incorrect assumptions about the mixing ratio cannot explain this observation. The elevated values may be coincidental, but this should be investigated in further experiments.

## 5.2. Measurements of Human Breath and in a Parking Garage

### 5.2.1. Human Breath

Two studies investigated human breath measurements and found lower-than-expected  $\Delta_{47}$  values for thermodynamic equilibrium [Eiler et al., 2004; Affek et al., 2006]. According to Eiler et al., 2004, the fractionation of  $\text{CO}_2$  during exsolution from blood into the lungs should actually increase  $\Delta_{47}$ , not decrease it. However, the studies were unable to fully explain these results, suggesting the presence of an unknown process.

For comparison, a human breath sample from one individual (male; 34 years; diet: plant-based) was collected on 28.06.2024 at approximately 11:00 UTC. The breath was collected using an evacuated flask. The sample was dried by using an ethanol-dry ice cold trap placed under a laboratory exhaust vent (Figure 5.5). To minimize contamination with ambient air, the tube to the flask was flushed with breath before the connection to the flask was tightened, just before opening the evacuated flask. Sample preparation with the Air Trap (Port 5) began at 15:10 UTC.  $\text{CO}_2$  was desublimated in the  $\text{CO}_2$  trap for only ten seconds, resulting in a measured pressure of  $\sim 14.3$  mbar (RPT sensor). This pressure, achieved in just ten seconds, indicates a high  $\text{CO}_2$  concentration (expected:  $\sim 4\text{-}5\%$   $\text{CO}_2$ ).



**Figure 5.5.:** Setup for sampling exhaled human breath. To minimize contamination with unexhaled air, the tube to the flask was flushed with breath before tightening, and just before opening the connection to the flask (left). To dry the sample, an ethanol-dry ice trap located under a laboratory exhaust vent was used (mid). The human breath was blown into the straw (right).

## 5.2. Measurements of Human Breath and in a Parking Garage

in exhaled air [e.g. *Das et al.*, 2020]). In contrast, comparable pressures were measured after eleven minutes of freezing CO<sub>2</sub> from ambient air ( $\sim 420$  ppm). Additionally, the low measured ( $10^3 C_{N_2O}/C_{CO_2}$ ) ratio of  $\sim 0.014$  indicates that only a negligible amount of unexhaled air was present.

The following values were determined from the measurement:  $\delta^{13}C = (-27.11 \pm 0.02) \text{‰}$ ,  $\delta^{18}O = (-7.38 \pm 0.04) \text{‰}$ ,  $\Delta_{47} = (0.839 \pm 0.018) \text{‰}$  (errors generously estimated; SEM of  $\Delta_{47}$  measurement was  $0.007 \text{‰}$ ).

The  $\delta^{13}C$  value is significantly depleted compared to the majority of values reported, which typically range from about  $-18$  to  $-25 \text{‰}$  [*Epstein et al.*, 1988; *Panteleev et al.*, 1999; *Eiler et al.*, 2004; *Affek et al.*, 2006; *Newman et al.*, 2008; *Yanes et al.*, 2010]. A tendency toward more depleted  $\delta^{13}C$  was also observed in three other samples taken from the same individual in 2018 ( $(-24.245 \pm 0.015) \text{‰}$ ;  $(-26.564 \pm 0.016) \text{‰}$ ;  $(-25.780 \pm 0.020) \text{‰}$  [*Eckhardt*, 2019]). Diet significantly impacts carbon isotope ratios in animal respiration [e.g. *DeNiro et al.*, 1978]. Therefore, the test participant's diet may be a significant factor in this observation. In a study by *O'Brien et al.*, 2021 unsweetened plant-based foods had lower  $\delta^{13}C$  values than unsweetened animal-based foods. Additionally, more depleted  $\delta^{13}C$  values were observed in hair and blood serum of individuals following a plant-based diet compared to omnivores [*Petzke et al.*, 2005; *Ellegård et al.*, 2019; *Matos et al.*, 2020; *Dierkes et al.*, 2023]. The  $\delta^{18}O$  value falls within the range of values reported in other studies [e.g. *Eiler et al.*, 2004; *Affek et al.*, 2006; *Newman et al.*, 2008].

The  $\Delta_{47}$  value measured here corresponds to  $(42.3 \pm 4.0) \text{ °C}$  ( $\pm 1.6 \text{ °C}$  using SEM of measurement). The expected range of body temperatures is from approximately  $36.3$  to  $37.4 \text{ °C}$ . This corresponds to a  $\Delta_{47}$  range of approximately  $0.867$  to  $0.862 \text{‰}$ . Therefore, the observed value is lower than expected. However, the lower expected value is still within two  $\sigma$  of the measurement. For comparison, the room temperature in the laboratory was  $\sim 25 \text{ °C}$ , corresponding to a  $\Delta_{47}$  value of  $\sim 0.924 \text{‰}$ . Samples taken from the same individual in 2018 yielded slightly higher values than the value obtained here ( $(0.841 \pm 0.023) \text{‰}$ ;  $(0.844 \pm 0.024) \text{‰}$ ;  $(0.861 \pm 0.022) \text{‰}$  [*Eckhardt*, 2019]). However, the first two values were also lower than expected, though not significantly so.

Although the deviation is not statistically significant, the tendency for  $\Delta_{47}$  to be lower than expected appears to corroborate the findings of *Eiler et al.*, 2004 and *Affek et al.*, 2006, underscoring the necessity of more in-depth research. These studies should incorporate  $\Delta_{48}$  to constrain potential fractionation effects.

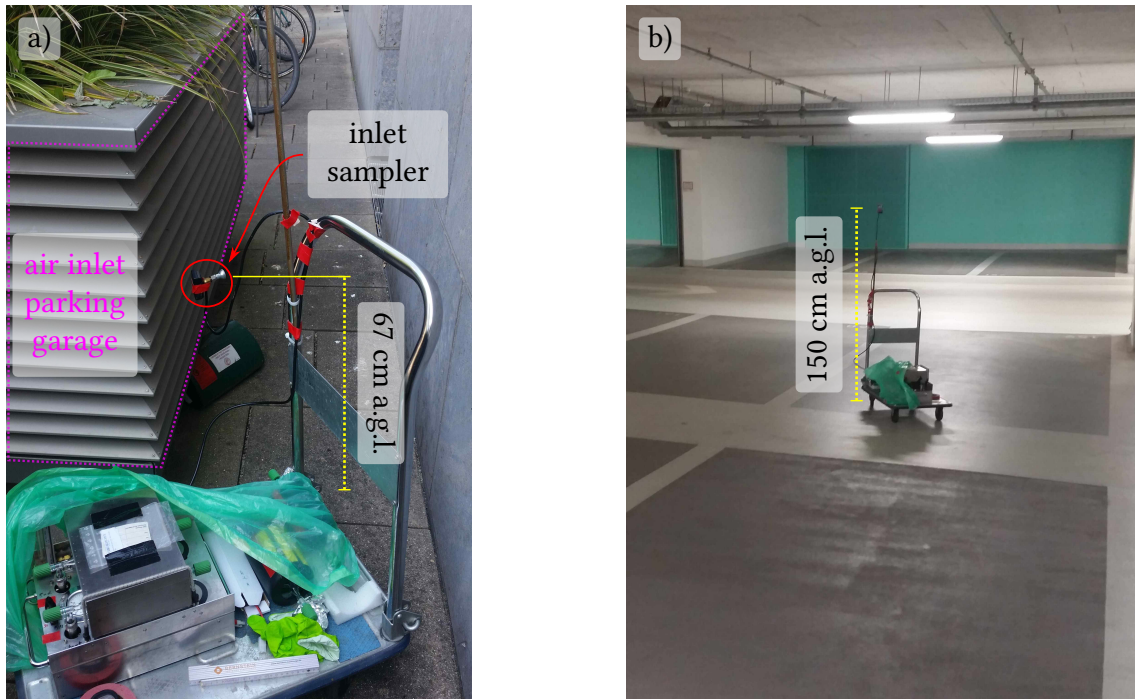
## 5. Mixing of $\Delta_{47}$ and Source + Ambient Air Measurements

### 5.2.2. Underground Parking Garage

In different studies,  $\Delta_{47}$  was measured in ambient air near motor vehicle emissions (tunnel, high-traffic roads) [Affek et al., 2006; Laskar, Mahata, and Liang, 2016; Laskar and Liang, 2016; Laskar et al., 2021]. The resulting  $\Delta_{47}$  values were lower than those expected from pure atmospheric temperatures, indicating significant contributions from high-temperature sources.

For comparison and further verification of the Air Trap's function, a sample was collected at an inlet height 150 cm above ground level in an underground parking garage on 27.06.2024 between 11:11 and 11:24 UTC (between parking lots 142 & 159 on level -1, Berliner Str. 41-49, 69120 Heidelberg, N49°25'6", E8°40'31") (Figure 5.6 b)). A second sample was collected at an inlet height of 67 cm above ground level outside of the garage, next to an air intake for the garage's air system between 10:44 and 10:57 UTC (Figure 5.6 a)). An additional ambient air sample was collected by the Air Trap (port 31) using the inlet at IUP's roof between 11:51 and 12:02 UTC. The distance between the parking garage and the inlet at IUP's roof is approximately 120 m (straight-line).

The samples from outside and inside the parking garage were collected in flasks. These



**Figure 5.6.:** a) Sampling site near an air inlet of the parking garage's ventilation system (pink). The used sampler (on the trolley) is equipped with two flasks. The air was dried using magnesium perchlorate. A temperature logger is attached next to the inlet of the sampler at 67 cm above ground level (red). b) Sampling site between parking lots 142 & 159 on level -1 inside the parking garage, with air intake at 150 cm above ground level



## 5.2. Measurements of Human Breath and in a Parking Garage

were evacuated and flushed with synthetic air ( $\sim 10$  min,  $\sim 3$  l/min) before the actual sampling. A flask sampler equipped with two flasks per measurement site was used, featuring a pump (PM 16029-86; Neuberger, Freiburg, Germany) for flushing and pressure buildup, a rotameter (DK 800 N; Krohne, Duisburg, Germany) for flow measurement, and a manometer (Empeo, Sankt Augustin, Germany) for end-pressure control. A tube filled with magnesium perchlorate was used to dry the air at the inlet and a temperature data logger (174H; Testo, Titisee-Neustadt, Germany) was fixed at the inlet height to record the ambient air temperature.

For sampling, the flasks outside the garage were flushed for 12 min, followed by 1 min with the outlet side closed to build up an excess pressure of 0.5 bar. The flasks inside the garage were flushed for 11 min, followed by about two minutes to build up an excess pressure of 0.2 bar (battery power was lower and magnesium perchlorate more saturated). Flows during flushing were around 1 l/min. Approximately nine cars drove by the sampling spot during the flushing period inside the garage. To minimize the potential influence of the experimenter's breath, the experimenter was only near the sampler at the beginning and end of the experiment and when switching to allow pressure to build up while holding breath. The air temperature in front of the parking garage was approximately  $(27.5 \pm 0.2 [2 \text{ SD}])$  °C. Including the  $\pm 0.5$  °C accuracy of the data logger this corresponds to a  $\Delta_{47}$  value of  $(0.911 \pm 0.003)$  ‰. The average temperature recorded inside the parking garage was  $(25.8 \pm 1.0 [2 \text{ SD}])$  °C. However, it decreased exponentially during the recording period. This may have been due to retardation from the higher outdoor temperatures measured beforehand and results in a potential systematic error of -2 °C. Including the manufacturer's accuracy, this corresponds to a  $\Delta_{47}$  value of approximately  $(0.920 \pm 0.007 + 0.010 [\text{sys}])$  ‰.

For various reasons, only one flask sample from each sampling site could be prepared and measured. The results of the measurements are summarized in Table 5.1. For background comparison, the two columns on the right show additional CRDS results for ambient air drawn from the IUP's roof inlet at the same times. The  $\Delta_{47}$  value for the sample collected in front of the parking garage (10:44-10:57 UTC) is within one SEM of the value collected by the Air Trap (11:51-12:02 UTC). The average of these two measurements is  $\Delta_{47}^{\text{background}} = (0.952 \pm 0.015)$  ‰, which can be assumed as the background value (generously error assumption). In contrast, the value in the parking garage  $(0.695 \pm 0.016 [\text{total error}])$  ‰ differs significantly from this value, as well as from the  $\Delta_{47}$  values calculated from the air temperatures inside and outside the garage (see above). This indicates a significant contribution from high-temperature CO<sub>2</sub> sources, likely originating primarily from car exhausts and, to a lesser extent, from human respiration.

## 5. Mixing of $\Delta_{47}$ and Source + Ambient Air Measurements

**Table 5.1.:** Results of IRMS measurements (columns 3-7) from samples collected on 27.06.2024 in front of a parking garage (10:44 - 10:57 UTC), inside a parking garage (11:11 - 11:24 UTC), and by the Air Trap via the connection to the inlet on IUP's roof (11:51 - 12:02). For background comparisons, columns 8-9 contain CRDS measurement results for ambient air drawn in at IUP's roof at the respective sampling times (column 1).

samp. time (UTC)	description	IRMS data					CRDS data sampled @ IUP roof	
		$10^3 \delta^{13}\text{C}$	$10^3 \delta^{18}\text{O}$	$10^3 \Delta_{47}$	$T_{\text{from } \Delta_{47}}$	$\frac{10^3 \text{C}_{\text{N}_2\text{O}}}{\text{C}_{\text{CO}_2}}$	$\text{C}_{\text{CO}_2}$	$10^3 \delta^{13}\text{C}$
					[°C]		[ppm]	
10:44 - 10:57	front parking garage	-9.374 $\pm 0.006^\dagger$	0.632 $\pm 0.010^\dagger$	0.950 $\pm 0.008$ $\pm 0.013^\dagger$	20.2 $\pm 1.4$ $\pm 2.4^\dagger$	0.8091 $\pm 0.0029$	427.0 $\pm 0.4$	-8.89 $\pm 0.08$
11:11 - 11:24	inside parking garage	-18.114 $\pm 0.004^\dagger$	-6.251 $\pm 0.010^\dagger$	0.695 $\pm 0.010$ $\pm 0.016^\dagger$	77.5 $\pm 2.7$ $\pm 4.3^\dagger$	0.4604 $\pm 0.0020$	424.1 $\pm 0.3$	-8.77 $\pm 0.07$
11:51 - 12:02	Air Trap inlet @ IUP's roof	-8.711 $\pm 0.006^\dagger$	1.174 $\pm 0.010^\dagger$	0.954 $\pm 0.006$ $\pm 0.012^\dagger$	19.5 $\pm 1.1$ $\pm 2.2^\dagger$	0.8027 $\pm 0.0028$	422.5 $\pm 0.2$	-8.65 $\pm 0.06$

Errors marked with  $\dagger$  are total errors, including systematic errors from calibration and corrections in addition to statistical SEM. Error for  $\frac{10^3 \text{C}_{\text{N}_2\text{O}}}{\text{C}_{\text{CO}_2}}$  is from Gaussian error propagation. All other errors are  $\pm 1$  SEM.

No direct  $\text{CO}_2$  measurements were performed inside or outside the parking garage. However, the  $\text{N}_2\text{O}/\text{CO}_2$  concentration ratio was measured (see Table 5.1). For the 11:51-12:02 UTC measurement, both  $\text{CO}_2$  concentration and  $\text{N}_2\text{O}/\text{CO}_2$  concentration ratios are known. Therefore, the  $\text{N}_2\text{O}$  concentration can be calculated as  $(339.1 \pm 1.2)$  ppb. Assuming this  $\text{N}_2\text{O}$  concentration is also valid for the parking garage, the  $\text{CO}_2$  concentration is estimated to be  $(736.5 \pm 4.2)$  ppm.

Eckhardt, 2019 took a measurement at almost the same location (parking lot 159) on 24.10.2018, between 13:50 and 14:20 (UTC). The results were  $\text{C}_{\text{CO}_2} = (584.510 \pm 0.066)$  ppm,  $\delta^{13}\text{C} = (-14.233 \pm 0.026)$  ‰,  $\delta^{18}\text{O} = (-3.486 \pm 0.047)$  ‰, and  $\Delta_{47} = (0.854 \pm 0.022)$  ‰. The  $\Delta_{47}$  value is significantly higher than the value measured here. However, a comparison of the  $\delta^{13}\text{C}$ ,  $\delta^{18}\text{O}$ , and  $\text{CO}_2$  concentrations suggest that the sample taken here has a higher source contribution. Measurements next to high-traffic streets also yielded slightly higher  $\Delta_{47}$  values [Affek et al., 2006; Laskar and Liang, 2016; Laskar, Mahata, and Liang, 2016]. Results of measurements in a tunnel are comparable or lower in  $\Delta_{47}$  [Laskar, Mahata, and Liang, 2016; Laskar et al., 2021]. However, the  $\text{CO}_2$  concentrations,  $\delta^{13}\text{C}$ , and  $\delta^{18}\text{O}$  values at the high-traffic streets suggest lower source contributions compared to the results here. The opposite is true for the tunnel measurements.

In order to determine the mean source values in the parking garage using Keeling plots,



## 5.2. Measurements of Human Breath and in a Parking Garage

it is necessary to have background values of CO<sub>2</sub> concentration,  $\delta^{13}\text{C}$ , and  $\delta^{18}\text{O}$  in addition to the assumed  $\Delta_{47}^{\text{background}} = (0.952 \pm 0.015) \text{‰}$ . Using the CRDS measurement results at the time of sampling inside the garage as background values yields  $C_{\text{CO}_2, \text{background}} = (424.1 \pm 0.9) \text{ ppm}$  and  $\delta^{13}\text{C}_{\text{background}} = (-8.77 \pm 0.12) \text{‰}$  (errors generously estimated). The  $\delta^{18}\text{O}$  background isotope value is estimated by averaging the measurements taken from 10:45 to 10:57 UTC and from 11:51 to 12:02 UTC, yielding a value of  $\delta^{18}\text{O}_{\text{background}} = (0.90 \pm 0.40) \text{‰}$  (error generously estimated).

Using the background values along with the results from the inside parking garage measurement and the estimated CO<sub>2</sub> concentration of  $(736.5 \pm 4.2) \text{ ppm}$ , a Keeling plot using York Fit [York et al., 2004] yields  $\delta^{13}\text{C}_{\text{source}} = (-30.80 \pm 0.25) \text{‰}$  and  $\delta^{18}\text{O}_{\text{source}} = (-15.96 \pm 0.57) \text{‰}$  for the mean source in the parking garage (see upper part Table 5.2). Correcting for mixing effects on  $\Delta_{47}$  according to Equation (5.4) results in  $\Delta_{47}^{\text{mix-corrected}} = (0.607 \pm 0.016) \text{‰}$ . Together with  $\Delta_{47}^{\text{background}}$ , this yields  $\Delta_{47}^{\text{source}} = (0.139 \pm 0.044) \text{‰}$ , corresponding to  $(455 \pm 110) \text{ °C}$ .

$\delta^{13}\text{C}_{\text{source}}$  is more depleted than literature values for car exhaust end members and tunnel measurements listed in Table 5.2.  $\delta^{13}\text{C}$  of car exhaust CO<sub>2</sub> emissions reflect the isotopic composition of the petroleum used [e.g. Popa et al., 2014].  $\delta^{13}\text{C}$  of petroleum varies depending on the origin of the raw oils, with a span of several per mil [e.g. Mook, 1986], with most reported values greater than -30 ‰ [e.g. Andres et al., 1994; Pugliese et al., 2017]. The modal value is around -26.5 ‰ [P. Tans, 1981; Andres et al., 1994]. The value here is still realistic, but not probable, particularly considering a  $\delta^{13}\text{C}$  mean source value measured in a tunnel in Heidelberg with  $(-27.17 \pm 0.04) \text{‰}$  [Großmann, 2022]. Contributions from human breath cannot explain this value, as they are more enriched (see subsection 5.2.1). A more depleted value could be explained by contributions from natural gas- [e.g. Andres et al., 1994; Newman et al., 2008; Pugliese et al., 2017] or autogas-powered vehicles (propane and butane) [e.g. Horváth et al., 2012; Lollar et al., 2008]. However, it is unrealistic that a car burning natural gas or autogas drove by, as only  $\sim 0.1 \text{ %}$  of cars in Germany use natural gas and  $\sim 0.6 \text{ %}$  use autogas [Kraftfahrt-Bundesamt, 2025b].

$\delta^{18}\text{O}_{\text{source}}$  is consistent with the range of reported values (see Table 5.2). CO<sub>2</sub> produced by combustion is expected to be close to the atmospheric value of O<sub>2</sub> [Ciais et al., 1997] ( $\delta^{18}\text{O}_{\text{VSMOW}} = (23.8 \pm 0.3) \text{‰}$  [Coplen, 2002]  $\hat{=}$   $\delta^{18}\text{O}_{\text{VPDB-CO}_2} = (-17.0 \pm 0.3) \text{‰}$ ). However, literature values show a variability of several per mil, suggesting that dependencies on factors such as other chemical species, catalyst type, temperature, and re-equilibration with present water may be involved [e.g. Affek et al., 2006; Popa et al., 2014]. Laskar et al., 2021 found a difference in the  $\delta^{18}\text{O}$  value of CO<sub>2</sub> emitted from diesel- and gasoline-

## 5. Mixing of $\Delta_{47}$ and Source + Ambient Air Measurements

**Table 5.2.:** The upper part of the table lists some literature results from tunnel and car exhaust measurements. The  $\delta^{18}\text{O}$  values were originally relative to VSMOW and were converted to VPDB- $\text{CO}_2$ . The lower part lists results from Keeling plots for the parking garage measurement. Since the  $\text{CO}_2$  concentration was not measured, it was estimated using the  $\text{N}_2\text{O}/\text{CO}_2$  concentration ratios. To do so, the  $\text{N}_2\text{O}$  concentration was calculated based on the Air Trap (inlet @ IUP's roof) measurement (11:51 - 12:02 UTC). Additional Keeling plots were performed assuming a 50 ppb higher  $\text{N}_2\text{O}$  concentration to estimate a systematic error. The  $\Delta_{47}$  result for the parking garage measurement indicates a high-temperature mean  $\text{CO}_2$  source.

		$10^3 \delta^{13}\text{C}$	$10^3 \delta^{18}\text{O}$	$10^3 \Delta_{47}$
<i>This Thesis</i>				
description		<i>mean end member in parking garage</i>		
Keeling plots with $C_{\text{CO}_2, \text{ parking garage}} = (736.5 \pm 4.2) \text{ ppm}$ (using $C_{\text{N}_2\text{O}} = (339.1 \pm 1.2) \text{ ppb}$ )		-30.80 $\pm 0.25$	-15.96 $\pm 0.57$	0.139 $\pm 0.044$
<b>For systematic error assumption:</b>				
Keeling plots with $C_{\text{CO}_2, \text{ parking garage}} = (845.1 \pm 4.5) \text{ ppm}$ (using $C_{\text{N}_2\text{O}} = (339.1 \pm 1.2) \text{ ppb} + 50 \text{ ppb}$ )		-27.53 $\pm 0.17$	-13.45 $\pm 0.42$	0.306 $\pm 0.036$
<i>Note: <math>C_{\text{CO}_2, \text{ parking garage}}</math> calculated via measured <math>C_{\text{N}_2\text{O}}/C_{\text{CO}_2}</math>. <math>C_{\text{N}_2\text{O}} = (339.1 \pm 1.2) \text{ ppb}</math> from Air Trap (inlet @ IUP's roof) measurement.</i>				
<i>Values from Literature</i>				
source	description	<i>car exhaust end member</i>		
<i>Eiler et al., 2004</i>	2 separate samples	-22.46 $\pm 0.08$	-16.56 $\pm 0.18$	probably altered or effected
		-25.18	-14.34	
<i>Affek et al., 2006</i>	by Keeling plots	-24.4	-11.1	0.41 <sup>[1]</sup>
	closest sample 5 cm outside exhaust pipe	$\pm 0.2$	$\pm 0.4$	$\pm 0.03$
<i>Laskar and Liang, 2016</i>	average of 2 samples	-27.70	-15.5	0.273
	~20 cm inside exhaust pipes	$\pm 0.03$	$\pm 0.07$	$\pm 0.021$
<i>Laskar et al., 2021</i>	average various samples	-26.8 <sup>G</sup>	-15.4 <sup>G</sup>	0.20 <sup>G</sup>
	~20 cm inside exhaust pipes	$\pm 0.3$	$\pm 1.3$	$\pm 0.07$
	G: gasoline powered	-26.8 <sup>D</sup>	-17.5 <sup>D</sup>	0.07 <sup>D</sup>
	D: diesel powered	$\pm 0.6$	$\pm 2.3$	$\pm 0.04$
<sup>[1]</sup> 0.39 ‰ using second order polynomial; 0.38 ‰ by regression analysis				
<i>mean end member in tunnel</i>				
<i>Laskar, Mahata, and Liang, 2016</i>	by Keeling plots	-26.76 $\pm 0.25$	-16.24 $\pm 0.32$	0.267 $\pm 0.036$
	for $\Delta_{47}$ second-order polynomial fit	-26.57 $\pm 0.07$	-17.30 $\pm 0.20$	0.141 $\pm 0.026$

## 5.2. Measurements of Human Breath and in a Parking Garage

operated vehicles (see Table 5.2).

As shown in Table 5.2,  $\Delta_{47}^{\text{source}}$  falls within three sigma of the published values for tunnel and car exhaust measurements by Laskar. The  $\Delta_{47}$  value given by Affek et al., 2006 is significantly higher, even when accounting for non-linearity in the Keeling plot or regression analysis. However, Affek's values are not represented in the reference frame of Dennis et al., 2011, making a quantitative comparison less meaningful. Furthermore, Affek's Keeling plot includes not only exhaust measurements but also data from a high-traffic road and ambient air sampled on a campus. These samples were collected over the course of several days or weeks. The values given by Laskar et al., 2021 are likely the most meaningful, as they measured various car models and collected extensive data for their tunnel measurement. Moreover, they found a difference in  $\Delta_{47}$  between gasoline-powered ( $\Delta_{47} = (0.20 \pm 0.07) \text{‰}$ ) and diesel-powered ( $\Delta_{47} = (0.07 \pm 0.04) \text{‰}$ ) vehicles.

The difference in  $\delta^{13}\text{C}$  could be explained by an incorrect  $\text{CO}_2$  concentration estimate in the parking garage. Therefore, the assumed  $\text{N}_2\text{O}$  concentration may be incorrect due to catalytic converters acting as a  $\text{N}_2\text{O}$  sink and source in gasoline- and diesel-operated vehicles, respectively [Laskar et al., 2021]. Laskar et al., 2021 results indicate a maximum enhancement of approximately 50 ppb  $\text{N}_2\text{O}$  in their tunnel measurements (12.5 km highway tunnel (heavy-duty trucks not allowed), Taiwan). Since 28.8 % of all cars were diesel-operated in Germany in 2024 [Kraftfahrt-Bundesamt, 2025a], it is probable that the  $\text{N}_2\text{O}$  concentration in the parking garage was also higher than assumed. A lower  $\text{N}_2\text{O}$  concentration would lead to even more depleted  $\delta^{13}\text{C}$  values and is therefore not considered. Furthermore, when comparing the measurement in front of the parking garage to the CRDS results for the same time, a slightly higher  $\text{N}_2\text{O}$  concentration at this site is also reasonable (Table 5.1). Otherwise, the estimated  $\text{CO}_2$  concentration in front of the parking garage would be  $(419.1 \pm 2.2) \text{ ppm}$ , which is lower than the  $\text{CO}_2$  concentration measured by the CRDS ( $(427.0 \pm 0.4) \text{ ppm}$ , Table 5.1). This seems unreasonable when considering the  $\delta^{13}\text{C}$  values (Table 5.1). Therefore, for a systematic error assumption for the Keeling plot results, a  $\text{N}_2\text{O}$  concentration 50 ppb higher ( $(389 \pm 1.2) \text{ ppb}$ ) is assumed. This results in a  $\text{CO}_2$  concentration in the garage of  $(845.1 \pm 4.5) \text{ ppm}$ . Keeling plots then yield  $\delta^{13}\text{C}_{\text{source}} = (-27.53 \pm 0.17) \text{‰}$ ,  $\delta^{18}\text{O}_{\text{source}} = (-13.45 \pm 0.42) \text{‰}$ ,  $\Delta_{47}^{\text{source}} = (0.306 \pm 0.036) \text{‰}$  (including non-linearity correction). This yields finally for the parking garage measurement:  $\delta^{13}\text{C}_{\text{source}} = (-30.80 \pm 0.25 + 3.28 \text{ (sys)}) \text{‰}$ ,  $\delta^{18}\text{O}_{\text{source}} = (-15.96 \pm 0.57 + 2.55 \text{ (sys)}) \text{‰}$ ,  $\Delta_{47}^{\text{source}} = (0.139 \pm 0.044 + 0.171 \text{ (sys)}) \text{‰}$ .

Using the full systematic error,  $\delta^{13}\text{C}_{\text{source}}$  falls within the published range of values (Table 5.2). However,  $\delta^{18}\text{O}_{\text{source}}$  appears slightly enriched compared to the values published by Laskar, but closer to the value published by Affek et al., 2006 (cf. Table 5.2).  $\Delta_{47}^{\text{source}}$

## 5. Mixing of $\Delta_{47}$ and Source + Ambient Air Measurements

corresponds better with *Laskar and Liang, 2016*, *Laskar, Mahata, and Liang, 2016* and *Affek et al., 2006* but worse with *Laskar et al., 2021* (cf. Table 5.2).

There may be a slight true shift towards more depleted  $\delta^{13}\text{C}$  values, considering the potential change in petroleum suppliers due to actual geopolitical circumstances [*Statistisches Bundesamt, 2023*]. However, this is beyond the scope of this work and should be studied with more extensive measurements. Given that there were some assumptions and only two data points for the Keeling plots, the quantitative results presented here should be viewed with caution. However, qualitatively, the measurement verified the potential of the newly built Air Trap by analyzing a sample with a clear evidence of a high-temperature source influence on  $\Delta_{47}$ .

## 5.3. Ambient Air Measurements in Heidelberg

As far as known, only *Affek et al., 2007* and *Laskar and Liang, 2016* have conducted ambient air measurements of  $\Delta_{47}$  in the lower troposphere under sub-urban/urban conditions without close source influence, and have monitored daily cycles or taken measurements over the course of days or months. Therefore, the measurements presented here still have unique features.

This section begins with an overview of ambient air measurements conducted in 2024, followed by a discussion regarding the annual trend. A nighttime inversion in October 2024 is then discussed. The section concludes with a discussion of the measurement results from exemplary periods in May and June of 2024, including a mean diurnal cycle.

All IRMS measurements presented were taken by automatic sampling ambient air drawn from the IUP roof inlet (see section 2.4 & chapter 3). These measurements are color-coded with ●. The CO<sub>2</sub> concentration data comes from CRDS measurements using the same inlet on the roof. For comparison purposes,  $\delta^{13}\text{C}$  measured by CRDS is also presented (gray). The CO<sub>2</sub> concentration data, color-coded with ●, represents the CO<sub>2</sub> concentration at the time of sampling for the IRMS measurements. Except for Figure 5.16, nonlinear mixing corrected  $\Delta_{47}$  values are represented with ◆. Unless otherwise specified, IRMS and CRDS data are presented with one-sigma SEM.

Additionally, some plots present precipitation and/or solar radiation data. These data are from the IUP's roof weather station. In plots showing individual measurements on specific days or over periods, the time of sampling is marked by a dotted line ranging from the top to the bottom of the plot. Nighttimes are represented by gray areas spanning the entire plot.

Having accurate background models for  $\Delta_{47}$  that rely on equilibration with integrated real-world leaf water temperatures for example is complex. Such models are beyond the scope of this work and require further research on  $\Delta_{47}$  and its equilibration processes under real-world conditions. Therefore,  $\Delta_{47}$  is only compared to a simple background model, relying on the direct transforming of air temperature measured at IUP's roof weather station. This model is represented by ■ or — in the following figures. It reflects CO<sub>2</sub> in contact with water at a temperature similar to that of the atmosphere during rapid re-equilibration, for example under the influence of carbonic anhydrase, acting as a catalyst. At least for equilibration with leaf water, this may serve as a rough estimate under poikilothermic conditions (slope between air and leaf water temperature is one [e.g. *Blonder et al., 2018*]) or as a rough reference for equilibration with other natural water bodies when averaged over days to weeks.

## 5. Mixing of $\Delta_{47}$ and Source + Ambient Air Measurements

### 5.3.1. Overview of Ambient Air Measurements in 2024

A total of 184 ambient air samples were collected in 2024, with 178 being used (Figure 5.7). The remaining samples were rejected due to issues such as no reference refill, preparation problems, or contamination (high  $\Delta_{48}$  or  $\Delta_{49}$ ). The representativeness of individual points for certain periods is revealed by comparing them with CRDS data and the mentioned  $\Delta_{47}$  background model, which are one-day averages with  $\pm 1$  SD. Most measurements were taken in May and June, and are discussed in detail under “Exemplary Periods: May and June”.

As discussed in subsection 4.3.3, long-term “D484276” measurements alone might suggest a slight systematic deviation of up to +0.02 ‰ in  $\Delta_{47}$  from January to early March. As also discussed there, no significant deviations regarding the different measurement protocols were evident. Nevertheless, ambient air measurements conducted using the old protocol (January) should be treated with caution.

Overall, the IRMS measurements show the following ranges:  $\delta^{13}\text{C} \approx -12.08$  to  $-8.40$  ‰,  $\delta^{18}\text{O} \approx -3.20$  to  $1.53$  ‰, and  $\Delta_{47} \approx 0.900$  to  $1.022$  ‰. Summer (01.04. - 30.09.) values are:  $\delta^{13}\text{C} \approx -11.05$  to  $-8.40$  ‰,  $\delta^{18}\text{O} \approx -1.84$  to  $1.53$  ‰, and  $\Delta_{47} \approx 0.912$  to  $1.022$  ‰; and winter (01.01. - 31.03. and 01.10. - 31.12.) values are:  $\delta^{13}\text{C} \approx -12.08$  to  $-9.08$  ‰,  $\delta^{18}\text{O} \approx -3.20$  to  $0.18$  ‰, and  $\Delta_{47} \approx 0.900$  to  $1.003$  ‰. The measurement on 23.10.2024 with the highest  $\text{CO}_2$  concentration  $\sim 531$  ppm and lowest  $\delta^{13}\text{C} \approx -13.00$  ‰ is excluded from the  $\delta^{13}\text{C}$  range. The variability of the isotope deltas is consistent with the ranges reported by Vardag et al., 2015 (Figure 7) for measurements in Heidelberg in December 2012/July 2013 ( $\delta^{13}\text{C} \approx -8$  to  $-12$  ‰ and  $\delta^{18}\text{O} \approx -4$  to  $2$  ‰).

### 5.3.2. Seasonal Trend 2024

To investigate the seasonal trend of ambient air data, only measurements taken between 13:00 and 17:00 UTC are considered. These measurements are averaged for each month and presented in Figure 5.8 on the first of each month. For April, August, and September, when there is only one measurement, the total error is used as the uncertainty. Otherwise, the SEM is used. The averages and SD of the comparison CRDS data and background models were calculated using all available data from 13:00 to 17:00 UTC each month.

The comparison CRDS data shows that the considered August measurement is not representative. The average of the IRMS measurements considered in January and October is close to one-sigma SD of the CRDS comparison data. Nevertheless, deviations of about 5 % in  $\text{CO}_2$  should have little effect on  $\Delta_{47}$ . Using the Keeling plots of the “Nighttime Inversion in October 2024” measurements (see heading below), an increase in  $\text{CO}_2$  of this magnitude

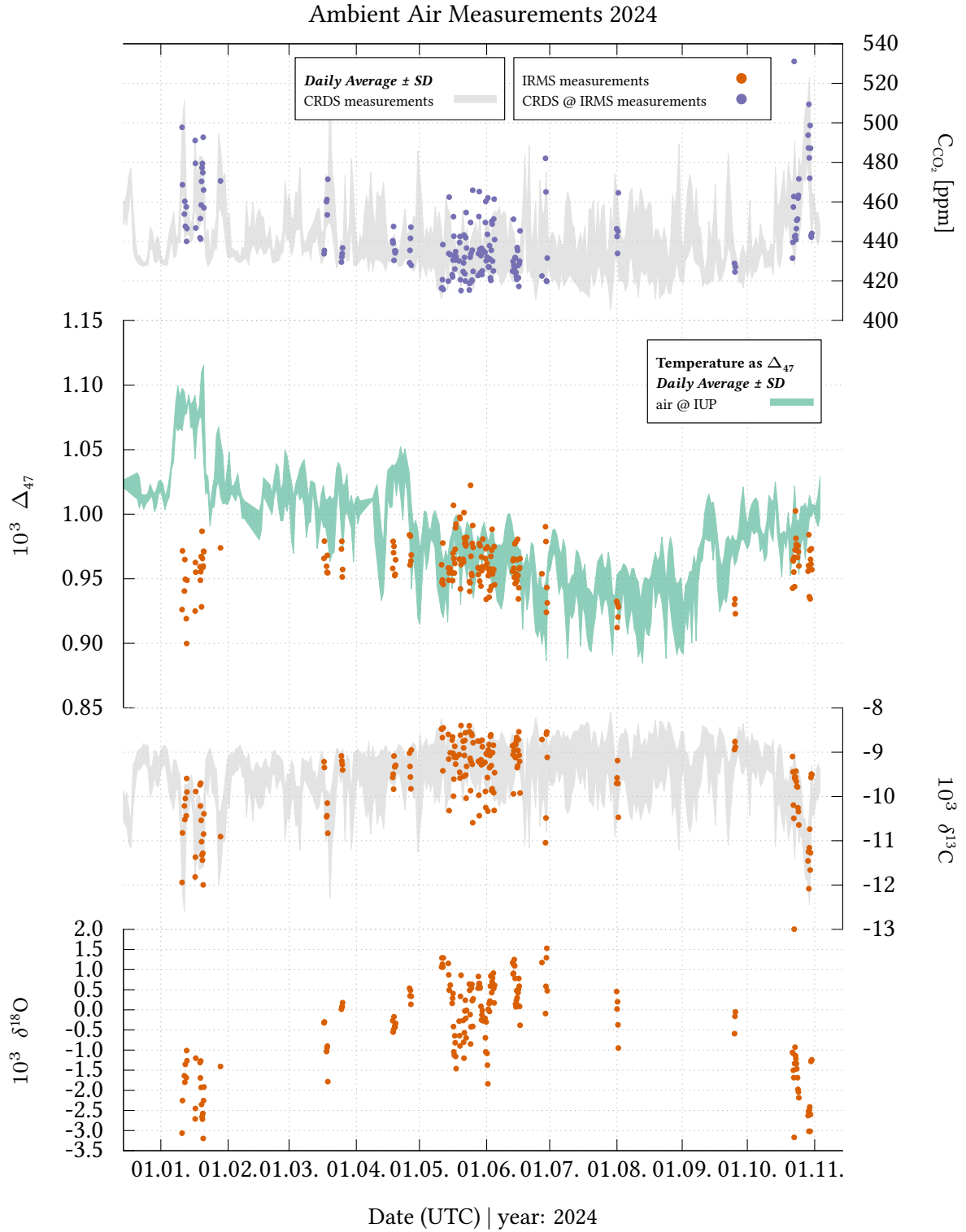
### 5.3. Ambient Air Measurements in Heidelberg

would result in an enhancement of less than 0.002 ‰ in  $\Delta_{47}$  for uncorrected mixing data (as given here). For corrected data, the  $\Delta_{47}$  values would be less than -0.01 ‰ lower. These deviations would not affect the general  $\Delta_{47}$  trend observed here. However, since the amount of IRMS data considered is small, the interpretation on  $\Delta_{47}$  is more qualitative.

**$\delta^{13}\text{C}$  &  $\delta^{18}\text{O}$ :** A clear annual trend is visible for  $\delta^{13}\text{C}$  and  $\delta^{18}\text{O}$ , with enriched values in summer and depleted values in winter. The summer values are consistent with the enrichment effect due to photosynthetic discrimination for both  $\delta^{18}\text{O}$  and  $\delta^{13}\text{C}$  [e.g. *Farquhar et al.*, 1989; *Farquhar et al.*, 1993; *Affek et al.*, 2014]. In contrast, photosynthetic activity significantly decreases in winter, allowing sources to dominate (see section 2.2 for typical source values). Additionally, anthropogenic heating sources with depleted isotopic values increase during this time [cf. isotopic values e.g. *Schumacher et al.*, 2011; *Pugliese et al.*, 2017]. Furthermore, long-term atmospheric inversion conditions in winter can trap  $\text{CO}_2$  emissions from sources throughout the day by preventing vertical atmospheric mixing. However,  $\delta^{18}\text{O}$  has more complex dependencies than  $\delta^{13}\text{C}$ . This is also evident from the larger errors in May and June, when 11 and 5 measurements were considered, respectively. The errors are 0.23 ‰ and 0.13 ‰ for  $\delta^{13}\text{C}$ , and 0.61 ‰ and 0.43 ‰ for  $\delta^{18}\text{O}$ , respectively. Photosynthetic discrimination of  $\delta^{18}\text{O}$  ( $\text{CO}_2$ ) depends strongly on  $\delta^{18}\text{O}$  ( $\text{H}_2\text{O}$ ) of leaf water [e.g. *Farquhar et al.*, 1993]. Additionally,  $\delta^{18}\text{O}$  ( $\text{CO}_2$ ) from soil respiration or diffusion-equilibration-retrodiffusion (“invasion effect”) has dependencies on  $\delta^{18}\text{O}$  ( $\text{H}_2\text{O}$ ) of rainwater, soil temperature and residence time [e.g. *Kapiluto et al.*, 2007; *Affek et al.*, 2014]. Therefore, the seasonal cycle of  $\delta^{18}\text{O}$  varies greatly depending on the geographical location of the measurement site [e.g. *Cuntz et al.*, 2003].

Previous studies have documented comparable seasonal cycles for  $\delta^{13}\text{C}$  [e.g. *Neubert*, 1998; *Vardag et al.*, 2016; *Pieber et al.*, 2022; *Cranton*, 2023]. The observed seasonal  $\delta^{18}\text{O}$  variability is consistent with published data from locations near Heidelberg [e.g. *Neubert*, 1998; BRN & HUN in *Peylin et al.*, 1999; ORL & HUN in *Cuntz et al.*, 2003; *Vardag et al.*, 2015]. Furthermore, the distinct summer (strong sink) and winter (stronger source contributions) conditions can explain the observed  $\text{CO}_2$  concentration trend, which is consistent with other studies [e.g. *Neubert*, 1998; *Schmidt et al.*, 2003].

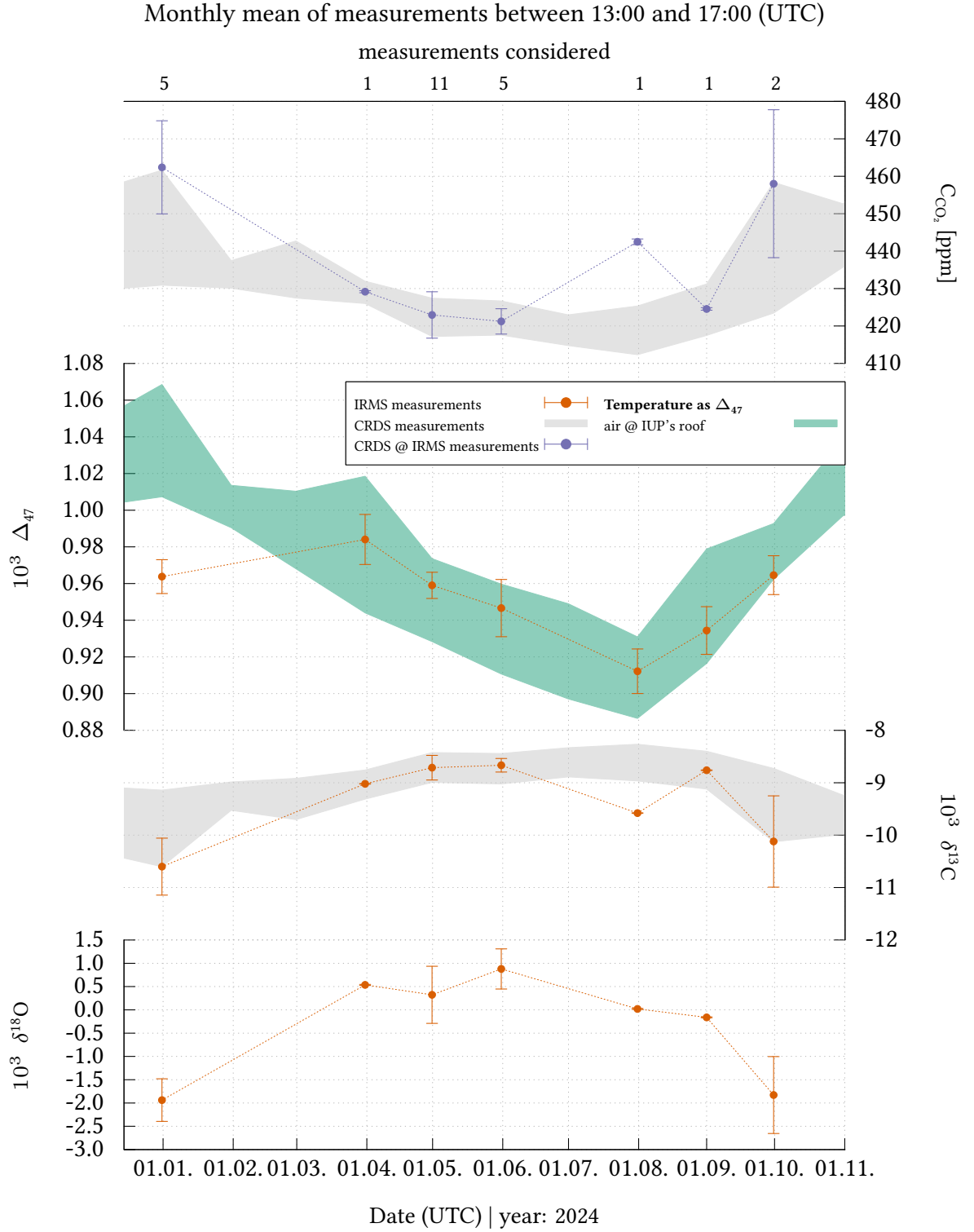
## 5. Mixing of $\Delta_{47}$ and Source + Ambient Air Measurements



**Figure 5.7.:** Overview of IRMS ambient air measurements used in 2024 (total 184/used 178). Comparison to daily average CRDS data and  $\Delta_{47}$  background levels indicates the representativeness of individual data points for certain periods. January measurements require caution due to transfer from an old measurement protocol and may have systematic deviations up to 0.02 ‰ in addition due to possible slight drift in calibration (see Figure C.5 on page 197). The IRMS measurements show the following variability:  $\delta^{13}\text{C} \approx -12.08$  to  $-8.40$  ‰,  $\delta^{18}\text{O} \approx -3.20$  to  $1.53$  ‰, and  $\Delta_{47} \approx 0.900$  to  $1.022$  ‰ (lowest  $\delta^{13}\text{C}$  with about  $-13.00$  ‰ is excluded).



### 5.3. Ambient Air Measurements in Heidelberg



**Figure 5.8.:** Averaged monthly measurements of samples taken between 13:00 and 17:00 UTC, plotted for each month on the first day of the month. The x2-axis represents the number of measurements considered. The standard error of the mean is used as the uncertainty, except for single measurements in April, August, and September, for which the total error is used. The CRDS and  $\Delta_{47}$  background data for comparison were calculated using all available data from 13:00 to 17:00 UTC each month. The August measurement is not representative; however,  $\Delta_{47}$  should not be significantly affected (see text). The lower winter values compared to the background model may be due to high-temperature  $CO_2$  source contributions that persist during the day and reduced re-equilibration towards ambient temperatures.

## 5. Mixing of $\Delta_{47}$ and Source + Ambient Air Measurements

$\Delta_{47}$ : Comparing the background model to the measurements in the high-biospheric active summer months, the measured values follow the model. According to *Adnew et al., 2021* and *Eiler et al., 2004*, uptake-dominated photosynthesis should yield  $\Delta_{47}$  values that are lower than expected from leaf water temperatures (see subsection 2.3.4). This is not evident here. One might assume that plant activity primarily influences the equilibrium value of  $\Delta_{47}$  at this time of year. However, the ambient  $\text{CO}_2$  measured here is still a mixture. This mixture likely contains smaller amounts from sources with lower  $\Delta_{47}$  values (higher temperatures) from combustion or animal respiration, as well as similar or slightly higher  $\Delta_{47}$  values from soil respiration that have not yet been re-equilibrated, e.g., through contact with leaf water.

Furthermore, even if the background model were used to compare equilibrated signals at leaf water temperatures, it should be noted that the model is likely not ideal for this purpose. Not only does the model include days on which no measurements were taken, but it also relies on air temperatures measured at IUP's roof rather than on regionally integrated leaf water temperatures. The air temperature at IUP is likely to be higher than the air temperature close to the majority of plants in the Heidelberg area [see *Stadt Heidelberg, 2025*, taking into account *GEO-NET Umweltconsulting GmbH, 2023*]. Most of these plants are likely to be found in forests or dense vegetation, which have cooler local air temperatures due to factors such as shade and evapotranspiration, in contrast to the semi-urban environment at IUP [e.g. *Taha et al., 1988; Bowler et al., 2010; Lee et al., 2016*]. However, transforming from air temperature to leaf temperature is complex and not straightforward. Direct heating from solar radiation and cooling from transpiration have a strong influence on leaf water temperatures [e.g. *Blonder et al., 2018; Zhou et al., 2023*]. Additionally, plants can control transpiration through stomata openness [e.g. *Hetherington et al., 2003; Peters et al., 2025*]. This results in a complex interplay, which can lead to both cooler and warmer leaf water temperatures than the local air temperature [e.g. *Michaletz et al., 2015; Deva et al., 2020; Still et al., 2022*]. This is dependent on a variety of factors, including absolute temperature, humidity, shadow, radiation, plant species, time of day, and factors governing plant conditions, especially water availability [e.g. *Urban et al., 2017; Blonder et al., 2018; Fauset et al., 2018; Zhou et al., 2023*].

Nevertheless, the observed similarity to ambient air temperatures indicates the presence of dominant sources and/or rapid re-equilibration with water reservoirs at similar temperatures. Therefore, it is conceivable that the summer values might be influenced by plant-related activities which utilize carbonic anhydrase as a catalyst, and that the observed signal could be influenced, for example, by the integrated leaf water temperature of the contributing plant species.

### 5.3. Ambient Air Measurements in Heidelberg

The significantly lower value in January, compared to the background model, may be attributed to two factors. Firstly, less and slower re-equilibration towards ambient temperatures. The measurements were conducted when the temperature was close to the freezing point of water. This may have prevented re-equilibration with water bodies, such as soil moisture. Furthermore, photosynthetic activity is lower in winter, resulting in less re-equilibration to leaf water temperatures. Secondly, lower  $\Delta_{47}$  values may be due to a greater contribution from high-temperature  $\text{CO}_2$  sources. These signals may also have persisted longer due to prolonged inversion weather conditions.

Compared to the interannual trend of  $\Delta_{47}$  in Pasadena (2004 and 2005) published by Affek et al., 2007, the annual trend here shows much lower fluctuations. Affek et al., 2007 collected samples at  $\sim 10$  a.m., when concentrations were close to the diurnal minimum. Samples were collected from a third-floor balcony on the Caltech campus (34.137°N, 118.128°W). They collected between zero and nine samples per month, for a total of 100. Affek's published measurements show significant interannual variability, with  $\Delta_{47}$  values ranging from  $(0.746 \pm 0.028) \text{‰}$  in March 2004 to  $(1.008 \pm 0.069) \text{‰}$  in August 2005. Furthermore, summer values are the highest, contradicting the results presented here. In 2004, summer values were below a direct air-temperature-to- $\Delta_{47}$  conversion; in 2005, they were above. Affek et al., 2007 stated that 2005 was one of the rainiest years on record in Southern California, resulting in high photosynthetic rates. Conversely, 2004 was significantly drier. However, this contradicts the expectation based on uptake-dominated photosynthesis that values would be lower, not higher. Affek et al., 2007 could explain their observations with a model that included assumptions and free variables. Yet, the discrepancy between Affek's results and the observations here is significant and not straightforward to explain. This highlights the need for more research under different environmental conditions.

Nevertheless, unlike Affek's results, measurements by Laskar and Liang, 2016 of suburban air collected in Taipei in October, November 2013 and January, February 2014 show significantly less variability ( $\Delta_{47} \approx 0.853$  to  $0.972 \text{‰}$ ). They collected 30 samples over 12 days from an open roof at the Institute of Earth Science Building, Academia Sinica (25°2'41" N, 121°36'52" E), with 2-3 samples per day. The results are generally lower than the  $\Delta_{47}$  values calculated from direct air temperature conversion, except for two days. The largest deviation was observed for the samples from mid-February, which is consistent with the results presented in this thesis for January. In addition, they collected eight samples from a grass field in front of the Department of Atmospheric Science, National Taiwan University Campus, (25°1' N, 121°30' E) on 14-16 November 2013. Measured  $\Delta_{47}$  were generally close to the direct air-temperature-to- $\Delta_{47}$  conversion,

### 5. Mixing of $\Delta_{47}$ and Source + Ambient Air Measurements

with a few values slightly lower. Further samples collected  $\sim 100$  m inside a dense natural forest at the west end of the Academia Sinica Campus on July 7, 14, and 28, as well as August 11 and 18, 2015, at 10:30 or 10:40 a.m., also showed values comparatively close to the  $\Delta_{47}$  from the direct air temperature conversion. Regarding the forest samples, *Laskar* and *Liang*, 2016 state that photosynthetic activity was probably not very strong at the ground level in the morning hours and that respiration was the dominant process. Both measurement sites suggest a strong governing effect of biospheric activity on  $\Delta_{47}$  values, which might be consistent with the main factors governing the signal observed here for daytime measurements on summer months.

### 5.3.3. Nighttime Inversion in October 2024

This nighttime measurement shows how to apply triple Keeling plots to ambient data and use the mixing correction according to Equations (5.4) and (5.5) for  $\Delta_{47}$ . The plot illustrates the significant impact of this correction, thereby demonstrating its necessity for interpreting ambient  $\Delta_{47}$  data.

Strong inversion weather conditions prevailed on the night of October 22-23, 2024, including penetrating fog in the morning. The ambient temperature ranged from approximately 18 °C at 12:10 UTC on October 22, 2024, to about 6 °C at 05:20 UTC on October 23, 2024. The average wind speed was approximately 1 m/s from 18:00 to 09:00 UTC, with only slight variations and no consistent wind direction. Average relative humidity increased from around 83 % between 17:00 and 18:00 UTC to  $\sim 103$  % between 03:00 and 04:00 UTC. It then declined from around 06:30 UTC, reaching already  $\sim 65$  % between 09:00 and 10:00 UTC. October 23, 2024 was a bright and sunny day following the clearing of morning fog. These conditions led to the highest CO<sub>2</sub> enhancement ( $\sim 531$  ppm) and lowest  $\delta^{13}\text{C}$  values ( $\sim -13.00$  ‰) recorded in 2024 for ambient air samples at times when the Air Trap was used for sampling. Figure 5.10 shows significant depletions of  $\delta^{18}\text{O}$  and  $\delta^{13}\text{C}$ , which are anticorrelated with CO<sub>2</sub>. Uncorrected mixing-effect  $\Delta_{47}$  data shows no significant trend with increasing CO<sub>2</sub> concentrations and remains relatively constant below the  $\Delta_{47}$  background model throughout the night.

The following values were obtained for the mean nightly source using Keeling plots with York fits (Figure 5.9):  $\delta^{13}\text{C}_{\text{source}} = (-30.16 \pm 0.38)$  ‰ and  $\delta^{18}\text{O}_{\text{source}} = (-13.32 \pm 0.22)$  ‰ (the four samples collected between 17:00 and 09:00 UTC are used). Combining these values with the background values shown in Figure 5.10 and applying Equations (5.4) and (5.5) to correct for mixing effects yielded the corrected  $\Delta_{47}$  values shown in Figures 5.9 and 5.10. The necessary background proportions ( $f_{\text{background}}$ ) were determined based on the CO<sub>2</sub> concentration increase relative to the minimum concentration at midday on October 22, 2024. Keeling plots of the uncorrected and corrected  $\Delta_{47}$  data yielded  $(0.980 \pm 0.062)$  and  $(0.784 \pm 0.063)$ , respectively. These values correspond to  $(14.8 \pm 11.4)$  °C and  $(54.7 \pm 15.7)$  °C, respectively.

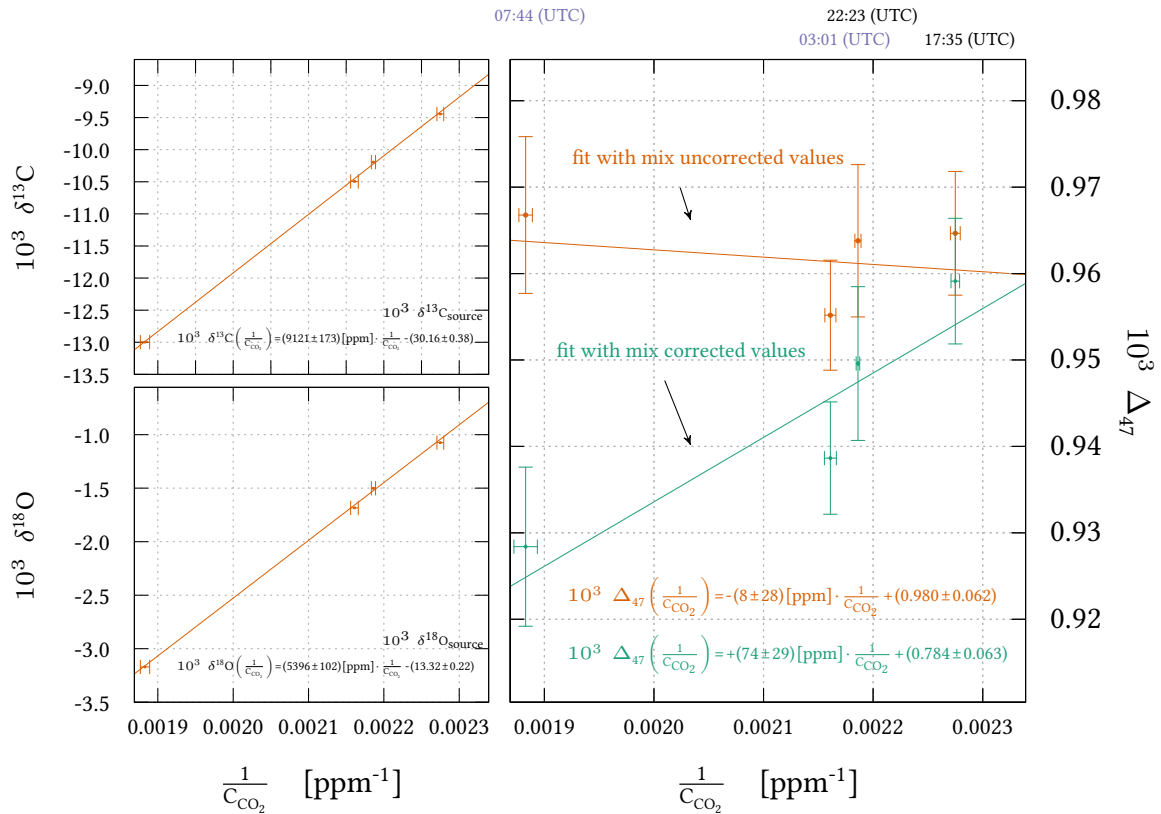
A constant  $\Delta_{47}$  background is assumed for the mixing correction and the Keeling plot. At least re-equilibration due to photosynthesis is not expected at night. Furthermore, re-equilibration in the atmosphere or on open water surfaces due to the absence of carbonic anhydrase (see subsection 2.3.4), as well as re-equilibration through diffusion-equilibration-retrodiffusion with soil water, likely play minor roles. Such effects would probably have affected the Keeling plot in  $\delta^{18}\text{O}$ . However, the linearity of the Keeling plot of  $\delta^{18}\text{O}$  indicates consistent source contributions throughout the measurement period ( $r^2$

### 5. Mixing of $\Delta_{47}$ and Source + Ambient Air Measurements

= 0.9992). Diffusion-equilibration-retrodiffusion with soil water is expected to result in nonlinearity in the Keeling plot of  $\delta^{18}\text{O}$ , but this may not be detectable for the observed mixing fraction [e.g. P. P. Tans, 1998; Seibt et al., 2006]. Nevertheless, such an effect would presumably yield significantly lower  $\delta^{18}\text{O}_{\text{source}}$ , as observed [cf. P. P. Tans, 1998 (Figure 5)]. Therefore, at least a strong invasion contribution is ruled out. Assuming a constant  $\Delta_{47}$  background seems plausible as a first-order approximation. Nevertheless, significant changes cannot be ruled out, and quantifying them is challenging without a better understanding of  $\Delta_{47}$  and its equilibration processes.

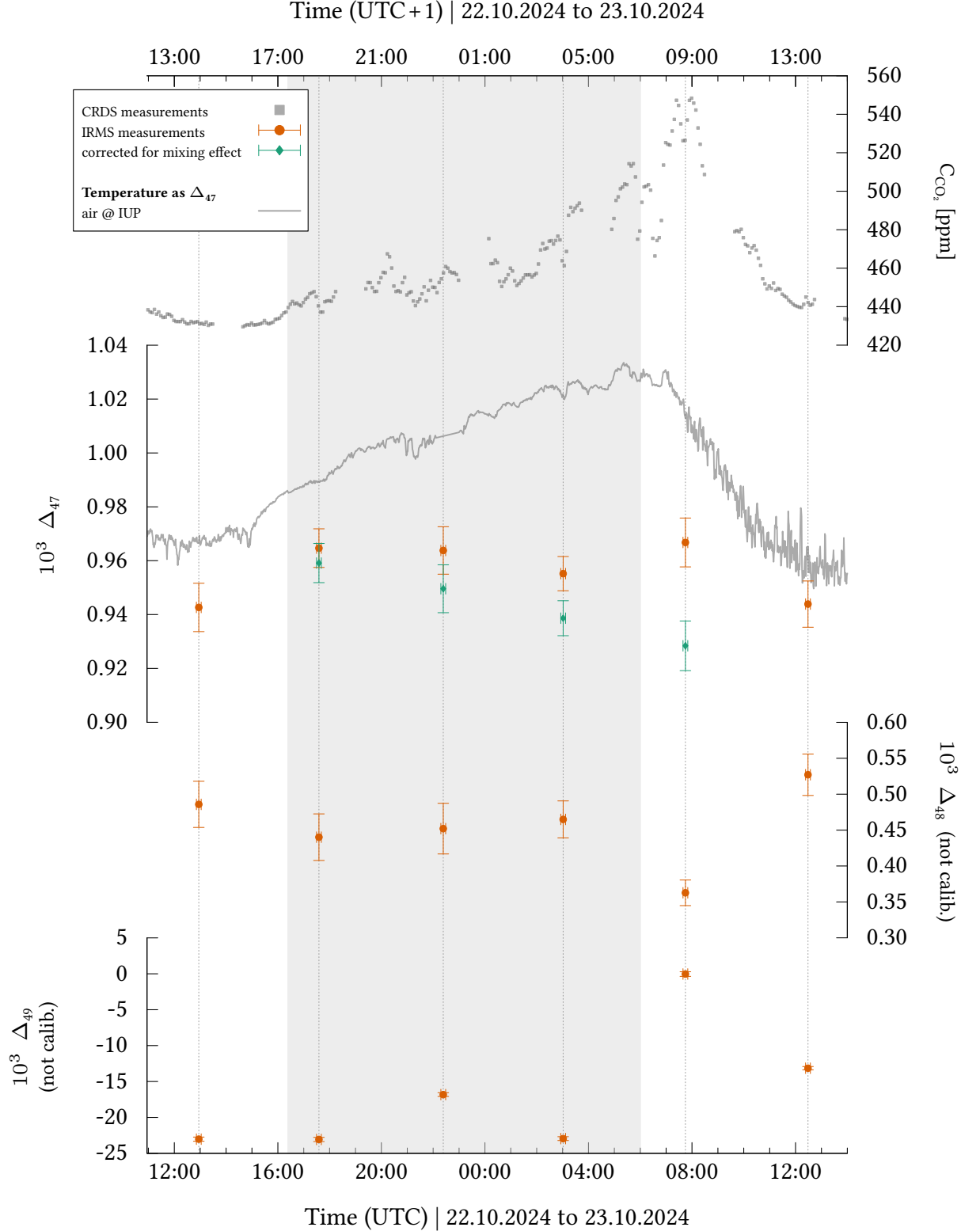
Under the assumption that the mixing corrected  $\Delta_{47}^{\text{source}}$  is accurate, this suggests a substantial contribution from a high-temperature source, such as the combustion of fossil fuels, which has undergone partial re-equilibration and/or is mixed with a low-temperature source, such as biospheric respiration.

Keeling Plots for Ambient Air Measurements: 22.10.2024 to 23.10.2024



**Figure 5.9.:** Keeling plots based on samples collected between 17:00 UTC on 22.10.2024 and 09:00 UTC on 23.10.2024 (Figure 5.10) yielded:  $\delta^{13}\text{C}_{\text{source}} = (-30.16 \pm 0.38) \text{‰}$ ,  $\delta^{18}\text{O}_{\text{source}} = (-13.32 \pm 0.22) \text{‰}$ , and for mixing uncorrected and corrected  $\Delta_{47}^{\text{source}} = (0.980 \pm 0.062)$  and  $(0.784 \pm 0.063)$ , respectively. The  $\Delta_{47}^{\text{source}}$  results demonstrate the significant impact of the mixing correction Equation (5.4). Mixing corrected  $\Delta_{47}^{\text{source}}$  indicates a contribution from a high-temperature  $\text{CO}_2$  source.

### 5.3. Ambient Air Measurements in Heidelberg



**Figure 5.10.:** Measurement results from samples collected during the nighttime inversion on October 22–23, 2024 (highest  $CO_2$  enhancement in 2024, at times when the Air Trap was used for sampling). The values required for the calculation of the mixing-corrected  $\Delta_{47}$  using Equation (5.4) were obtained as follows:  $\delta^{13}C_{source}$  and  $\delta^{18}O_{source}$  were derived from Keeling plots (Figure 5.9), and the background values are the indicated measurements (green circles). The background  $CO_2$  contribution ( $f_{background}$ ) stems from the  $CO_2$  concentration enhancement compared to the daytime minimum. As seen,  $\delta^{13}C$ ,  $\delta^{18}O$ , and mixing-corrected  $\Delta_{47}$  are anticorrelated with  $CO_2$  enhancement.

## 5. Mixing of $\Delta_{47}$ and Source + Ambient Air Measurements

$\delta^{13}\text{C}_{\text{source}}$  determined here falls within the average winter and summer values reported by *Vardag et al.*, 2016 and *Cranton*, 2023 for Heidelberg:  $\sim -32\text{‰}$  and  $\sim -32.0\text{‰}$ , respectively; and  $\sim -26\text{‰}$  and  $\sim -27.4\text{‰}$ , respectively. *Vardag et al.*, 2015 observed a large difference in the average source of  $\delta^{18}\text{O}$  between measurements in December 2012 ( $\sim -28\text{‰}$ ) and July 2013 ( $\sim -12\text{‰}$ ) in Heidelberg. The value determined here falls within this range, but is closer to the summer value.

A comparable measurement with sampling at IUP's roof from morning to midday on October 22, 2018, yielded  $\delta^{13}\text{C}_{\text{source}} = (-30.36 \pm 0.25)\text{‰}$ , within the one-sigma range, as well as  $\delta^{18}\text{O}_{\text{source}} = (-6.7 \pm 3.1)\text{‰}$  and  $\Delta_{47}^{\text{source}} = (0.675 \pm 0.022)\text{‰}$ , within the two-sigma range [*Eckhardt et al.*, 2022]. However, the  $\delta^{18}\text{O}$  error is comparatively large and the Keeling plot showed significant deviation from linearity. Since the measurements were taken during the day, a significant photosynthetic sink effect is still probable at this time of year, which could have affected especially  $\delta^{18}\text{O}$ .

A simple approach involving a set of coupled equations can be used to estimate the bulk isotopic composition of a mean ecosystem respiration source (including both heterotrophic and autotrophic respiration [*Schmiede et al.*, 2023]) and its proportion relative to a mean fossil fuel source:

$$\delta^{13}\text{C}_{\text{source}} = f_{\text{fossil fuel}} \cdot \delta^{13}\text{C}_{\text{fossil fuel}} + (1 - f_{\text{fossil fuel}}) \cdot \delta^{13}\text{C}_{\text{respiration}} \quad , \quad (5.12)$$

$$\delta^{18}\text{O}_{\text{source}} = f_{\text{fossil fuel}} \cdot \delta^{18}\text{O}_{\text{fossil fuel}} + (1 - f_{\text{fossil fuel}}) \cdot \delta^{18}\text{O}_{\text{respiration}} \quad , \quad (5.13)$$

$$\Delta_{47}^{\text{source}} + \Delta_{47}^{\text{mix corr.}} = f_{\text{fossil fuel}} \cdot \Delta_{47}^{\text{fossil fuel}} + (1 - f_{\text{fossil fuel}}) \cdot \Delta_{47}^{\text{respiration}} \quad . \quad (5.14)$$

$f_{\text{fossil fuel}}$  being the proportion of the fossil fuel source to the combined mean source values. The latter were determined by the Keeling plots (Figure 5.9). Correspondingly, the proportion of the ecosystem respiration source is  $f_{\text{respiration}} = 1 - f_{\text{fossil fuel}}$ . No alteration of the corresponding source values due to re-equilibration is assumed.  $\Delta_{47}^{\text{mix corr.}}$  in Equation (5.14) is calculated according to Equations (5.4) and (5.5), using  $f_{\text{fossil fuel}}$ ,  $\delta^{13}\text{C}_{\text{fossil fuel}}$ ,  $\delta^{18}\text{O}_{\text{fossil fuel}}$  for “background”, and  $\delta^{13}\text{C}_{\text{respiration}}$ ,  $\delta^{18}\text{O}_{\text{respiration}}$  for “source” values. Incidentally, this approach demonstrates another advantage of having correction Equation (5.4) to constrain nonlinearity.

This set of equations is solved by assuming  $\delta^{13}\text{C}_{\text{fossil fuel}} = (-32.5 \pm 2.5)\text{‰}$ , based on the Heidelberg value determined by *Vardag et al.*, 2016 in November and December of 2012, and by assuming  $\delta^{18}\text{O}_{\text{fossil fuel}} = (-17.3 \pm 3.0)\text{‰}$  (error generously estimated), with respect to *Affek et al.*, 2014. Additionally,  $\Delta_{47}^{\text{fossil fuel}} = (0.25 \pm 0.10)\text{‰}$  (error generously estimated) is assumed based on measurements taken on cars and in tunnels (see Table 5.2). This value is a compromise between *Laskar et al.*, 2021, which yielded a slightly lower value,



### 5.3. Ambient Air Measurements in Heidelberg

and the potential contributions of sources with slightly lower temperatures. Respired  $\text{CO}_2$  is assumed to be in equilibrium with the corresponding water reservoirs in contact [Laskar and Liang, 2016]. Therefore,  $\Delta_{47}^{\text{respiration}}$  is estimated from the background model in Figure 5.10 as  $(0.98 \pm 0.02) \text{ ‰}$ . A Monte Carlo simulation with 100,000 runs was performed, taking into account the given errors as one-sigma standard deviations in Gaussian distributions. This yielded  $\delta^{13}\text{C}_{\text{respiration}} = (-29.1 \pm 1.6) \text{ ‰}$ ,  $\delta^{18}\text{O}_{\text{respiration}} = (-11.6 \pm 2.0) \text{ ‰}$ , and  $f_{\text{fossil fuel}} = (28 \pm 10) \%$ , corresponding to  $f_{\text{respiration}} = (72 \pm 10) \%$ .

$\delta^{13}\text{C}_{\text{respiration}}$  is in consistency with results obtained by Vardag et al., 2016 for measurements in October 2012 (Figure 5(b)). To the best of knowledge, no  $\delta^{18}\text{O}_{\text{respiration}}$  has been published for a location near Heidelberg that considers all biospheric heterotrophic and autotrophic respiration sources, excluding fossil fuel contributions. However, the value determined here is consistent with the range of values determined by Neubert, 1998 (Figure 54) for soil respiration measurements from September to November 1995 at two locations near Heidelberg: Sandhausen (sandy soil) and Maisbach (loess-clay soil). Furthermore, it is closer to the summer value reported by Vardag et al., 2015, which is where more biospheric influences should have contributed, in contrast to the reported winter value.

Vardag et al., 2016 used the Stochastic Time-Inverted Lagrangian Transport (STILT) model [Lin et al., 2003], incorporating various input parameters, such as the respiration  $\text{CO}_2$  fluxes from the Vegetation Photosynthesis and Respiration Model (VPRM) [Mahadevan et al., 2008], to calculate that the proportion of  $\text{CO}_2$  from fossil sources in Heidelberg reaches a minimum of around 20 % in summer and can be about 90-95 % on cold winter days. The value determined here falls between these two values, but is clearly closer to the summer value. This is certainly plausible due to an still active biosphere and pleasant temperatures.

Although the results of this more quantitative approach should be interpreted with caution due to underlying assumptions, it has been demonstrated that  $\Delta_{47}$  may impose valuable constraints on models.

#### 5.3.4. Exemplary Periods: May and June – Mean Diurnal Cycle

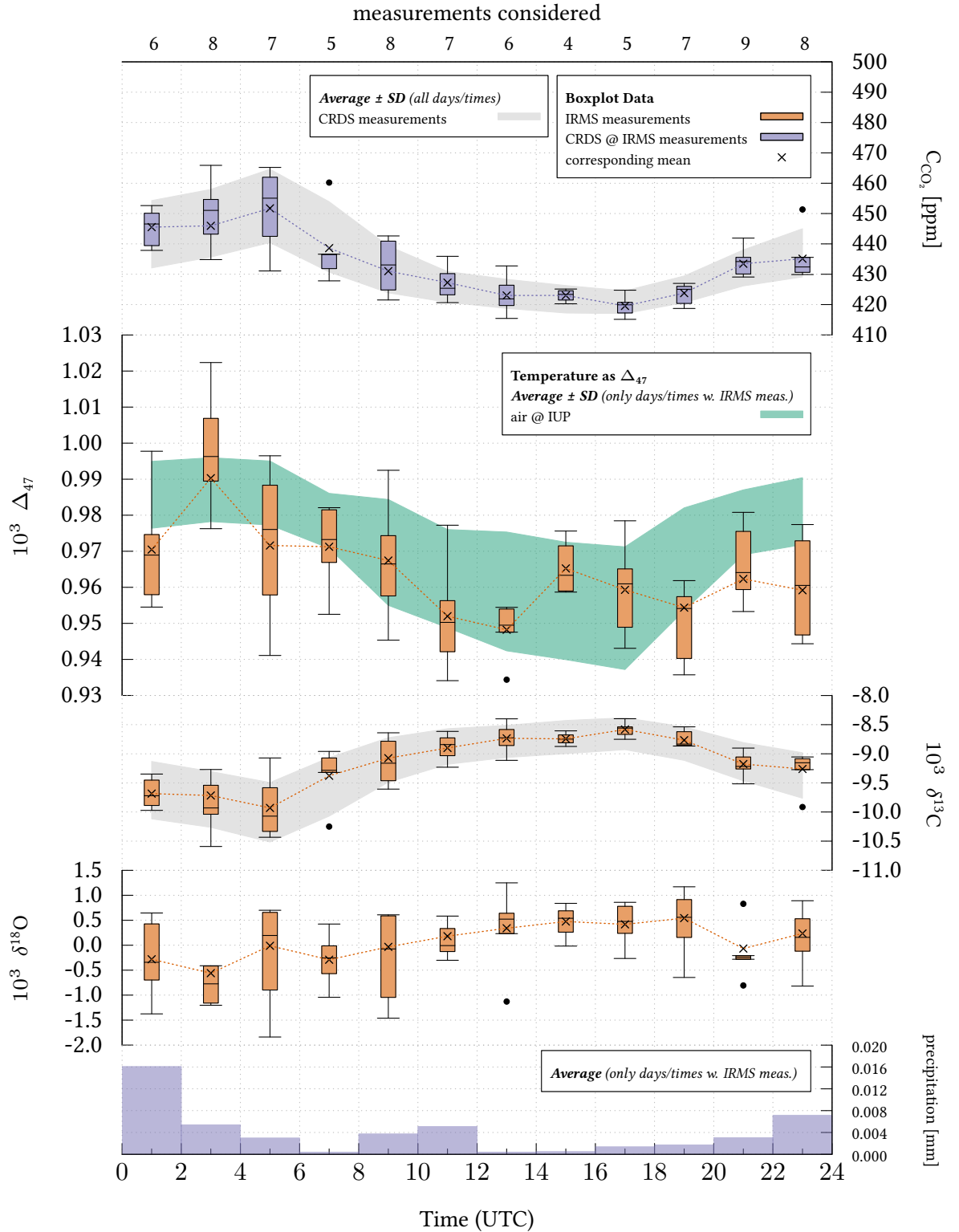
Three measurement periods of intense ambient air IRMS measurements within mid-May to mid-June 2024 are analyzed exemplarily. Since precipitation is particularly relevant for interpreting  $\delta^{18}\text{O}$  and  $\Delta_{47}$ , it is noteworthy that May 2024 was the wettest May in Baden-Württemberg since records began in 1881 [LUBW, 2025 (p. 12)]. This was accompanied by a flood peak of the Neckar in Heidelberg on the night of June 2-3. [Stadt Heidelberg, 2024]. The data is analyzed based on a mean diurnal cycle and individual measurement results over the entire period. Additionally, Keeling plots were created for some nighttime  $\text{CO}_2$  enhancements using York fits to determine  $\delta^{13}\text{C}_{\text{source}}$  and  $\delta^{18}\text{O}_{\text{source}}$ . This was not done for  $\Delta_{47}$  because the nighttime  $\text{CO}_2$  enhancements were too low to satisfactorily quantify the results determined by Keeling plots. Additionally, compared to the previously discussed “Nighttime Inversion in October 2024” example, more re-equilibration was plausible due to frequent rainfall and increased carbonic anhydrase activity (shorter nights and more biospheric activity). Therefore,  $\Delta_{47}$  is only qualitatively interpreted in relation to the background model.

The results of 89 individual IRMS measurements conducted on about 20 days are shown in Figures 5.12 - 5.14. The green circles in the subplots of  $\delta^{13}\text{C}$  and  $\delta^{18}\text{O}$  mark the samples used to determine the mean  $\delta^{13}\text{C}_{\text{source}}$  and  $\delta^{18}\text{O}_{\text{source}}$  by the Keeling plots. Keeling plots were only performed if there were at least three data points. York fit results with Pearson's  $r^2$  values  $< 0.9$  were rejected. The  $\delta^{13}\text{C}_{\text{source}}$  and  $\delta^{18}\text{O}_{\text{source}}$  values are summarized in Table D.3 on page 204. Additionally, the table lists the daily minimum  $\text{CO}_2$  concentrations ( $\text{C}_{\text{CO}_2\text{-min}}$ ) before nightly enhancement and the maximum morning  $\text{CO}_2$  concentrations ( $\text{C}_{\text{CO}_2\text{-max}}$ ). The column  $\delta^{13}\text{C}_{\text{min}}$  lists the mean daily minimum  $\delta^{13}\text{C}$  values, calculated from CRDS  $\delta^{13}\text{C}$  measurements taken 20 minutes before and after the daily  $\text{CO}_2$  minimums.

A mean diurnal cycle is shown in Figure 5.11. To represent one month, this includes 80 measurements taken between May 17 and June 17 at 00:00 UTC. For the analysis, the day was divided into two-hour intervals, with each interval containing the measurements taken within that interval. The x-axis shows the time in UTC, and the x2-axis shows the respective number of measurements considered. In addition to the values plotted as box plots, the crosses correspond to the respective mean values, which are connected by dashed lines to improve visibility. To assess the representativeness of the IRMS measurements, the mean values ( $\pm\text{SD}$ ) of the CRDS measurements are plotted in subplots for  $\text{C}_{\text{CO}_2}$  and  $\delta^{13}\text{C}$  using all data from the entire period. These data suggest that the IRMS measurements represent the period accurately. For the  $\Delta_{47}$  background model (mean  $\pm\text{SD}$ ) and the precipitation subplot (mean), only the data at times in which an IRMS

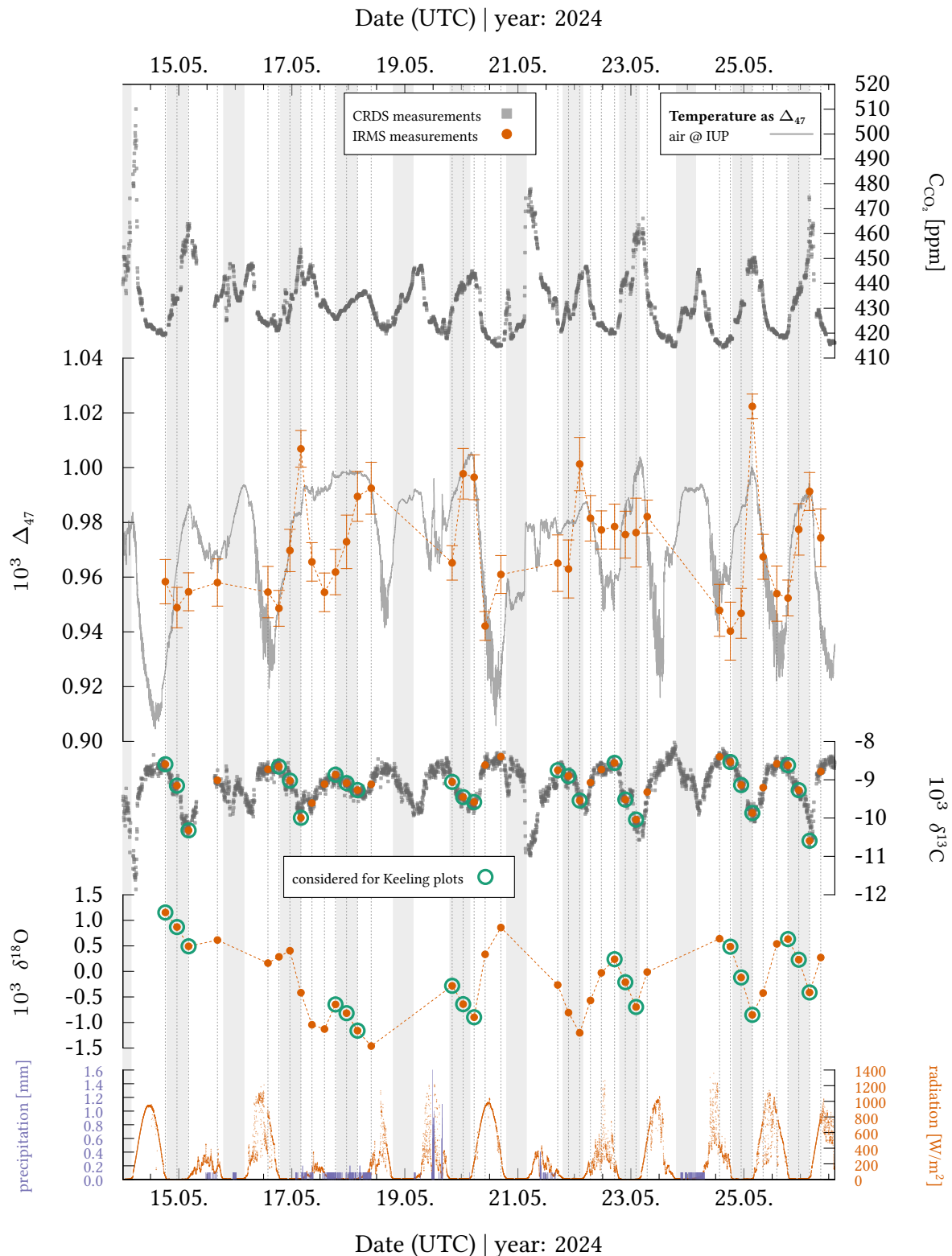
### 5.3. Ambient Air Measurements in Heidelberg

#### Diurnal Cycle | 2-Hourly Boxplots and Averages | 17.05.2024 - 17.06.2024



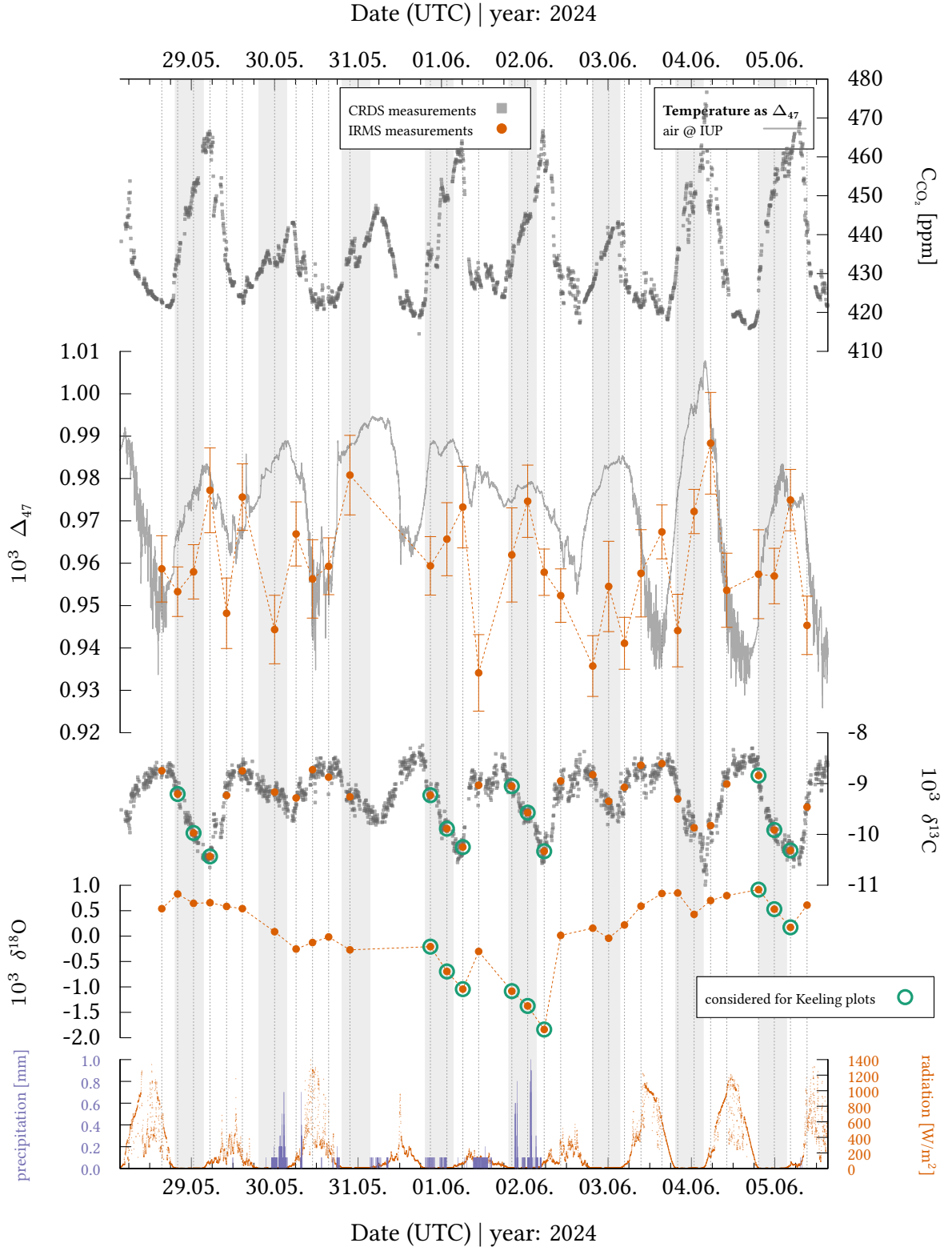
**Figure 5.11.:** Diurnal cycle for May 17 to June 17, 2024 (0 UTC). The day was divided into two-hour intervals, with each interval containing measurements taken within that interval. The x2-axis shows the number of IRMS measurements considered, respectively. To evaluate representativeness of IRMS data, all available CRDS data for  $C_{CO_2}$  and  $\delta^{13}C$  from the entire period are plotted in the background (mean  $\pm$  SD). For  $\Delta_{47}$  background model (mean  $\pm$  SD) and precipitation data (mean), only periods within which IRMS measurements were actually taken were considered.  $\Delta_{47}$  shows two notable changes: one in the morning at 2–4 UTC and another between 12–14 UTC and 14–16 UTC.

### 5. Mixing of $\Delta_{47}$ and Source + Ambient Air Measurements



**Figure 5.12.:** Measurement results for example period one (14.05.-26.05.) of three from mid-May to mid-June. CRDS measurements for  $C_{CO_2}$  and  $\delta^{13}C$  are shown in gray. IRMS measurements are shown in orange. Weather data is from IUP's roof weather station. Green circles in  $\delta^{13}C$  and  $\delta^{18}O$  subplots indicate data used for Keeling plots. A superimposed trend due to precipitation is observable in the  $\delta^{18}O$  data.  $\Delta_{47}$  is compared to background model in gray. Significantly higher values are observed on some mornings.

### 5.3. Ambient Air Measurements in Heidelberg



**Figure 5.13.:** Measurement results for example period two (28.05.-05.06.) of three from mid-May to mid-June. CRDS measurements for  $C_{CO_2}$  and  $\delta^{13}C$  are shown in gray. IRMS measurements are shown in orange. Weather data is from IUP's roof weather station. Green circles in  $\delta^{13}C$  and  $\delta^{18}O$  subplots indicate data used for Keeling plots.  $\Delta_{47}$  is compared to background model in gray. Extraordinarily low  $\delta^{18}O$  values were observed on the night of June 1-2 when heavy precipitation occurred.

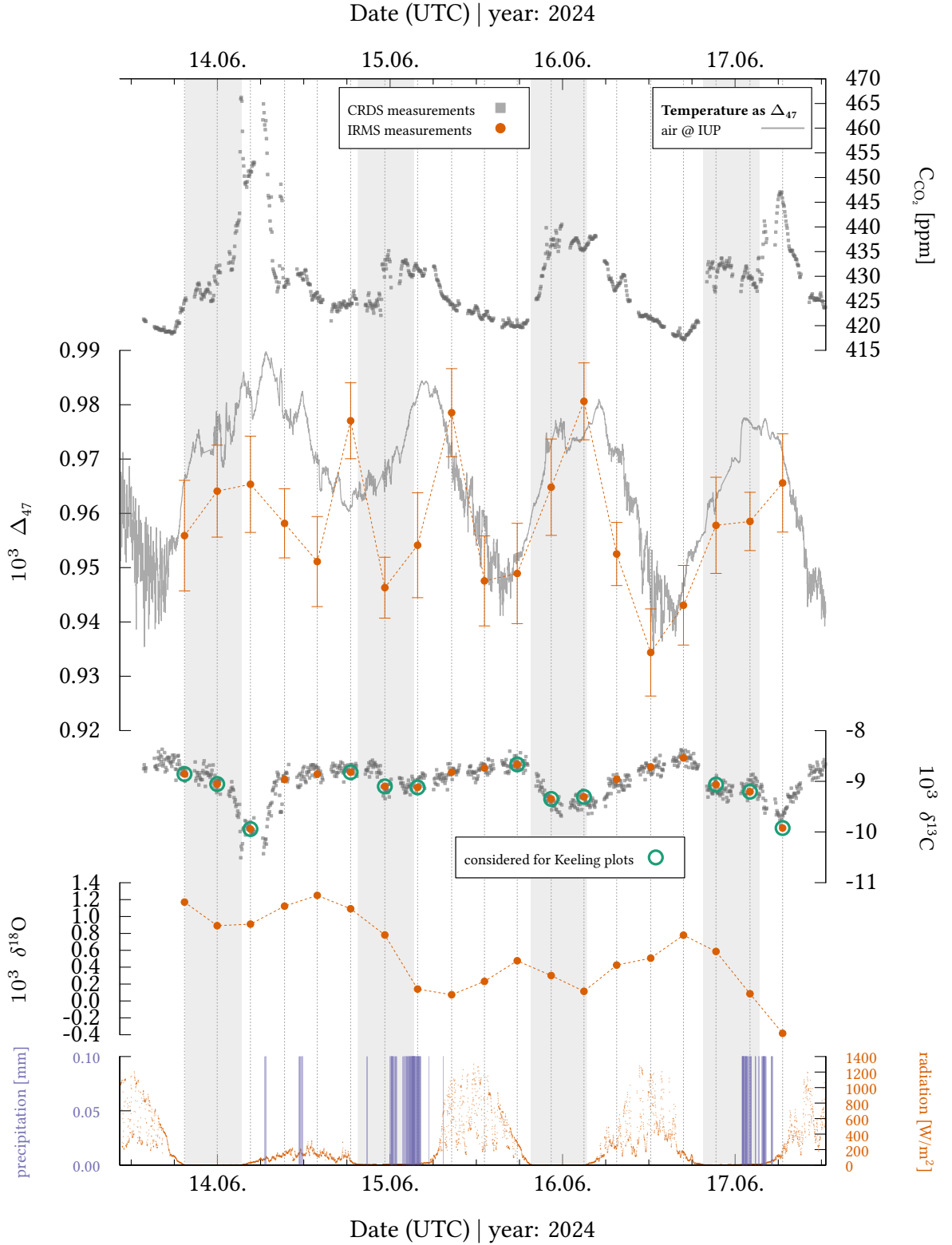
## 5. Mixing of $\Delta_{47}$ and Source + Ambient Air Measurements

measurement actually took place were taken into account. For the considered period in the diurnal cycle, sunrise and sunset shifted from approximately 3:40 to 3:20 UTC and 7:05 to 7:35 UTC, respectively. The mean times of sunrise, noon, and sunset were approximately 3:27, 11:25, and 7:22 UTC, respectively.

**CO<sub>2</sub>:** The CO<sub>2</sub> concentrations varied between daytime minima  $C_{\text{CO}_2-\text{min}} \approx 414.1$  to 425.6 ppm and morning maxima  $C_{\text{CO}_2-\text{max}} \approx 433.3$  to 476.6 ppm for the  $\sim 20$  days with IRMS measurements shown in Figures 5.12 - 5.14. Considering only the  $C_{\text{CO}_2}$  measurements, taken at the same times as the IRMS measurements and accounted for in the diurnal cycle, the lowest CO<sub>2</sub> concentration was  $(419.6 \pm 3.7 \text{ [SD]})$  ppm during the 16–18 UTC interval. The highest value,  $(452 \pm 12 \text{ [SD]})$  ppm, occurred during the 4–6 UTC interval. The amplitude was  $(32 \pm 13 \text{ [SD]})$  ppm. *Cranton, 2023* determined the times for minimum and maximum CO<sub>2</sub> concentrations in Heidelberg for spring (March, April, May) at 16 UTC and 5 UTC, with an amplitude of  $(29 \pm 1 \text{ [SEM]})$  ppm. For summer (June, July, August), the minimum and maximum concentrations occurred at 15 UTC and 5 UTC, with an amplitude of  $(36 \pm 2 \text{ [SEM]})$  ppm. The amplitude determined in this work falls within the values specified by *Cranton, 2023*. The time of maximum  $C_{\text{CO}_2}$  is consistent. The minimum is closer to the summer value, though only to the lower bound of the two-hour time interval. This can be partially explained by the fact that the IRMS measurement times are not entirely representative, and possibly by the smaller time intervals used by *Cranton, 2023*. In contrast, at the Schneefernerhaus high-mountain station in Germany (47°25'00"N, 10°58'46"E), the amplitude for summer (April - September) is approximately 2 ppm [*Hoheisel et al., 2023*]. This significant difference in amplitudes is consistent with stronger local influences from biospheric signals and fossil fuel emissions in Heidelberg compared to the continental background.

**$\delta^{13}\text{C}$ :** During the period under consideration, the  $\delta^{13}\text{C}$  measured by IRMS ranged from  $\sim -10.6$  to  $-8.4 \text{ ‰}$  (Figures 5.12 - 5.14). The mean  $\delta^{13}\text{C}$  values measured by IRMS in the diurnal cycle ranged from  $(-9.93 \pm 0.49) \text{ ‰}$  (4-6 UTC) to  $(-8.58 \pm 0.14) \text{ ‰}$  (16-18 UTC), with an amplitude of  $(1.35 \pm 0.51) \text{ ‰}$  (errors:  $\pm \text{SD}$ ). As expected,  $\delta^{13}\text{C}$  shows a good anticorrelation with CO<sub>2</sub> concentration because anthropogenic and biogenic sources are in general more depleted in  $\delta^{13}\text{C}$  than the atmospheric background (see previous discussions). For Heidelberg in spring (March, April, May), *Cranton, 2023* determined a minimum of  $(-9.93 \pm 0.05) \text{ ‰}$  at 4 UTC and a maximum of  $(-8.62 \pm 0.02) \text{ ‰}$  at 16 UTC, with an amplitude of  $(1.31 \pm 0.05) \text{ ‰}$ . For summer (June, July, August), a minimum of  $(-9.93 \pm 0.08) \text{ ‰}$  at 5 UTC and a maximum of  $(-8.35 \pm 0.02) \text{ ‰}$  at 15 UTC, with an amplitude of  $(1.58 \pm 0.09) \text{ ‰}$ .

### 5.3. Ambient Air Measurements in Heidelberg



**Figure 5.14.:** Measurement results for example period three (13.06.-17.06.) of three from mid-May to mid-June. CRDS measurements for  $C_{CO_2}$  and  $\delta^{13}C$  are shown in gray. IRMS measurements are shown in orange. Weather data is from IUP's roof weather station. Green circles in  $\delta^{13}C$  and  $\delta^{18}O$  subplots indicate data used for Keeling plots.  $\Delta_{47}$  is compared to background model in gray.

## 5. Mixing of $\Delta_{47}$ and Source + Ambient Air Measurements

was determined (errors:  $\pm$ SEM). Both spring and summer minimums are consistent with the minimum determined in this work. The maximum observed in this work is closer to the spring value of *Cranton*, 2023, for both  $\delta^{13}\text{C}$  and timing. Therefore, the amplitude is also closer to the spring values, which could be partly due to more measurements being considered in May than in June for the evaluation here. The same reasoning about timing is valid as that discussed for  $\text{C}_{\text{CO}_2}$ . As with  $\text{C}_{\text{CO}_2}$ , the amplitude of  $\delta^{13}\text{C}$  in Heidelberg is larger than at Schneefernerhaus (see above), with spring (March, April, May) and summer (June, July, August) having amplitudes of approximately 0.2 ‰ and 0.4 ‰, respectively [*Ghasemifard et al.*, 2019]. This further supports the argumentation on the higher  $\text{C}_{\text{CO}_2}$  amplitude.

$\delta^{13}\text{C}_{\text{source}}$  were determined for 16 nights in the considered period, ranging from -26.65 to -30.19 ‰ (see Table D.3; page 204), with a mean of  $(-27.98 \pm 0.85 \text{ [SD]})$  ‰ (median:  $\sim -27.94$  ‰). This value is within one SD of the maximum yearly source value of  $(-27.4 \pm 2.9 \text{ [SD]} \pm 0.1 \text{ [SEM]})$  ‰, which occurs in June, as determined by *Cranton*, 2023 based on an analysis of data from several years between 2014 and early 2023 (Heidelberg). It differs a bit more with about three standard deviations from the smoothed maximum summer values of  $\sim -26$  ‰, as determined by *Vardag et al.*, 2016, based on data from 2011 to mid-2015 (Heidelberg). However, this is not a monthly mean, and the more enriched summer values may be due to just a few days.

**$\delta^{18}\text{O}$ :** The measured  $\delta^{18}\text{O}$  for the considered period range from  $\sim -1.8$  to  $1.2$  ‰ (Figures 5.12 - 5.14). These values fall within the range of  $-2$  to  $2$  ‰, as measured by *Vardag et al.*, 2015 (Figure 7) for July 2013 (Heidelberg). As seen in Figures 5.12 - 5.14,  $\delta^{18}\text{O}$  exhibits superimposed depletion during rainy periods, a phenomenon also observed by *Vardag et al.*, 2015. This is consistent with strong governing by the hydrological cycle [e.g. *Farquhar et al.*, 1993; *Affek et al.*, 2014]. The usual nightly depletion (anticorrelated with  $\text{C}_{\text{CO}_2}$ ) is caused by  $\text{CO}_2$  sources that are typically more depleted in  $\delta^{18}\text{O}$  than background [e.g. *Schumacher et al.*, 2011; *Affek et al.*, 2014]. Conversely, the substantial enrichments on May 20 and 25 are notable examples for daytime photosynthetic discrimination [e.g. *Farquhar et al.*, 1993]. Yet, in the absence of photosynthetic discrimination, precipitation can lead to markedly depleted  $\delta^{18}\text{O}$  values, as seen on the night of June 1st-2nd, for example.

These factors also lead to a large variability in the  $\delta^{18}\text{O}$  box plot data (Figure 5.11). Nonetheless, a slight anticorrelation to  $\text{CO}_2$  concentration is evident, with lower values at night (nighttime source contributions) and higher values during the day (photosynthetic discrimination). The mean minimum is  $(-0.56 \pm 0.52 \text{ [SD]})$  ‰ (2-4 UTC) and the mean



### 5.3. Ambient Air Measurements in Heidelberg

maximum ( $0.54 \pm 0.63$  [SD]) ‰ (18-20 UTC).

Interpreting  $\delta^{18}\text{O}_{\text{source}}$  results of Keeling plots requires caution, as they are known to exhibit nonlinearities due to diffusion-equilibrium-retrodiffusion (invasion) [e.g. P. P. Tans, 1998; Seibt et al., 2006]. As shown for  $\Delta_{47}$  (Figure 5.3), such nonlinearity may appear linear when  $C_{\text{CO}_2}$  enhancements are low, resulting in  $r^2 \geq 0.9$  for linear York fits (see Figure 5 in P. P. Tans, 1998). Seibt et al., 2006 reported values 3 to 15 ‰ lower than expected when measuring soil respiration using Keeling plots, potentially caused by invasion. Of the 16 nights in the investigated period, only nine had  $r^2 \geq 0.9$ , and four of those nine nights had nocturnal rain (colored red in Table D.3; page 204). The results from these four nights are not discussed further as they may have been affected (e.g. not appearing nonlinearities). The  $\delta^{18}\text{O}_{\text{source}}$  values from the remaining five nights (14.05.-15.05., 22.05.-23.05., 24.05.-25.05., 25.05.-26.05. and 04.06.-05.06.) were approximately -6.8 ‰, -10.1 ‰, -19.0 ‰, -10.9 ‰ and -13.2 ‰, respectively. The seen variability in  $\delta^{18}\text{O}_{\text{source}}$  should be mainly caused by biospheric respiration, as significant changes in  $\delta^{18}\text{O}_{\text{source}}$  from fossil fuel are implausible. Additionally, fossil fuels should contribute only a minor fraction to the total source mixture at this time of year [cf. Vardag et al., 2016]. A lower  $\delta^{18}\text{O}_{\text{source}}$  is observed on the night of 24.05.-25.05. (blue in Table D.3; page 204) compared to the nights before (22.05.-23.05) and after (25.05.-26.05). Qualitatively, this is possibly due to morning precipitation on 24.05. and less time for  $\delta^{18}\text{O}$  ( $\text{H}_2\text{O}$ ) enrichment in the interacting water bodies through evapotranspiration compared to the other nights when there was a full day without precipitation. However, the value for night 24.05.-25.05. appears at least for soil respiration a little too depleted [see Neubert, 1998 (p. 56)], but may be explained by a mix with additional fossil fuel components if not slightly changed due to non-linearity.  $\delta^{18}\text{O}_{\text{source}}$  determined for the night of June 4-5 is more depleted than those of May 22-23 and May 25-26, despite having two whole days without precipitation beforehand. This might be explained by the extraordinary precipitation in the night of 01.06.-02.06. in combination with the yearly groundwater peak observed in many regions of Baden-Württemberg at the end of May/early June [see LUBW, 2025 (p. 18)]. The enrichment of  $\delta^{18}\text{O}$  ( $\text{H}_2\text{O}$ ) may have occurred more slowly due to the increased amount of  $\text{H}_2\text{O}$ , which may have affected respiration sources over a longer period. Lastly, of the five nights under consideration, the highest  $\delta^{18}\text{O}_{\text{source}}$  was determined for the night of May 14–15. This might be explained by the fact that the period of frequent rainfall did not begin until later. Prior to that night, there were some sunny days (high evapotranspiration) and no precipitation for one week, except for a brief event on May 13 (see Figure D.1; page 205). Compared to the subsequent period, it is reasonable to assume that water bodies were more enriched in  $\delta^{18}\text{O}$  ( $\text{H}_2\text{O}$ ).

## 5. Mixing of $\Delta_{47}$ and Source + Ambient Air Measurements

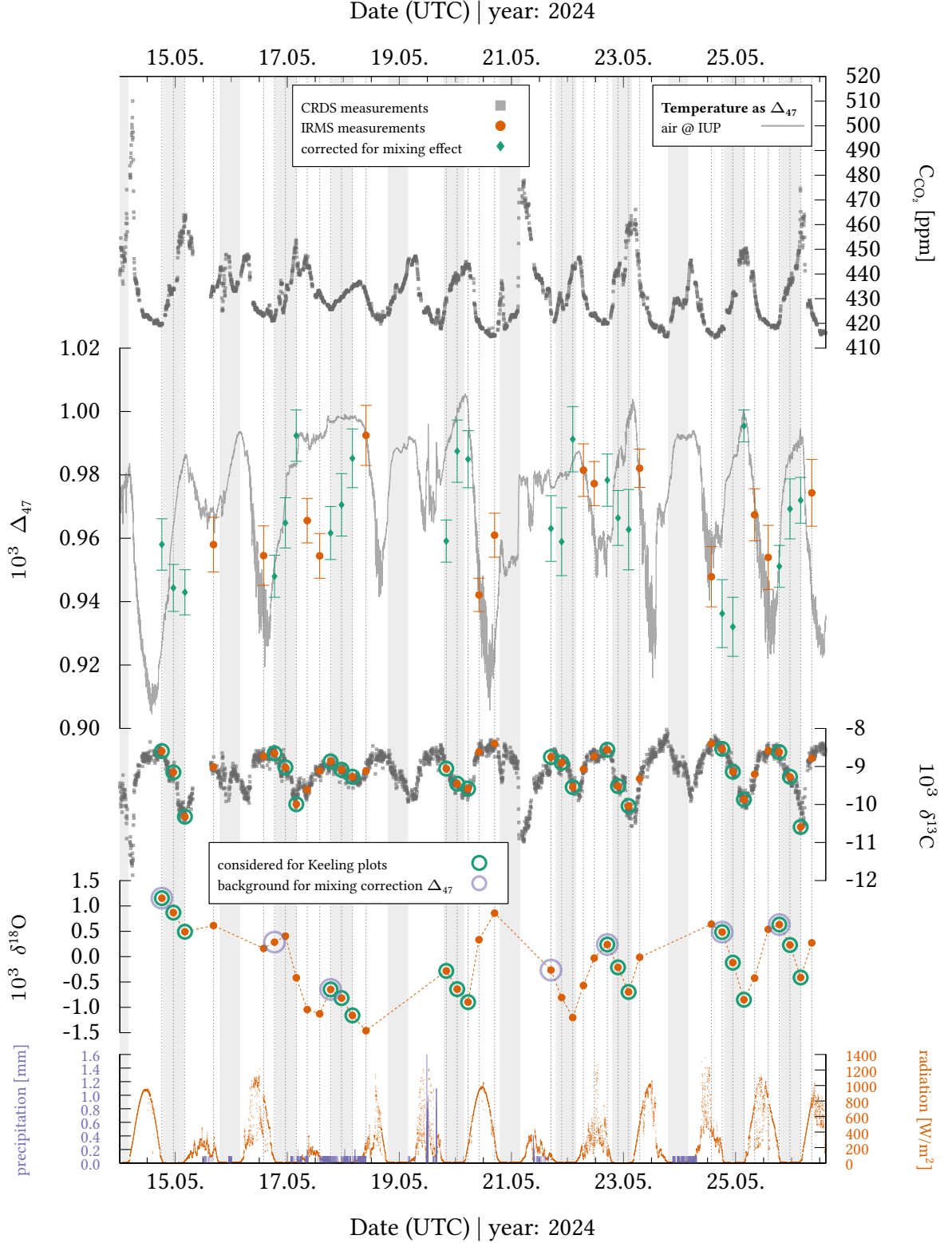
However, even if this qualitative interpretation has been somewhat accurate, it is still an oversimplification. For instance, temperature variations, soil complexity, and the physical condition of the plants were not considered. Finally, on July 2, 2013, Vardag et al., 2015 determined an  $\delta^{18}\text{O}_{\text{source}}$  value of approximately -12 ‰ in Heidelberg, which falls within the range of the five values determined here.

$\Delta_{47}$ : For the  $\sim 20$  days under consideration,  $\Delta_{47}$  ranged from 0.93 to 1.02 ‰ (Figures 5.12 - 5.14). This corresponds to an equilibration temperature ranging from 23.9 to 8.0 °C. The mean of all 89 measurements was  $\Delta_{47} = (0.964 \pm 0.017 \text{ [SD]}) \text{ ‰}$ , which corresponds to an equilibration temperature of  $(17.7 \pm 3.1) \text{ °C}$ . The median was  $\Delta_{47} \approx 0.959 \text{ ‰}$ , corresponding to 18.6 °C. These values are consistent with the mean ambient air temperature of  $(16.7 \pm 3.3 \text{ [SD]}) \text{ °C}$  measured by IUP's roof weather station over the three time periods: May 14–26, May 28–June 5, and June 13–17. In the diurnal cycle, the mean minimum is  $(0.948 \pm 0.008 \text{ [SD]}) \text{ ‰}$  (12–14 UTC) and the mean maximum is  $(0.990 \pm 0.021 \text{ [SD]}) \text{ ‰}$  (2–4 UTC). These correspond to temperatures of  $(20.6 \pm 1.5) \text{ °C}$  and  $(13.1 \pm 3.7) \text{ °C}$ , respectively. Two notable changes are observed: one within the time interval (2–4 UTC) and one between the time intervals (12–14 UTC) and (14–16 UTC). As shown in Figures 5.12 - 5.14, the morning peak can be observed shortly before or after sunrise, especially on May 17, 22, and 26, with  $\Delta_{47}$  clearly above the background model. This correlates with peak  $\text{CO}_2$  concentrations and anticorrelates with  $\delta^{18}\text{O}$  and  $\delta^{13}\text{C}$  values.

To rule out contamination as the cause for the morning peaks, Figures D.2 - D.3 (page 206f) present uncalibrated  $\Delta_{48}$  and  $\Delta_{49}$  for comparison. No systematic enhancement is visible for the discussed morning values. This makes contamination unlikely, as the most probable contaminants would also influence  $\Delta_{48}$  and  $\Delta_{49}$  [e.g. Eiler et al., 2004]. Considering the contamination vectors of  $\Delta_{47}$  to  $\Delta_{49}$  published by Fiebig et al., 2024, at least contamination by  $\text{NO}_2$ ,  $\text{SO}$ ,  $\text{CCl}$ ,  $\text{CS}$ , or  $\text{CH}_3\text{S}$  cannot explain the observed values.

The morning values could also be partly explained by the nonlinear mixing effect. However, unlike the measurements discussed under “Nighttime Inversion in October 2024”, the prerequisites for the correction might be worse. This is due to the possibility of increased re-equilibration and changing mean source composition caused by the regular precipitation events and increased biospheric activity at this time of year. At least for nights with Keeling plots of  $\delta^{18}\text{O}$  that have York fits with  $r^2 < 0.9$  or unusually depleted  $\delta^{18}\text{O}_{\text{source}}$ , re-equilibration or change in mean source composition may have occurred to some extent. Nevertheless, the correction is applied to each night within the period under investigation in order to examine the potential effects of mixing. It should be understood as a rough estimate, though. Figure 5.15 is the equivalent of Figure 5.12, but with nightly

### 5.3. Ambient Air Measurements in Heidelberg



**Figure 5.15.:** This graphic corresponds to Figure 5.12, but has been modified to include mixing-effect corrected  $\Delta_{47}$  data at nights (green), using Equations (5.4) & (5.5). Additionally, blue circles in the subplot of  $\delta^{18}\text{O}$  represent data used as  $\delta^{18}\text{O}_{\text{background}}$  in the correction. For some days, including May 19,  $\delta^{18}\text{O}_{\text{background}}$  was estimated by extrapolation. The values used for  $\delta^{18}\text{O}_{\text{source}}$ ,  $\delta^{13}\text{C}_{\text{source}}$ ,  $\delta^{13}\text{C}_{\text{background}}$ , and  $f_{\text{background}}$  are discussed in the text. As shown, the morningly risen  $\Delta_{47}$  values in Figure 5.12 may be explainable by the mixing effect. However, the corrected data should be viewed as a rough estimate, as the prerequisites for an accurate correction may be flawed.

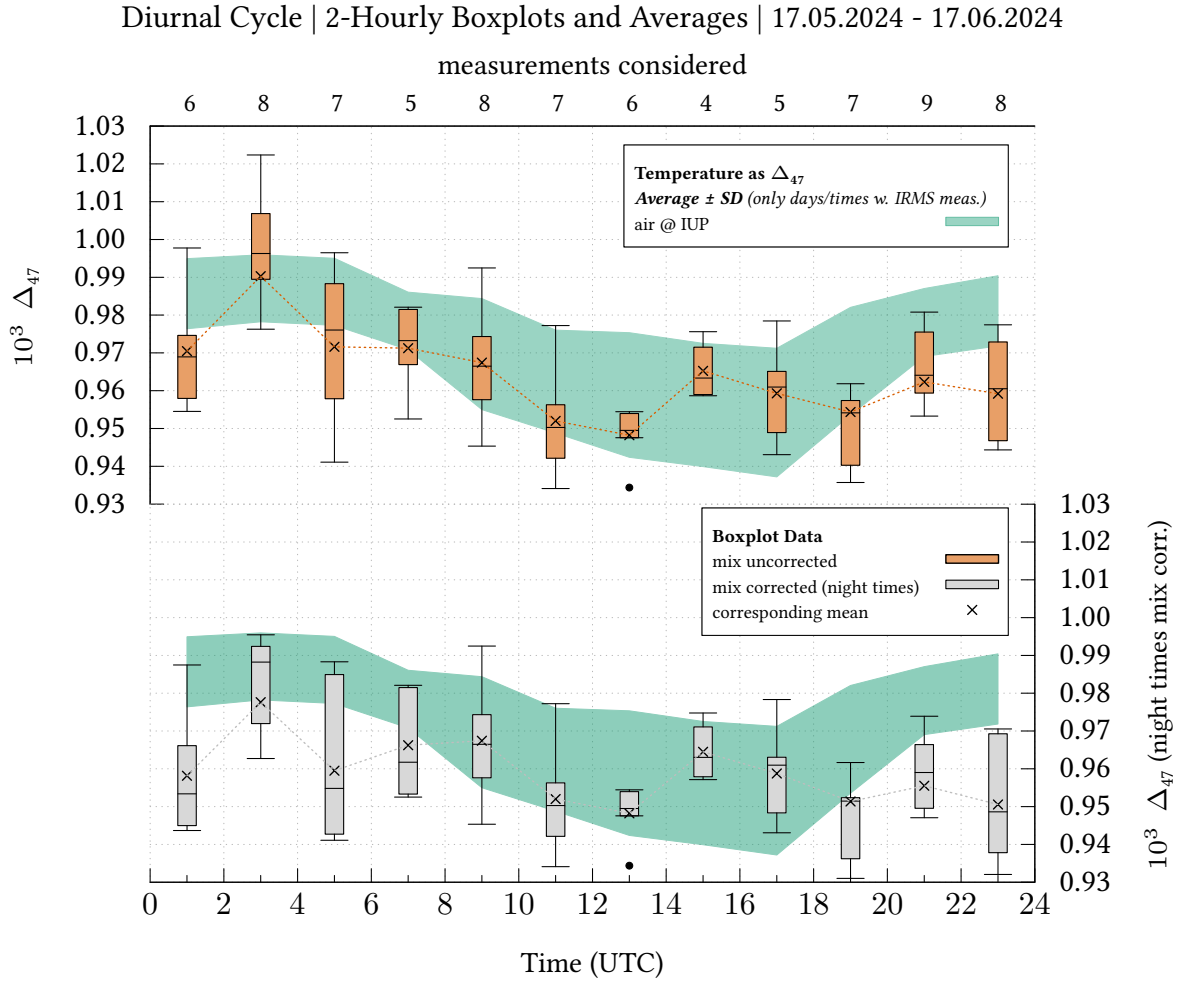
## 5. Mixing of $\Delta_{47}$ and Source + Ambient Air Measurements

mixed-corrected  $\Delta_{47}$  (green) using Equations (5.4) and (5.5). The corresponding Figures for 5.13 and 5.14 are Figures D.5 and D.6 (page 109f), respectively. Figure 5.16 provides a direct comparison of a diurnal cycle with uncorrected data (orange) and one which includes mixed-corrected data (gray). Daytime morning values may also be influenced by mixing, but are not corrected due to complications with photosynthetic sink activity.  $\delta^{13}\text{C}_{\text{source}}$  from Keeling plots were used for the correction (cf. Table D.3; page 204). For nights without a Keeling plot,  $\delta^{13}\text{C}_{\text{source}} = (-27.92 \pm 0.57 \text{ [SD]}) \text{ ‰}$ , determined as the mean from the results for nights spanning May 16-17 to June 15-16, was used.  $\delta^{13}\text{C}_{\text{background}}$  values were determined from  $\delta^{13}\text{C}$  measured by CRDS twenty minutes before and after the respective daily  $\text{CO}_2$  minimum. These ranged from -8.31 to -8.85 ‰. Keeling plot results for  $\delta^{18}\text{O}_{\text{source}}$  were only used for nights that were not color-coded red in Table D.3 on page 204. For all other nights,  $\delta^{18}\text{O}_{\text{source}} = (-11.4 \pm 3.4 \text{ [2 SD]}) \text{ ‰}$  was used, which was determined as the mean from the nights of May 22-25, May 25-26, and June 4-5. The results of the measurements indicated by the blue circles in Figures 5.15, D.5 (p. 209) and D.6 (p. 210) were used as  $\delta^{18}\text{O}_{\text{background}}$ , respectively. For some days, such as May 19, the  $\delta^{18}\text{O}_{\text{background}}$  values were estimated by extrapolation. The background fraction  $f_{\text{background}}$  was calculated from  $\text{C}_{\text{CO}_2}$  enhancements relative to the daytime minimum. As seen in Figure 5.15, the morningly enhanced  $\Delta_{47}$  values might be in part explainable by the mixing effect. Nevertheless, the diurnal cycle in Figure 5.16, which includes mixing-corrected data of  $\Delta_{47}$ , still indicates a peak between 2-4 UTC. This daily mean maximum of  $(0.978 \pm 0.017 \text{ [SD]}) \text{ ‰}$  corresponds to  $(15.2 \pm 3.1) \text{ °C}$ .

Qualitative discussion on  $\Delta_{47}$ : The mixing-corrected and uncorrected diurnal cycles of  $\Delta_{47}$  closely resemble the background model. However, as mentioned earlier in “Seasonal Trend 2024”, this background model may not be an ideal representation of a potential signal governed by re-equilibration with leaf water. Furthermore, the measured daytime signal is also a mixture. Therefore, there are likely gases equilibrated with leaf water temperatures from hours or days prior, as well as gases from other sources whose equilibration temperatures differ from those expected from ambient air temperatures. Considering the mean diurnal cycle, at least the effect of gas fractions coupled to ambient air temperatures (e.g., leaf water from hours or days prior) should be smoothed out to some extent. However, this may not be true for individual daytime temperatures when there are unusually large fluctuations and deviations from the previous day’s mean temperature. Nevertheless, the similarities to the background model suggest a significant re-equilibration with bodies of water close to the same temperature as the air. This largely aligns with expectations for most plant-related processes.

Now, consider the peak observed shortly before or after sunrise within the 2-4 UTC

### 5.3. Ambient Air Measurements in Heidelberg



**Figure 5.16.:** Comparison of the diurnal cycle from Figure 5.11 having mixing-effect uncorrected  $\Delta_{47}$  (above) to one including corrected data (below; using Equations (5.4) & (5.5); only nights). The parameters used for the correction are discussed in the text. The cycle including corrected data should be viewed as a rough estimate, as the prerequisites for an accurate correction may be flawed. Nevertheless, accounting for the mixing-effect lowers the morning peak. Daytime morning values may also be influenced by mixing, which could result in slightly lower values. However, these values are not corrected due to the complexities of photosynthetic sink activity. Besides the still apparent morning peak, another notable change in the diurnal cycle occurs between 12–14 UTC and 14–16 UTC.

time interval. If accurate, the distinctive timing of this peak could indicate a biospheric signal. One could speculate that this is related to re-equilibration with comparatively cold leaf water when some stomata open in the early morning, or to a change in the composition of the types of respiration. It could also indicate diffusion through soil, as *Eiler et al., 2004* hypothesized for elevated values, or another process involving an incomplete  $\text{CO}_2\text{-H}_2\text{O}$  equilibrium, which could be caused by rapid diffusion or kinetic isotope effects, as *Affek et al., 2014* hypothesized for elevated values.

Furthermore, it can only be speculated what the slight shift between 12–14 UTC and

## 5. Mixing of $\Delta_{47}$ and Source + Ambient Air Measurements

14-16 UTC could indicate. As shown in Figure 5.11, there were no significant changes in  $C_{CO_2}$ ,  $\delta^{13}C$ ,  $\delta^{18}O$ , or mean precipitation during this period. It should be noted that insufficient data availability and poor data distribution cannot be entirely excluded as possible causes of this effect. The six data points for 12-14 UTC are from the beginning (May 17, 24, and 25) and end (June 14, 15, and 16) of the considered period, whereas the points for the 14-16 UTC interval are from May 28, 29, and 30 and June 3. However, the background model, which considers only the time of actual sampling, does not show such a significant change between these time intervals. The same plot using three-hour time intervals also shows a slight change, albeit more smoothed out (see Figure D.7 on page 211). Interestingly, a slight peak is also observed in the greenhouse experiments of *Laskar and Liang, 2016* for days with a data point in the afternoon. On July 31, 2015, the  $\Delta_{47}$  value at 17:25 was  $(0.929 \pm 0.013) \text{‰}$ . The measurements at 15:00 and 21:30 were  $(0.877 \pm 0.015) \text{‰}$  and  $(0.911 \pm 0.012) \text{‰}$ , respectively. On August 4, 2015, the results were  $(0.896 \pm 0.011) \text{‰}$  at 14:00,  $(0.944 \pm 0.014) \text{‰}$  at 16:15, and  $(0.921 \pm 0.010) \text{‰}$  at 19:15. If these afternoon peaks in data from this work and reported by *Laskar and Liang, 2016* are not coincidental, they might indicate a change in photosynthesis. Gross Primary Production changes during the day, with the maximum typically occurring in the late morning [see *Pan et al., 2024*]. The afternoon peak could speculatively indicate a shift from uptake-dominated to a more exchange-dominated photosynthetic activity, leading to a higher  $\Delta_{47}$  value.

However, more studies with continuous measurements in different seasons and environmental conditions are necessary to determine whether this observations in the morning and afternoon are real signals and what they might indicate.

The observations on  $\Delta_{47}$  made here are still pioneering, both in terms of their scope and nature. Under certain conditions,  $\Delta_{47}$  appears to offer valuable insights into the local carbon cycle. Furthermore, it has been shown that some of the changes in  $\Delta_{47}$  might be partially attributed to the mixing effect. Overall, all observations and interpretations should be treated with caution, as they are based on a limited dataset. There are also very few comparative measurements or laboratory studies that would allow for a more robust interpretation. To improve understanding, it is recommended that these measurements continue and be supplemented by studies at other locations.

## 6. Conclusion and Prospect

### Conclusion

Within the scope of this work, a automatic preparation line coupled to an MAT 253+ IRMS was constructed for measuring  $\delta^{13}\text{C}$ ,  $\delta^{18}\text{O}$ , and  $\Delta_{47}$  of atmospheric  $\text{CO}_2$  samples. The system is fully integrated with the existing mass spectrometer software, enabling user-friendly operation. A preparation process takes approximately 90 minutes. A GC was integrated into the system to separate  $\text{CO}_2$  from hydrocarbons. Unlike in most laboratories [see *Petersen et al.*, 2016 (Table 1)], cooling is not required for this step, simplifying handling. To the best of knowledge, there is currently no other fully automated system worldwide for preparing atmospheric samples for measuring multiply substituted  $\text{CO}_2$  isotopologues.

The measurement method was adapted to improve the integration time-to-total measurement time ratio. Unlike most laboratories, which use integration times of 26 s or less [e.g. *Huntington et al.*, 2009; *Laskar and Liang*, 2016; *Bernecker et al.*, 2023], a sample integration time of 200 s per cycle with fewer cycles was employed. This reduced the cumulative idle time without integration when switching between sample and working gas. To maintain intensity ratios independent of absolute signal height, two-second time slices were integrated. This also enabled the filtering of outliers. The final measurement protocol included a single acquisition with 20 cycles. The initial intensity was set to approximately 8 V at  $m/z$  44. Thus, the total integration time was 4000 s. The total measurement time was approximately three hours, including peak center, bellows adjustment, and measurement at  $m/z$  18,  $m/z$  40, and  $m/z$  30.

The achieved reproducibility of 0.005 ‰ ( $n = 44$ ) for  $\delta^{13}\text{C}$ , 0.01 ‰ ( $n = 44$ ) for  $\delta^{18}\text{O}$ , and 0.011 ‰ ( $n = 57$ ) for  $\Delta_{47}$  is comparable to or better than that of other studies [cf. *Werner et al.*, 2001; *Huntington et al.*, 2009; *Affek et al.*, 2006; *Laskar, Yui, et al.*, 2016; *Fiebig et al.*, 2019]. In particular, the high reproducibility of  $\delta^{13}\text{C}$  and  $\delta^{18}\text{O}$  is significantly better, compared to laboratories that also published measurements of atmospheric  $\Delta_{47}$  [cf. *Affek et al.*, 2007; *Laskar and Liang*, 2016]. The  $\Delta_{47}$  reproducibility was achieved with lower intensities than those used by other laboratories, and therefore with less sample flow. In addition, successful calibration for  $\Delta_{48}$  was also demonstrated, which has only

## 6. Conclusion and Prospect

been reported in a few studies [e.g. *Fiebig et al.*, 2019; *Swart et al.*, 2021; *Bernecker et al.*, 2023; *Lucarelli et al.*, 2023].

Additionally, correction equations for isobaric N<sub>2</sub>O interference on  $\delta^{13}\text{C}$  and  $\delta^{18}\text{O}$  were reproduced [cf. *Ghosh et al.*, 2004] and updated based on the mean tropospheric N<sub>2</sub>O isotopic bulk composition according to *Kaiser et al.*, 2003. Similar equations were determined for the correction of  $\Delta_{47}$ ,  $\Delta_{48}$ , and  $\Delta_{49}$ . An optimized method to determine the N<sub>2</sub>O/CO<sub>2</sub> concentration ratio was also developed.

Furthermore, an equation to correct the nonlinearity in  $\Delta_{47}$  that occurs when two CO<sub>2</sub> gases with different bulk isotopic compositions are mixed was determined [e.g. *Eiler et al.*, 2004; *Defliese et al.*, 2015; *Laskar, Mahata, and Liang*, 2016]. It was theoretically shown that this equation can be applied to multicomponent mixtures to correct nonlinearities between arbitrary two mixed gases, such as a background gas mixture and a source gas mixture. This enables the creation of a Keeling plot with a linear fit to identify the  $\Delta_{47}$  end member. This is useful when the nonlinearity due to low C<sub>CO<sub>2</sub></sub> excess is not apparent, making a nonlinear fit impossible. This was demonstrated in practice using measurements taken in a parking garage and on a nocturnal measurement conducted in October 2024.

The results on the  $\Delta_{47}$  end member from the parking garage measurement, in which vehicle exhaust was likely the primary source of CO<sub>2</sub>, as well as the human breath measurement, confirmed the findings of previous studies on these sources [cf. *Affek et al.*, 2006; *Laskar, Mahata, and Liang*, 2016; *Laskar et al.*, 2021].

Automated preparation enabled measurements of  $\Delta_{47}$  on ambient air CO<sub>2</sub> with a temporal density and continuity not achieved in any other known study. A seasonal trend of  $\Delta_{47}$  based on midday measurements exhibited significantly less variability than the two-year cycle observed by *Affek et al.*, 2007 and was more comparable to measurements conducted by *Laskar and Liang*, 2016. It revealed that  $\Delta_{47}$  levels were lower in winter than equilibrated at ambient air temperatures. During the summer months, the signal corresponded to ambient air temperatures. The winter deviation was attributed to weaker biospheric re-equilibration and sources, as well as stronger influences from high-temperature-equilibrated fossil fuel sources. The close correspondence to ambient air temperature in summer was evaluated as an indication of relatively fast equilibration with water reservoirs that follow ambient air temperatures. It was assumed that this might be attributed to plant-related processes in which carbonic anhydrase serves as a catalyst. Thanks to continuous automated measurements, a mean diurnal cycle of  $\Delta_{47}$  could be obtained for the period from May 17 to June 17, 2024. The  $\Delta_{47}$  values in this cycle closely resembled the corresponding values for equilibration at ambient air



temperatures for most time intervals. Two pronounced changes occurred within the time intervals of 2–4 UTC and 14–16 UTC. The cause of these changes could not be determined, though biospheric reasons were speculated. Mean source values of  $\delta^{18}\text{O}$  were also determined during the aforementioned month, and their changes agreed well with the expected coupling of oxygen isotopes in  $\text{CO}_2$  to the water cycle [see e.g. *Affek et al.*, 2014]. Moreover, an evaluation of nocturnal measurement data from October 22–23 demonstrated that  $\Delta_{47}$  may serve as a valuable constraint for models when estimating source fractions.

## Prospect

The future production of temperature-equilibrated  $\text{CO}_2$  standards intended for long-term use should occur under optimized drying conditions. To minimize potential re-equilibration, storage could be optimized, e.g., by using a refrigerator. If stable standards are available, it is advised to use the PBL correction method proposed by *Bernecker et al.*, 2023. This could lead to better reproducibility and might reduce drifts in  $\Delta_{48}$  and  $\Delta_{49}$ . To improve accuracy, testing a higher-intensity measurement protocol could be considered. However, higher intensities do not necessarily lead to better results [see *Swart et al.*, 2021]. At higher intensities, it may be necessary to adjust the bellows more precisely to minimize the difference in intensity between the sample and the working standards during measurement [e.g. *Fiebig et al.*, 2016; *Swart et al.*, 2021]. Therefore, it is recommended that the bellows be controlled by a stepper motor and higher-quality pressure sensors to more precisely control and adjust the volumes. This would in addition eliminate the need for regularly readjusting the bellows control device, which is also necessary in other laboratories [e.g. *Swart et al.*, 2021]. In the future, cooling the GC should also be considered, as this may enable  $\text{N}_2\text{O}$  separation, as was achieved by *Laskar, Yui, et al.*, 2016. It is also recommended that the multitasking provided for in the programming but not finalized be completed so that measurements and processing can be carried out in parallel. This would allow seven to eight measurements instead of five samples per day. Additionally, it is worth considering the use of an additional multiblock valve with cooling fingers and a cooling trap for temporarily storing prepared samples. This would allow for the collection of more samples in shorter periods, such as at night, for later measurement. Furthermore, integrating the continuous  $\text{CO}_2$  data measured by the CRDS into the system would allow for intelligent sample collection.

Despite the limited time available for measurements after setting up the automated preparation system, numerous ambient air measurements were carried out thanks to automation. In the future, the system's potential should be further exploited to conduct

## 6. Conclusion and Prospect

continuous ambient air and atmospheric source measurements.

Further measurements in parking garages or tunnels, could help to constrain the  $\Delta_{47}$  end member of cars. Annual cycles based on larger data sets could improve understanding of  $\Delta_{47}$  and possibly yield exciting insights, for example into the presumed transition to stronger re-equilibration through plant activity or clarify the pronounced changes in the diurnal cycle. In particular, it would be interesting to carry out more measurements in winter, as re-equilibration may be weaker and fossil sources may contribute significantly to the signal. In addition to the laboratory studies on  $\Delta_{47}$  under photosynthetic gas exchange [Eiler et al., 2004; Adnew et al., 2022], further tests should be conducted in which environmental parameters, such as temperature and photosynthetic conditions (e.g., water availability) are altered. One option would be to conduct a study in the Heidelberg Botanical Garden greenhouse. In addition to air measurements, leaf temperature could be recorded using infrared sensors. It would also be interesting to conduct a detailed study on soil respiration using chamber tests, as no study has measured  $\Delta_{47}$  in this manner, to as far as is known.

Furthermore, including  $\Delta_{48}$ , particularly for human breath sample measurements, could provide valuable insights. Since high  $\text{CO}_2$  concentrations are present for human breath samples, high measurement accuracy could be achieved by measuring the same flask multiple times. This method could also enable the determination of  $\Delta_{49}$ . Combining these tracers could help narrow down possible fractionation and its cause. It is recommended to examine  $\Delta_{49}$  more closely. Although resolving the expected equilibration signal may be difficult, its greater mass difference from  $m/z$  44 could make the effects of fractionation more pronounced.

The automated preparation line developed thus forms a solid foundation for numerous other scientific studies. These can deepen understanding of the local carbon cycle and provide fundamental knowledge about multiple substituted isotopologues in  $\text{CO}_2$  through measurements of  $\delta^{13}\text{C}$ ,  $\delta^{18}\text{O}$ ,  $\Delta_{47}$ , ( $\Delta_{48}$ , and  $\Delta_{49}$ ).





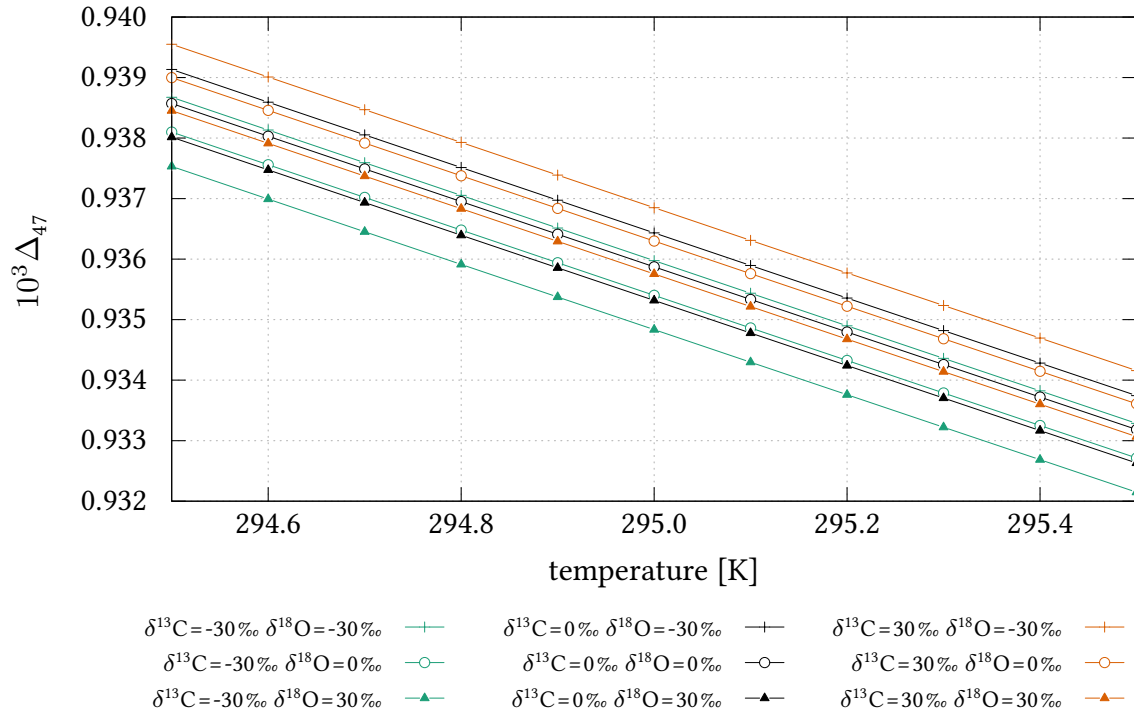
# Appendices

## A. Supplementary Material on Chapter 2

### A.1. Additional Figures and Tables

**Table A.1.:** The table lists the zero point energies and normal mode wave numbers of all stable CO<sub>2</sub> isotopologues and the corresponding symmetry numbers  $\sigma$  ( $\varpi_2^+$  is doubly degenerate). The data, except for the symmetry numbers, are taken from *Wang et al., 2004*. According to *Wang et al., 2004* the potential energy surfaces from *Zúñiga et al., 2001* were used for the calculations.

isotopologue	$\varpi_0$ [cm <sup>-1</sup> ]	$\varpi_1$ [cm <sup>-1</sup> ]	$\varpi_2^+$ [cm <sup>-1</sup> ]	$\varpi_3$ [cm <sup>-1</sup> ]	$\sigma$
<sup>16</sup> O <sup>12</sup> C <sup>16</sup> O	2525.394	1348.479	670.315	2387.185	2
<sup>16</sup> O <sup>13</sup> C <sup>16</sup> O	2472.905	1348.479	651.237	2319.243	2
<sup>16</sup> O <sup>12</sup> C <sup>17</sup> O	2507.955	1328.175	667.609	2377.682	1
<sup>16</sup> O <sup>12</sup> C <sup>18</sup> O	2492.277	1309.544	665.205	2369.462	1
<sup>16</sup> O <sup>13</sup> C <sup>17</sup> O	2455.240	1328.154	648.452	2309.472	1
<sup>17</sup> O <sup>12</sup> C <sup>17</sup> O	2490.437	1308.042	664.892	2367.872	2
<sup>16</sup> O <sup>13</sup> C <sup>18</sup> O	2439.355	1309.467	645.976	2301.041	1
<sup>17</sup> O <sup>12</sup> C <sup>18</sup> O	2474.686	1289.553	662.478	2359.382	1
<sup>17</sup> O <sup>13</sup> C <sup>17</sup> O	2437.498	1308.042	645.654	2299.360	2
<sup>18</sup> O <sup>12</sup> C <sup>18</sup> O	2458.866	1271.185	660.056	2350.649	2
<sup>17</sup> O <sup>13</sup> C <sup>18</sup> O	2421.542	1289.536	643.168	2290.624	1
<sup>18</sup> O <sup>13</sup> C <sup>18</sup> O	2405.519	1271.185	640.673	2281.620	2



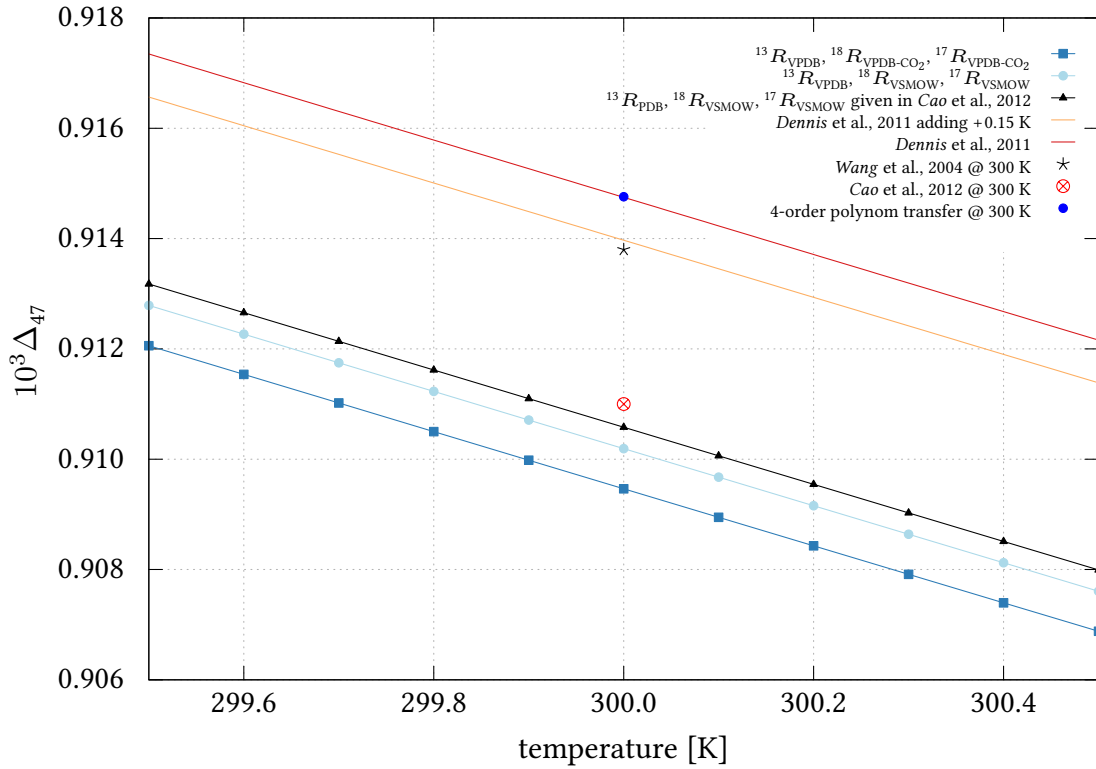
**Figure A.1.:** The plot shows the calculated slight dependence of  $\Delta_{47}$  on the bulk isotopic composition, varied for  $\delta^{13}\text{C}$  and  $\delta^{18}\text{O}$  from  $-30\text{‰}$  to  $+30\text{‰}$ . It can be seen that the deviations are particularly large when  $\delta^{13}\text{C}$  and  $\delta^{18}\text{O}$  deviate in an anticorrelated manner. The deviation is much smaller for a correlated deviation. Overall, the dependence is smaller than the usual measurement accuracy and is also probably partially compensated by correction steps and calibration.



**Figure A.2.:** Intake for ambient air located at the southeast corner of IUP's roof at approximately 31 m above ground level.

## A.2. Discussion on Reference Frames for $\Delta_{47}$

Figure A.3 compares various theoretical reference frame (RF) values of  $\Delta_{47}$  at 300 K. The values provided by Wang et al., 2004 ( $\Delta_{47} = 0.9138 \text{ ‰}$ ) and Cao et al., 2012 ( $\Delta_{47} = 0.911 \text{ ‰}$ ) are represented by  $\star$  and  $\otimes$ , respectively. The commonly used reference frame function Equation (2.26) [Dennis et al., 2011] is represented by —. As discussed in section 2.3.3, the discrepancy with Wang primarily stems from approximating the zero point of temperature as  $-273 \text{ °C}$  instead of  $-273.15 \text{ °C}$ . An adjusted version of Equation (2.26) that incorporates this difference is shown with —. Values calculated using the international standard values given in Table 2.1 (page 8) are marked with  $\blacksquare$  using  $^{13}R_{\text{VPDB}}$ ,  $^{17}R_{\text{VPDB-CO}_2}$ , and  $^{18}R_{\text{VPDB-CO}_2}$ , as well as  $\bullet$  using  $^{13}R_{\text{VPDB}}$ ,  $^{17}R_{\text{VSMOW}}$ , and  $^{18}R_{\text{VSMOW}}$ .  $\blacktriangle$  indicates a calculation performed using the international standard values provided by Cao et al., 2012. The slight discrepancy between the value provided by Cao et al., 2012 ( $\Delta_{47} = 0.911 \text{ ‰}$ ) and the one calculated here ( $\Delta_{47}(300\text{K}) \approx 0.91058 \text{ ‰}$ ) is likely due to rounding.



**Figure A.3.:** A comparison between the calculation of  $\Delta_{47}$  with respect to different international standards according to Table 2.1 is displayed by  $\blacksquare$  and  $\bullet$ . Additionally, the values provided by Wang et al., 2004 ( $\star$ ) and Cao et al., 2012 ( $\otimes$ ) are shown. Data points marked with ( $\blacktriangle$ ) are calculated based on the international standards stated by Cao et al., 2012. Furthermore, the function (—) Equation (2.26) according to Dennis et al., 2011 and a function (—) that corrects this by a term 0.15 K are displayed. The value given by Cao et al., 2012 at 300 K is marked with  $\otimes$ . The use of the transfer function Equation (A.1) between  $\blacksquare$  and — is indicated by  $\bullet$ .



The discrepancy between the values calculated by Wang et al., 2004 (equations (9i) through (9iv)) and by Cao et al., 2012 (equations (11a) through (11c)) cannot be explained by their different approaches. When  $\Delta_{47}$  was calculated at 300 K using both methods and the same international standards, the results agreed to 11 decimal places. (“fsolve” from the “scipy.optimize” package in Python was used). Cao et al., 2012 stated that they used  $^{13}R_{\text{PDB}} = 11237.2 \cdot 10^6$  [Craig, 1957], as well as  $^{17}R_{\text{VSMOW}} = 379.9 \cdot 10^6$  and  $^{18}R_{\text{VSMOW}} = 2005.2 \cdot 10^6$  [De Laeter et al., 2003]. Wang et al., 2004 stated that they used  $^{13}R_{\text{PDB}}$  according to Craig, 1957, as well as  $^{17}R_{\text{VSMOW}}$  and  $^{18}R_{\text{VSMOW}}$  according to IUPAC, 1994. The exact values were not specified. However, the discrepancy is too significant to be fully explained by slight deviations in the exact values of the international standards employed. Additionally, the discrepancy with Wang et al., 2004 might be due in part to differences in numerical calculations and/or the rounding of fundamental physical constants.

Regarding the proposed international measurement standards by Daëron et al., 2016, it would be more appropriate to use a reference frame adapted to them. One option would be to utilize the reference frame calculated with the values from Table 2.1 (page 8) for  $^{13}R_{\text{VPDB}}$ ,  $^{17}R_{\text{VPDB-CO}_2}$ , and  $^{18}R_{\text{VPDB-CO}_2}$  (—), which is henceforth referred to as  $\Delta_{47}^{\text{RF, VPBD-CO}_2}$ . However, as mentioned in section 2.3.3, this was not done to mitigate the complexity of conversion and ensure comparability. To convert theoretical calculations given in the reference frame  $\Delta_{47}^{\text{RF, VPBD-CO}_2}$  to experimental values given in the reference frame  $\Delta_{47}^{\text{RF, Dennis et al., 2011}}$  after Equation (2.26), the following function was determined (calculated between 270 and 521 K):

$$\begin{aligned} \Delta_{47}^{\text{RF, Dennis et al., 2011}} = & 0.0356786 \left( \Delta_{47}^{\text{RF, VPBD-CO}_2} \right)^4 - 0.153599 \left( \Delta_{47}^{\text{RF, VPBD-CO}_2} \right)^3 \\ & + 0.204821 \left( \Delta_{47}^{\text{RF, VPBD-CO}_2} \right)^2 + 0.903512 \Delta_{47}^{\text{RF, VPBD-CO}_2} \\ & + 0.0147695 . \end{aligned} \quad (\text{A.1})$$

Applying this function at 300 K yields the point indicated by ● in Figure A.3.

### A.3. Old versus New Measurement Protocol

Table A.2 lists some of the differences between the old and new measurement protocol. The change to the new protocol for regular measurements was made at the end of January/early February 2024. Beyond the deviations that are not discussed further, the following differences in the bellow adjustment and the acquisition function were made:

**Bellow Adjustment:** To achieve a more precise alignment, the decline in  $m/z$  44 between bellows adjustments is accounted for. Additionally, measurements of the control parameters have been included (see subsection 2.5.5). Furthermore, the adjustment is optimized for scenarios where the desired intensity of either the sample or reference side is not attained due to a lack (bellow at minimum) or excess (bellow at maximum) of gas. With the standard function, the measurement often begins with a different initial intensity at  $m/z$  44 in such cases. In the custom code, the adjustment is aligned to the higher or lower intensity depending on which bellow is adjustable.

**Acquisition Function:** The latest version of the custom acquisition function records not only the intensity, but also the measurement time, source pressure, and respective bellows pressure.

**Table A.2.:** Some differences between the old and new measurement protocol (changed end of January/early February 2024).

parameter	old protocol	new protocol
idle time	15 s	for $m/z$ 45 & 46: 55 s for $m/z$ 47 - 49: 15 s
integration time	26 s	200 s
number of slices	1, (13 after 27.01.2024)	100
slice start for $^{45}R$ & $^{46}R$	1	21
slice start for $^{47}R$ to $^{49}R$	1	1
typical number of acquisitions	8, 10	1, 2
typical number of cycles	10	10 (2 acquisitions); 17, 20 (1 acquisition)
bellow adjustment	standard function	own code
bellow adjustment for $m/z$ 44	6 V	8 V
acquisition function	standard function	own code
measurement $m/z$ 18, $m/z$ 40, $m/z$ 30	at end of acquisition	at start of acquisition
used for abort if threshold reached	$m/z$ 49 (added 2023/2024)	$m/z$ 18, $m/z$ 40, $m/z$ 49

## Transfer of Results from Old to New Measurement Protocol

Measurements performed using the old and new protocols yield slightly different results for the same sample. The difference between  $\delta^{13}\text{C}$  and  $\delta^{18}\text{O}$  is partly due to a dependency of the measured values  $^{45}\delta$  and  $^{46}\delta$ , which depend slightly on the absolute values  $^{45}\delta$  and  $^{46}\delta$ , respectively, in combination with the absolute signal at  $m/z$  44 (see appendix A.5). The latter differs between the protocols (see Table A.2). Additionally, an idle time of 15 seconds is insufficient when there are large differences in the bulk isotopic composition between the sample and the reference. Therefore, the means of the data obtained by the different integration times differ. To reduce dependence on this effect for  $\delta^{13}\text{C}$  and  $\delta^{18}\text{O}$ , the new measurement protocol discards the first 40 seconds of integration time at  $m/z$  45 and 46.

Differences in results obtained using the two protocols were investigated for 17 samples prepared between March 8 and April 21, 2024. These samples were measured using the new protocol, followed by the old protocol. The following functions for transferring results obtained using the old protocol to the new one were determined from these measurements and have been used in this thesis (data is in laboratory frame;  $^{45}\delta - ^{49}\delta$  is in respect to “Oberlahnstein”):

$$10^3 \ ^{45}\delta_{\text{transfer to new protocol}} = 10^3 \ ^{45}\delta_{\text{old protocol}} \cdot (1 + (151 \pm 3) 10^{-5}) \quad , \quad (\text{A.2})$$

$$10^3 \ ^{46}\delta_{\text{transfer to new protocol}} = 10^3 \ ^{46}\delta_{\text{old protocol}} \cdot (1 + (324 \pm 6) 10^{-5}) \quad , \quad (\text{A.3})$$

$$10^3 \ ^{47}\delta_{\text{transfer to new protocol}} = 10^3 \ ^{47}\delta_{\text{old protocol}} \cdot (1 + (18 \pm 2) 10^{-4}) - (33 \pm 4) 10^{-3} \quad , \quad (\text{A.4})$$

$$10^3 \ ^{48}\delta_{\text{transfer to new protocol}} = 10^3 \ ^{48}\delta_{\text{old protocol}} - (31 \pm 3) 10^{-2} \cdot 10^3 \ \Delta_{48, \text{old protocol}} - (41 \pm 8) 10^{-3} \quad , \quad (\text{A.5})$$

$$10^3 \ ^{49}\delta_{\text{transfer to new protocol}} = 10^3 \ ^{49}\delta_{\text{old protocol}} (1 - (3.9 \pm 1.2) 10^{-1}) - (16 \pm 5) 10^{-2} \cdot 10^3 \ \Delta_{49, \text{old protocol}} - (4.6 \pm 1.1) \quad , \quad (\text{A.6})$$

$$10^3 \ \delta^{13}\text{C}_{\text{transfer to new protocol}} = 10^3 \ \delta^{13}\text{C}_{\text{old protocol}} \cdot (1 + (145 \pm 4) 10^{-5}) + (58 \pm 6) 10^{-4} \quad , \quad (\text{A.7})$$

$$10^3 \ \delta^{18}\text{O}_{\text{transfer to new protocol}} = 10^3 \ \delta^{18}\text{O}_{\text{old protocol}} \cdot (1 + (321 \pm 6) 10^{-5}) + (302 \pm 9) 10^{-4} \quad , \quad (\text{A.8})$$

$$10^3 \ \Delta_{47, \text{transfer to new protocol}} = 10^3 \ \Delta_{47, \text{old protocol}} - (7 \pm 2) 10^{-4} \cdot 10^3 \ ^{47}\delta_{\text{old protocol}} - (33 \pm 4) 10^{-3} \quad , \quad (\text{A.9})$$

$$10^3 \ \Delta_{48, \text{transfer to new protocol}} = 10^3 \ \Delta_{48, \text{old protocol}} \cdot (1 - (34 \pm 5) 10^{-2}) - (37 \pm 7) 10^{-4} \cdot 10^3 \ ^{48}\delta_{\text{old protocol}} - (40 \pm 8) 10^{-3} \quad , \quad (\text{A.10})$$

$$10^3 \ \Delta_{49, \text{transfer to new protocol}} = 10^3 \ \Delta_{49, \text{old protocol}} \cdot (1 - (16 \pm 5) 10^{-2}) - (4.0 \pm 1.2) 10^{-1} \cdot 10^3 \ ^{49}\delta_{\text{old protocol}} - (4.6 \pm 1.1) \quad . \quad (\text{A.11})$$

## A.4. Background Correction

The background/pressure baseline (PBL) [He et al., 2012] correction used here is applied in dependence of the signal measured at  $m/z$  47.5. It essentially follows the procedure described in Haun, 2017 (based on Bernasconi et al., 2013). To determine the pressure baseline correction functions, peak scans were performed by incrementally increasing the high voltage by 0.0005 kV from 9.5499 to 9.6999 kV. This was done at different signal levels by admitting different amounts of gas to the source. For  $m/z$  44–46, background intensities were calculated by taking the mean of the signals to the left of the peak. For  $m/z$  47–49, data from both sides of the peaks were considered, and a linear fit was applied. Then, the virtual background values at the  $m/z$  44 peak center high voltage value was calculated from these fits. For  $m/z$  47.5, the mean of data close to the  $m/z$  44 peak center high voltage value was calculated. Second-order polynomials were applied to the  $m/z$  44–49 background intensities determined in this way as a function of the intensity at  $m/z$  47.5 ( $I_{47.5}$ ). The following functions were used in this work:

$$I_{44, \text{PBL}} = (42.5 \pm 3.6) 10^{-6} \cdot (I_{47.5})^2 - (17.8 \pm 1.3) 10^{-2} , \quad (\text{A.12})$$

$$I_{45, \text{PBL}} = (16.3 \pm 1.1) 10^{-6} \cdot (I_{47.5})^2 + (23.4 \pm 1.6) 10^{-4} \cdot I_{47.5} - (22.5 \pm 6.6) 10^{-3} , \quad (\text{A.13})$$

$$I_{46, \text{PBL}} = (32.0 \pm 8.3) 10^{-7} \cdot (I_{47.5})^2 + (74.8 \pm 1.9) 10^{-4} \cdot I_{47.5} + (30.0 \pm 1.7) 10^{-2} , \quad (\text{A.14})$$

$$I_{47, \text{PBL}} = (54.0 \pm 2.6) 10^{-5} \cdot (I_{47.5})^2 + (781.7 \pm 6.0) 10^{-3} \cdot I_{47.5} + (72.7 \pm 1.4) 10^{-1} , \quad (\text{A.15})$$

$$I_{48, \text{PBL}} = (32.9 \pm 1.5) 10^{-5} \cdot (I_{47.5})^2 + (690.7 \pm 3.4) 10^{-3} \cdot I_{47.5} + (41.8 \pm 1.9) 10^{-1} , \quad (\text{A.16})$$

$$I_{49, \text{PBL}} = -(3.9 \pm 3.7) 10^{-5} \cdot (I_{47.5})^2 + (936.3 \pm 7.1) 10^{-3} \cdot I_{47.5} + (116.6 \pm 3.4) 10^{-1} . \quad (\text{A.17})$$

Equations (A.12) to (A.16) were determined by a weighted mean of the factors obtained from six individual determinations of pressure baseline correction functions from April 12, 2024, to December 20, 2024. Equation (A.17) uses the pressure baseline correction from August 29, 2023. The combined functions of (A.12) to (A.17) are in the following referred to as the “final” pressure baseline correction.

This correction was applied by subtracting the values obtained from equations (A.12) to (A.17) from the measured intensities at  $m/z$  44–49, respectively. This was done after adding back the background noise values, which were initially subtracted by the mass spectrometer software. For  $m/z$  47–49 in particular, the background values were significantly negative and decreased further with higher intensity at  $m/z$  44 (lower  $m/z$  47.5). This phenomenon has been associated with secondary electrons scattered by the  $m/z$  44 ion beam [e.g. He et al., 2012; Fiebig et al., 2016].

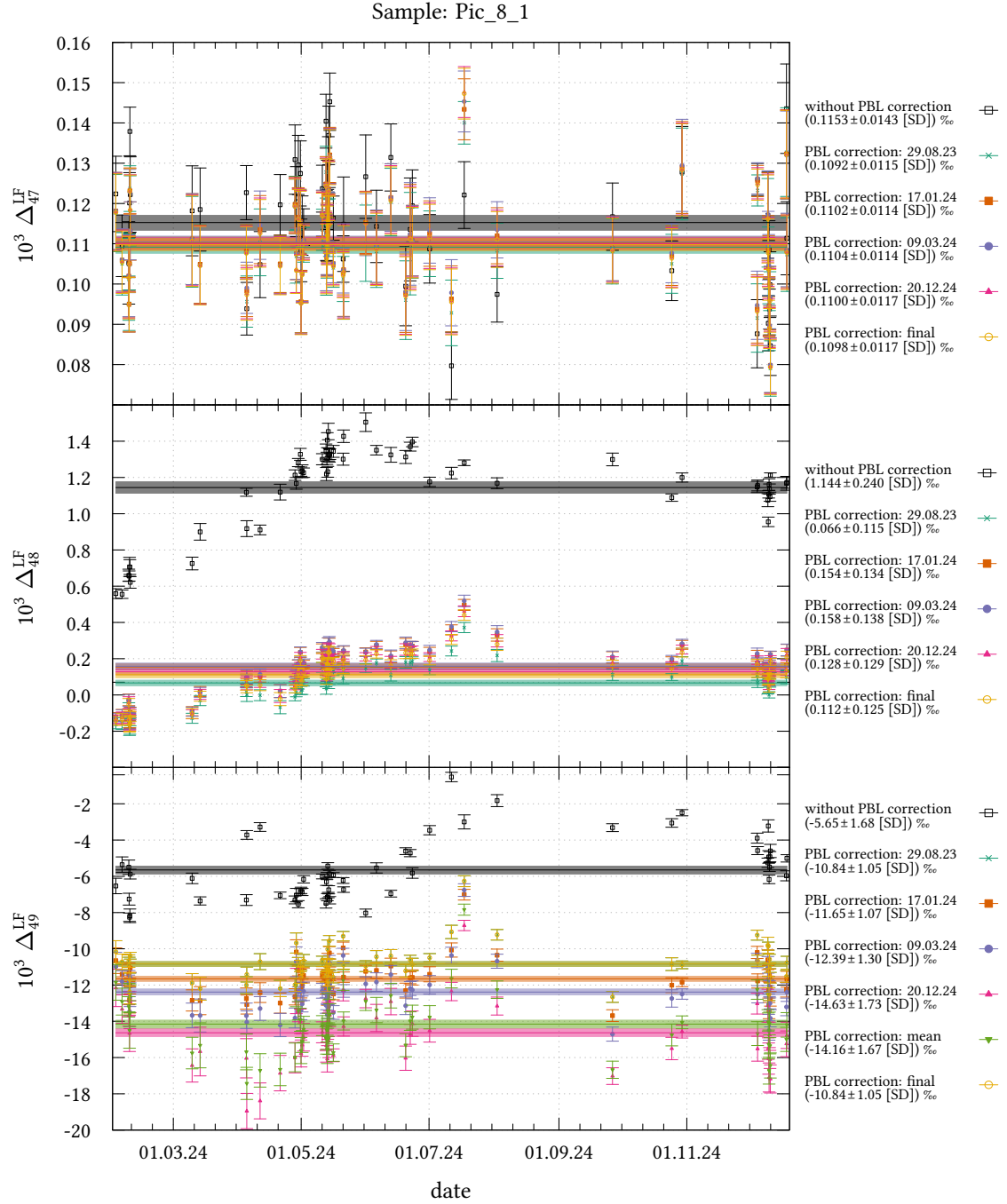
## Comparison of Background Corrections

Several studies have shown that the pressure baseline (PBL) correction improves reproducibility and reduces or eliminates the dependency of  $\Delta_{47}^{\text{LF}}$  on  $^{47}\delta$ ,  $\Delta_{48}^{\text{LF}}$  on  $^{48}\delta$ , and  $\Delta_{49}^{\text{LF}}$  on  $^{49}\delta$  [e.g. He et al., 2012; Bernasconi et al., 2013; Meckler et al., 2014; Fiebig et al., 2016; Fiebig et al., 2019; Bernecker et al., 2023]. The latter is further discussed in subsection 4.3.3.

Figure A.4 illustrates the effect that different determined background corrections have on the  $\Delta_{47}^{\text{LF}}$ ,  $\Delta_{48}^{\text{LF}}$ , and  $\Delta_{49}^{\text{LF}}$  measurement results of the “Pic\_8\_1” gas cylinder in 2024 (see SD in the legend). In addition to the “final” PBL correction, it shows four individual PBL corrections, which are indicated by their determination dates. It also shows the results “without PBL correction”, but with consideration of the background noise measurement. Additionally, it shows a “mean” PBL correction. This correction is identical to the “final” correction, except at m/z 49. There, the weighted mean of the six individual PBL corrections was employed, which were also considered at m/z 44–48.

As the standard deviations demonstrate, applying the PBL correction results in greater reproducibility in  $\Delta_{47}^{\text{LF}}$  and  $\Delta_{48}^{\text{LF}}$  than using a background noise measurement alone. The same is true for  $\Delta_{49}^{\text{LF}}$ , except for the PBL correction determined on December 20, 2024. There are only slight differences in reproducibility between the various PBL corrections applied to  $\Delta_{47}^{\text{LF}}$  and  $\Delta_{48}^{\text{LF}}$ . This was expected since the factors determined in these functions did not differ much. However, larger differences are observable for  $\Delta_{49}^{\text{LF}}$ . Surprisingly, the background correction for 2023 yields the greatest reproducibility. Therefore, its factors likely correspond more closely to those of the “correct” correction. This correction evens out the spring 2024 trend compared to the “mean” correction. However, the “correct” PBL correction was likely not determined for  $\Delta_{48}^{\text{LF}}$  and  $\Delta_{49}^{\text{LF}}$ . At least, it could not be determined in a way that clearly eliminates their dependency on  $^{48}\delta$  and  $^{49}\delta$ , respectively (cf. Figures C.3 (a) and C.4 (a); page 195f). According to Fiebig et al., 2019, negative slopes in the dependency of  $\Delta_{48}^{\text{LF}}$  on  $^{48}\delta$  indicate overestimation of the PBL correction. This was observed in  $\Delta_{47}^{\text{LF}}$  (Figure 4.6 (a); page 67),  $\Delta_{48}^{\text{LF}}$  (Figure C.3 (a); page 195), and  $\Delta_{49}^{\text{LF}}$  (Figure C.4 (a); page 196), so an overestimation is likely. Bernecker et al., 2023 proposed an alternative method involving the iterative adjustment of the linear factors in equations (A.15) to (A.17) to eliminate the dependence of  $\Delta_{48}^{\text{LF}}$  on  $^{47}\delta$ ,  $\Delta_{48}^{\text{LF}}$  on  $^{48}\delta$ , and  $\Delta_{49}^{\text{LF}}$  on  $^{49}\delta$ . This method could not be tested within the scope of this work.

Due to the clearly visible trends in  $\Delta_{48}^{\text{LF}}$  and  $\Delta_{49}^{\text{LF}}$  that could not be corrected during this work, they can only be used qualitatively. A better approach to determine the factors in the PBL correction should be investigated in the future, as it could address these trends and improve reproducibility. Since PBL correction affects trends and reproducibility, an alternative approach could be to optimize the factors iteratively in this regard.



**Figure A.4.:** The figure illustrates how different background corrections affect the reproducibility (using SD) of “Pic\_8\_1” gas cylinder measurements. “without PBL correction” refers to the standard background correction performed by the mass spectrometer software (subtracting background noise level). The background corrections marked with “mean” and “final” are based on PBL correction determined between 12.04.2024 and 20.12.2024, with “final” being used throughout this thesis and differing from “mean” only for  $m/z$  49, where parameters from the correction of 29.08.2023 are used. Significant differences in reproducibility and drift of  $\Delta_{49}^{LF}$ , but not  $\Delta_{47}^{LF}$  and  $\Delta_{48}^{LF}$ , are caused by the different determined PBL corrections. However, significant improvements in reproducibility were observed for  $\Delta_{47}^{LF}$  to  $\Delta_{49}^{LF}$  in the “final” correction compared to the “without PBL correction”.

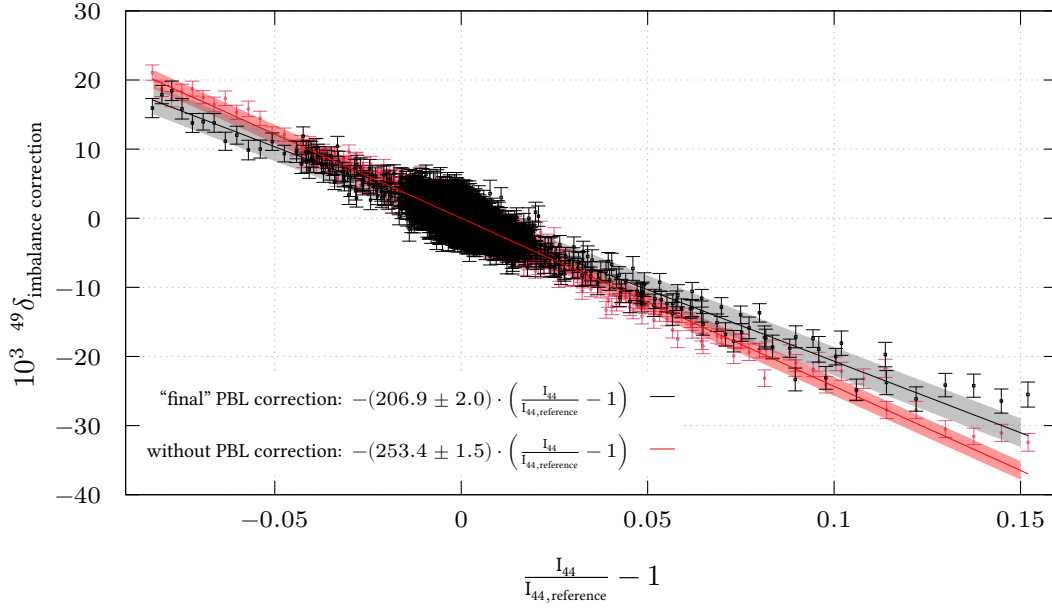
## A.5. Correction for Imbalance on m/z 44

A dependence on an imbalance at m/z 44 between the reference and the sample (hereafter referred just as “imbalance”) for data without pressure baseline (PBL) correction was found by *Fiebig et al.*, 2016 for  $\Delta_{47}$  and *Bernecker et al.*, 2023 for  $\Delta_{47}$  and  $\Delta_{48}$  (see appendix A.4 for details on the PBL correction). However, sufficient PBL correction was found to nearly eliminate this dependency, as well as the dependencies of  $\Delta_{47}$  on  $^{47}\delta$ ,  $\Delta_{48}$  on  $^{48}\delta$ , and  $\Delta_{49}$  on  $^{49}\delta$ . As discussed in appendix A.4, the PBL correction used in this work was probably insufficient for  $\Delta_{48}$  and  $\Delta_{49}$  (cf. Figures C.3 (a) and C.4 (a); page 195f). In comparison, the dependence of  $\Delta_{47}$  on  $^{47}\delta$  was found to be low with the applied PBL correction (cf. Figure 4.6 (a); page 67). For  $^{47}\delta$ , which largely dominates  $\Delta_{47}$ , only a negligible dependence was found in the PBL-corrected data in cases of extremely strong imbalances. Therefore, the effect of imbalance on  $^{47}\delta$  ( $\Delta_{47}$ ) is not discussed further in the following or corrected within this thesis.

The new measurement protocol involves long measurement times and fewer pressure adjustments, typically only one. Therefore, large imbalances can evolve when the sample and reference bellow do not contain the same amount of gas (same volume and pressure). Figure A.8 (a) shows an example of such an imbalance. Instead of investigating the imbalance dependency on the  $\delta^{13}\text{C}$ ,  $\delta^{18}\text{O}$ ,  $\Delta_{48}$ , and  $\Delta_{49}$  levels, it was examined on the  $^{45}\delta$ ,  $^{45}\delta$ ,  $^{48}\delta$ , and  $^{49}\delta$  levels. This is because it is assumed that an imbalance causes equations (2.32) through (2.36) not to exactly equal equations (2.37) through (2.41) (see page 26f for equations). For this analysis, 249 measurements from various samples taken between February 2 and November 25, 2024, were examined. The  $^{45}\delta$  to  $^{49}\delta$  from this set of measurements were normalized by subtracting the respective sample’s  $^{45}\delta$  to  $^{49}\delta$  values under the iterative adjustment of the correction functions discussed below (200 runs). This normalization process yielded 4,464 data points for all cycles of the different measurements considered for  $^{45}\delta$  to  $^{49}\delta$ , respectively. A dependency on the imbalance was found for  $^{45}\delta$ ,  $^{45}\delta$ ,  $^{48}\delta$ , and  $^{49}\delta$ . The imbalance is expressed as the relative deviation in intensity at m/z 44 between the sample ( $I_{44}$ ) and the reference ( $I_{44,\text{reference}}$ ):

$$\frac{I_{44}}{I_{44,\text{reference}}} - 1 .$$

Figure A.5 illustrates this for  $^{49}\delta$ . This graphic compares data with the “final” PBL correction to data without the PBL correction (background noise subtracted; see appendix A.4). As expected based on the observations by *Fiebig et al.*, 2016 and *Bernecker et al.*, 2023, the PBL correction reduces dependency on imbalance. However, contrary to their observations, significant dependency remains. This once again suggests that the



**Figure A.5.:** The graph shows the dependence of  $^{49}\delta$  on the relative imbalance between the intensity at m/z 44 for the sample and the reference. A comparison is made on the effects of using the “final” versus not using the pressure baseline (PBL) correction. See appendix A.4 for details on these corrections. As can be seen, the slope is affected by the choice of the background correction.

determined PBL correction was insufficient.

Another dependency on the absolute value of  $I_{44}$  was found for  $^{45}\delta$  and  $^{46}\delta$  when they are not equal to zero. This dependency was likely found to be present for the higher masses as well, but it was negligible and is therefore not considered here. This effect is expressed as the deviation of the signal mean value from the sample ( $I_{44}$ ) and reference ( $I_{44,\text{reference}}$ ) from a base value of 8000 mV, multiplied by  $^{45}\delta$  or  $^{46}\delta$ , respectively:

$$\left(8000 \text{ [mV]} - \frac{I_{44} + I_{44,\text{reference}}}{2}\right) \cdot 10^3 \delta^{45},$$

$$\left(8000 \text{ [mV]} - \frac{I_{44} + I_{44,\text{reference}}}{2}\right) \cdot 10^3 \delta^{46}.$$

The following correction functions were determined by fitting the iterative normalized data using a combination of Python and gnuplot along with the nonlinear least-squares Marquardt-Levenberg algorithm:

$$10^3 \delta_{\text{imbalance correction}}^{45} = -(72 \pm 3) 10^{-9} \text{ [mV}^{-1}] \cdot \left(8000 \text{ [mV]} - \frac{I_{44} + I_{44,\text{reference}}}{2}\right) \cdot 10^3 \delta^{45} + (252 \pm 4) 10^{-3} \cdot \left(\frac{I_{44}}{I_{44,\text{reference}}} - 1\right), \quad (\text{A.18})$$



$$10^3 {}^{46}\delta_{\text{imbalance correction}} = -(330 \pm 5) 10^{-9} [\text{mV}^{-1}] \cdot \left( 8000 [\text{mV}] - \frac{I_{44} + I_{44,\text{reference}}}{2} \right) \cdot 10^3 {}^{46}\delta \\ + (634 \pm 6) 10^{-3} \cdot \left( \frac{I_{44}}{I_{44,\text{reference}}} - 1 \right) \quad , \quad (\text{A.19})$$

$$10^3 {}^{48}\delta_{\text{imbalance correction}} = -(27 \pm 2) 10^{-1} \cdot \left( \frac{I_{44}}{I_{44,\text{reference}}} - 1 \right) \quad , \quad (\text{A.20})$$

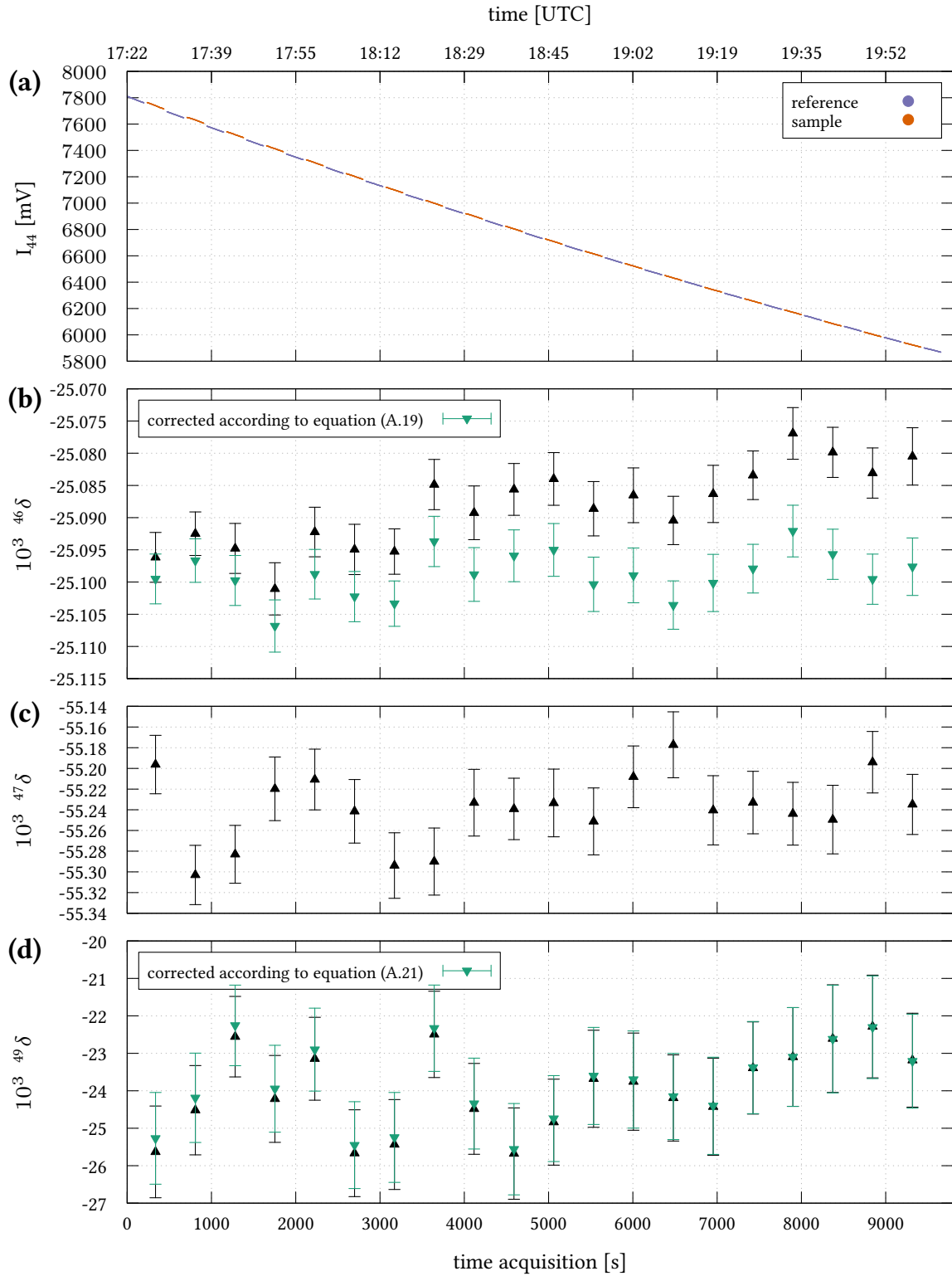
$$10^3 {}^{49}\delta_{\text{imbalance correction}} = -(207 \pm 2) \cdot \left( \frac{I_{44}}{I_{44,\text{reference}}} - 1 \right) \quad . \quad (\text{A.21})$$

These functions were applied by subtracting from  ${}^{45}\delta$ ,  ${}^{46}\delta$ ,  ${}^{48}\delta$ , and  ${}^{49}\delta$ , respectively. The corrected values were then used for further  $\delta^{13}\text{C}$ ,  $\delta^{18}\text{O}$ ,  $\Delta_{48}$ , and  $\Delta_{49}$  calculations, as described in subsection 2.5.6. This correction is included for data referred to in this work as being in the laboratory frame (LF). For the  $\Delta_{47}$  calculation, uncorrected  ${}^{47}\delta$ , along with uncorrected  ${}^{45}\delta$  and  ${}^{46}\delta$ , were used.

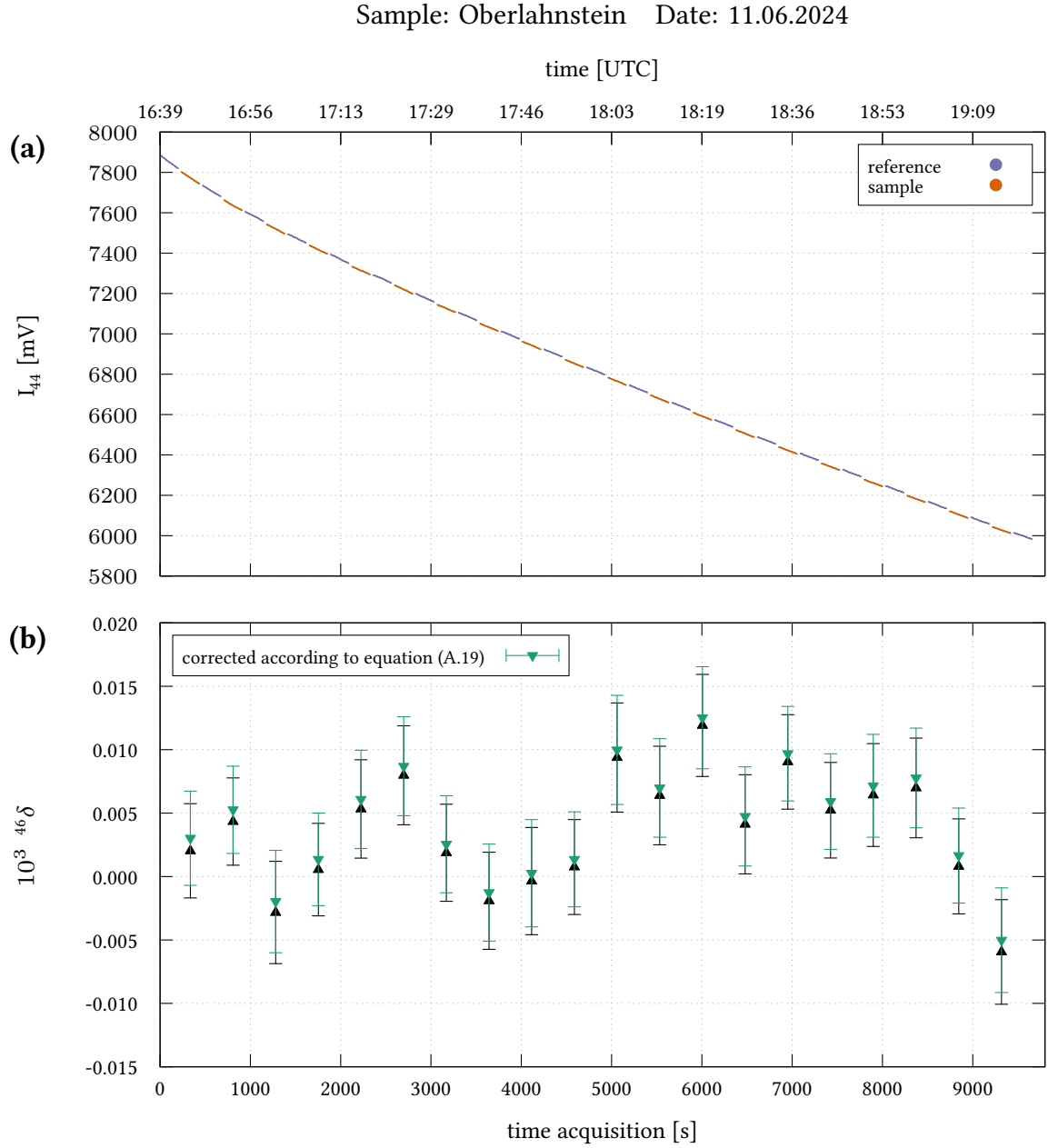
Figure A.6 shows a measurement with almost no imbalance. The effect, which depends on the absolute value of  $I_{44}$ , is visible in  ${}^{46}\delta$ . It also illustrates the correction according to Equation (A.19). In contrast, the ‘‘Oberlahnstein’’ measurement shown in Figure A.7 does not exhibit this effect on  ${}^{46}\delta$  because its value is nearly zero. Figure A.8 shows significant imbalance evolution, causing negative and positive drifts in  ${}^{46}\delta$  and  ${}^{49}\delta$ , respectively. It also shows the effect of the corresponding corrections equations (A.19) and (A.21), respectively.

Bernecker et al., 2023 identified the correct PBL correction factors by iteratively adjusting these factors to eliminate dependence of  $\Delta_{47}$  on  ${}^{47}\delta$ ,  $\Delta_{48}$  on  ${}^{48}\delta$ , and  $\Delta_{49}$  on  ${}^{49}\delta$ . Since a proper PBL correction seems to nearly eliminate dependence on imbalance [Fiebig et al., 2016; Bernecker et al., 2023], an alternative approach could be to adjust the PBL factors with respect to this goal. Whether this approach would work could not be tested within the scope of this work. However, one possible benefit is that a set of standards with the same equilibrium temperature but different  ${}^{47}\delta$ ,  ${}^{48}\delta$ , and  ${}^{49}\delta$  would not be necessary. Only measurements with significant imbalance evolution would be necessary. Additionally, this approach could determine the PBL correction factors for  $m/z$  45 and  $m/z$  46. It would also be interesting to investigate whether dependence on the absolute value of  $I_{44}$  disappears with a proper PBL correction. Though both were insignificant, analysis of the complete  ${}^{47}\delta$  dataset suggested that the impact on the absolute value of  $I_{44}$  was greater than the imbalance effect. This contrasts with observations for the other masses with poorer PBL corrections, for which the impact on the absolute value of  $I_{44}$  was smaller or negligible compared to the imbalance effect. This finding potentially suggests that this effect is of a different nature. An analysis with a proper PBL correction for all masses might provide more insight into this.

Sample: EG50\_LW Date: 01.06.2024

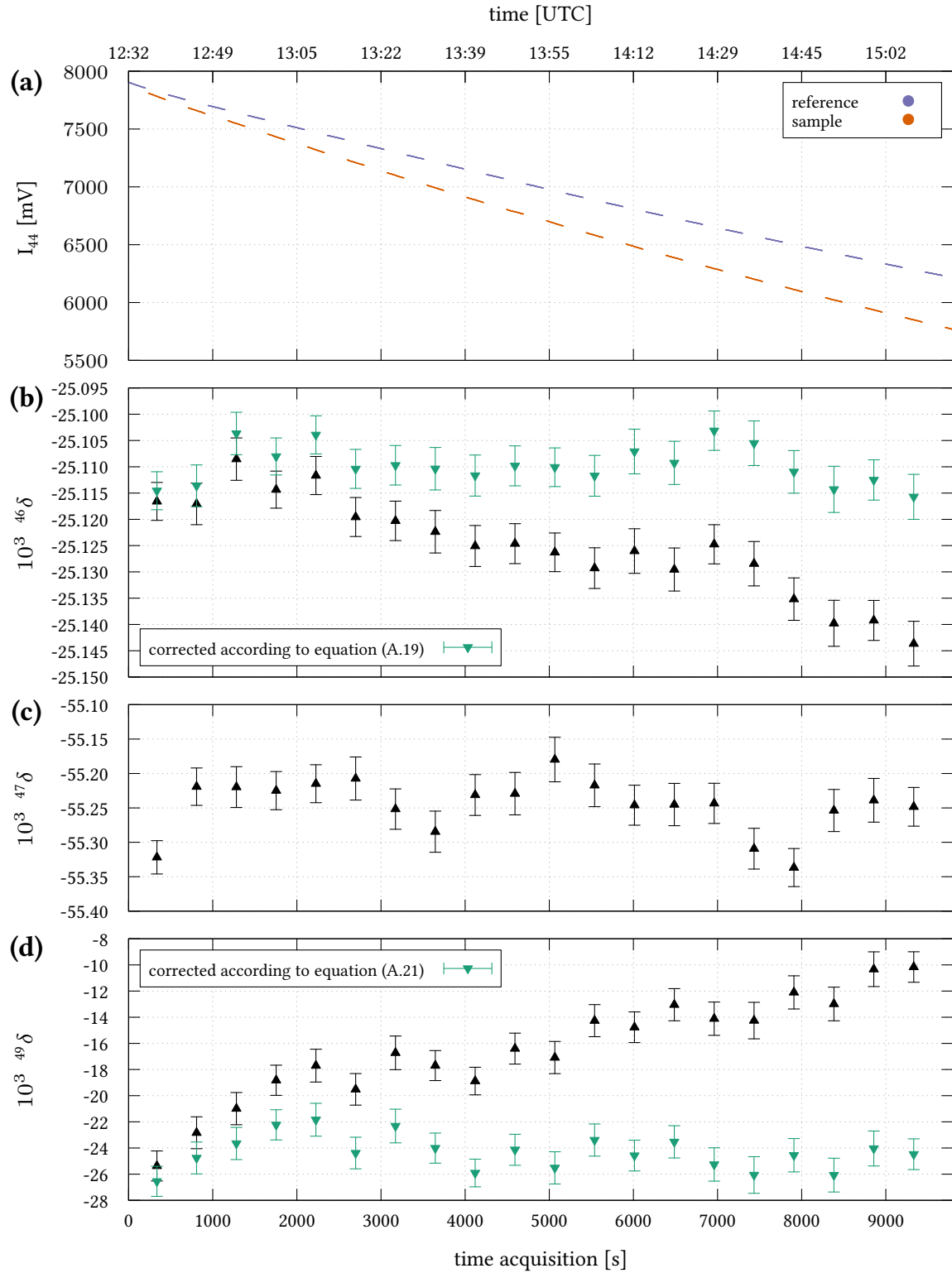


**Figure A.6.:** This is an example of a good measurement with almost no imbalance at  $m/z$  44 between the sample and the reference (a). However, a drift is still visible in  $^{46}\delta$  ( $\blacktriangle$ ) and is corrected by applying Equation (A.19) ( $\blacktriangledown$ ) (b). This drift is not caused by the imbalance, but rather by another effect dependent on the absolute value of  $I_{44}$  and  $^{46}\delta$ . This effect is not significantly observable for  $^{47}\delta$  (c) and  $^{49}\delta$  (d).



**Figure A.7.:** In this measurement, “Oberlahnstein” from a glass container is measured as a sample against the reference gas “Oberlahnstein”. This is a good measurement with almost no imbalance at  $m/z$  44 between the sample and the reference (a). Compared to Figure A.6, no observable drift is present for  $^{46}\delta$  (b). This is because the  $^{46}\delta$  value is close to zero, so the effect depending on the absolute  $I_{44}$  does not appear.


Sample: EG50\_LW Date: 24.06.2024



**Figure A.8.:** This is an example of a poor measurement, showing a significant imbalance at  $m/z$  44 between the sample and the reference. This was caused by refilling the reference bellow with approximately 20 % more gas than in the sample bellow. This imbalance results in a negative drift in  $^{46}\delta$  (b), no significant effect in  $^{47}\delta$  (c), and a positive drift in  $^{49}\delta$  (d). Equations (A.19) and (A.21) correct the drifts in  $^{46}\delta$  and  $^{49}\delta$  ( $\blacktriangleleft$ ), respectively. If the imbalance were reversed, the drifts would be inverted. The superimposed effect on the absolute value of  $I_{44}$  partially counteracts the observed  $^{46}\delta$  drift caused by the imbalance (cf. Figure A.6).

## B. Supplementary Material on Chapter 3

### B.1. Tubing & Connection Elements

Stainless steel tubes (electropolished or anodically cleaned, 1/4" external diameter, 0.035" wall thickness, Dockweiler, Neustadt-Glewe, Germany) were used for the construction. The tubings were cut, deburred, bent, and cleaned before assembly. Swagelok (Solon, Ohio, U.S.) products were used almost exclusively as connecting elements (clamping rings, T-pieces, reducers, etc.). In a few of these connections, 10  $\mu\text{m}$  screen filters (10SR2-10 & 10SR4-10; VICI, Schenkon, Switzerland) were inserted; these are marked with the symbol  in Figure 3.3. Each connection was tested for vacuum tightness by evacuating to  $\sim 10^{-3}$  mbar and monitoring pressure increase. Exemplary a close-up of a section of the Air Trap is shown in Figure B.1. This shows, among other things, the freezing fingers of the  $\text{H}_2\text{O}$  [D6-E7] and  $\text{CO}_2$  trap [C6-C7].



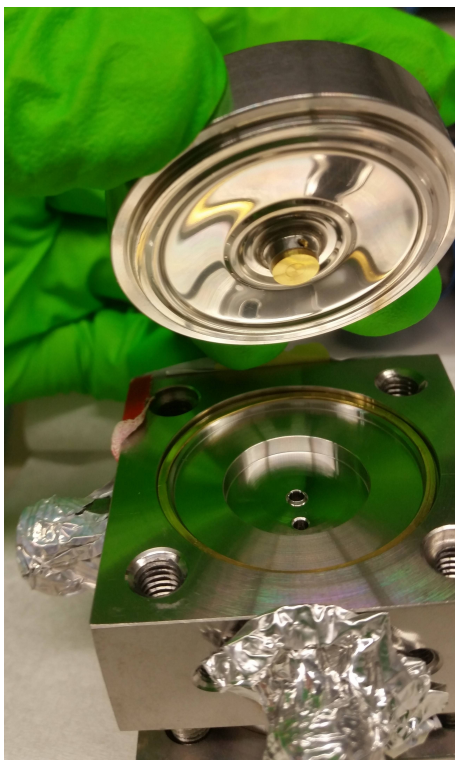
**Figure B.1.:** The picture shows a close-up example of the basic structure of the Air Trap, including some of the installed stainless steel tubes. In addition to the central pressure sensor RPT [C6], the freezing fingers of the “ $\text{CO}_2$  trap” [C6-C7] can be seen on the right and those of the “ $\text{H}_2\text{O}$  trap” [D6-E7] on the left.

## B.2. Pneumatically actuated Valves

The Air Trap is equipped with three types of pneumatically actuated valves. These valves are actuated by three-port solenoid valves (V100 series; SMC, Sotokanda, Chiyoda-ku, Tokyo, Japan), which are controlled directly by the IRMS electronics with the exception of ArdV 1 to 3.

The most commonly used valves are the pneumatically actuated diaphragm valves  $\bowtie$  (Figure B.2). These valves are normally open and seal via a gold stamp that is pressed onto a round sharp stainless steel edge. One of the 3-valve manifolds installed in the Air Trap comes from the original LSCE system. All others were removed from a IRMS MAT252 and the associated instruments (see Figure B.22 on page 180). These were cleaned using deionized water, ethanol, an ultrasonic bath and compressed air (see Figure B.23 on page 181). The gold stamps were either replaced or ground smooth by the IUP's precision engineering workshop.

The second type of used valves are bellows sealed valves with a PCTFE spindle tip (SS-4BK-1C; Swagelok, Solon, Ohio, U.S.; Figure B.3). These globe valves (AT SW1 [C8] & ArdV 3 [A3]) are normally closed and shown with the symbol  $\bowtie$  in Figure 3.3.

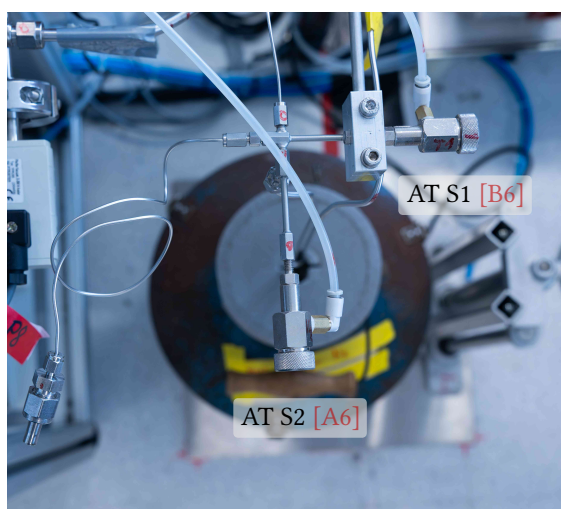


**Figure B.2.:** The picture shows an example of one of the many pneumatically actuated gold stamp diaphragm valves installed. These are shown in Figure 3.3 with the symbol  $\bowtie$ .



**Figure B.3.:** The picture shows valve AT SW1 [C8], one of the pneumatically operated globe valves installed. Valves of this type are shown in Figure 3.3 with the symbol  $\bowtie$ .



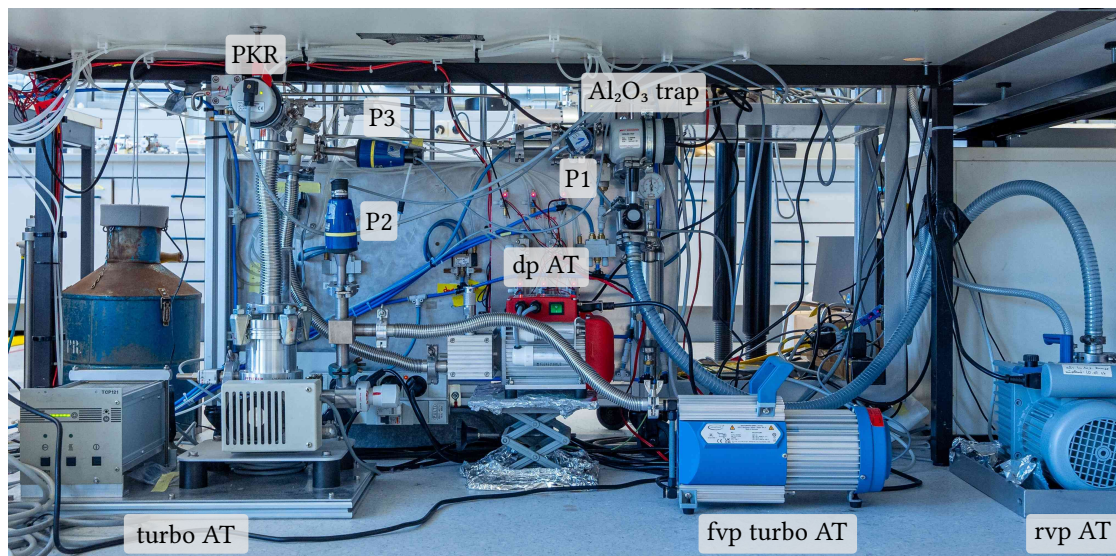


**Figure B.4.:** The valves shown are labeled with the symbol  $\bowtie$  in Figure 3.3. They are characterized by a very low dead volume. In addition, the lower valve block can be heated so that it can be placed in a GC oven, as is the case with AT S3 & AT S4 [B8]. However, the pneumatic control head must not exceed a temperature of 100°C [Trajan Scientific Australia Pty Ltd, 2017].

The third valve type (SGE Analytical Science, Victoria, Australia; now: MOVV valve, Trajan, Victoria, Australia) corresponds to the valves shown in Figure B.4 and are labeled with the symbol  $\bowtie$  in Figure 3.3 (page 32). The four valves used (AT S1 - AT S4) are installed on the inlet and outlet side of the GC. The valves are characterized by an extremely low dead volume and can withstand elevated temperatures. Therefore they were placed directly into the GC with their lower parts (see Figure B.24 b) on page 182). To prevent that the pneumatic control heads do not exceed a temperature of ~100°C [Trajan Scientific Australia Pty Ltd, 2017], a fan  $\ddagger$ <sup>7</sup> (612 JH; ebm-papst, St. Georgen, Germany) was fitted above the pneumatic control heads of AT S3 & AT S4 [B8] (see Figure 3.6 on page 37). The fan is controlled via a temperature switch (TSM 1000; H-TRONIC, Hirschau, Germany; see Figure B.8 a) on page 149). The temperature switch reads the temperature at the pneumatic control head of AT S3 via a PT1000 1/10DIN temperature sensor (otom, Bräunlingen, Germany; see Figure B.24 a) on page 182).

### B.3. Pumps

Figure B.5 shows the pumps used as part of the Air Trap. The diaphragm pump (dp AT) [F6] (MVP 015-2; Pfeiffer Vacuum, Asslar, Germany) is used to pump the H<sub>2</sub>O trap and to pump pressures of approximately  $> 10$  mbar. In the range between  $\sim 10$  mbar and  $\sim 10^{-2}$  mbar, the rotary vane pump (rvp AT) [E/F5] (RZ 6; vacuubrand, Wertheim, Germany) is used. An Al<sub>2</sub>O<sub>3</sub> trap (FL20K; Edwards, Burgess Hill, UK) is mounted above a manual butterfly valve in the suction area of this pump. This trap is intended to intercept possible backflowing oil vapors from the pump. The turbo molecular pump (turbo AT) [F5] (TMH 064 121; Pfeiffer Vacuum, Asslar, Germany) is used for further evacuation. With this pump pressures in the lower  $10^{-4}$  mbar range in the area of the CO<sub>2</sub> trap are reached. The fore vacuum pump (fvp turbo AT) [F6] (MD 1; vacuubrand, Wertheim, Germany) provides a backing vacuum for the turbo molecular pump (turbo AT) of  $\sim 1$  mbar.



**Figure B.5.:** The picture shows the Air Trap pumps. In the upper part of the picture, the Al<sub>2</sub>O<sub>3</sub> trap of the rotary vane pump can be seen directly above the butterfly valve. The pressure sensors P1, P2, P3, and PKR monitor the rotary vane pump (rvp AT), fore vacuum pump (fvp turbo AT), diaphragm pump (dp AT), and turbo molecular pump (turbo AT), respectively.



## B.4. Cold Traps

Figure B.6 shows the four cold traps of the Air Trap. Each trap has a pneumatic lifting platform on which Dewars are placed. The platforms were either from the LSCE system ( $\text{H}_2\text{O}$  and  $\text{CO}_2$  traps) or custom-built by IUP's precision mechanics workshop (GC and SB traps). The  $\text{H}_2\text{O}$ ,  $\text{CO}_2$ , and GC traps are all equipped with single-stage air cylinders (CD85E25-300-B; SMC, Sotokanda, Chiyoda-ku, Tokyo, Japan). However, the pneumatic control system of the GC trap enables the platform to stop at any position. The SB trap's lifting platform can be adjusted to 280 mm or 300 mm via a three-stage air cylinder (RZQL40TF-300-280; SMC). Both the  $\text{H}_2\text{O}$  and  $\text{CO}_2$  trap consist of two freezing fingers  $\ddagger^4$ , which are designed as described in *Werner et al., 2001*. These consist of an outer 0.25" stainless steel tube with an inner 0.125" stainless steel tube. The SB trap consists of a 1/8" single-side welded stainless steel tube  $\S^1$ , and the GC trap consists of a 1/8" U-tube. The  $\text{CO}_2$  and SB traps employ 3L Dewars filled with liquid nitrogen ( $-196^\circ\text{C}$ ), while the GC trap uses a larger 5L dewar. The  $\text{H}_2\text{O}$  Dewar is filled with a mixture of ethanol dry ice (approximately  $-72^\circ\text{C}$ ). Typically, all Dewars require refilling once daily during operation, although longer intervals may be possible without affecting performance.



**Figure B.6.:** The picture shows the four traps of the Air Trap. Dewars are placed on all four pneumatically operated platforms. The  $\text{H}_2\text{O}$  trap shown on the left contains a Dewar filled with ethanol dry ice ( $-72^\circ\text{C}$ ). The other three Dewars contain liquid  $\text{N}_2$  ( $-196^\circ\text{C}$ ).

### Application within Sample Preparation

**H<sub>2</sub>O trap:** This trap is used to catch H<sub>2</sub>O during the AT step. A Pt1000 temperature sensor (otom, Bräunlingen, Germany) was added to monitor the H<sub>2</sub>O trap's temperature during operation.

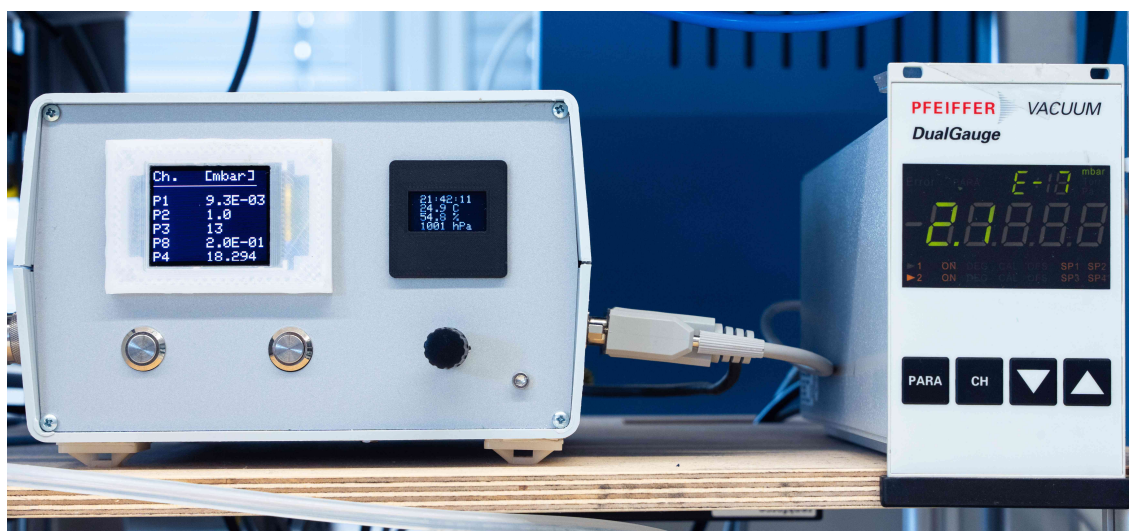
**CO<sub>2</sub> trap:** The CO<sub>2</sub> trap is used twice: first in the AT step to separate CO<sub>2</sub> from N<sub>2</sub>, O<sub>2</sub>, and Ar, and secondly after the GC step to collect the sample. A third freezing finger, located between valves AT 161 & AT 162 [C5], prevents vapors from freezing into the sample fingers when pumping with the rotary vane pump (rvp AT, [E,F5]). This design avoids the need for an oil-free pump or additional trap behind the pump.

**GC trap:** The trap is used at the beginning of the GC step to focus the sample. The platform stops in two positions: first, when the lowest point of the U-trap is immersed in liquid N<sub>2</sub> for cryogenic pumping from the CO<sub>2</sub> trap; and second, at the top position for removal of non-condensable gases after CO<sub>2</sub> freezing. The first position is determined by a pressure drop read by the RPT sensor [C6]. This procedure ensures that the CO<sub>2</sub> desublimates at approximately the same point regardless of the liquid nitrogen level in the Dewar.

**SB trap:** In the SB step, this trap is used to transfer the prepared sample into the sample bellow via cryogenic pumping. The two positions of the cold trap system are used to freeze and then safely pump out the non-condensed gases. This additional pumping step decreases the probability of O<sub>2</sub> and N<sub>2</sub> residues, which according to *Werner et al., 2001* would lead to the formation of NO<sub>2</sub> in the ion source and would affect the measurement of *m/z* 46 and higher.

## B.5. Multifunctional Device

Figure B.7 shows the custom-built so-called “Multifunction Device” on the left. The device is equipped with a microcontroller (MEGA 2560 REV3; Arduino, Monza, Italy) and can read out eight pressure sensors via two analog-digital converters (ADS1115; AZ-Delivery, Deggendorf, Germany). Additionally, the device features sensors that measure room pressure (LPS22; adafruit, New York City, U.S.), as well as room temperature and humidity (DHT 22; AZ-Delivery, Deggendorf, Germany). It is equipped with two RS232 interfaces (MIKROE-2864; MIKROE, Belgrade, Serbia), of which one is used for communication with the spectrometer’s computer. Furthermore it controls a module with eight relays (TC-9072496; TRU COMPONENTS, Chicago, Illinois, U.S.) . Three of these relays are used to control the valves ArdV 1 to 3. The remaining relays are utilized for safety-related functions. With one of these, the device is able to lower the lifting platform of the cold traps autonomously. A detailed description of the security features can be found in appendix B.13 (page 157).



**Figure B.7.:** The custom-built, Multifunctional Device is on the left side of the image. It is used, among other things, to read the pressure sensors P1, P2, P3 and P8. Furthermore, it initiates safety steps, for example, if the connection to the IRMS computer stops. On the right side of the picture, the control device (TPG 262; Pfeiffer Vacuum, Asslar, Germany) for the pressure sensors PKR and TPR is shown.

## B.6. Pressure Sensors

### P1, P2, P3 & P8

The pressure sensors P1 [D5/6], P2 [F6], P3 [E/F6] and P8 [B4] are connected to the Multifunction Device (see page 147). The sensors P1, P2 and P3 (TR 201 A; Leybold, Köln, Germany) monitor the pressure of the rotary vane pump (rvp AT), fore vacuum pump (fvp turbo AT) and diaphragm pump (dp AT), respectively. P8 (TPR 265; Pfeiffer Vacuum, Asslar, Germany) is used to monitor the vacuum in the area between the different pumps and is used to control the switching between them.

### PKR & TPR

The PKR (PKR 251; Pfeiffer Vacuum, Asslar, Germany) [F4] and TPR (TPR 280; Pfeiffer Vacuum, Asslar, Germany) [A5] pressure sensors are connected to the control device (TPG 262; Pfeiffer Vacuum, Asslar, Germany; see Figure B.7 on page 147) which communicates with the spectrometer's computer. The PKR sensor is used to monitor the generated vacuum of the turbo molecular pump (turbo AT). The TPR sensor measures the vacuum in the GC trap and the adjacent connecting tubes during preparation.

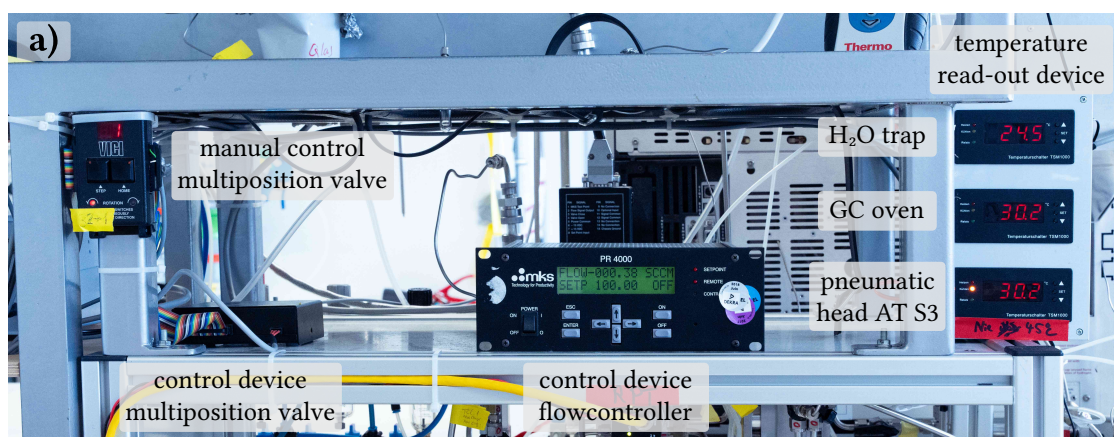
### RPT

The RPT pressure sensor (RPT 200 AR; Pfeiffer Vacuum, Asslar, Germany) is used to monitor pressure in the CO<sub>2</sub> trap. It is equipped with a pirani sensor that can measure down to approximately  $\sim 10^{-4}$  mbar, as well as a piezoresistive sensor that can measure gas type independently from approximately 1 mbar [Pfeiffer Vacuum GmbH, 2024]. The sensor communicates directly with the spectrometer's computer via RS485.



## B.7. Mass Flow Controller

At the AT step, a mass flow controller 1179A  $\dagger^6$  [E7] set by the PR4000 control unit to 100 mL/min ensures a constant flow of ambient air enters the system (both: MKS, Andover, Massachusetts; see Figure B.8). A needle valve  $\dagger^2$  [B5], located between the CO<sub>2</sub> trap and the pumps, restricts the flow over the H<sub>2</sub>O and CO<sub>2</sub> traps (see Figure B.12 on page 153 for an image). This valve is adjusted to maintain a constant pressure of approximately 100 mbar in the CO<sub>2</sub> trap during the AT step. This increases the residence time of the air in the traps and raises the partial pressures. However, the pressure generated in the traps must not become too high to avoid freezing significant amounts of O<sub>2</sub> and Ar. According to *Werner et al., 2001*, a pressure of less than 500 mbar prevents these gases from being frozen to any significant extent.

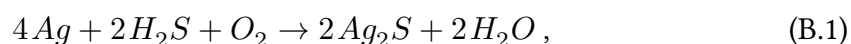


**Figure B.8.:** a): On the right side of the image, there is a housing with three temperature switches. From top to bottom, these show the temperatures of the H<sub>2</sub>O trap, the GC oven, and the pneumatic head at AT S3 [B8]. The bottom one controls the fan that cools the pneumatic head. On the left side, the control unit and a manual control device of the multiposition valve  $\dagger^9$  are shown. In the center, there is the control unit of the mass flow controller  $\dagger^6$  [E7] shown in picture b). In addition, picture b) shows the silver wool trap  $\dagger^5$  [E6].



## B.8. Silver Wool Trap

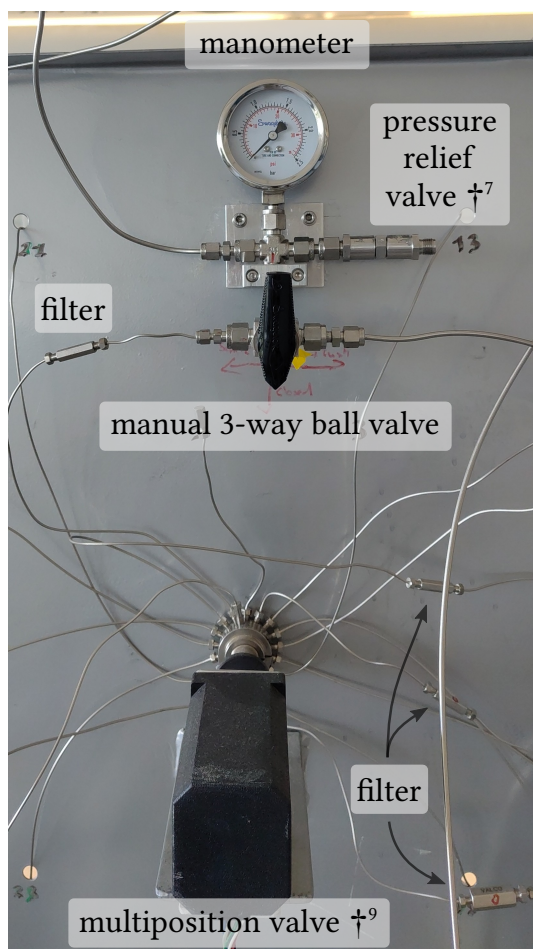
The so-called silver wool trap †<sup>5</sup> [E6] is installed between the mass flow controller and the H<sub>2</sub>O trap (see Figure B.8 b) on page 149). It consists of a cylindrical glass tube (length: ~51 mm) and is integrated into the system via Ultra-Torr fittings. The trap is filled with about 1150 mg silver wool and is used to remove elemental S [Eagle et al., 2010] and H<sub>2</sub>S from the atmospheric samples. In other laboratories such a trap is usually installed in the immediate vicinity of a GC column or Porapak<sup>TM</sup> Q trap [e.g. Davies et al., 2017]. However, unlike these systems, which are largely designed to process carbonates, this system is designed to process air samples, which means that O<sub>2</sub> is present in the initial sample. Due to the reaction:



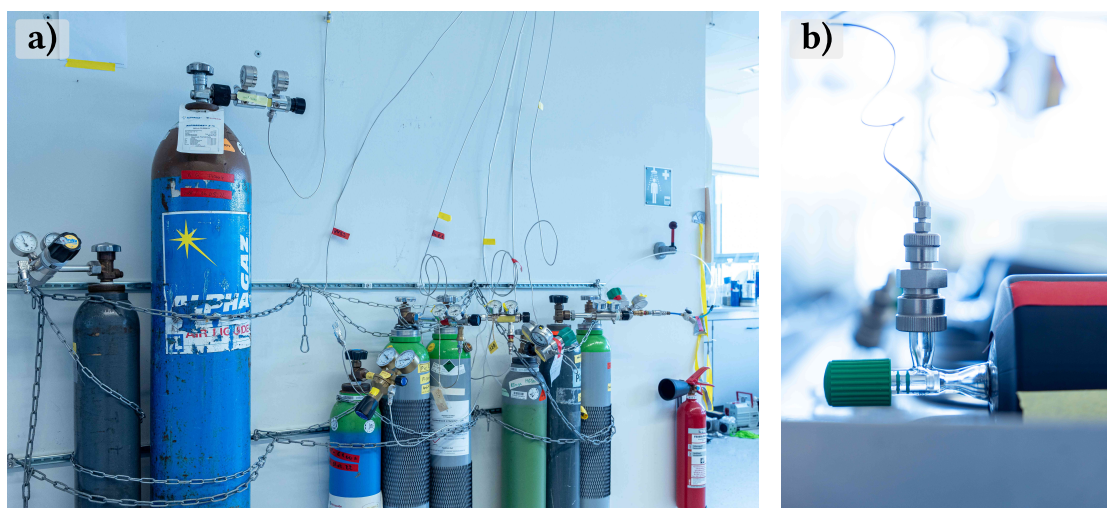
it was placed in front of the H<sub>2</sub>O trap where O<sub>2</sub> is present. Additionally, placing the trap in front of the GC would likely cause turbulence, increase the dead volume, and therefore reduce the GC's resolution.

## B.9. Multiposition Valve, Gas Cylinders & Ambient Air Access

A multiposition valve †<sup>9</sup> (VICI, Schenkon, Switzerland; see Figure B.10) is used for automatic sampling of Heidelberg ambient air, gas cylinders, or flask samples using Ultra-Torr fittings (Swagelok, Solon, Ohio, U.S.; see Figure B.11 b)). Half of the 32 ports are blindly closed, so that only the odd-numbered 16 ports are available for measurements. Port 1 is closed and serves as the so called “Home position”. It is accessed when in idle or in a safety situation (see appendix B.13 on page 157). Two pressurized gas cylinders “Pic\_8\_1” and “D484276” are connected to ports 3 and 17 (see Figure B.11 a); Table B.1 (page 155)). All ports are protected by filters (VICI, Schenkon, Switzerland). Port 31 provides access to the Heidelberg ambient air sampled at the roof of the IUP ‡<sup>12</sup> (see section 2.4 on page 19). A pressure relief valve †<sup>7</sup> is adjusted to allow an inlet pressure of up to ~1 bar (see Figure B.10).



**Figure B.10.:** The components shown here can be found in Figure 3.3 in area [D7-E8]. The 32 port multiposition valve †<sup>9</sup> can be seen in the lower part of the picture. It is used for automatic sampling of Heidelberg ambient air, gas cylinders, or flask samples. The 1/8" tube that carries ambient air from the roof of the IUP to port 31 is visible in the upper left corner of the image. The pressure at this port can be read with the manometer and is adjusted with the pressure relief valve †<sup>7</sup>. This valve was set to allow an overpressure of about 1 bar. The manual 3-way valve can be used to flush the tube or for manual access to the ambient air.

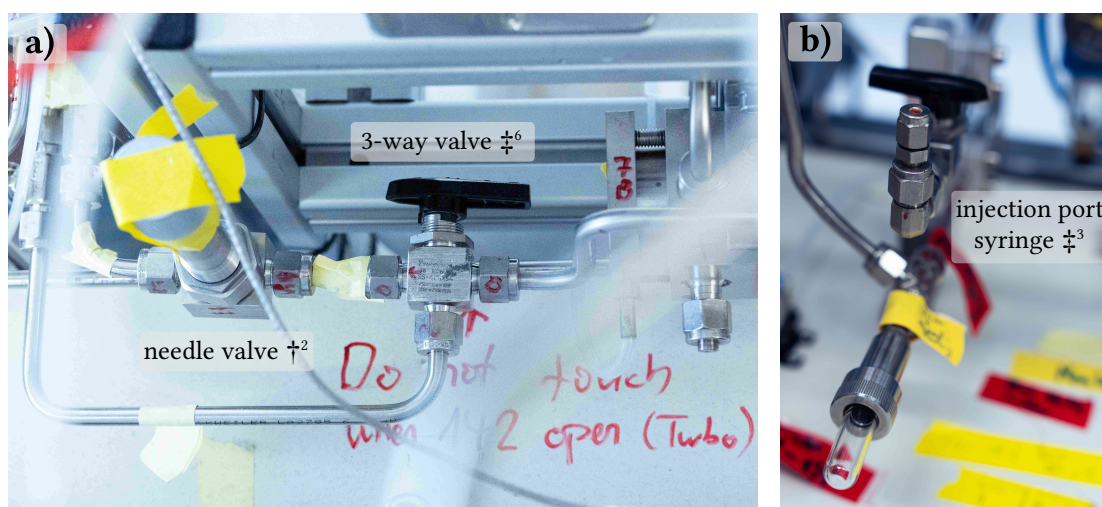


**Figure B.11.:** In a) the gas cylinder holder constructed together with the gas cylinders used can be seen. This holder is positioned opposite the rear of the Air Trap (see Figure 3.2 b). The 1/8" tubes are routed to the Air Trap's multiposition valve via the ceiling. b) shows the connection of a flask via a Ultra-Torr fitting.



## B.10. Injection via Syringe & External Access to Pump Unit

Figure B.12 b) shows an injection port  $\ddagger^3$  [A4] to inject gases via a syringe. In order to gain access to the processing line using this port, it is necessary to switch the 3-way valve  $\ddagger^6$  [B5] depicted in Figure B.12 a). A tube, situated beneath the injection port (see Figure B.12 b)) allows manual access to the Air Trap's pump unit  $\dagger^3$  by switching valve MV 143 [E5] via a finger valve (VHK3A-04F-04F; SMC, Sotokanda, Chiyoda-ku, Tokyo, Japan). Additionally, valves AT 141, AT 142, and AT 162 can be manually actuated using finger valves to control the pumps. For example, using the Ultra-Torr fitting seen in Figure B.12 b), flasks can be evacuated. The tube extending upwards in this image is connected to the manual preparation line used for preparing equilibrated CO<sub>2</sub> standards, which is discussed in section 4.3 (see Figure C.2 on page 193 for an image).

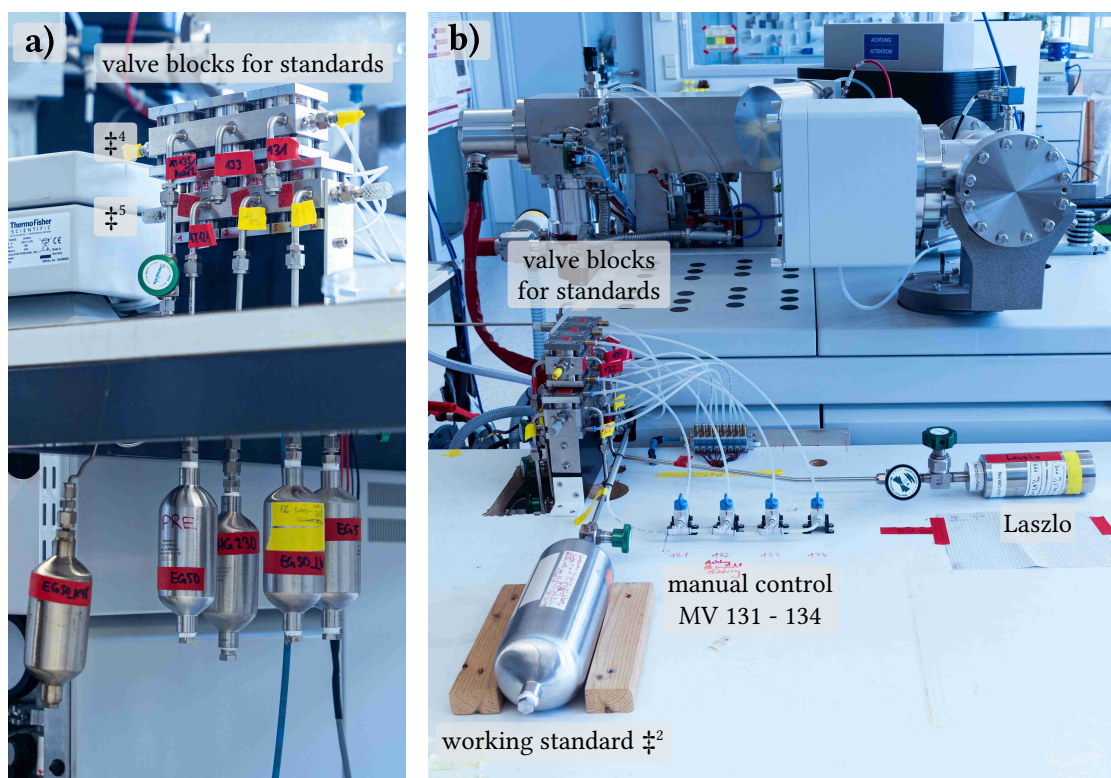


**Figure B.12.:** In a), the needle valve  $\dagger^2$  [B5] is visible and has been adjusted to maintain a pressure of approximately 100 mbar in the CO<sub>2</sub> trap during the AT step. The upper part of b) shows the inlet used for sample injection via a syringe  $\ddagger^3$  [A4]. The lower portion of the figure depicts the access for the manual line (upward-pointing line) and an Ultra-Torr fitting, which can be employed, for instance, to evacuate flasks. To utilize the access via the syringe, the 3-way valve  $\ddagger^6$  [B5] depicted in a) must be switched.

## B.11. Valve Blocks for Standards

To enable the automatic and regular measurement of CO<sub>2</sub> standards, two 6-port valve blocks ( $\ddagger^4$  [B-C4] and  $\ddagger^5$  [D-E4]) were attached to the Air Trap (see Figure B.13). 150 ml stainless steel vessels (FITOK, Offenbach am Main, Germany) containing temperature-equilibrated CO<sub>2</sub> standards were connected (see Table B.1 (page 155) for assignment). To facilitate multiple measurements of these standards, the volume within the blocks is used as an intermediate volume for splitting. To reduce these volumes a 1/16" stainless steel tube was positioned within the inner connection of each valve block. Valves MV 131 to 134 are operated manually via the finger valves shown in Figure B.13 b).

Additionally, a one-liter sample container (4L-SC18-DN4-1000-F2, SS 304L; FITOK, Offenbach am Main, Germany) containing the working standard “Oberlahnstein”  $\ddagger^2$  [F2-3] was connected to valve AT 31 for automatic refilling of the reference bellows (see Figure B.13 b)).



**Figure B.13.:** The valve blocks  $\ddagger^4$  [B-C4] and  $\ddagger^5$  [D-E4] are illustrated in the images. Figure a) shows pure CO<sub>2</sub> standards in 150 ml stainless steel vessels connected to these. Figure b) additionally shows the CO<sub>2</sub> standard “Laszlo” [F4] and finger valves to actuate MV 131 to 134. Moreover, the image shows a one-liter stainless steel vessel filled with the working standard “Oberlahnstein”  $\ddagger^2$  [F2-3], which is connected to valve AT 31 for automatic refilling of the reference bellows.

## B. Supplementary Material on Chapter 3

**Table B.1.:** This table lists the standards that were used for this work. The temperature-equilibrated standards were produced as described in section 4.3. “Pic\_8\_1” is a gas cylinder of Heidelberg ambient air filled with a compressor. “D484276” is a gas cylinder containing CO<sub>2</sub> in natural air purchased from Deuste Gas Solutions GmbH (Schömborg, Germany).  $\delta^{18}\text{O}$  values are uncalibrated.  $\Delta_{47}$  values are calibrated.

name	valve	$10^3 \delta^{13}\text{C}$	$10^3 \delta^{18}\text{O}$	$T_{\text{equilibrium}} [^\circ\text{C}]$	$10^3 \Delta_{47}$
<b>Temperature-Equilibrated Standards</b> Periods considered: $\delta^{13}\text{C}$ 2024   $\delta^{18}\text{O}$ 01.06.2024 - 31.12.2024 <i>connected to valve blocks <math>\ddagger^4</math> &amp; <math>\ddagger^5</math> with the exception of EG50_LW, here for both <math>\delta^{13}\text{C}</math> &amp; <math>\delta^{18}\text{O}</math> only until 15.12.2024</i>					
EG5	AT 126	n = 18 -4.6564 SD: $\pm 0.0040$ SEM: $\pm 0.0010$	n = 8 -4.899 SD: $\pm 0.008$ SEM: $\pm 0.003$	4.6 $\pm 0.2$	1.041 <sup>[1]</sup> $\pm 0.002$
		n = 12 -4.787 SD: $\pm 0.006$ SEM: $\pm 0.002$	n = 7 -13.148 SD: $\pm 0.011$ SEM: $\pm 0.004$	49.8 $\pm 0.3$	0.805 <sup>[1]</sup> $\pm 0.002$
		n = 11 -35.234 SD: $\pm 0.005$ SEM: $\pm 0.002$	n = 6 -13.543 SD: $\pm 0.012$ SEM: $\pm 0.005$	49.8 $\pm 0.3$	0.805 <sup>[1]</sup> $\pm 0.002$
EG50	AT 121	n = 13 -35.8124 SD: $\pm 0.0035$ SEM: $\pm 0.0010$	n = 7 -34.621 SD: $\pm 0.011$ SEM: $\pm 0.005$	49.8 $\pm 0.3$	0.805 <sup>[1]</sup> $\pm 0.002$
		n = 21 -4.7147 SD: $\pm 0.0040$ SEM: $\pm 0.0009$	n = 10 -9.379 SD: $\pm 0.009$ SEM: $\pm 0.003$	233.8 $\pm 3.0$	0.331 <sup>[1]</sup> $\pm 0.005$
EG50_N48	ArdV 2				
EG50_LW	AT 125				
HG230	AT 123				
[1] calculated from $T_{\text{equilibrium}}$					
<b>30 L gas cylinders</b> Periods considered: $\Delta_{47}$ 01.02.2024-01.11.2024 <i>connected to multiposition valve</i>					
Pic_8_1	port 3	Jena <sup>[3]</sup>			
ambient air		-10.334 $\pm 0.009$	-2.476 $\pm 0.011$	15.9 <sup>[6]</sup> SD: $\pm 1.8$ SEM: $\pm 0.4$	n = 45 0.974 SD: $\pm 0.010$ SEM: $\pm 0.002$
filled on 09.02.2017 <sup>[2]</sup>		Heidelberg			
CO <sub>2</sub> : (419.012 $\pm$ 0.006) ppm N <sub>2</sub> O: (320.98 $\pm$ 0.06) ppb $\delta^{13}\text{C}$ , $\delta^{18}\text{O}$ & $\Delta_{47}$ are N <sub>2</sub> O corrected		-10.321 <sup>[4]</sup> $\pm 0.003$	-2.375 <sup>[4]</sup> $\pm 0.008$		
D484276	port 17	Jena <sup>[3]</sup>			
CO <sub>2</sub> in natural air		-3.320 $\pm 0.006$	-14.341 $\pm 0.012$	21.0 <sup>[6]</sup> SD: $\pm 2.3$ SEM: $\pm 0.8$	n = 12 0.946 SD: $\pm 0.012$ SEM: $\pm 0.004$
CO <sub>2</sub> : (601.39 $\pm$ 0.03) ppm		Heidelberg			
		-3.318 <sup>[5]</sup> SD: $\pm 0.005$ SEM: $\pm 0.001$	-14.305 <sup>[5]</sup> SD: $\pm 0.010$ SEM: $\pm 0.002$		
[2] average daily temperature was (1.5 $\pm$ 1.0) $^\circ\text{C}$ [3] measured by MPI-BGC Jena in winter 2024/2025 [4] from fit, see section 4.2 [5] Period: 01.01.2024 - 31.12.2024 (n = 25) [6] calculated from $\Delta_{47}$					
<b>working standard</b> $\Delta_{47}$ measured for Oberlahnstein in glass container <i>filled from gas cylinder on 09.07.2020</i>					
Oberlahnstein	AT 31				
filled from gas cylinder on 10.03.2023 to 1.5 bar (absolute)		-4.42 <sup>[7]</sup>	-9.79 <sup>[7]</sup>	20.8 <sup>[8]</sup> SD: $\pm 2.0$ SEM: $\pm 1.5$	n = 2 <sup>[9]</sup> 0.947 SD: $\pm 0.011$ SEM: $\pm 0.008$
[7] $\delta^{13}\text{C}$ & $\delta^{18}\text{O}$ are defined working standard [8] calculated from $\Delta_{47}$ [9] 01.03.2024-01.07.2024					

## **B.12. Programming**

The automated preparation line is primarily controlled using the mass spectrometer's control software, "Isodat", and its "Isodat Script Language" (ISL) (see Figure B.25 for an image of the mass spectrometer's computer; page 183).

Most valves and lifting platforms are controlled directly from the 24 V outputs of the MAT253+ (see appendix B.5 for exceptions). One Python script controls the gas chromatograph (GC), and three others communicate with the RPT pressure sensor, the TPG (PKR and TPR pressure sensors), and the Multifunctional Device, respectively. These scripts run continuously and store data, such as pressure values or GC parameters, in ".csv" files. Communication between Isodat and these scripts uses virtual serial ports on the mass spectrometer's computer. An additional Python script, which is started by Isodat on demand, operates the multiposition valve.

Many ISL scripts and libraries have been written, including a library for automatic reference refill or acquisition. The code for the preparation line is written in multiple scripts. For instance, there is one script for the AT step and another for the GC step. This makes it easy to omit or add steps, depending on the preparation (cf. Figure 3.1 for the different steps; page 30).

Parallel measurement and preparation could not be finalized within the scope of this work. However, most of the code was written to enable this. Therefore, the final implementation should not require much effort. One of the biggest problems is Isodat's poor multitasking implementation, which can lead to unforeseen errors. Additionally, printing user information from scripts running in parallel could result in unintended scenarios. The safest approach is to run different scripts in separate Isodat programs. One script for acquisition could run in "Isodat Acquisition", as is currently done. A second script for preparation could run in "Isodat Instrument Control".

## **B.13. Security Features and Error Handling**

Several safety functions have been implemented in order to address specific cases of undesired or unanticipated system states. These system states include, but are not limited to:

- stopping of the ISL script due to a programming error,
- GC errors, e.g. shutdown due to leakage,
- recurring communication errors between devices,
- reading pressures outside a predefined range, e.g.
  - freezing in the AT step (pressure must not be < 75 mbar and not > 115 mbar),
  - if predefined vacuum conditions are not reached after certain times,
  - if pressures are too high during an initial test of the pumps.

In all these cases and more, the running ISL script attempts to establish an orderly and safe state. This process involves closing specific valves, lowering the trap's lifting platforms, switching the multiposition valve to the home position, and sending an SMS containing the word "Error" to the user via the Multifunctional Device, which sends a signal to a "CM2100" device (Mobeye, 's-Hertogenbosch, Netherlands).

In the event of a complete failure of the mass spectrometer's computer, Isodat program, or ISL script, the Multifunctional Device will initiate a safe system state. To this end, the device monitors communication with the mass spectrometer's computer and the status of the software. If communication is lost for more than 30 minutes, the device will initiate the following steps:

1. the multiposition valve is switched to the home position,
2. the lifting platforms of the traps are lowered,
3. the message "Fatal error" is sent to the user by SMS.

The 30-minute delay is intended to allow the potentially still running ISL script to establish an orderly safety condition in the event of a loss of contact with the Multifunctional Device. This is because the Multifunctional Device cannot close most valves, and it is sometimes better to close the valves before lowering the trap's lifting platforms (e.g., if there is a connection to the turbo AT in the event of frozen CO<sub>2</sub> in a trap).

**Power Failure:** The system should be able to withstand a complete loss of power. In this case, all valves will close and the lifting platforms for the traps will lower. Additionally, the user will receive an SMS indicating that power or compressed air has failed. Unforeseen problems may be caused by a partial power failure that only affects certain devices,

## *Appendices*

such as the GC or Multifunctional Device. In this case, however, if an preparation is running, the script should detect this after some time and cause an orderly shutdown of the preparation. Major problems are especially likely to occur if this happens in the GC step. Note that if the mass spectrometer's computer crashes or shuts down while the IRMS is still powered on, the valves will remain in their last position. The user will then receive an SMS message indicating a "Fatal Error".

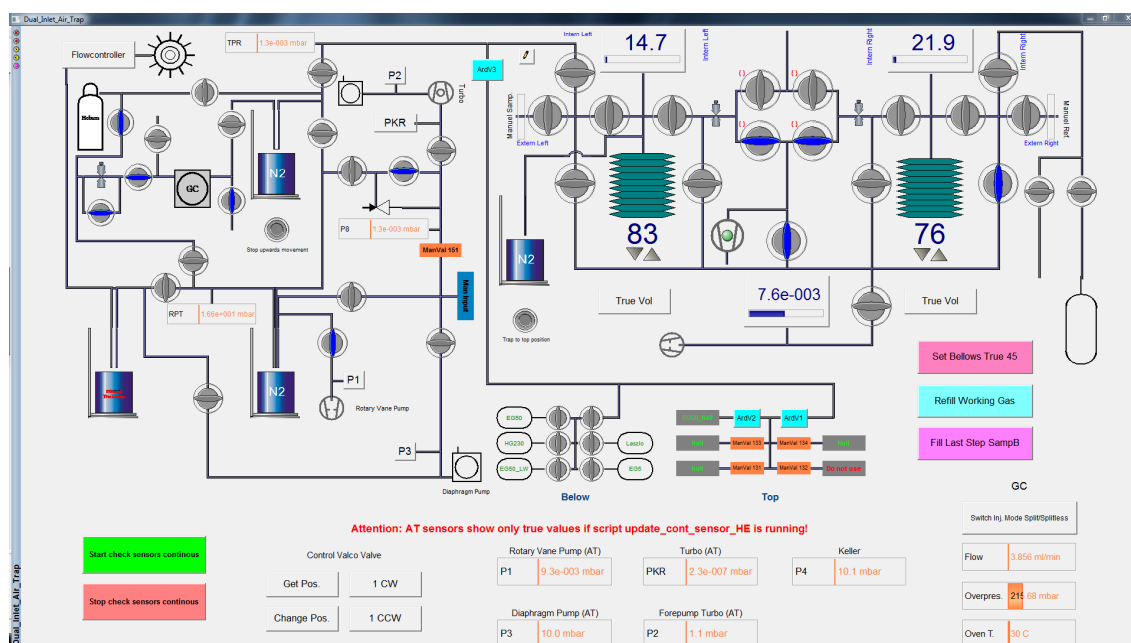
**Failure of Compressed Air Supply:** The biggest problem occurs when the compressed air supply fails because most of the valves are normally open. A buffer volume and a check valve that closes the connection to the house's pressure supply can temporarily compensate for a short-term pressure drop. However, since the system is not completely airtight, the normally open valves will eventually open, even when the pneumatics are not in use. The worst-case scenario is that, in the absence of a simultaneous power failure, over-pressurized He from the GC system could enter the vacuum system toward the pumps. A bypass system connected to an external gas cylinder was planned but could not be finalized during this work. It is also recommended that critical connections, such as those to the pumps and GC, be equipped with normally closed valves in the future. Nevertheless, the user will receive an SMS indicating a power or compressed air supply failure.

## B.14. Operation

### Graphical User Interface

The automatic preparation line was integrated into the previous graphical user interface (GUI), which included the Dual Inlet system. Figure B.14 shows the final implementation, and Figure B.27 (page 186) shows the original. The GUI provides an overview of all valves, lift platforms, pressure sensors, and GC parameters, such as flow, temperature, and pressure. It enables manual control of individual valves and raising or lowering of lift platforms via mouse interaction. However, there are no safeguards to prevent the direct connection of pumps or the introduction of over-pressurized He into the vacuum system during manual switching.

**Buttons:** In addition, individual buttons can be used to start specific scripts. The readout and thus the display of the sensors can be started with the button “Start check sensors continuous” and stopped with the button “Stop check sensors continuous”. After starting the readout, the sensor values are updated approximately every 1.5 seconds. Caution: The values otherwise displayed are the last read values. In the case of an preparation, this script is paused to avoid generating simultaneous queries. The updating of sensor values should not be started manually while the preparation is running. The multiposition valve can



**Figure B.14.:** Graphical user interface (GUI) which displays the elements of the automatic preparation line alongside those of the original GUI for the Dual Inlet system. The GUI enables manual control of the preparation line’s valves and lift platforms. It can also display current sensor values. Additionally, certain ISL scripts can be initiated via buttons.

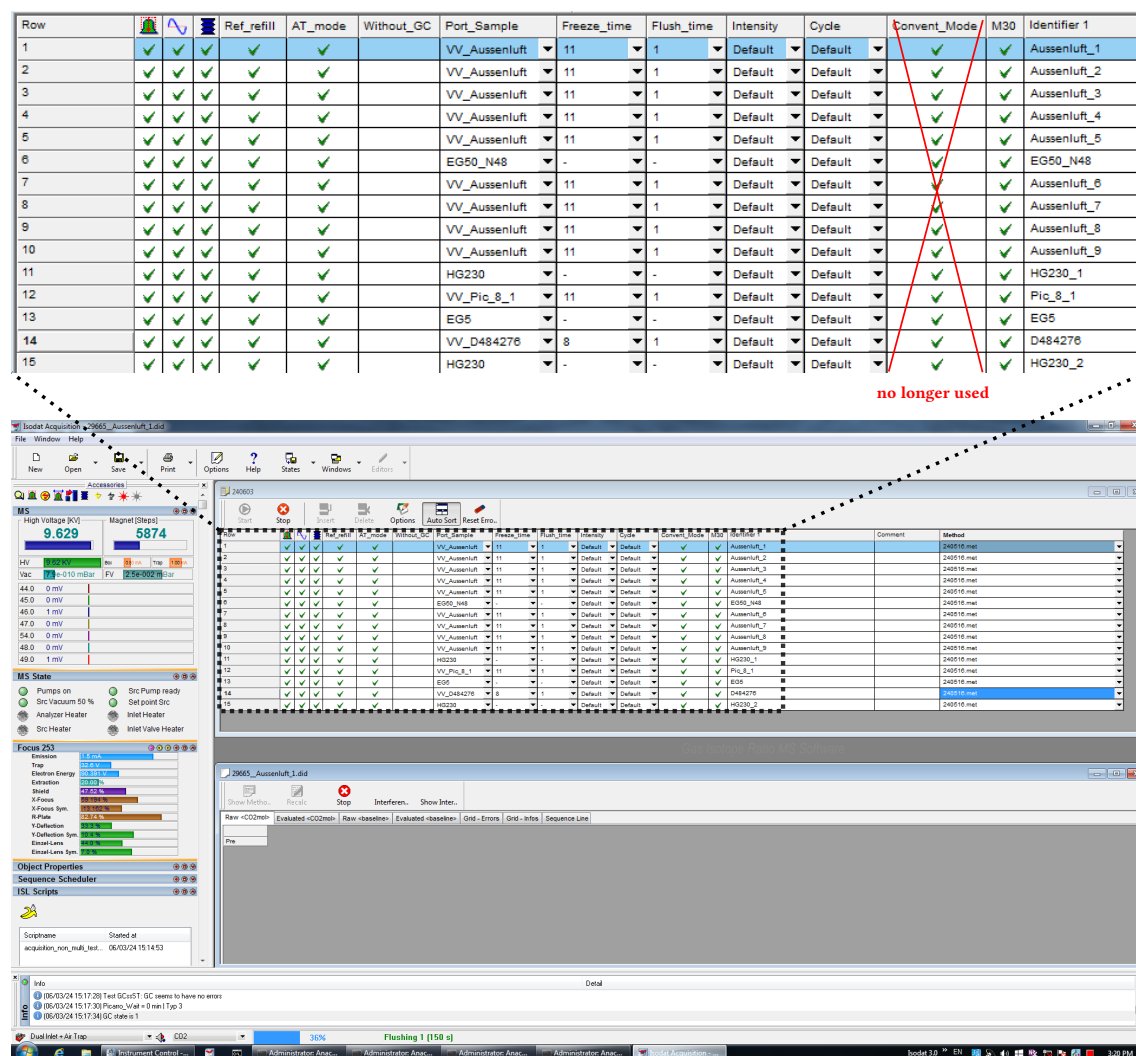
be manually controlled using the four buttons under the heading “Control Valco Valve”. The “Get Pos.” button displays the current position. Clockwise or counterclockwise movement is enabled by pressing “1 CW” or “1 CCW”, respectively. Pressing the “Change Pos.” button makes an input field appear where the user can select any valve position. In this case, the multiposition valve will switch to the desired position via the shortest route, either clockwise or counterclockwise. The three valves connected to the Multifunctional Device can be controlled via the buttons “ArdV 1”, “ArdV 2” and “ArdV 3”. When clicked, an infobox appears to notify the user of the current position and ask if the position should be changed or the process aborted. The “Refill Working Gas” button can be used to manually start the automatic reference refill described in appendix B.15. After pressing the button, the user is prompted to enter the desired target pressure for the end of the refill process. The “Fill Last Step SmpB” button can be used to automatically complete the last step of manually filling the sample bellow with a sample connected to DI 21. The “True Volume” button provides the user with the actual volume value of the respective bellows, including the correction value discussed in appendix B.16. The “Set Bellows True 45” button sets the reference and sample bellow to the currently known actual volume of 45 %. This is intended for manually adjusting the potentiometers, which are part of the bellow control (see appendix B.16). The “Switch Inj. Mode Split/Splitless” button is used to manually switch the flow controller of the GC between the modes “Split” or “Splitless”. The buttons “Stop upwards movement” and “Trap to top position” should only be used by very experienced users. Using them in the wrong order with the raising or lowering of the lifting platform can lead, in the worst case, to jerky lowering of the platform, destruction of the Dewar, or damage to other components.

### User Interface to Start Measurements and Preparations

By default, measurements are started with the “Isodat Acquisition” program. An example is shown in Figure B.15. A desired measurement sequence can be specified using so-called sequences (see *Thermo Fisher Scientific*, 2016). By selecting the method in the last column of this sequence, an ISL script can be specified for the measurement. In the methods selected here, the default Dual Inlet script has been replaced by a user-defined script. In addition to the actual measurement, this script can also start the automatic preparation. The following columns have been added to those originally available in the sequence window: “Ref\_refill”, “AT\_mode”, “Without\_GC”, “Port\_Sample”, “Freeze\_time”, “Flush\_time”, “Intensity”, “Cycle”, and “M30”. Each row corresponds to one acquisition. In the shown sequence, there is only one acquisition for each measurement, so each row corresponds to a new sample preparation and measurement.



**Relevant Inputs for Preparation:** The checkbox in the “AT\_mode” column must be checked if an automatic preparation is to take place before the measurement. If this is not checked, the other columns relevant for the preparation will be ignored. The “Port\_Sample” column can be used to call up a selection in which the sample to be measured can be selected. In this way, port 29 can be selected for a gas cylinder other than “Pic\_8\_1” or “D484276”, or ports 5 and 9 of the multiposition valve can be selected to which flasks can be connected. The sample will be prepared according to its connection as shown in Figure 3.3 using the name selected here (see also Table B.1; page 155). The checkbox in the “Without\_GC” column can be used to select whether the preparation should be performed without a GC step (see subsection 3.2.2). This works only for the preparation of samples



**Figure B.15.:** The figure shows the “Isodat Acquisition” program of Thermo Fisher Scientific. Sequences can be used to schedule measurements (see *Thermo Fisher Scientific*, 2016). An enlarged view of one such sequence is shown at the top. In addition to the default columns, extra columns have been added to set variables for preparations and measurements.

## *Appendices*

connected to the multiposition valve and not for those connected to the valve blocks. The freeze time within the AT step can be changed (in minutes) using a drop-down box in the “Freeze\_Time” column. An additional flush time within the AT step, before the sample is frozen by the CO<sub>2</sub> trap, can be selected using a drop-down menu in the “Flush\_time” column. When ports 5 and 9 are selected, i.e. when measuring flasks, this additional field is ignored and a standard purging time of 15 seconds is used. For gas cylinders, at least 1 should be selected here. This corresponds to an additional flush time of 1 minute to the standard 4 minutes when using gas cylinders or when selecting “VV\_Aussenluft” (port 31) - in this case the total flush time would be 5 minutes. See Appendix B.20 for an experiment on different flush times.

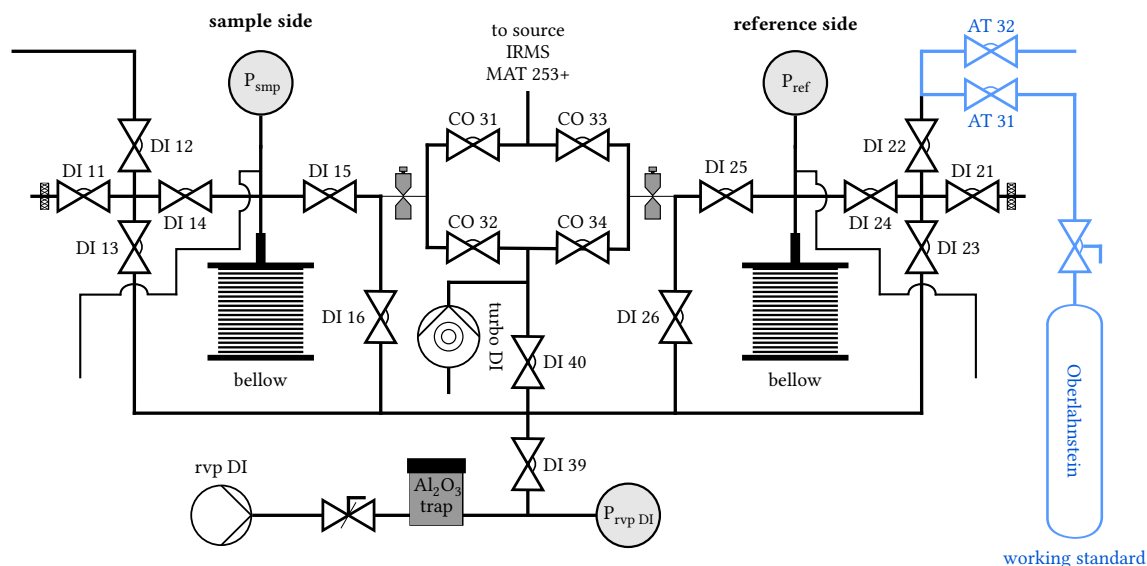
**Columns for Measurement:** The checkbox in the “Ref\_refill” column can be used to select whether an automatic reference refill should take place before the measurement starts. The columns “Intensity”, “Cycle” and “M30” only affect measurements using the new protocol (which is determined by the method). “Intensity” can be used to change the start signal at m/z 44, and “Cycle” can be used to select a number of cycles different from the default (defaults are 8000 mV and 20 cycles). If the “M30” checkbox is selected, a m/z 30 measurement will be performed (see subsection 2.5.5).

## B.15. Automatic Reference Refill

In order to automate the preparation line, it was necessary to enable the reference bellow to refill automatically. To avoid an imbalance between the sample and reference at  $m/z$  44 and the associated effects (see appendix A.5), it was also necessary to refill the reference bellow with the same amount of gas as the sample bellow. Additionally, if the reference gas is reused, it will have been fractionated by the previous measurement. This slight fractionation occurs from the capillaries, which connect the bellows to the changeover valves. This significantly impacts the resulting  $\delta^{13}\text{C}$  and  $\delta^{18}\text{O}$  values. Fractionation also occurs during the initial measurement or when a sample is measured again. However, if the sample and reference gas contain the same amount of gas, they will be fractionated simultaneously, balancing out the effect. An associated experiment is discussed in appendix B.19 on page 174ff.

### Implementation into Dual Inlet System

Figure B.16 shows the relevant section from Figure 3.3 (page 32) to illustrate the structure of the automatic reference refill system. In addition to the Dual Inlet system, the elements added for reference refill are shown in blue. On March 10, 2023, a 1-liter stainless steel



**Figure B.16.:** The figure illustrates the section [A3-F3] of the schematic Figure 3.3. In addition to the Dual Inlet system (see subsection 2.5.2), the parts that were added for the automatic reference refill are shown in blue. A 1-liter stainless steel vessel filled with the working standard “Oberlahnstein” was connected via valve AT 32 and a 1/4” electropolished stainless steel tube.

## Appendices

vessel (4L-SC18-DN4-1000-F2, SS304L; FITOK, Offenbach am Main, Germany; hereinafter referred to as  $V_{\text{Oberlahnstein}}$ ) was filled from a gas cylinder containing “Oberlahnstein” to an absolute pressure of approximately 1.5 bar. Via a 1/4" electropolished stainless steel tube (Dockweiler, Neustadt-Glewe, Germany) and the AT 31 valve, the vessel was connected to the Dual Inlet system (see Figure B.13 on page 154 for an image of the vessel). The AT 32 valve is intended to connect another working standard, e.g., when switching from an old reference to a new one. However, it could also be used to refill  $V_{\text{Oberlahnstein}}$  without disconnecting it from the AT 31 valve. The volume between the AT 31, AT 32, and DI 22 valves (hereafter referred to as  $V_{\text{initial split}}$ ) splits the gas for up to three reference refills.

### Reference Refill Process

From August 10, 2023, to December 20, 2024, a total of 582 automatic reference refills were made using the split with the intermediary volume  $V_{\text{initial split}}$ . Of these, the intermediary volume was refilled 310 times from  $V_{\text{Oberlahnstein}}$ .

For the automatic reference refill, the volume of the sample bellow was first set to 70 %. The pressure read was the pressure to be achieved by the reference refill at the reference bellow at an volume of 70 %. Using a volume of 70 % enabled pressure adjustments in both directions later on. The following relationship between the pressure measured at the sample bellow  $P_{\text{SB}}$  and reference bellow  $P_{\text{RB}}$  was determined and taken into account:

$$P_{\text{RB}} = 0.954035 \cdot (P_{\text{SB}})^{1.01205} . \quad (\text{B.2})$$

An algorithm was implemented that automatically determined how to use different intermediate volumes in combination with the variation of the reference bellow to achieve the desired pressure from the initially available gas in the intermediate volume  $V_{\text{initial split}}$ . Additionally, if the pressure after refilling was too low for the next refill, the remaining gas in the intermediate volume  $V_{\text{initial split}}$  was automatically exchanged with new gas from  $V_{\text{Oberlahnstein}}$ .

Different types of splits were used to achieve the desired pressure. The pre-evacuated intermediate volume between valves DI 21, DI 22, DI 23, and DI 24 was referred to as the “small split”. For the reference bellow set to 70 %, the pressure changed according to the following function:

$$P_{\text{RB}}^{\text{small split}} = P_{\text{RB}} \cdot 0.907 , \quad (\text{B.3})$$

The usage of the previously evacuated volume between DI 13, DI 16, DI 40, DI 39, DI 26, and DI 23 was designated as a “large split”, which led to the following pressure reduction (reference bellow at 70 %):

$$P_{RB}^{\text{large split}} = P_{RB} \cdot 0.582 . \quad (\text{B.4})$$

Furthermore, equations have been determined that calculate the volume to which the reference bellow must be reduced  $V_{RB}^{\text{reduce for split}}$  in order to achieve the desired pressure  $P_{RB}^{\text{desired}}$  at 70 % volume after the split, given the pressure before the split at 70 % volume  $P_{RB}^{\text{before}}$ . The following applies to the “small split”:

$$V_{RB}^{\text{reduce for split}} = \left( \frac{P_{RB}^{\text{desired}}}{0.606169 \cdot P_{RB}^{\text{before}}} \right)^{\frac{1}{0.122852}} , \quad (\text{B.5})$$

and for the “large split”:

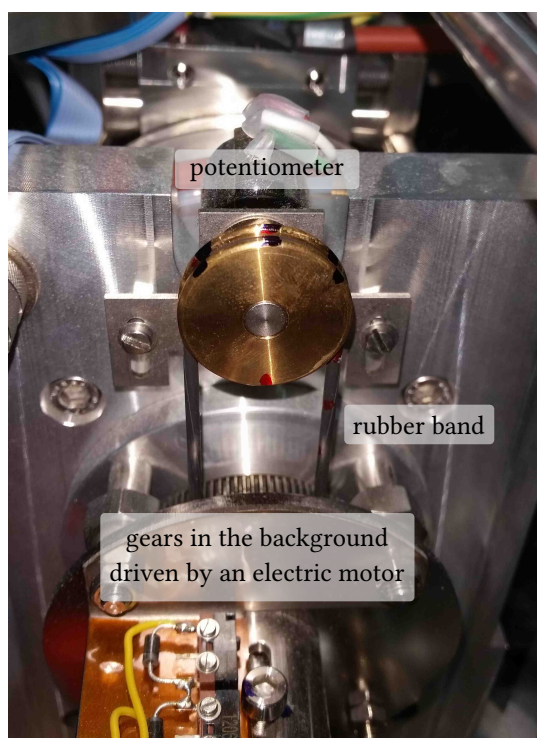
$$V_{RB}^{\text{reduce for split}} = \left( \frac{P_{RB}^{\text{desired}}}{0.123861 \cdot P_{RB}^{\text{before}}} \right)^{\frac{1}{0.494628}} . \quad (\text{B.6})$$

To achieve the desired pressure using the reference refill algorithm, it was crucial to have a consistent relationship between the bellow volume read by the mass spectrometer software and the actual bellow volumes. However, over time, the reported volume values increasingly differed from the actual physical bellow volumes. For instance, 70 % of the reported volume equaled 50 % of the actual volume. This issue and how it was addressed are detailed in appendix B.16.

## B.16. Determination of actual Bellow Volumes

The relationship between the bellow volumes reported by the mass spectrometer software and the actual volumes is changing. Electric motors control the bellows by reducing or increasing their volume via gears. A potentiometer measures the status of this adjustment. Figure B.17 shows the potentiometer and part of the control system. The figure also shows a rubber band. The band transmits the rotation of the gears to the potentiometer. Unfortunately, this design is not very resilient. Due to slippage of the rubber band, for example, the actual setting between the potentiometer and gears becomes out of sync. This discrepancy always goes in the same direction, with the reported value becoming increasingly larger than the actual value. This prevents the bellows from opening fully. To counteract this, the rubber band and potentiometer must be manually readjusted. If measurements are taken daily, this adjustment will be necessary every six to eight weeks to avoid an offset of  $\gtrsim 20\%$  or more. Other laboratories [e.g. Swart et al., 2021] have reported similar behavior and the need for readjustment.

However, for the functions discussed in appendix B.15 that the algorithm uses to fill the reference bellow with the same amount of gas as the sample bellow, the actual volume of the bellows must be known as accurately as possible. For this reason, functions that depend on the relative pressure change  $\Delta P$  and the volume change  $\Delta V$  reported by the mass spectrometer software were determined to yield the initial actual volume of the change  $V^{\text{actual start}}$ . These functions for the sample bellow (SB) and reference bellow (RB)



**Figure B.17.:** Part of the control system of the sample bellow is shown. The sample bellow itself is in the back (see Figure B.26 on page 185 for orientation). The lower part of the picture shows a gear used to adjust the sample bellow, which is driven by an electric motor. At the top is a potentiometer that provides the mass spectrometer software with the position of the sample bellow. The wheel in front of the potentiometer adjusts it. Transmission between the wheel and the gears occurs via a rubber band. The rubber band runs through grooves on the gears, and rotation is transmitted by friction through the tightened band. Unfortunately, this mechanism is not very resilient, so the setting detected by the potentiometer becomes increasingly inaccurate.

are as follows<sup>(1)</sup>:

$$\begin{aligned} V_{SB}^{\text{actual start}} = & -2635.16 \cdot (\Delta V_{SB})^{-0.0220971} \cdot (\Delta P_{SB})^{0.000484162} \\ & + 2718.37 \cdot (\Delta P_{SB})^{-0.0227529} + 1.10819 \cdot (\Delta V_{SB})^{0.9523} \\ & + 5.7173 \cdot (\Delta V_{SB})^{-0.445169} \cdot (\Delta P_{SB})^{0.677187} \end{aligned} \quad , \quad (B.7)$$

$$\begin{aligned} V_{RB}^{\text{actual start}} = & -2878.28 \cdot (\Delta V_{RB})^{-0.0217774} \cdot (\Delta P_{RB})^{0.000485198} \\ & + 2961.05 \cdot (\Delta P_{RB})^{-0.0218289} + 1.06184 \cdot (\Delta V_{RB})^{0.972084} \\ & + 5.81042 \cdot (\Delta V_{RB})^{-0.671273} \cdot (\Delta P_{RB})^{0.822817} \end{aligned} \quad , \quad (B.8)$$

$$\begin{aligned} \text{with} \quad \Delta P_b &= \left( \frac{P_b^{\text{end}}}{P_b^{\text{start}}} - 1 \right) \cdot 100 \\ \Delta V_b &= V_b^{\text{start}} - V_b^{\text{end}} \end{aligned} \quad , \quad b \in \{SB, RB\} \quad .$$

From these, correction values are determined as follows:

$$V_{SB}^{\text{corr}} = V_{SB}^{\text{start}} - V_{SB}^{\text{actual start}} \quad , \quad (B.9)$$

$$V_{RB}^{\text{corr}} = V_{RB}^{\text{start}} - V_{RB}^{\text{actual start}} \quad . \quad (B.10)$$

This determination of the correction values is done automatically for the sample and reference bellow before each reference refill by adjusting the volume from 75 % to 30 %. The correction values are then considered in the volume adjustment functions, including the function that determines a new correction value.

Unfortunately, this method is not perfect. Deviations greater than 15-20 % require readjusting the potentiometer and rubber band to ensure that the reference refills reach the desired pressure<sup>(2)</sup>. However, the described method enabled the automatic refill of the reference bellow with a similar amount of gas as in the sample bellow. This mitigated the impact of pressure imbalances.

A simpler approach to determining the volume correction values might be to slowly decrease the volume until it reaches the lower physical limit. This physical limit should correspond to 0 % of the controllable volume. The reported value by the software would then provide the correction value. Unfortunately, this approach could not be tested within the scope of this work, but it should be evaluated in the future.

<sup>(1)</sup> These functions are overfitted; however, they are not intended to accurately describe a physical relationship. Furthermore, they are not entirely independent of  $P^{\text{start}}$ . There is an additional function that adjusts the correction value slightly in relation to the pressure  $P^{\text{start}}$ , which was present when equations (B.7) and (B.8) were determined.

<sup>(2)</sup> The software has been programmed to issue a warning if the deviation exceeds 20 %. If the deviation exceeds 27 %, the script will stop and prompt the user to adjust the potentiometer and rubber band.

## *Appendices*

As an alternative, revising the entire control and readout system would make sense. As part of this work and the work of *Schmid*, 2023, a prototype was built using a much more accurate stepper motor and light barriers for bellow adjustment. This design likely enables more precise volume control, which could increase measurement accuracy by ensuring better-matched gas volumes and pressure adjustments. However, this system could not be implemented within the scope of this work, but it should be considered in the future.



## B.17. Drift of $\delta^{13}\text{C}$ & $\delta^{18}\text{O}$ with Number of Reference Refills

A significant drift in  $\delta^{13}\text{C}$  was observed in all samples measured in 2024 for an increasing number of reference refills from the stainless steel vessel containing the working standard into the intermediate volume between AT 31 and DI 22 (hereafter referred to as “refill number”; see appendix B.15 for a description of the reference refill). A similar drift was also noticeable in the  $\delta^{18}\text{O}$  measurements of the “D484276” gas cylinder. A superimposed trend in  $\delta^{18}\text{O}$  was observed for the temperature-equilibrated  $\text{CO}_2$  standards “EG5”, “EG50”, “EG50\_N48”, “EG50\_LW”, and “HG230” (see subsection 4.3.4). Figure B.18 shows the change of the normalized  $\delta^{13}\text{C}_{\text{norm}}$  and  $\delta^{18}\text{O}_{\text{norm}}$  with the refill number. The samples used are listed in the legend, along with their respective  $\delta^{13}\text{C}$  and  $\delta^{18}\text{O}$  ( $\text{N}_2\text{O}$ -uncorrected and uncalibrated). Measurements of “Pic\_8\_1” are only considered up to May 23, 2024 (refill number 181). At that time, the  $\text{N}_2\text{O}$  concentration of the sample in this cylinder was determined. Unfortunately, this measurement reduced the cylinder’s pressure to about 20 bar, which likely affected the  $\delta^{13}\text{C}$  and  $\delta^{18}\text{O}$  values of measurements (see section 4.2).

To normalize the  $\delta^{13}\text{C}$  and  $\delta^{18}\text{O}$  values in Figure B.18 for the different samples, the means were calculated for refill numbers up to 100 and then subtracted from the individual values. The first measurement of each temperature-equilibrated  $\text{CO}_2$  standard showed significant differences in  $\delta^{13}\text{C}$  and  $\delta^{18}\text{O}$ , so these were excluded from the mean calculation. These measurements, as well as all other outliers, are marked with ●.

The following functions were determined by fitting the observed trends:

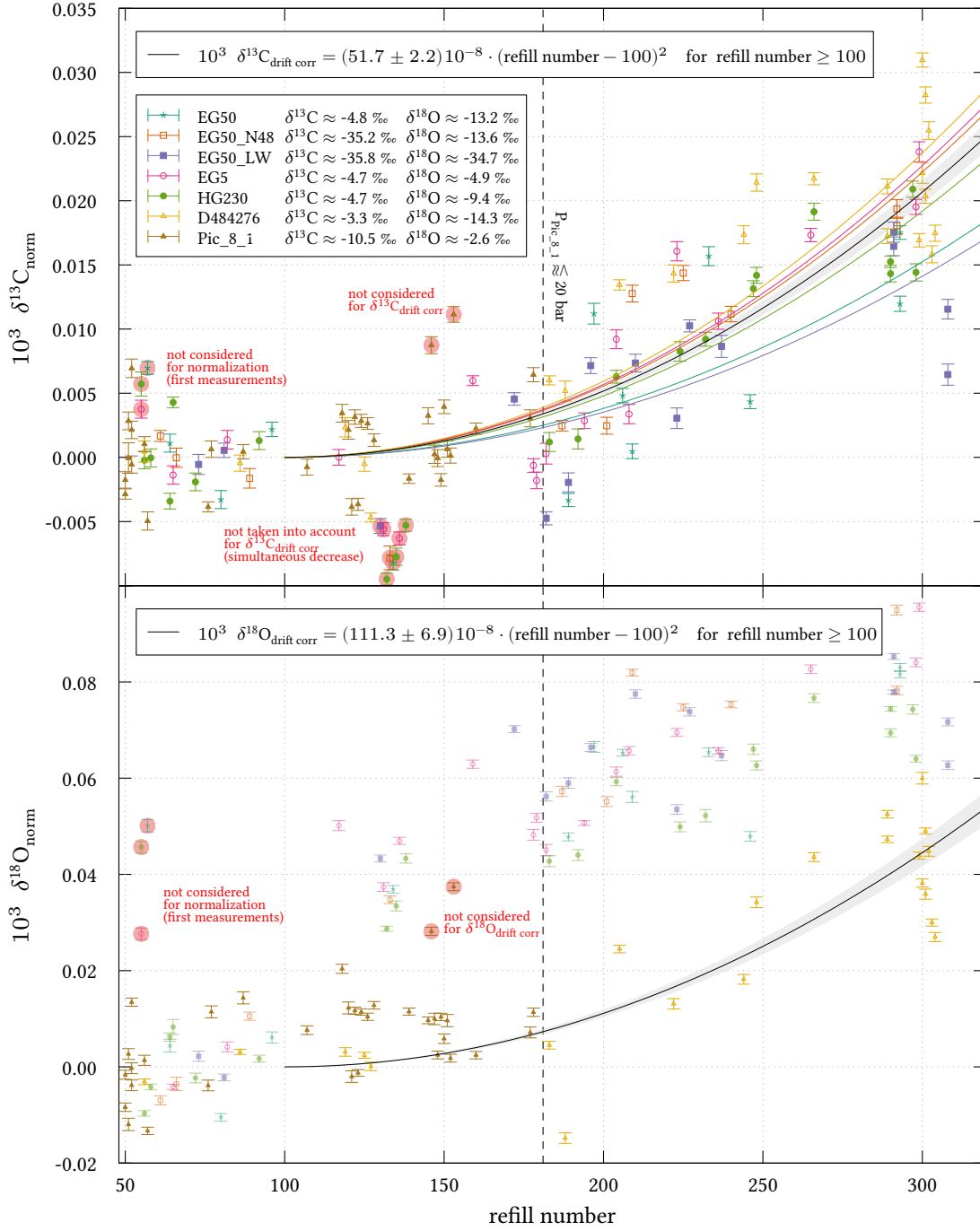
$$10^3 \delta^{13}\text{C}_{\text{drift corr}} = (51.7 \pm 2.2) 10^{-8} \cdot (\text{refill number} - 100)^2, \quad (\text{B.11})$$

$$10^3 \delta^{18}\text{O}_{\text{drift corr}} = (111.3 \pm 6.9) 10^{-8} \cdot (\text{refill number} - 100)^2. \quad (\text{B.12})$$

For these fits, only data with refill numbers  $\geq 100$  were considered. For  $\delta^{13}\text{C}_{\text{drift corr}}$ , all samples listed in the legend were considered. For  $\delta^{18}\text{O}_{\text{drift corr}}$ , only the “Pic\_8\_1” and “D484276” measurements were considered.  $\delta^{13}\text{C}$  measurements between refill numbers 128 and 139 exhibited simultaneous depletion and were excluded. Additionally, the two “Pic\_8\_1” measurements at refill numbers 146 and 153 were excluded for  $\delta^{13}\text{C}_{\text{drift corr}}$  and  $\delta^{18}\text{O}_{\text{drift corr}}$  (these are the fractionated  $\delta^{13}\text{C}$  and  $\delta^{18}\text{O}$  from the test discussed in subsection 3.2.5).

No systematic dependence on the absolute value of  $\delta^{13}\text{C}$  was observed when applying individual fits in the form of Equation (B.11) to the different samples. Additionally, no dependence on the refill number was observed for  $\Delta_{47}$ .

## Appendices



**Figure B.18.:** The graphic shows, the change of normalized  $\delta^{13}\text{C}_{\text{norm}}$  and  $\delta^{18}\text{O}_{\text{norm}}$  in respect to the number of reference refills from the vessel containing the working standard into the intermediate volume between AT 31 and DI 22 (referred to as “refill number”). The samples under consideration and their corresponding isotope delta values are listed in the legend. To normalize the data, the mean value of each sample was determined up to refill number 100. Then, these mean values were subtracted from the respective measured values. The trend observed in  $\delta^{13}\text{C}$  was fitted using all samples, while the trend observed in  $\delta^{18}\text{O}_{\text{norm}}$  was fitted using “D484276” and “Pic\_8\_1”. The result is shown at the top of the respective diagram. Values marked with ● were excluded from normalization and fitting. For  $\delta^{13}\text{C}_{\text{norm}}$ , these fits were performed individually for each sample in addition. As can be seen, there is no systematic relationship with the total  $\delta^{13}\text{C}$  value. (Errors: SEM of measurement)

Measurements conducted in this thesis with refill numbers  $\geq 100$  were corrected regarding the trends described by equations (B.11) and (B.12), as follows:

$$10^3 \delta^{13}\text{C} = 10^3 \delta^{13}\text{C}_{\text{drift uncorrected}} - 10^3 \delta^{13}\text{C}_{\text{drift corr}} , \quad (\text{B.13})$$

$$10^3 \delta^{18}\text{O} = 10^3 \delta^{18}\text{O}_{\text{drift uncorrected}} - 10^3 \delta^{18}\text{O}_{\text{drift corr}} . \quad (\text{B.14})$$

These correction were applied prior to the  $\text{N}_2\text{O}$  corrections and  $\delta^{18}\text{O}$  calibration, according to subsection 4.1.1 and section 4.2, respectively.

Another effect on  $\delta^{13}\text{C}$  and  $\delta^{18}\text{O}$  was observed depending on the multiple uses of the gas in the intermediate volume between AT 31 and DI 22. This effect likely occurred in conjunction with the split type used to adjust the pressure as desired. Additionally, this dependence appeared to change with an increasing refill number. The larger dispersion seen with higher refill numbers in Figure B.18 can be attributed to this effect. Between refill numbers 71 and 176 (March 29, 2024, to May 20, 2025), reference refills were permitted only with one use of the intermediate volume.

The trends described by equations (B.11) and (B.12) are assumed to be caused by a depletion in  $\delta^{13}\text{C}$  and  $\delta^{18}\text{O}$  of the refilled working gas due to a decreasing pressure in its stainless steel vessel. This decrease in pressure may have also altered the effects of using the intermediary volume multiple times, as well as the effects of the different splits, on the isotopic composition. For the respective first refill using the intermediate volume between AT 31 and DI 22, the initial pressure in the reference bellow decreased from 60.7 mbar at refill number 50, to 39.2 mbar at refill number 150, to 25.9 mbar at refill number 250, and finally to 21.4 mbar at refill number 310. However, since the refill number correlates strongly with time, it cannot be ruled out that the observed drifts are caused by something else. However, a much smaller drift can be seen at the end of 2024 when plotted against time. During this period, significantly fewer measurements were taken. This caused the refill number to increase less sharply, weakening the correlation between the refill number and time. For this reason, the hypothesis regarding the refill number and the associated decrease in the working standard's pressure is preferred.

As the refill number increases, the hypothesized depletion of  $\delta^{13}\text{C}$  and  $\delta^{18}\text{O}$  in the refilled reference gas might be related to one or more of the following: 1. Pressure-dependent desorption/absorption on the inner surface of the sample cylinder, possibly combined with desorption/absorption from the metal surfaces of the splitting volumes; or 2. Pressure diffusion induced by gas flow when opening evacuated volumes to perform splits, which cannot be compensated for within the allotted time for pressure equilibration. Effusion can be virtually ruled out because it would lead to an enrichment of  $\delta^{13}\text{C}$  and

## *Appendices*

$\delta^{18}\text{O}$  in the reference gas. This would result in an observed trend of increasingly depleted values for the measured samples, which is the opposite of what is seen in Figure B.18.

Assuming the hypothesis that a decrease in the pressure of the working gas results in changes in the measured  $\delta^{13}\text{C}$  and  $\delta^{18}\text{O}$  is correct, an initial pressure of  $\sim 1.5$  bar in the working gas vessel should only be used approximately up to refill number 100 to achieve optimal results. Alternatively, the bellow could be refilled directly via a gas cylinder. To obtain optimal  $\delta^{13}\text{C}$  and  $\delta^{18}\text{O}$  measurements, the gas in the intermediate volume between AT 31 and DI 22 should also only be used once.

## **B.18. Duration of Preparation & Measurement**

### **Duration of Air Trap Preparation**

It is not possible to give an exact preparation time as it may vary slightly depending on factors such as the time required to achieve a specific target vacuum in a particular step. In addition, the duration of the preparation depends on the sample being prepared, the parameters selected for e.g. “Freeze Time” and “Flush Time”, and the sample that follows. For example, if the next sample is a standard connected to the valve blocks (see appendix B.11), there will be an initial preparation for this standard at the end of the current preparation. This means that the corresponding valve block will be evacuated and then the corresponding valve for the standard (next preparation) will be opened for a small split to the valve block.

For example, preparing a sample from the gas cylinder “Pic\_8\_1”, including the GC step (freeze time: 11 minutes; flush time: 1 minute; no preparation of a subsequent standard), takes approximately 1 hour and 27 minutes. Without GC step such a preparation takes about 50 minutes. An additional 9 minutes are required if a standard is prepared for the next preparation. The preparation of a standard connected to the valve block takes about 1 hour and 9 minutes.

### **Duration of Automatic Reference Refill**

An automatic reference refill will take approximately 16 minutes ( $\pm$ several minutes depending on the split). An additional 5 to 6 minutes will be required to prepare the intermediate volume between valves AT 31 and DI 22 if the last reference refill is performed before it is refilled.

### **Duration of Measurement**

A measurement with 20 cycles and one acquisition takes about 2 hours and 53 minutes (including “PeakCenter”, “Default Background Measurement”, “Bellows Adjustment” and m/z 18, m/z 40 and m/z 30 measurements). Each additional cycle takes approximately 8 minutes. The total integration time for such a sample is 4000 seconds ( $\approx$  1 hour and 7 minutes).

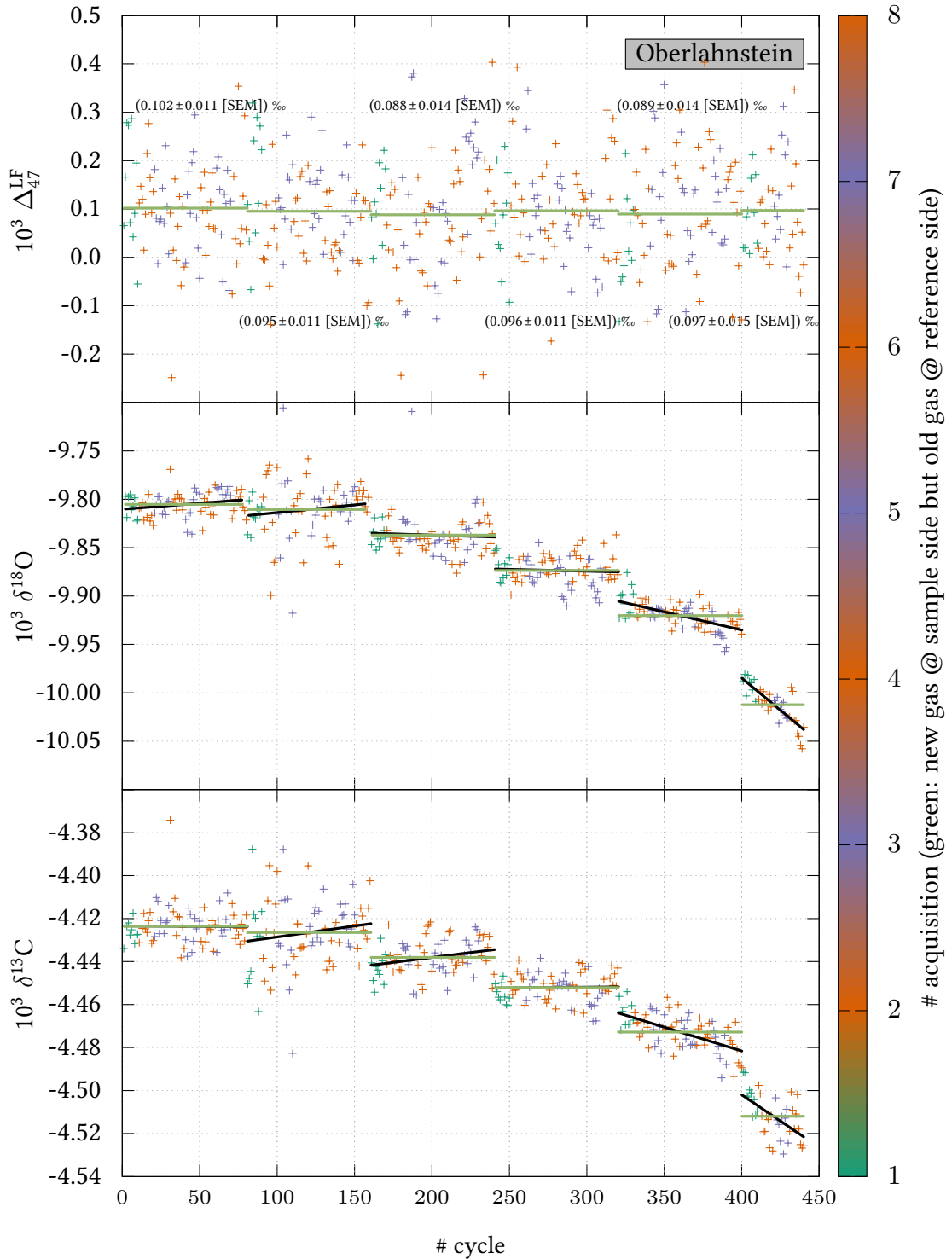
## B.19. Experiment on Reusing Reference Gas

Reusing the reference gas affects the resulting  $\delta^{13}\text{C}$  and  $\delta^{18}\text{O}$  of a measurement. To illustrate this, six measurements were performed between March 12 and 13, 2019. Before the first measurement, both the reference and the sample bellow were filled with “Oberlahnstein”. For subsequent measurements, only the sample bellow was refilled with “Oberlahnstein”. Therefore, the subsequent measurements started with the gas left in the reference bellow. The results of this experiment are shown in Figure B.19. On this graph’s color scale, the first measurement starts in green (i.e., when the sample bellow was refilled). Each measurement consisted of eight acquisitions, each with ten cycles, except for the last measurement, which had only four acquisitions (old measurement protocol). The lines — and — indicate the means and linear fit, respectively, over the cycles of a given measurement.

As the number of measurements increases, a depletion of  $\delta^{13}\text{C}$  and  $\delta^{18}\text{O}$  becomes noticeable. However, this is not an effect of the measured sample gas, the results of which are plotted here. Rather, it is a result of the reference gas becoming increasingly enriched. This is likely due to effusion, whereby the lighter isotopologues escape more quickly and easily through the capillaries connecting the bellows with the changeover valves. The linear fits also show that fractionation within a measurement becomes apparent from the fifth measurement onward. This is because the sample bellow was completely refilled each time, so the amounts within the bellows differed increasingly. This likely resulted in fractionation within an acquisition that did not cancel out entirely and became noticeable.

No significant change can be detected within the measurement uncertainties for  $\Delta_{47}^{\text{LF}}$ . This is likely because the fractionation is largely eliminated in the  $\Delta_{47}^{\text{LF}}$  calculation. In addition to  $^{47}\delta$ ,  $\delta^{13}\text{C}$  and  $\delta^{18}\text{O}$  are included in the calculation. Although  $^{47}\delta$  was not examined here, it seems plausible that fractionation occurred in this case as well.

The effect is probably even stronger when using the new measurement protocol because the bellows should empty more quickly at a higher  $m/z$  44. Therefore, the reference gas should be refilled for each individual measurement. Not refilling the working standard may cause the WMO/IAEA network compatibility goal of 0.01 ‰ for  $\delta^{13}\text{C}$  [see WMO/IAEA, 2016; Table 1] to be missed after the first or second reuse. The observation on the fractionation of  $\delta^{13}\text{C}$  and  $\delta^{18}\text{O}$  for the reuse of the working standard is consistent with the experiments by Yan et al., 2022, who also recommend frequent refilling of the reference gas to avoid such effects.



**Figure B.19.:** The graphs show the results of an experiment in which both reference and sample bellow were first filled with "Oberlahnstein". Then, six measurements were conducted. The first acquisition of each measurement is always marked in green. For each measurement, "Oberlahnstein" was refilled into the sample bellow and measured against the remaining gas in the reference bellow. Means and linear fits over the cycles of a given measurement are marked with — and —, respectively. A clear depletion of  $\delta^{13}C$  and  $\delta^{18}O$  is observed. This is likely due to enrichment of the reference gas. However, there is no significant change within the uncertainty for  $\Delta_{47}^{LF}$ .

## B.20. Experiment on “Flush Time” in AT step

A systematic investigation of the effect of the flush time in the AT step could not be carried out within the scope of this work. Only two test measurements of “Pic\_8\_1” were performed. Once with a selection of 6 minutes on May 16, 2024, and once with a selection of 0 minutes on May 18, 2024 (0 corresponds to the default flush time of 4 minutes). The two measurements were compared with the average of ten other measurements of “Pic\_8\_1” in the period from May 11, 2024 to May 21, 2024:  $\delta^{13}\text{C} = (-10.496 \pm 0.003 \text{ [SD]}) \text{ ‰}$  and  $\delta^{18}\text{O} = (-2.561 \pm 0.004 \text{ [SD]}) \text{ ‰}$  (not  $\text{N}_2\text{O}$ -corrected or calibrated). The additional flush time of 6 minutes showed no systematic deviation from these mean values. For the measurement with an additional flush time of 0 minutes, however, a significant depletion of  $\Delta(\delta^{13}\text{C}) \approx -0.009 \text{ ‰}$  and  $\Delta(\delta^{18}\text{O}) \approx -0.024 \text{ ‰}$  was observed. No significant deviation was observed for  $\Delta_{47}$ ,  $\Delta_{48}$ ,  $\Delta_{49}$ , and  $^{30}\Lambda$ .

Based on these two measurements, it can be concluded that an additional flush time of 1 minute is sufficient. The omission of this additional flush time has a significant effect on  $\delta^{13}\text{C}$  and  $\delta^{18}\text{O}$ . However, as this has only been demonstrated by these two measurements, this statement should be treated with caution and systematically re-examined in the future.



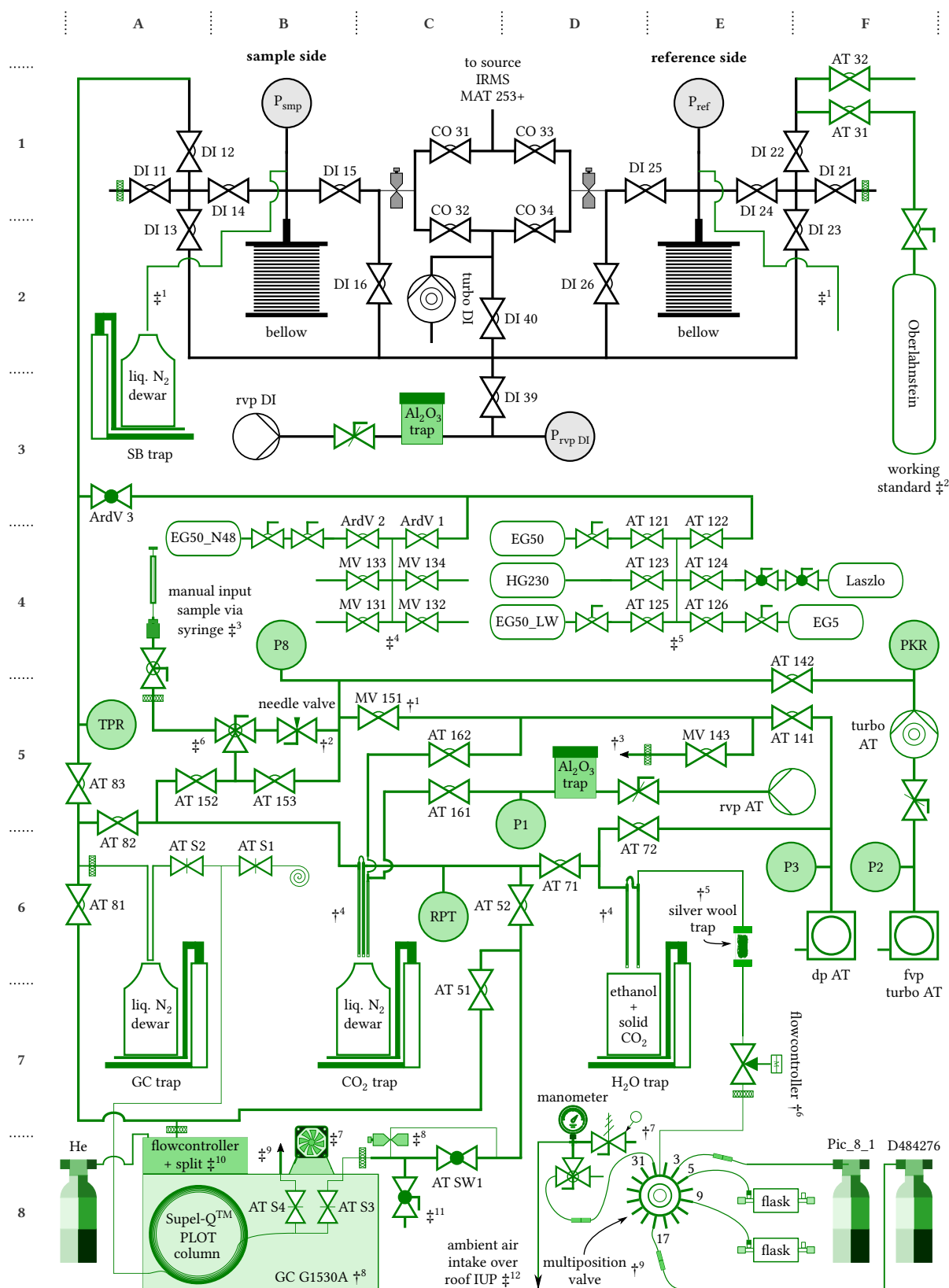
## **B.21. Test on Ambient Air Intake Line**

On January 10, 2024, a test was conducted to determine whether an ambient air sample would change as it was drawn in through the air intake at IUP's roof and distributed by the pumps in the pump room to the Air Trap and other devices (see section 2.4 for a more detailed description of the air intake). For the test, a gas cylinder ("N73\_3") filled with ambient air was connected to the intake at around 13:35 UTC. Sampling through port 31 of the Air Trap's multiposition valve yielded:  $\delta^{13}\text{C} = (-9.692 \pm 0.001 \text{ [SEM]}) \text{ ‰}$ ,  $\delta^{18}\text{O} = (-1.103 \pm 0.002 \text{ [SEM]}) \text{ ‰}$ , and  $\Delta_{47} = (0.936 \pm 0.010 \text{ [SEM]}) \text{ ‰}$  ( $\text{N}_2\text{O}$ -corrected and calibrated). Prior to the test, the gas cylinder was measured three times while connected directly to the preparation line via port 29 of the multiposition valve. The mean values obtained from these measurements were  $\delta^{13}\text{C} = (-9.693 \pm 0.002 \text{ [SD]}) \text{ ‰}$ ,  $\delta^{18}\text{O} = (-1.119 \pm 0.006 \text{ [SD]}) \text{ ‰}$ ,  $\Delta_{47} = (0.945 \pm 0.004 \text{ [SD]}) \text{ ‰}$ . Considering the SD from the mean of the three prior measurements,  $\delta^{13}\text{C}$  of the test measurement falls within one SD, while  $\delta^{18}\text{O}$  and  $\Delta_{47}$  are within three SDs. Therefore, the differences are insignificant, and no notable systematic effects due to the intake line have been assumed.

## B.22. Additional Figures and Tables

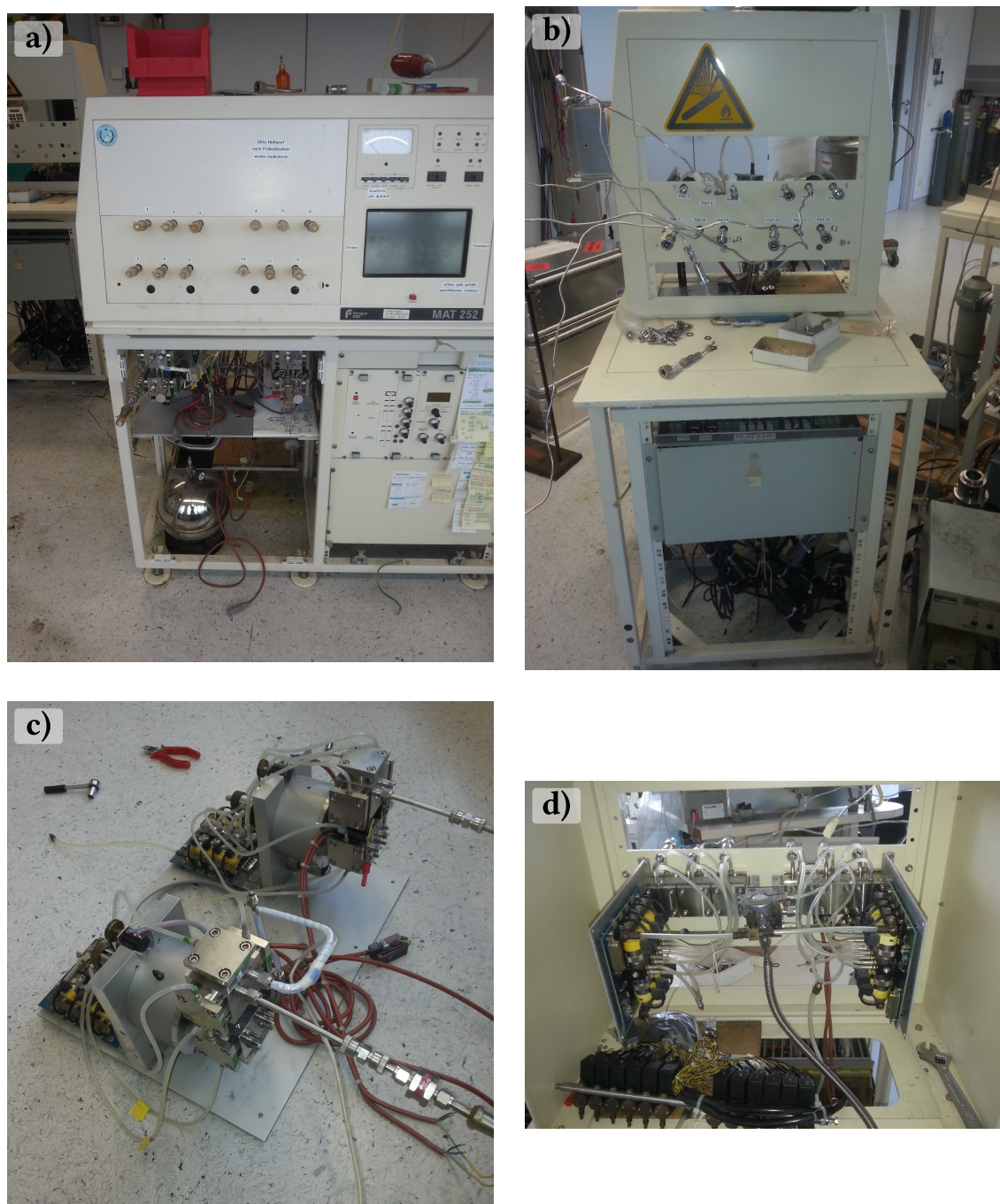


**Figure B.20.:** The graphic shows the basic structure of the preparation line at the pick-up at the Climate and Environment Sciences Laboratory (LSCE) in France on May 14, 2019. The basic metal frame including two lifting platforms and the connection options for flasks via the multiport valve can be seen.

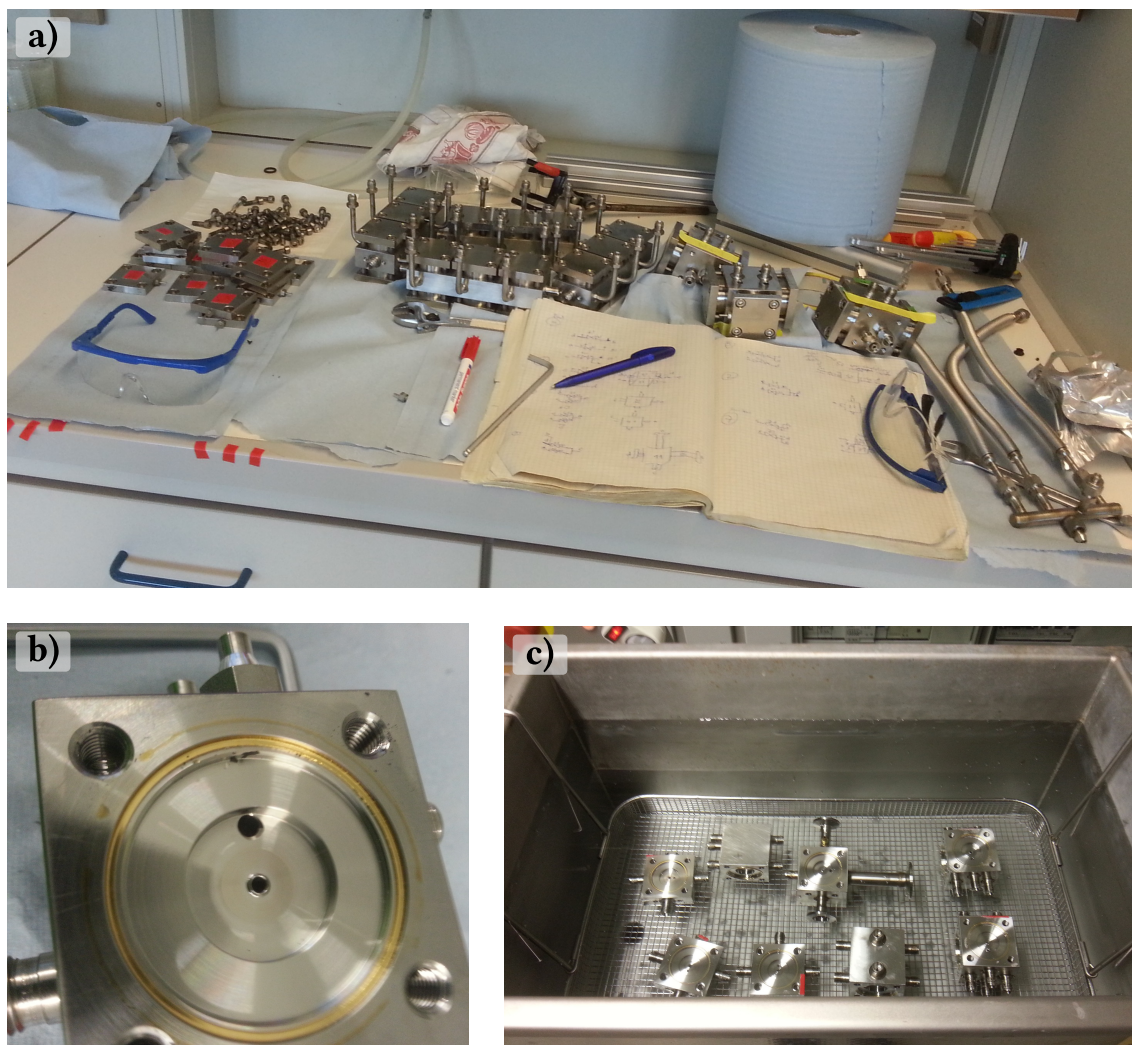


**Figure B.21.:** The figure shows in green the changes compared to the Dual Inlet system that existed before the start of the thesis. A legend can be found on page 33 in chapter 3.



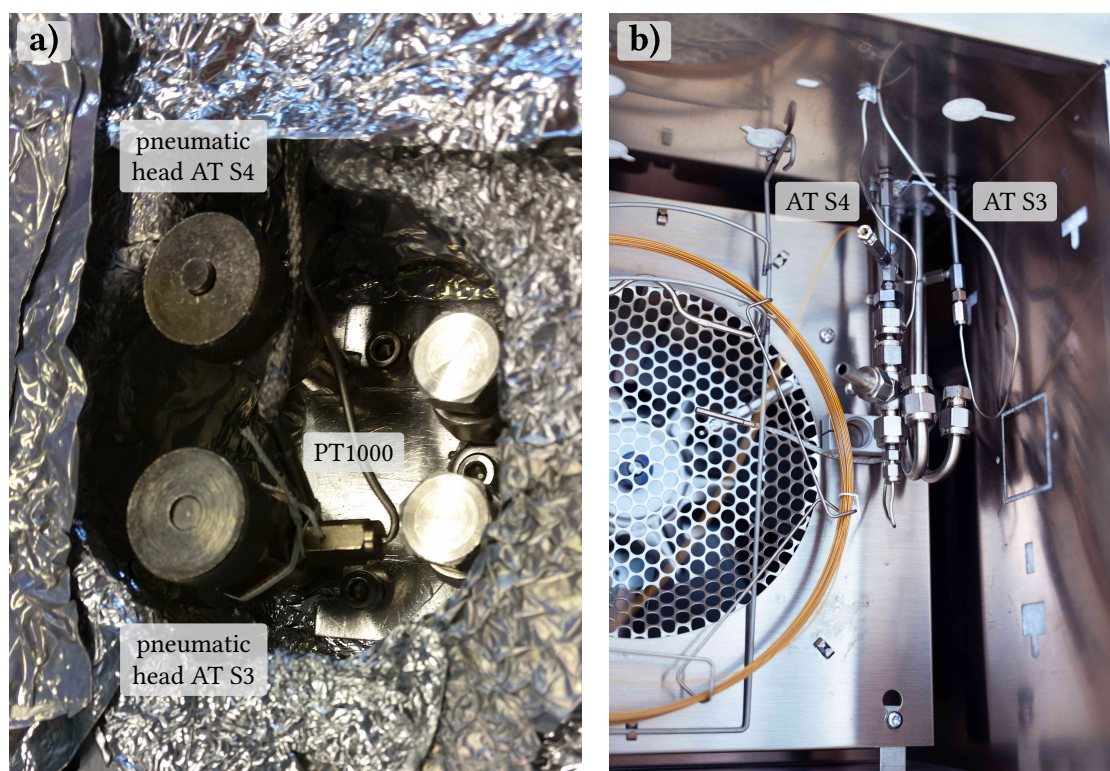


**Figure B.22.:** In spring 2022, the long-used a) IRMS MAT252 [Neubert, 1998] and associated extensions, such as a b) preparation module for atmospheric flask samples, were dismantled. Some parts, in particular the pneumatically operated diaphragm valves, were reused for the construction of the Air Trap in this work. c) shows the dismantled Dual Inlet system of the MAT252. Image d) shows the valve blocks belonging to b) from the inside.



**Figure B.23.:** The valves and other components removed from the IRMS MAT252 (see Figure B.22) were a) disassembled and cleaned before being reused for the Air Trap (Figure 3.2). b) shows an example of a valve contaminated with oil and dust. All valves were cleaned with deionized water and ethanol using cotton swabs and laboratory paper towels and flushed out with compressed air. In addition to these steps, cleaning was also carried out in an c) ultrasonic bath. If necessary, some of these steps were repeated several times. In addition, the gold stamps (see Figure B.2 on page 142) were replaced or ground down by the precision engineering workshop of the IUP to ensure that the valves close tightly.





**Figure B.24.:** The pictures show the valves AT S3 & AT S4 [B8] installed in/on the GC. a) shows the valve heads and PT1000 temperature sensor mounted on AT S3. This is used to control the fan (see Figure 3.6) that cools the valves during baking. b) shows the valves inside the oven.

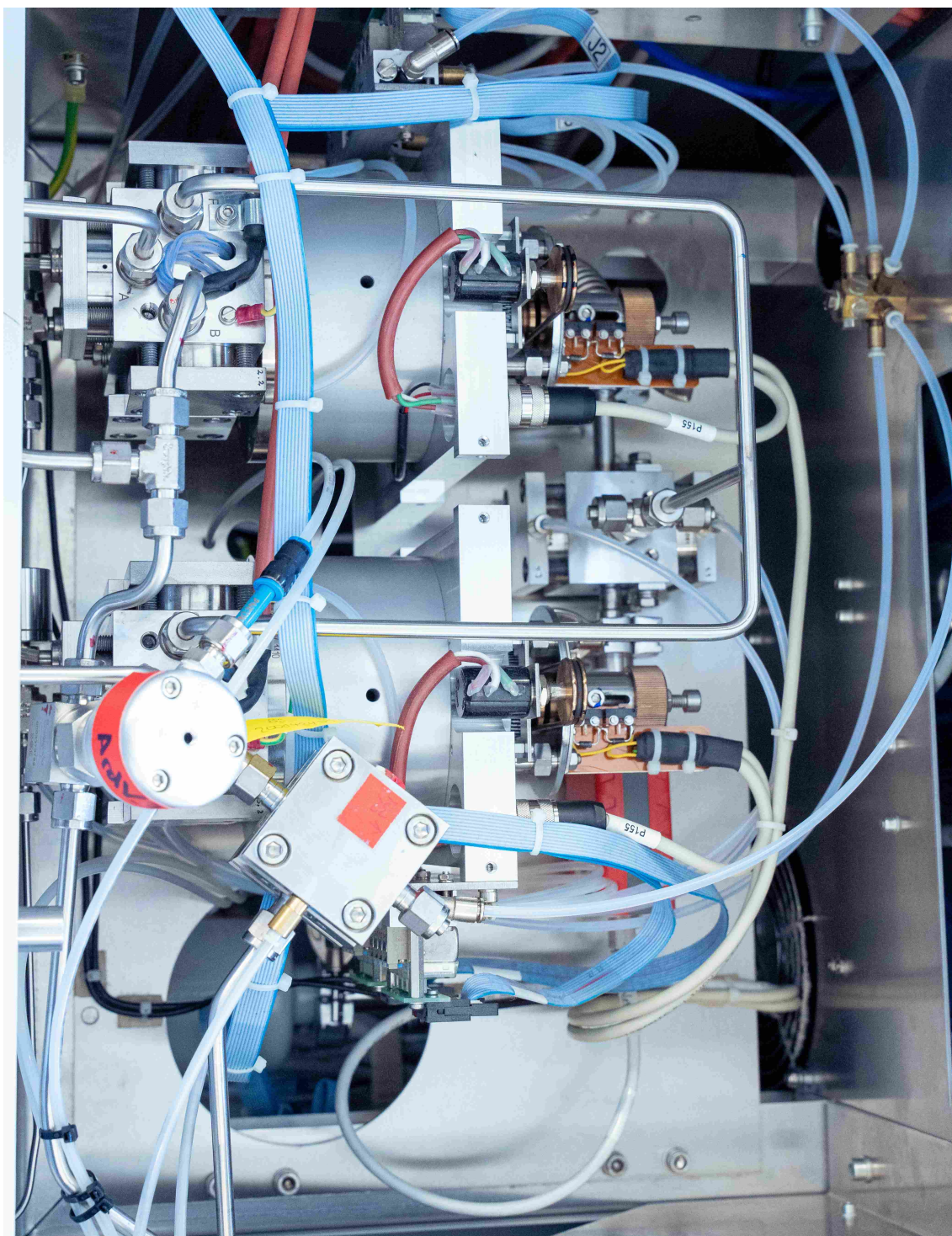


**Figure B.25.:** The two pictures show the workstations with the Li7000 CO<sub>2</sub>/H<sub>2</sub>O analyzer a) and the mass spectrometer's computer b).

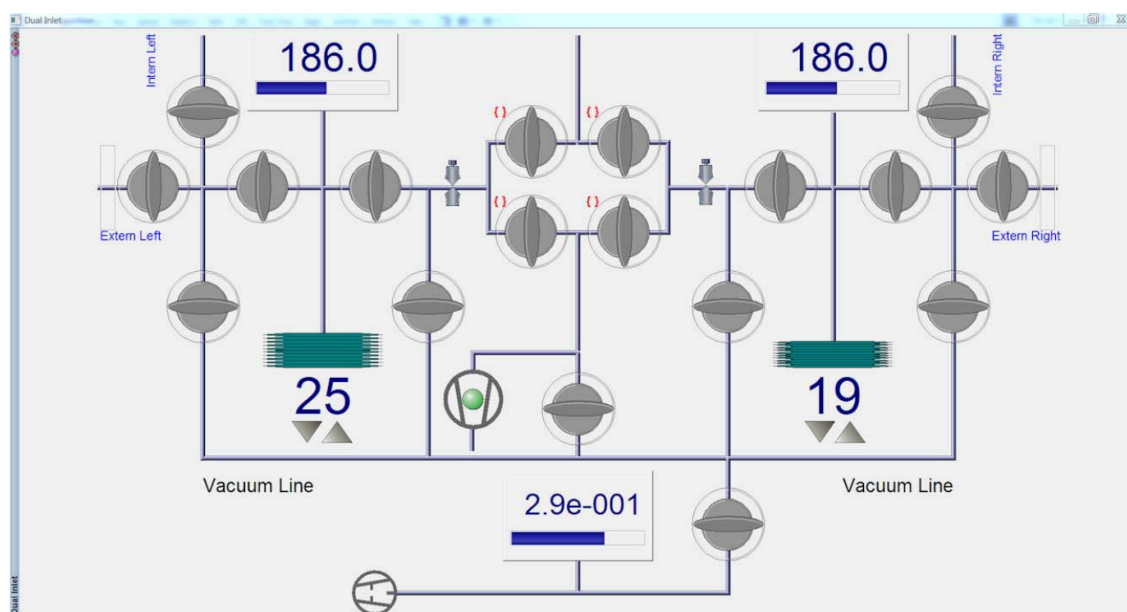
**Table B.2.:** Overview of information on column baking from other laboratories using the same column. This overview does not claim to be complete. In *Huntington et al., 2009*, an additional baking at 220 °C for six hours once every 24 hours is specified.

author	flow rate [ml/min]	T [°C]	duration
<i>Affek et al., 2006</i>	3 (during sampling; unclear baking)	150	between samples
<i>Ghosh et al., 2006</i>	5	200	> 30 min between samples
<i>Huntington et al., 2009</i>	3 (during sampling; unclear baking)	150	between samples

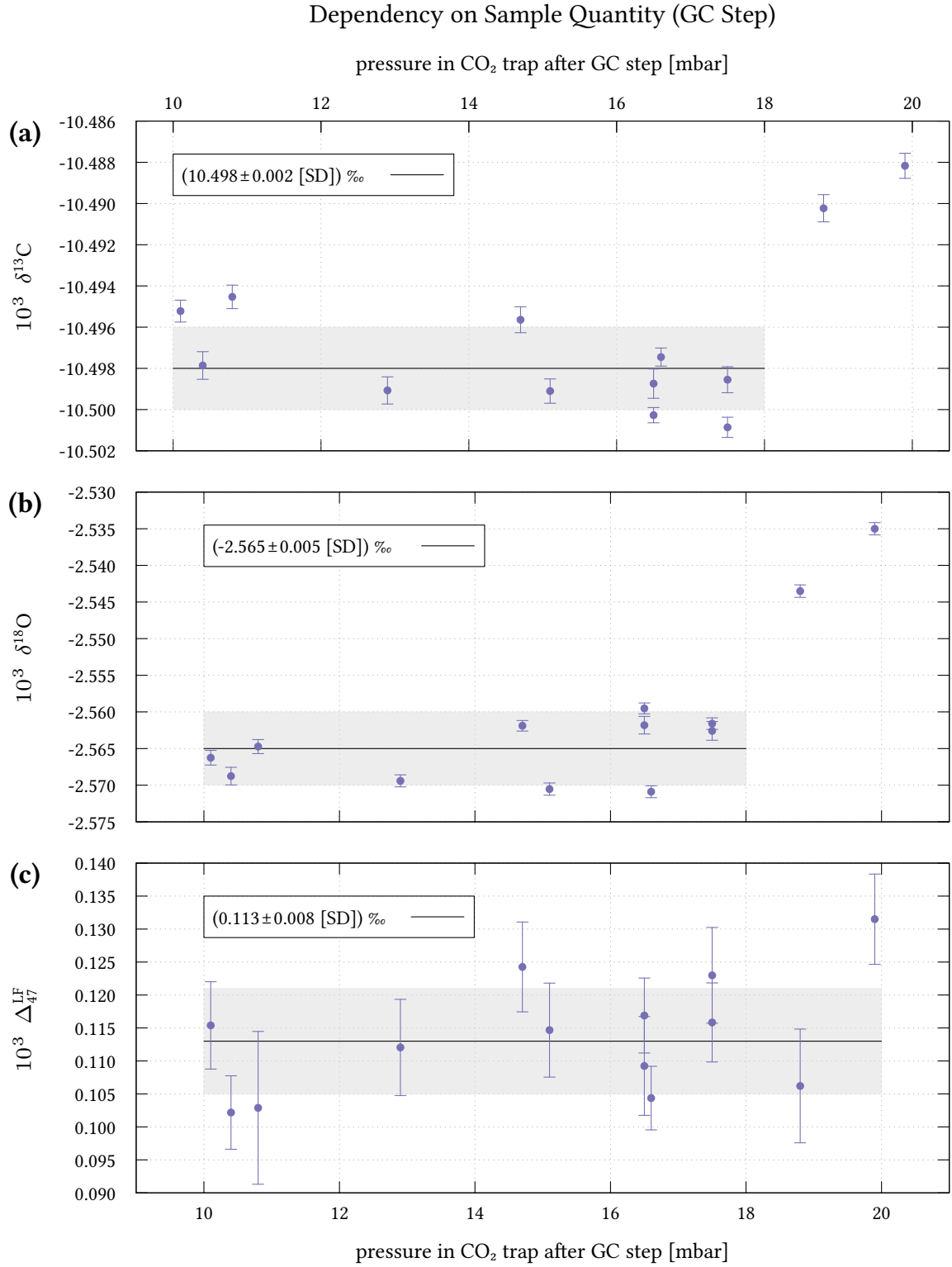




**Figure B.26.:** This image shows the Dual Inlet system of the IRMS MAT253+. The sample bellow is at the top and the reference bellow is at the bottom.



**Figure B.27.:** The figure shows the original GUI of the Dual Inlet system in the IRMS control program “Isodat”. [Image source: *Thermo Fisher Scientific*, 2016 (Figure 4-1)]



**Figure B.28.:** Thirteen measurements of “Pic\_8\_1” were conducted from May 11 to May 21, 2024. The freezing time in the AT step was varied to sample different quantities. The graphic presents the results of this experiment in dependency of the pressure measured by the RPT sensor after the GC step in the CO<sub>2</sub> trap. The data are uncalibrated and uncorrected for dependencies on N<sub>2</sub>O and  $^{47}\delta$  on  $\Delta_{47}^{\text{LF}}$ . The results at ~18.8 and ~19.9 mbar differ significantly for  $\delta^{13}\text{C}$  (a) and  $\delta^{18}\text{O}$  (b). No significant dependency was observed for  $\Delta_{47}^{\text{LF}}$  (c). (Errors (data): SEM)

## *Appendices*

## C. Supplementary Material on Chapter 4

### C.1. Additional N<sub>2</sub>O Correction Functions

In addition to the correction functions given in section 4.1, correction functions based on VSMOW for the oxygen isotopes were calculated (see Table 2.1). It should be noted that the range of  $\delta^{18}\text{O}_{\text{VSMOW}} \in \{-50, -49, \dots, 10\}$  considered for the calculation does not represent the full range of typical samples in terms of VSMOW. The following functions were obtained:

$$10^3 \delta^{13}\text{C}_{\text{VPDB}}^{\text{N}_2\text{O corr}} = -(10087 \pm 7) 10^{-7} \cdot 10^3 \delta^{13}\text{C}_{\text{VPDB}} \cdot \xi - (955 \pm 5) 10^{-8} \cdot 10^3 \delta^{18}\text{O}_{\text{VSMOW}} \cdot \xi - (3566 \pm 4) 10^{-4} \cdot \xi, \quad (\text{C.1})$$

$$10^3 \delta^{18}\text{O}_{\text{VSMOW}}^{\text{N}_2\text{O corr}} = -(453 \pm 2) 10^{-8} \cdot 10^3 \delta^{13}\text{C}_{\text{VPDB}} \cdot \xi - (10063 \pm 4) 10^{-7} \cdot 10^3 \delta^{18}\text{O}_{\text{VSMOW}} \cdot \xi - (4769 \pm 4) 10^{-4} \cdot \xi, \quad (\text{C.2})$$

$$10^3 \Delta_{47}^{\text{N}_2\text{O corr}} = (315 \pm 2) 10^{-6} \cdot 10^3 \delta^{13}\text{C}_{\text{VPDB}} \cdot \xi + (201 \pm 8) 10^{-6} \cdot 10^3 \delta^{18}\text{O}_{\text{VSMOW}} \cdot \xi + (161 \pm 2) 10^{-3} \cdot \xi, \quad (\text{C.3})$$

$$10^3 \Delta_{48}^{\text{N}_2\text{O corr}} = (16 \pm 2) 10^{-7} \cdot 10^3 \delta^{13}\text{C}_{\text{VPDB}} \cdot \xi + (1082 \pm 6) 10^{-6} \cdot 10^3 \delta^{18}\text{O}_{\text{VSMOW}} \cdot \xi - (4367 \pm 9) 10^{-5} \cdot \xi - (212 \pm 7) 10^{-6} \cdot \xi^2, \quad (\text{C.4})$$

$$10^3 \Delta_{49}^{\text{N}_2\text{O corr}} = (6853 \pm 8) 10^{-7} \cdot 10^3 \delta^{13}\text{C}_{\text{VPDB}} \cdot \xi + (111 \pm 9) 10^{-5} \cdot 10^3 \delta^{18}\text{O}_{\text{VSMOW}} \cdot \xi + (131 \pm 4) 10^{-2} \cdot \xi. \quad (\text{C.5})$$

Additionally, correction values were calculated for  $^{45}\delta$  through  $^{49}\delta$  with respect to the work standard “Oberlahnstein”:

$$10^3 \delta_{\text{Oberlahnstein}}^{45\text{N}_2\text{O corr}} = -(9470 \pm 5) 10^{-7} \cdot 10^3 \delta^{13}\text{C}_{\text{VPDB}} \cdot \xi - (3687 \pm 2) 10^{-8} \cdot 10^3 \delta^{18}\text{O}_{\text{VPDB-CO}_2} \cdot \xi - (3524 \pm 2) 10^{-4} \cdot \xi, \quad (\text{C.6})$$

$$10^3 \delta_{\text{Oberlahnstein}}^{46\text{N}_2\text{O corr}} = -(7445 \pm 6) 10^{-9} \cdot 10^3 \delta^{13}\text{C}_{\text{VPDB}} \cdot \xi - (10163 \pm 5) 10^{-7} \cdot 10^3 \delta^{18}\text{O}_{\text{VPDB-CO}_2} \cdot \xi - (5033 \pm 3) 10^{-4} \cdot \xi, \quad (\text{C.7})$$

$$10^3 \delta_{\text{Oberlahnstein}}^{47\text{N}_2\text{O corr}} = -(9725 \pm 5) 10^{-7} \cdot 10^3 \delta^{13}\text{C}_{\text{VPDB}} \cdot \xi - (10157 \pm 5) 10^{-7} \cdot 10^3 \delta^{18}\text{O}_{\text{VPDB-CO}_2} \cdot \xi - (6922 \pm 4) 10^{-4} \cdot \xi, \quad (\text{C.8})$$

$$10^3 \delta_{\text{Oberlahnstein}}^{48\text{N}_2\text{O corr}} = -(1498 \pm 2) 10^{-8} \cdot 10^3 \delta^{13}\text{C}_{\text{VPDB}} \cdot \xi - (20117 \pm 9) 10^{-7} \cdot 10^3 \delta^{18}\text{O}_{\text{VPDB-CO}_2} \cdot \xi - (10187 \pm 6) 10^{-4} \cdot \xi, \quad (\text{C.9})$$

## Appendices

$$10^3 \cdot {}^{49}\delta_{\text{Oberlahnstein}}^{\text{N}_2\text{O corr}} = -(1643 \pm 2) 10^{-8} \cdot 10^3 \delta^{13}\text{C}_{\text{VPDB}} \cdot \xi - (1588 \pm 2) 10^{-8} \cdot 10^3 \delta^{18}\text{O}_{\text{VPDB-CO}_2} \cdot \xi - (635 \pm 4) 10^{-5} \cdot \xi \quad (\text{C.10})$$

The same was done for a virtual work gas, for which the carbon and oxygen isotopes corresponded to VPDB and VPDB-CO<sub>2</sub>, respectively:

$$10^3 \cdot {}^{45}\delta_{\text{VPDB, VPDB-CO}_2}^{\text{N}_2\text{O corr}} = -(9428 \pm 5) 10^{-7} \cdot 10^3 \delta^{13}\text{C}_{\text{VPDB}} \cdot \xi - (3670 \pm 2) 10^{-8} \cdot 10^3 \delta^{18}\text{O}_{\text{VPDB-CO}_2} \cdot \xi - (3508 \pm 2) 10^{-4} \cdot \xi \quad (\text{C.11})$$

$$10^3 \cdot {}^{46}\delta_{\text{VPDB, VPDB-CO}_2}^{\text{N}_2\text{O corr}} = -(7372 \pm 6) 10^{-9} \cdot 10^3 \delta^{13}\text{C}_{\text{VPDB}} \cdot \xi - (10064 \pm 5) 10^{-7} \cdot 10^3 \delta^{18}\text{O}_{\text{VPDB-CO}_2} \cdot \xi - (4984 \pm 3) 10^{-4} \cdot \xi \quad (\text{C.12})$$

$$10^3 \cdot {}^{47}\delta_{\text{VPDB, VPDB-CO}_2}^{\text{N}_2\text{O corr}} = -(9587 \pm 5) 10^{-7} \cdot 10^3 \delta^{13}\text{C}_{\text{VPDB}} \cdot \xi - (10013 \pm 5) 10^{-7} \cdot 10^3 \delta^{18}\text{O}_{\text{VPDB-CO}_2} \cdot \xi - (6824 \pm 4) 10^{-4} \cdot \xi \quad (\text{C.13})$$

$$10^3 \cdot {}^{48}\delta_{\text{VPDB, VPDB-CO}_2}^{\text{N}_2\text{O corr}} = -(1469 \pm 2) 10^{-8} \cdot 10^3 \delta^{13}\text{C}_{\text{VPDB}} \cdot \xi - (19725 \pm 9) 10^{-7} \cdot 10^3 \delta^{18}\text{O}_{\text{VPDB-CO}_2} \cdot \xi - (9989 \pm 5) 10^{-4} \cdot \xi \quad (\text{C.14})$$

$$10^3 \cdot {}^{49}\delta_{\text{VPDB, VPDB-CO}_2}^{\text{N}_2\text{O corr}} = -(1604 \pm 2) 10^{-8} \cdot 10^3 \delta^{13}\text{C}_{\text{VPDB}} \cdot \xi - (1550 \pm 2) 10^{-8} \cdot 10^3 \delta^{18}\text{O}_{\text{VPDB-CO}_2} \cdot \xi - (620 \pm 4) 10^{-5} \cdot \xi \quad (\text{C.15})$$

This was also done for a virtual work gas, for which the carbon and oxygen isotopes corresponded to VPDB and VSMOW, respectively:

$$10^3 \cdot {}^{45}\delta_{\text{VPDB, VSMOW}}^{\text{N}_2\text{O corr}} = -(9439 \pm 5) 10^{-7} \cdot 10^3 \delta^{13}\text{C}_{\text{VPDB}} \cdot \xi - (3594 \pm 2) 10^{-8} \cdot 10^3 \delta^{18}\text{O}_{\text{VSMOW}} \cdot \xi - (3499 \pm 2) 10^{-4} \cdot \xi \quad (\text{C.16})$$

$$10^3 \cdot {}^{46}\delta_{\text{VPDB, VSMOW}}^{\text{N}_2\text{O corr}} = -(7179 \pm 6) 10^{-9} \cdot 10^3 \delta^{13}\text{C}_{\text{VPDB}} \cdot \xi - (10060 \pm 5) 10^{-7} \cdot 10^3 \delta^{18}\text{O}_{\text{VSMOW}} \cdot \xi - (4773 \pm 3) 10^{-4} \cdot \xi \quad (\text{C.17})$$

$$10^3 \cdot {}^{47}\delta_{\text{VPDB, VSMOW}}^{\text{N}_2\text{O corr}} = -(9591 \pm 5) 10^{-7} \cdot 10^3 \delta^{13}\text{C}_{\text{VPDB}} \cdot \xi - (10006 \pm 5) 10^{-7} \cdot 10^3 \delta^{18}\text{O}_{\text{VSMOW}} \cdot \xi - (6687 \pm 4) 10^{-4} \cdot \xi \quad (\text{C.18})$$

$$10^3 \cdot {}^{48}\delta_{\text{VPDB, VSMOW}}^{\text{N}_2\text{O corr}} = -(1476 \pm 2) 10^{-8} \cdot 10^3 \delta^{13}\text{C}_{\text{VPDB}} \cdot \xi - (19720 \pm 9) 10^{-7} \cdot 10^3 \delta^{18}\text{O}_{\text{VSMOW}} \cdot \xi - (9981 \pm 5.0) 10^{-4} \cdot \xi \quad (\text{C.19})$$

$$10^3 \cdot {}^{49}\delta_{\text{VPDB, VSMOW}}^{\text{N}_2\text{O corr}} = -(1586 \pm 2) 10^{-8} \cdot 10^3 \delta^{13}\text{C}_{\text{VPDB}} \cdot \xi - (1499 \pm 2) 10^{-8} \cdot 10^3 \delta^{18}\text{O}_{\text{VSMOW}} \cdot \xi - (601 \pm 3) 10^{-5} \cdot \xi \quad (\text{C.20})$$

## C.2. Re-Equilibration of CO<sub>2</sub> with and without Water

According to *Clog et al., 2015*,  $\Delta_{47}$  at time  $t$  during CO<sub>2</sub> re-equilibration can be calculated as follows:

$$10^3 \Delta_{47}(t) = 10^3 \Delta_{47_{\text{equilibration}}} + (10^3 \Delta_{47_{\text{initial}}} - 10^3 \Delta_{47_{\text{equilibration}}}) \times e^{-k \cdot t} \quad (\text{C.21})$$

Here,  $\Delta_{47_{\text{initial}}}$  is the initial equilibrium value of the gas, and  $\Delta_{47_{\text{equilibration}}}$  is the value to which the gas re-equilibrates.  $k$  is the reaction rate constant. According to *Kalb et al., 2020*,  $k$  in dependence of temperature  $T$  can be calculated for pure CO<sub>2</sub> that comes into contact with water in a limited shaken volume (borosilicate glass tubes) as follows:

$$k(T)[\text{h}^{-1}] = (3300 \pm 1400)[\text{h}^{-1}] \times \exp \left( \frac{-(22.9 \pm 1.6) \left[ \frac{\text{kJ}}{\text{mol}} \right]}{8.314 \left[ \frac{\text{J}}{\text{mol} \cdot \text{K}} \right] \cdot T[\text{K}]} \right) \quad (\text{C.22})$$

*Eobaldt, 2019* conducted experiments on the equilibrium of high-purity CO<sub>2</sub> sealed in glass tubes at temperatures ranging from 90 to 400 °C in the absence of liquid water. He determined  $k(T)$  as follows:

$$k(T)[\text{h}^{-1}] = (51500 \pm 4600)[\text{h}^{-1}] \times \exp \left( \frac{-(51.7 \pm 3.7) \left[ \frac{\text{kJ}}{\text{mol}} \right]}{8.314 \left[ \frac{\text{J}}{\text{mol} \cdot \text{K}} \right] \cdot T[\text{K}]} \right) \quad (\text{C.23})$$



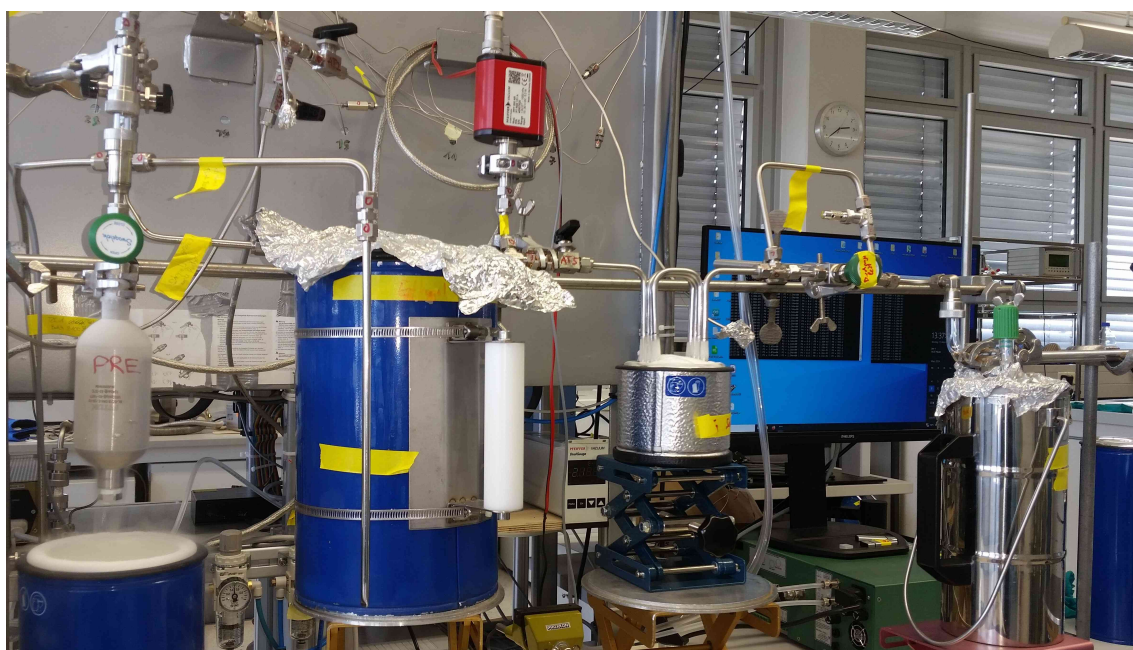
### **C.3. Supplementary Material on Calibration**

#### **Images on Production of temperature-equilibrated CO<sub>2</sub> Standards**



**Figure C.1.:** This image shows the ~190 mL glass cylinder used as a re-equilibration vessel for producing temperature-equilibrated CO<sub>2</sub> standards. The image also shows the temperature-regulated water bath (F3/S; Haake Fisons) used for re-equilibration.





**Figure C.2.:** This is the manual preparation line used to transfer the re-equilibrated standards from the re-equilibration vessels on the right to the stainless steel sample containers on the left. This image shows the final step of the process when the  $\text{CO}_2$  has been transferred to the stainless steel container. Initially, the trap on the right side of the image is immersed in an ethanol-dry ice bath to remove remaining water.

## Data on Calibration

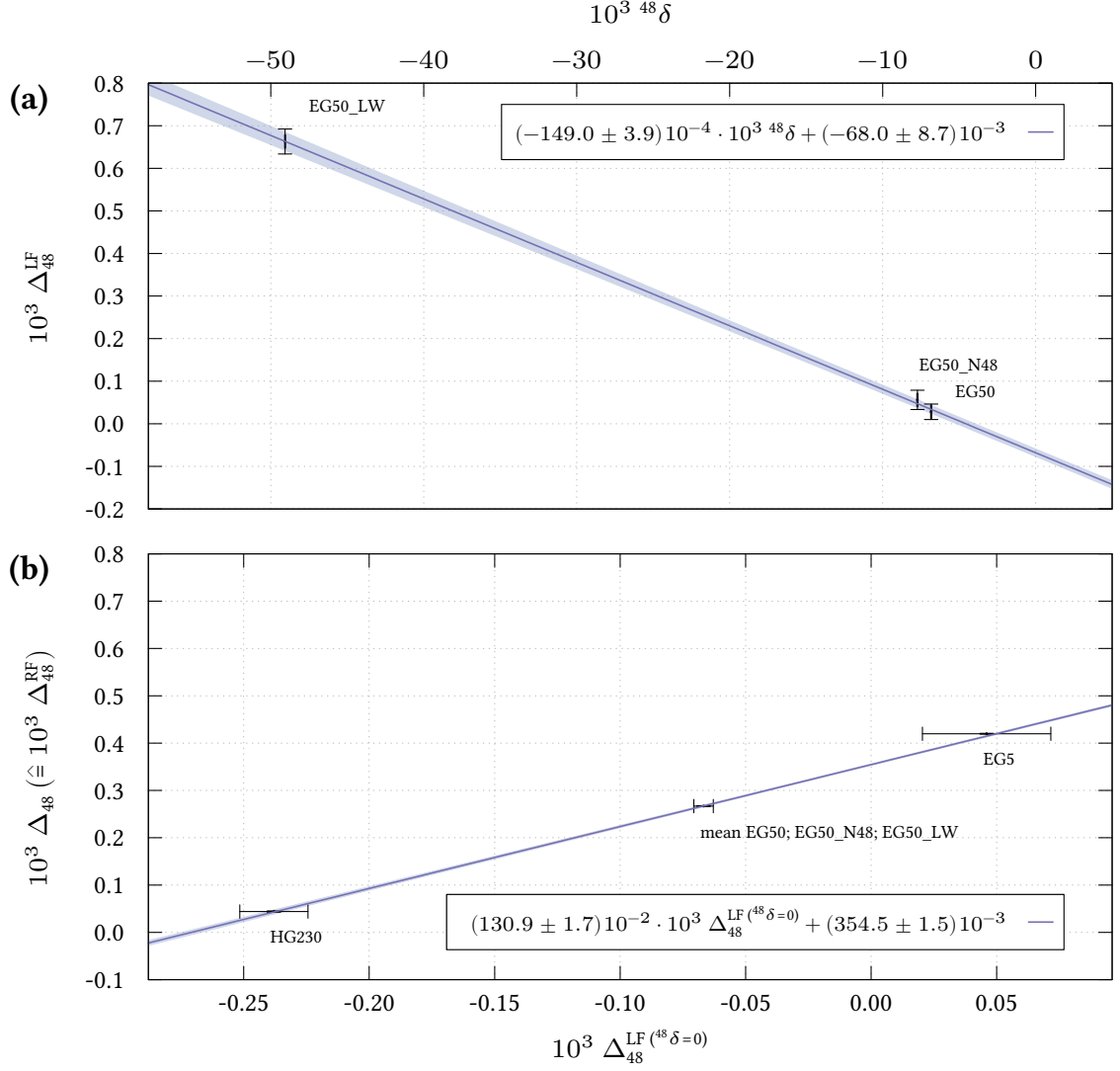
**Table C.1.:** The measured equilibration temperatures of the produced temperature-equilibrated standards are listed in column 2. The errors were generously estimated based on the SD of the temperature readings during the equilibration process. The temperatures were used to calculate  $\Delta_{47}^{\text{RF}}$ ,  $\Delta_{48}^{\text{RF}}$ , and  $\Delta_{49}^{\text{RF}}$  in the reference frame (RF). Equation (2.26), provided by *Dennis et al., 2011*, was used to calculate  $\Delta_{47}^{\text{RF}}$ .  $\Delta_{48}^{\text{RF}}$  and  $\Delta_{49}^{\text{RF}}$  were calculated as described in section 2.3.

Standard	$T_{\text{equilibration}} [^{\circ}\text{C}]$	$10^3 \Delta_{47}^{\text{RF}}$	$10^3 \Delta_{48}^{\text{RF}}$	$10^3 \Delta_{49}^{\text{RF}}$
HG230	233.8 $\pm 3.0$	0.331 $\pm 0.005$	0.0440 $\pm 0.0013$	0.736 $\pm 0.011$
EG5	4.6 $\pm 0.2$	1.041 $\pm 0.002$	0.4198 $\pm 0.0009$	2.558 $\pm 0.004$
EG50	49.8 $\pm 0.3$	0.805 $\pm 0.002$	0.2669 $\pm 0.0008$	1.924 $\pm 0.004$
EG50_LW	49.8 $\pm 0.3$	0.805 $\pm 0.002$	0.2669 $\pm 0.0008$	1.924 $\pm 0.004$
EG50_N48	49.8 $\pm 0.3$	0.805 $\pm 0.002$	0.2669 $\pm 0.0008$	1.924 $\pm 0.004$

**Table C.2.:** Mean measurement results for the temperature-equilibrated CO<sub>2</sub> standards. This data was used to correct the dependencies of  $\Delta_{47}^{\text{LF}}$  on  $^{47}\delta$ ,  $\Delta_{48}^{\text{LF}}$  on  $^{48}\delta$ , and  $\Delta_{49}^{\text{LF}}$  on  $^{49}\delta$ . Due to observed drift in the standards over time, only initial measurements taken after production were used to calculate the listed means. Errors are weighted SEM of considered measurements.

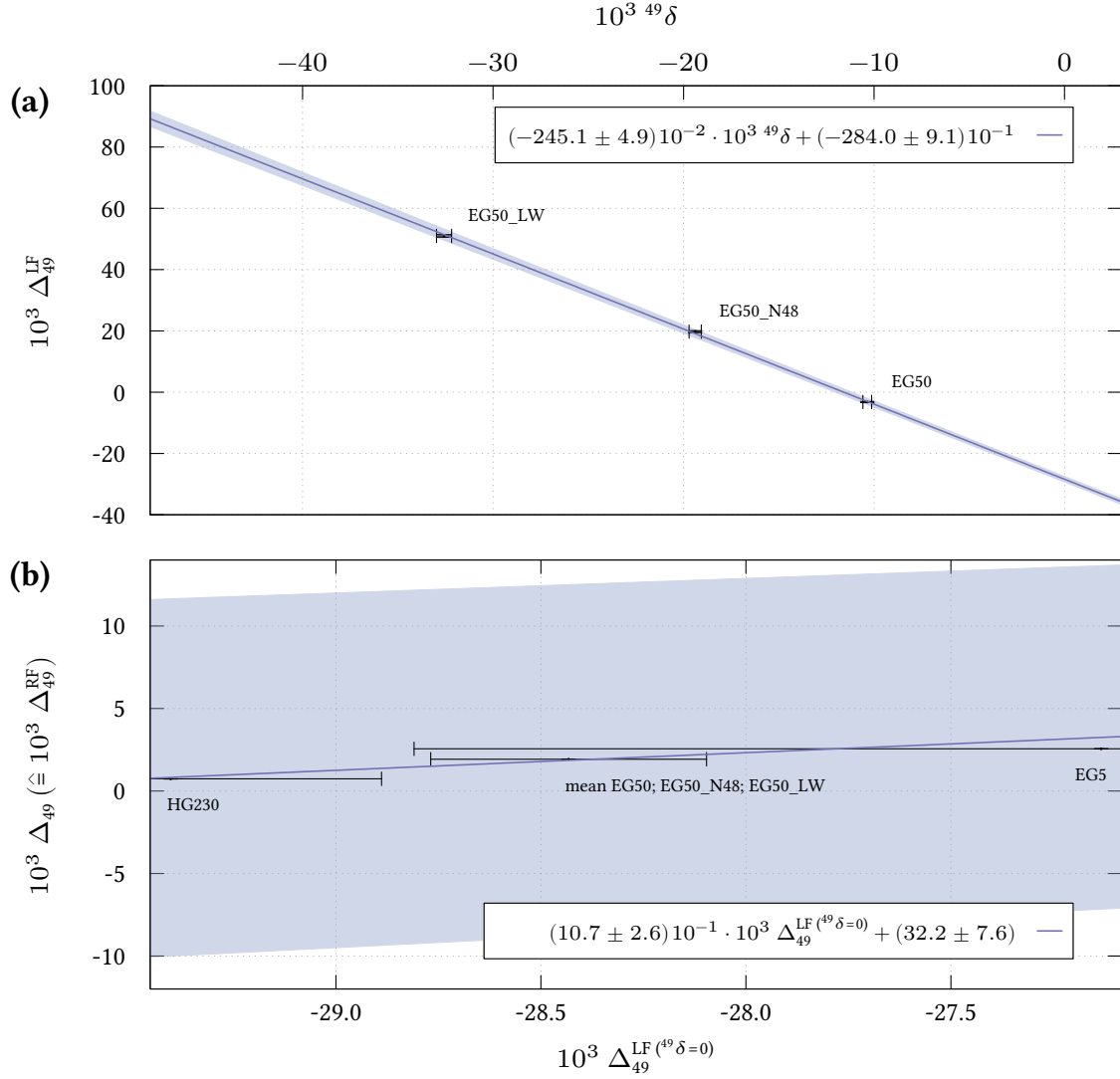
Standard	$10^3 ^{47}\delta$	$10^3 \Delta_{47}^{\text{LF}}$	$10^3 ^{48}\delta$	$10^3 \Delta_{48}^{\text{LF}}$	$10^3 ^{49}\delta$	$10^3 \Delta_{49}^{\text{LF}}$
HG230	-0.383 $\pm 0.024$	-0.499 $\pm 0.001$	0.507 $\pm 0.022$	-0.246 $\pm 0.014$	-8.39 $\pm 0.12$	-8.85 $\pm 0.12$
EG5	4.862 $\pm 0.015$	0.094 $\pm 0.004$	9.699 $\pm 0.034$	-0.099 $\pm 0.026$	-5.13 $\pm 0.63$	-14.55 $\pm 0.63$
EG50	-3.897 $\pm 0.011$	-0.102 $\pm 0.011$	-6.829 $\pm 0.033$	0.028 $\pm 0.019$	-10.36 $\pm 0.23$	-3.21 $\pm 0.19$
EG50_LW	-55.264 $\pm 0.013$	-0.056 $\pm 0.004$	-49.064 $\pm 0.028$	0.663 $\pm 0.030$	-32.57 $\pm 0.40$	51.00 $\pm 0.44$
EG50_N48	-33.781 $\pm 0.001$	-0.084 $\pm 0.005$	-7.730 $\pm 0.037$	0.056 $\pm 0.023$	-19.39 $\pm 0.32$	19.76 $\pm 0.34$

### Calibration of $\Delta_{48}$ and Correction on $^{48}\delta$



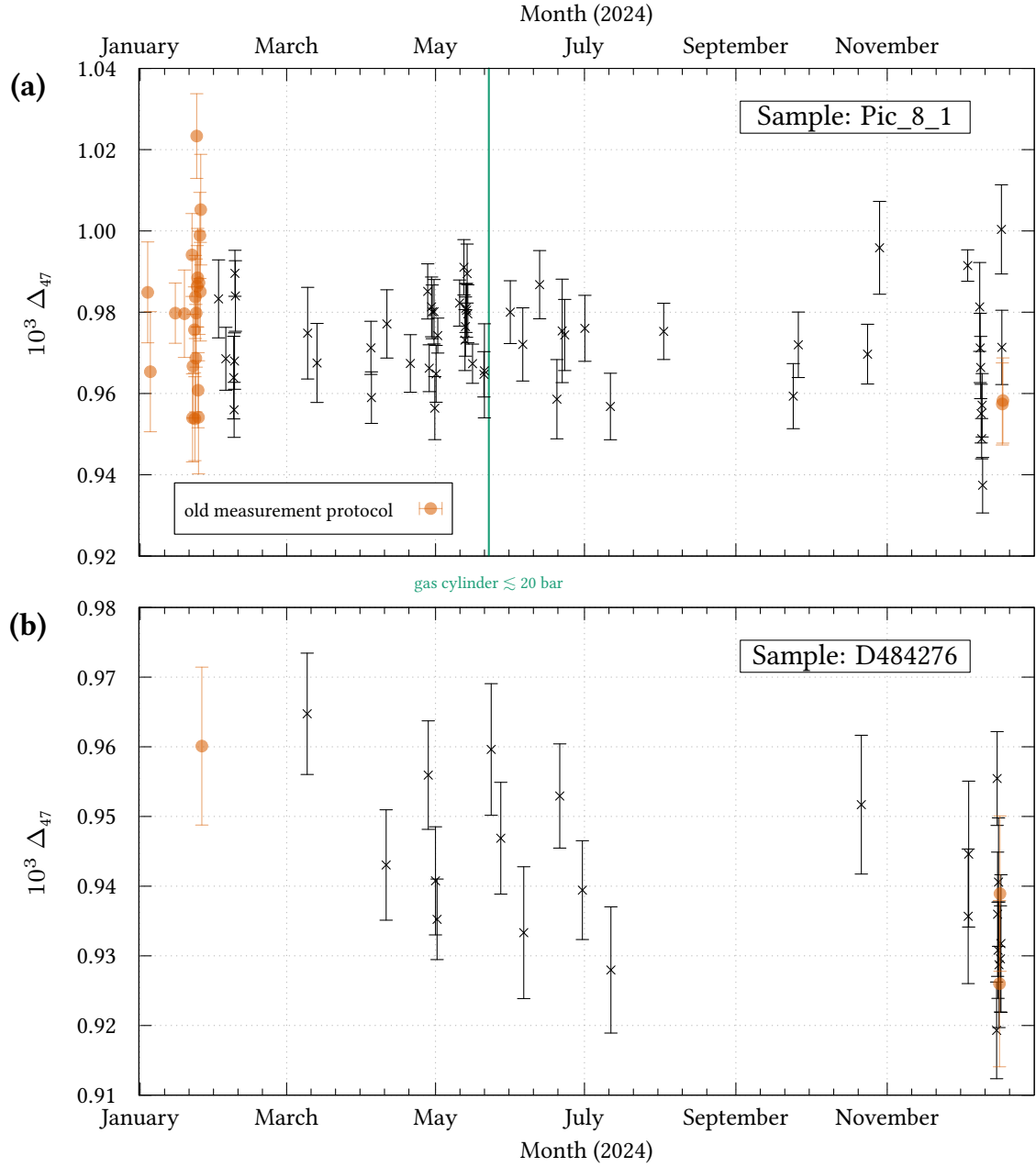
**Figure C.3.:**  $\Delta_{48}^{\text{LF}}$  in the laboratory frame (LF) plotted against  $^{48}\delta$  for “EG50”, “EG50\_N48”, and “EG50\_LW”, which have the same equilibration temperature of  $\sim 49.8^\circ\text{C}$  (a). The slope of the fitted line is used to adjust the value of  $\Delta_{48}^{\text{LF}}$  as if  $^{48}\delta$  were equal to zero. (b) shows  $\Delta_{48}^{\text{RF}}$  for the corresponding equilibration temperatures plotted against the correspondingly corrected  $\Delta_{48}^{\text{LF}} ({}^{48}\delta=0)$ .  $\Delta_{48}^{\text{RF}}$  is calculated as described in section 2.3.  $\Delta_{48}^{\text{LF}} ({}^{48}\delta=0)$  of “EG50”, “EG50\_N48”, and “EG50\_LW” was weighted averaged. The linear fitted function can be used for calibration. However, due to a superimposed drift in  $\Delta_{48}^{\text{LF}}$ , this was only valid from early March to early May of 2024. Nevertheless, the successful calibration on  $\Delta_{48}$  indicates the quality of the preparation and the selected measurement method.

### Calibration of $\Delta_{49}$ and Correction on $^{49}\delta$



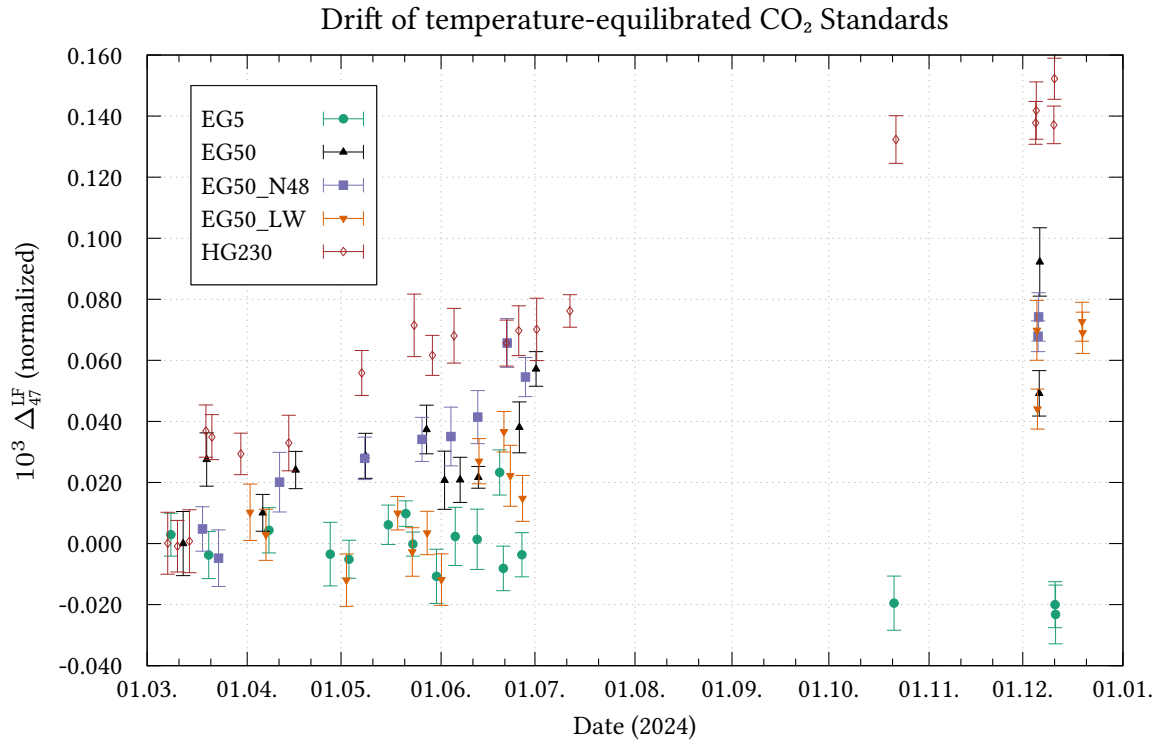
**Figure C.4.:**  $\Delta_{49}^{\text{LF}}$  in the laboratory frame (LF) plotted against  $^{49}\delta$  for “EG50”, “EG50\_N48”, and “EG50\_LW”, which have the same equilibration temperature of  $\sim 49.8$  °C (a). The slope of the fitted line is used to adjust the value of  $\Delta_{49}^{\text{LF}}$  as if  $^{49}\delta$  were equal to zero. (b) shows  $\Delta_{49}^{\text{RF}}$  for the corresponding equilibration temperatures plotted against the correspondingly corrected  $\Delta_{49}^{\text{LF}} ({}^{49}\delta = 0)$ .  $\Delta_{49}^{\text{RF}}$  is calculated as described in section 2.3.  $\Delta_{49}^{\text{LF}} ({}^{49}\delta = 0)$  of “EG50”, “EG50\_N48”, and “EG50\_LW” was weighted averaged. The calibration curve is unreliable due to the uncertainty of the data. More frequent measurements of the calibration standards may have enabled reliable calibration. However, due to a drift in the calibration standards and an overlaying drift in  $\Delta_{49}^{\text{LF}}$ , this was not possible within the scope of this work.

### Calibrated $\Delta_{47}$ for Measurements of “Pic\_8\_1” and “D484276”

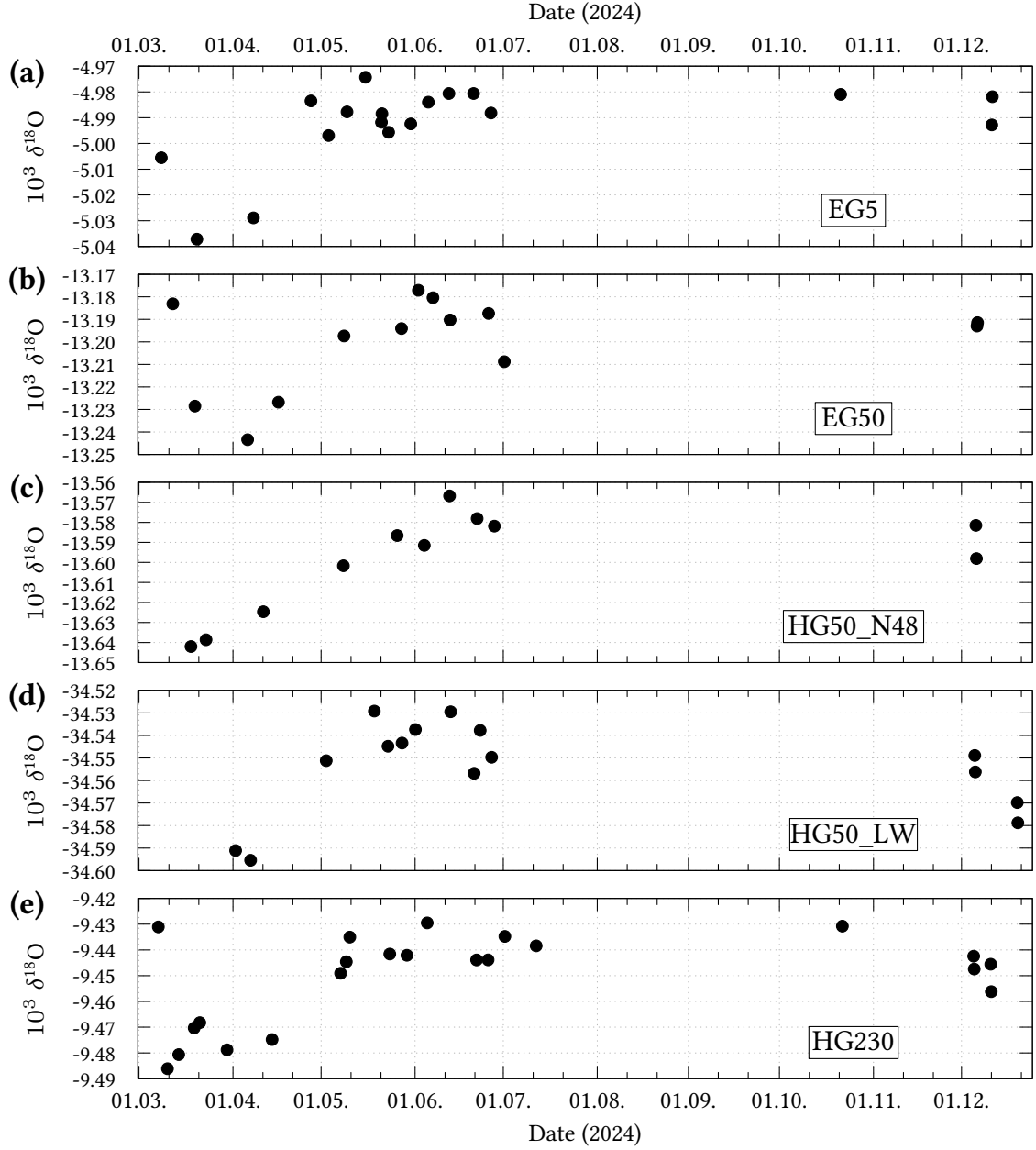


**Figure C.5.:** The graph shows the calibrated  $\Delta_{47}$  for measurements of “Pic\_8\_1” and “D484276”, conducted in 2024, with statistical SEM errors. Measurements performed according to the old protocol are marked in orange (see subsection 2.5.4). No major trends are evident. Based on the “D484276” results (b) alone, one might conclude that the values are slightly higher in January to early March, by up to 0.02 ‰. Additionally,  $\Delta_{47}$  results from “Pic\_8\_1” (a) appear stable at gas cylinder pressures below 20 bar. However, dispersion increases in December, especially in the “Pic\_8\_1” results. This could be due to the sharply declining working standard and the differences it causes in the intermediate volume’s multiple use in the refill process.

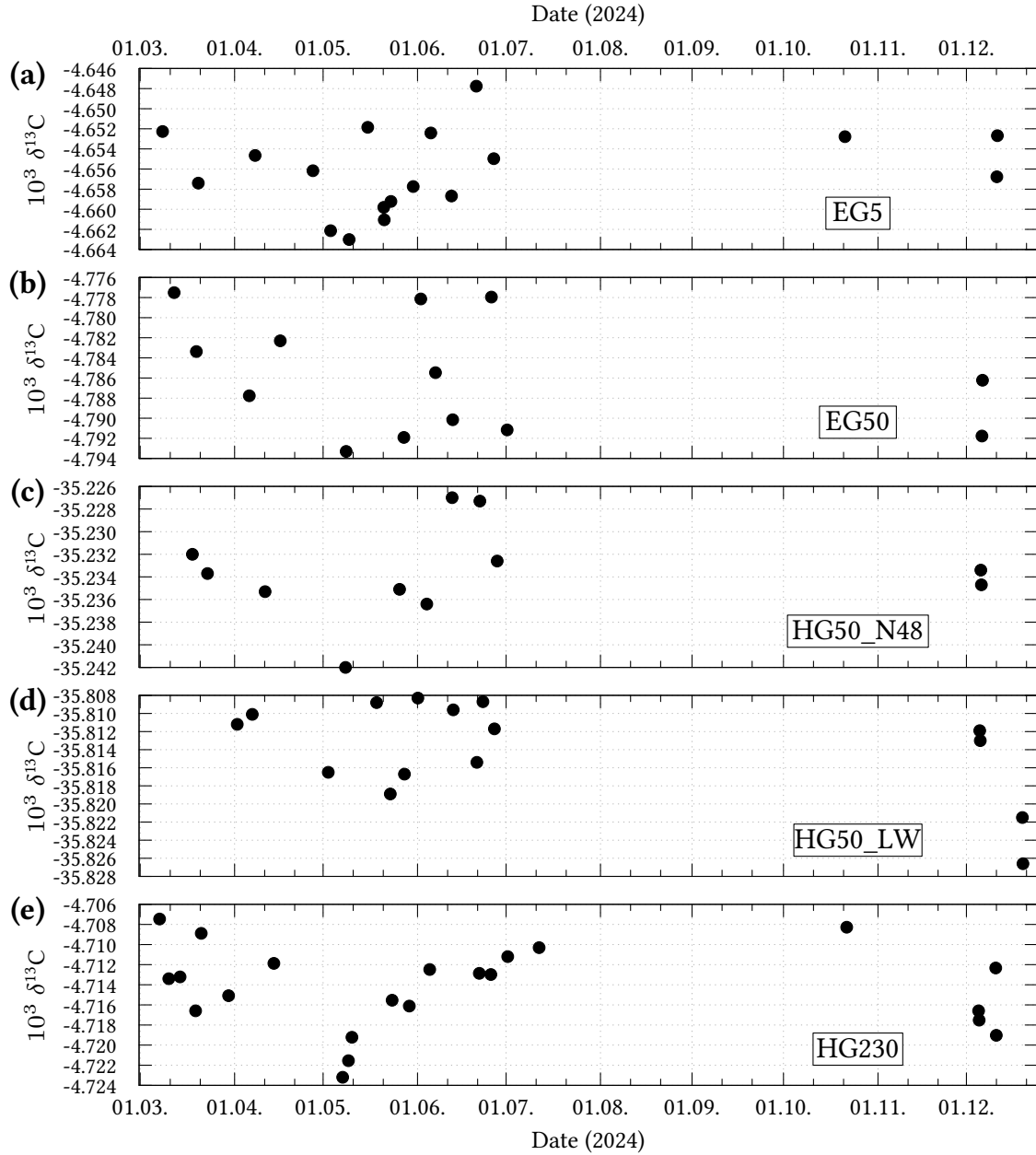
## Drift of Standards for $\Delta_{47}$



**Figure C.6.:** The observed drift of the temperature-equilibrated CO<sub>2</sub> standards is shown (errors: SEM). The data are presented in the laboratory frame (LF) and have been normalized by subtracting the mean of the initial measurements taken after preparing the standards. Standard “EG5”, equilibrated at  $\sim 4.6$  °C, is drifting toward a lower  $\Delta_{47}^{LF}$  (higher temperatures). The other standards, equilibrated at  $\sim 49.8$  °C and  $\sim 233.8$  °C, are drifting toward higher  $\Delta_{47}^{LF}$  (lower temperatures). This suggests drift toward room temperature, which was approximately 24 °C. Due to this drift, only the initial measurements of these standards could be used for calibration.



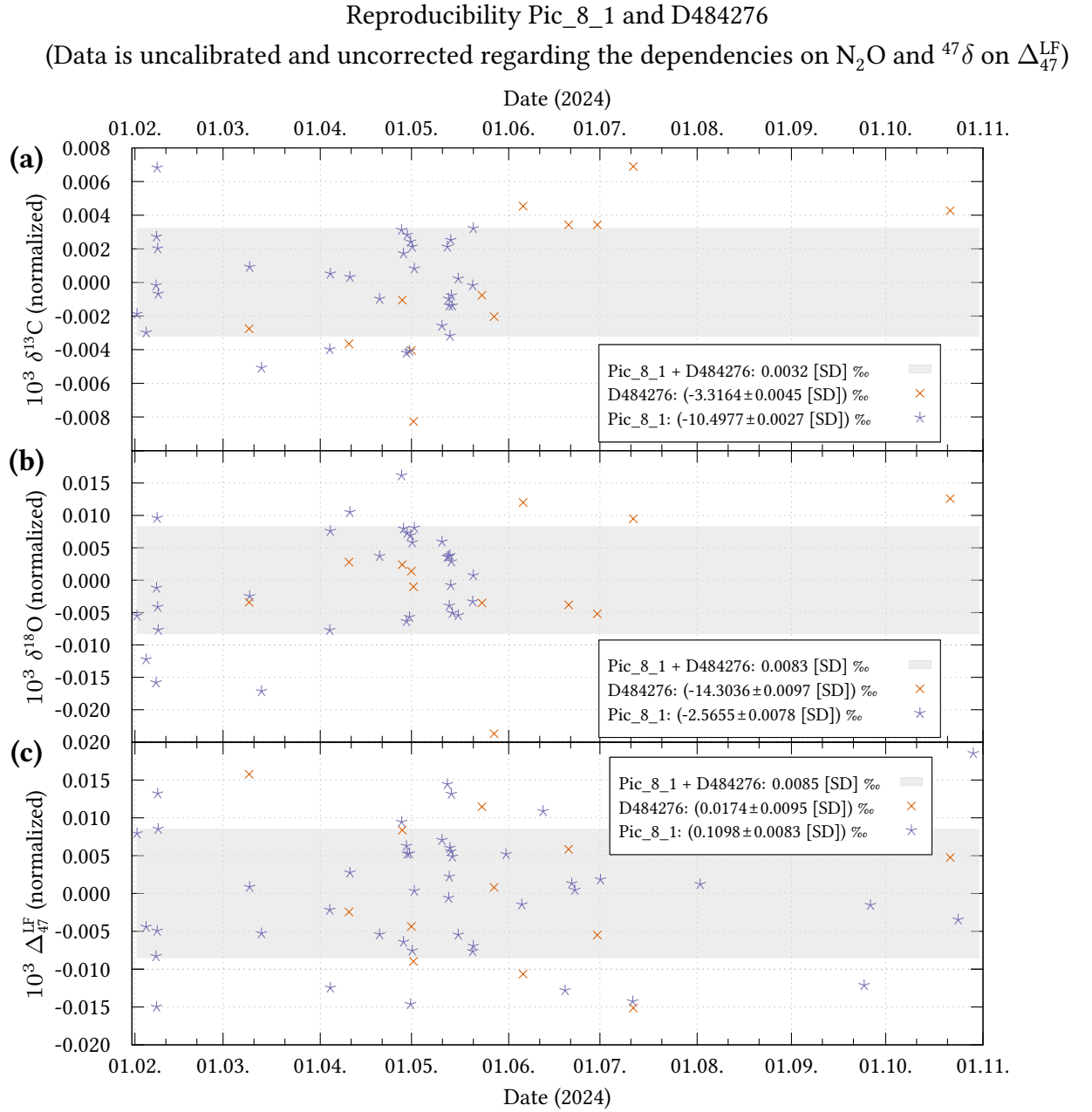
**Figure C.7.:** Drift in calibrated  $\delta^{18}\text{O}$  of temperature-equilibrated  $\text{CO}_2$  standards: “EG5” (a), “EG50” (b), “EG5\_N48” (c), “EG50\_LW” (d), and “HG230 ”(e). Interestingly, “EG”, “EG50”, and “HG230” all exhibit higher initial results, forming a large dip. After a few months, the  $\delta^{18}\text{O}$  values of all standards appear to stabilize, possibly indicating isotopic equilibrium with trace amounts of water or stabilization of the inner surface of the cylinders. The “EG50\_LW” values in December might have been affected by emptying the standard or by altered reference refill effects when using the intermediate volume, since it is also seen in  $\delta^{13}\text{C}$  (see Figure C.8).



**Figure C.8.:**  $\delta^{13}\text{C}$  of temperature-equilibrated  $\text{CO}_2$  standards over time: “EG5” (a), “EG50” (b), “EG5\_N48” (c), “EG50\_LW” (d), and “HG230 ”(e). Interestingly, “EG”, “EG50”, and “HG230” all exhibit higher initial results, forming a large dip. The “EG50\_LW” values in December might have been affected by emptying the standard or by altered reference refill effects when using the intermediate volume, since it is also seen in  $\delta^{18}\text{O}$  (see Figure C.7).



## C.4. Supplementary Material on Reproducibility



**Figure C.9.:** Reproducibility of (raw)  $\delta^{13}\text{C}$  (a),  $\delta^{18}\text{O}$  (b), and  $\Delta_{47}^{\text{LF}}$  (c) measurements from gas tanks “Pic\_8\_1” and “D484276” over the period of February 1 - November 1, 2024, expressed as SD. Compared to pure background-corrected raw data, only corrections on imbalance at  $m/z$  44 (see appendix A.5; page 135ff) and drift with number of reference refills (see appendix B.17; page 169ff) were applied to  $\delta^{13}\text{C}$  and  $\delta^{18}\text{O}$ . Measurement values were normalized to their respective means (see legend).  $\delta^{13}\text{C}$  and  $\delta^{18}\text{O}$  were excluded for “Pic\_8\_1” results after May 23, 2024, due to gas tank depletion and related superimposed drift (see section 4.2; page 59). For the 44 considered measurements the SD for  $\delta^{13}\text{C}$  and  $\delta^{18}\text{O}$  are conservatively rounded to  $\sim 0.005$  ‰ and  $0.01$  ‰, respectively. The SD for the 57  $\Delta_{47}^{\text{LF}}$  results is  $\sim 0.009$  ‰.

## *Appendices*

## D. Supplementary Material on Chapter 5

### D.1. Supplementary Material on Nonlinear Mixing of $\Delta_{47}$

**Table D.1.:** Measurement results of the temperature-equilibrated CO<sub>2</sub> standards for the relevant time periods of  $\Delta_{47}$  mixing experiments 1 and 2 (Errors:  $\pm 1$  SD). These data are used to calculate the theoretical values of the mixing experiments and apply the mixing correction Equation (5.4).

CO <sub>2</sub> -standard	Period (2024)	# of data	$10^3 \delta^{13}\text{C}$	$10^3 \delta^{18}\text{O}$	$10^3 \Delta_{47}$	$T_{\text{from } \Delta_{47}} [\text{K}]$
EG5	20.06.-28.06.	4	$-4.653 \pm 0.005$	$-4.899 \pm 0.006$	$1.043 \pm 0.003$	$277.4 \pm 0.4$
EG50_LW	12.06.-28.06.	4	$-35.811 \pm 0.004$	$-34.619 \pm 0.013$	$0.825 \pm 0.011$	$318.6 \pm 2.5$
EG50_N48	22.06.-29.06.	2	$-35.230 \pm 0.004$	$-13.540 \pm 0.003$	$0.861 \pm 0.010$	$310.8 \pm 2.0$
HG230	22.06.-02.07.	3	$-4.712 \pm 0.002$	$-9.378 \pm 0.006$	$0.416 \pm 0.004$	$455.6 \pm 1.6$

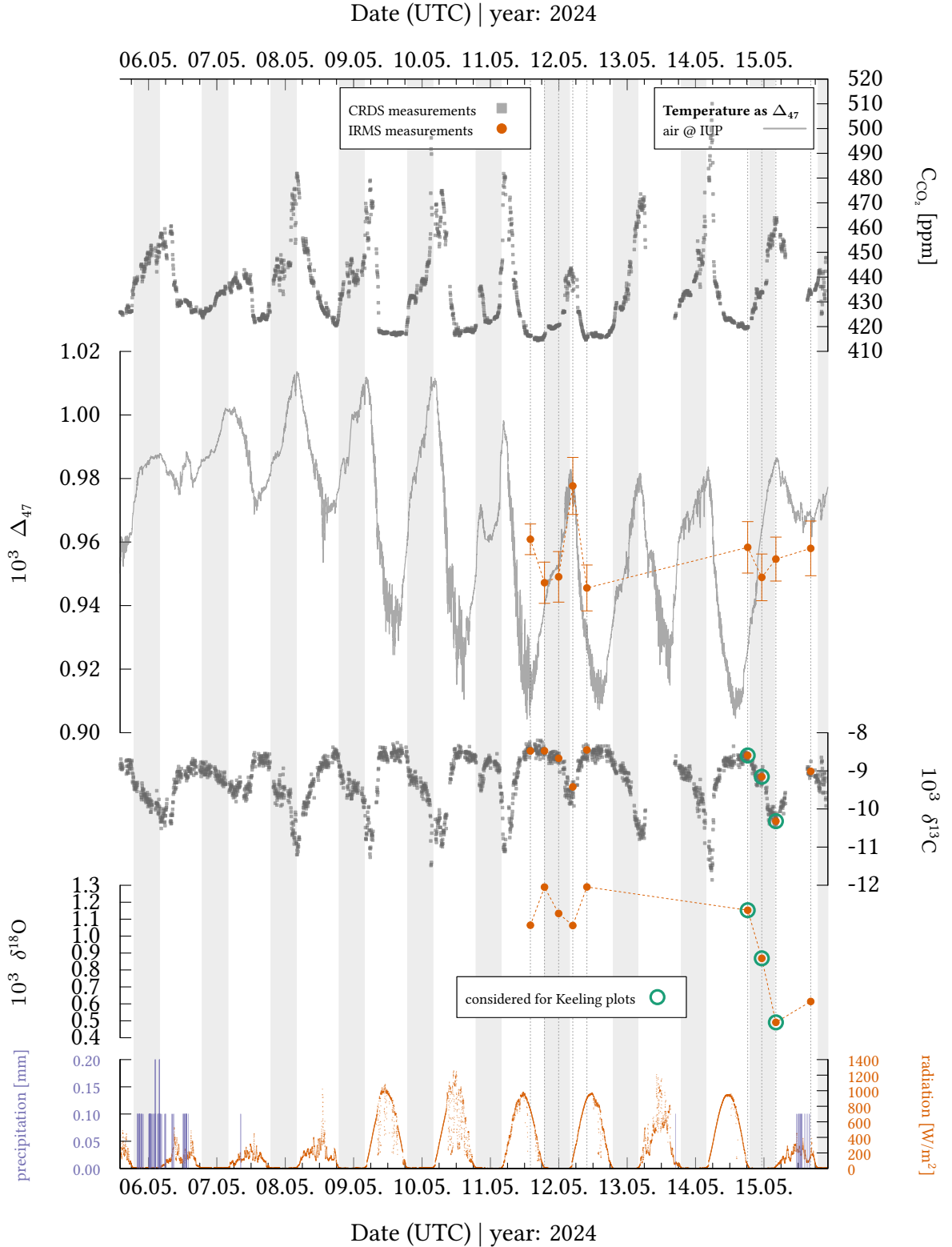
**Table D.2.:** Measurement results of  $\Delta_{47}$  mixing experiments 1 and 2. Additional theoretical values  $\Delta_{47}^{\text{mix (theory)}}$  were calculated from mixing fractions  $f$  and temperature-equilibrated CO<sub>2</sub> standards results (see Table D.1). Mixing fractions  $f$  were determined from pressure sensor readings during mixture preparation.  $\Delta_{47}^{\text{mix-corrected}}$  is calculated using Equation (5.4) and results of temperature-equilibrated CO<sub>2</sub> standards. Errors of  $\Delta_{47}$  are  $\pm 1$  SEM and total errors. The latter are marked with  $\dagger$  and include systematic errors from calibration and corrections.

Time	$f$	$10^3 \delta^{13}\text{C}$	$10^3 \delta^{18}\text{O}$	$10^3 \Delta_{47}$	$10^3 \Delta_{47}^{\text{mix (theory)}}$	$10^3 \Delta_{47}^{\text{mix-corrected}}$
$\Delta_{47}$ mixing experiment 1: two-component mixture ( $f = f_{\text{EG5}}$ )						
20/06/2024 19:33:15	$0.464 \pm 0.003$	$\approx -21.348$	$\approx -20.838$	$1.209 \pm 0.010 \pm 0.018^\dagger$	1.160	$0.986 \pm 0.019^\dagger$
21/06/2024 19:49:44	$0.317 \pm 0.003$	$\approx -25.855$	$\approx -25.106$	$1.108 \pm 0.007 \pm 0.016^\dagger$	1.100	$0.914 \pm 0.017^\dagger$
22/06/2024 19:46:43	$0.713 \pm 0.003$	$\approx -13.632$	$\approx -13.514$	$1.178 \pm 0.007 \pm 0.014^\dagger$	1.169	$0.995 \pm 0.015^\dagger$
$\Delta_{47}$ mixing experiment 2: three-component mixture						
01/07/2024 02:04:58	$f_{\text{EG5}} = 0.424 \pm 0.003$ $f_{\text{EG50\_N48}} = 0.318 \pm 0.003$	$\approx -14.440$	$\approx -8.880$	$0.890 \pm 0.008 \pm 0.013^\dagger$	0.870	

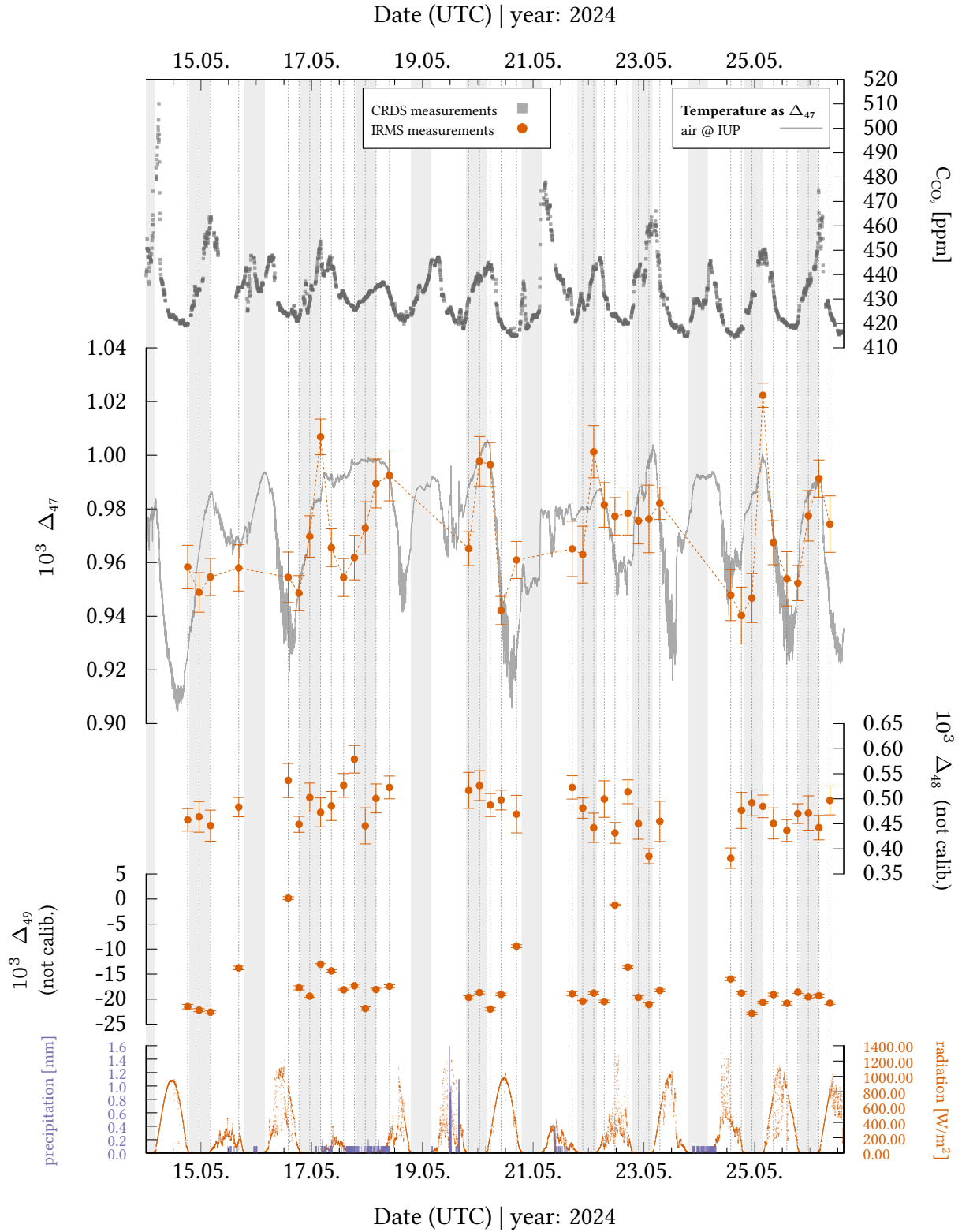
## D.2. Supplementary Material on Ambient Air Measurements

**Table D.3.:**  $\delta^{13}\text{C}_{\text{source}}$  and  $\delta^{18}\text{O}_{\text{source}}$  ( $\pm$ fit error) were obtained from Keeling plots using York fits for the nights listed in column 1.  $\delta^{13}\text{C}_{\text{min}}$  ( $\pm$ SD) are the means of CRDS measurements taken 20 minutes before and after the midday  $\text{CO}_2$  minimum ( $\text{C}_{\text{CO}_2\text{-min}}$ ).  $\text{C}_{\text{CO}_2\text{-max}}$  is the maximum nightly  $\text{CO}_2$  concentration.  $\delta^{18}\text{O}_{\text{source}}$  displayed using this color code are from measurements taken on nights with no rain, and at least 12 hours had passed since the last rainfall. Only results from Keeling plots with a Pearson's  $r^2$  of  $\geq 0.9$  are considered.

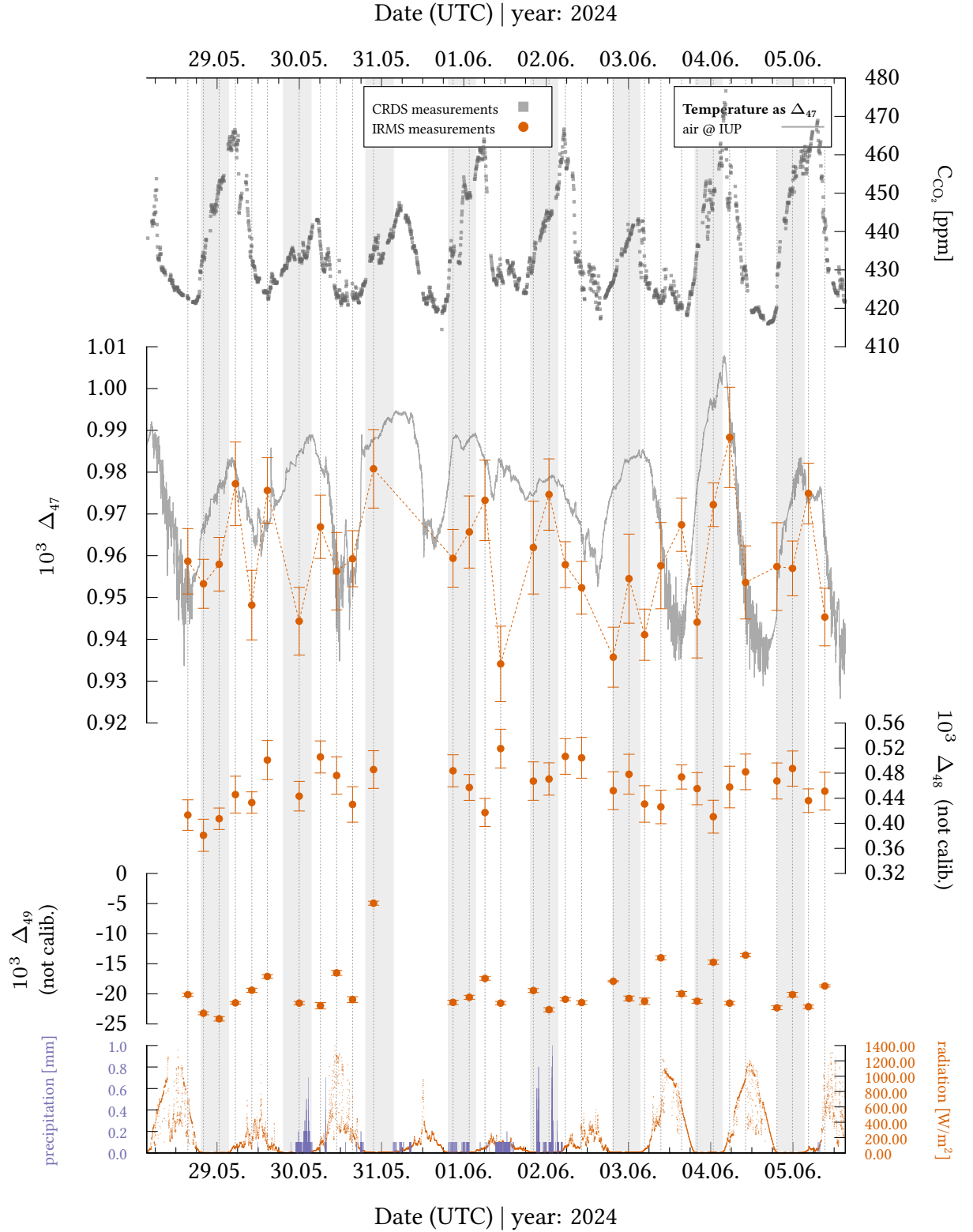
Night	$10^3 \delta^{13}\text{C}_{\text{source}}$	$10^3 \delta^{18}\text{O}_{\text{source}}$	comment	$10^3 \delta^{13}\text{C}_{\text{min}}$	$\text{C}_{\text{CO}_2\text{-min}}$ [ppm]	$\text{C}_{\text{CO}_2\text{-max}}$ [ppm]
14.05.-15.05.	-26.65 $\pm 0.10$ $r^2 \approx 0.99$	-6.80 $\pm 0.10$ $r^2 \approx 0.99$		-8.61 $\pm 0.11$	419.0	463.9
16.05.-17.05.	-28.42 $\pm 0.21$ $r^2 \approx 0.99$	$r^2 < 0.9$	nightly rain	-8.59 $\pm 0.05$	420.9	453.7
17.05.-18.05.	-28.75 $\pm 0.14$ $r^2 \approx 0.99$	-27.84 $\pm 0.20$ $r^2 \approx 0.95$	nightly rain	-8.95 $\pm 0.11$	425.6	437.0
19.05.-20.05.	-28.03 $\pm 0.34$ $r^2 \approx 0.99$	-27.35 $\pm 0.50$ $r^2 \approx 0.97$	midday 19.05. & little nightly rain	-8.55 $\pm 0.10$	417.8	444.9
21.05.-22.05.	-27.92 $\pm 0.17$ $r^2 \approx 0.99$	$r^2 < 0.9$		-8.62 $\pm 0.10$	420.5	446.9
22.05.-23.05.	-27.84 $\pm 0.17$ $r^2 \approx 0.99$	-10.12 $\pm 0.10$ $r^2 \approx 0.98$		-8.66 $\pm 0.10$	419.7	466.1
24.05.-25.05.	-27.97 $\pm 0.17$ $r^2 \approx 0.99$	-18.99 $\pm 0.17$ $r^2 \approx 0.99$	morning 24.05. rain	-8.29 $\pm 0.06$	414.1	450.5
25.05.-26.05.	-27.41 $\pm 0.20$ $r^2 \approx 0.99$	-10.89 $\pm 0.13$ $r^2 \approx 0.99$		-8.54 $\pm 0.11$	417.9	474.7
28.05.-29.05.	-27.55 $\pm 0.30$ $r^2 \approx 0.99$	$r^2 < 0.9$		-8.71 $\pm 0.10$	421.3	466.5
31.05.-01.06.	-28.21 $\pm 0.17$ $r^2 \approx 0.99$	-15.04 $\pm 0.13$ $r^2 \approx 0.99$	nightly rain	-8.39 $\pm 0.07$	414.5	464.1
01.06.-02.06.	-28.94 $\pm 0.20$ $r^2 \approx 0.99$	-12.59 $\pm 0.12$ $r^2 \approx 0.99$	heavy nightly rain	-8.70 $\pm 0.12$	423.9	466.1
04.06.-05.06.	-27.96 $\pm 0.44$ $r^2 \approx 0.99$	-13.24 $\pm 0.35$ $r^2 \approx 0.96$		-8.52 $\pm 0.05$	416.0	468.9
13.06.-14.06.	-27.54 $\pm 0.14$ $r^2 \approx 0.99$	$r^2 \ll 0.9$		-8.59 $\pm 0.08$	418.3	466.2
14.06.-15.06.	-26.73 $\pm 0.31$ $r^2 \approx 0.99$	$r^2 \ll 0.9$	nightly rain	-8.75 $\pm 0.07$	421.0	433.3
15.06.-16.06.	-27.61 $\pm 0.23$ $r^2 \approx 0.99$	$r^2 \ll 0.9$		-8.64 $\pm 0.03$	419.6	438.2
16.06.-17.06.	-30.19 $\pm 0.27$ $r^2 \approx 0.99$	$r^2 \ll 0.9$	nightly rain	-8.50 $\pm 0.12$	417.2	447.1



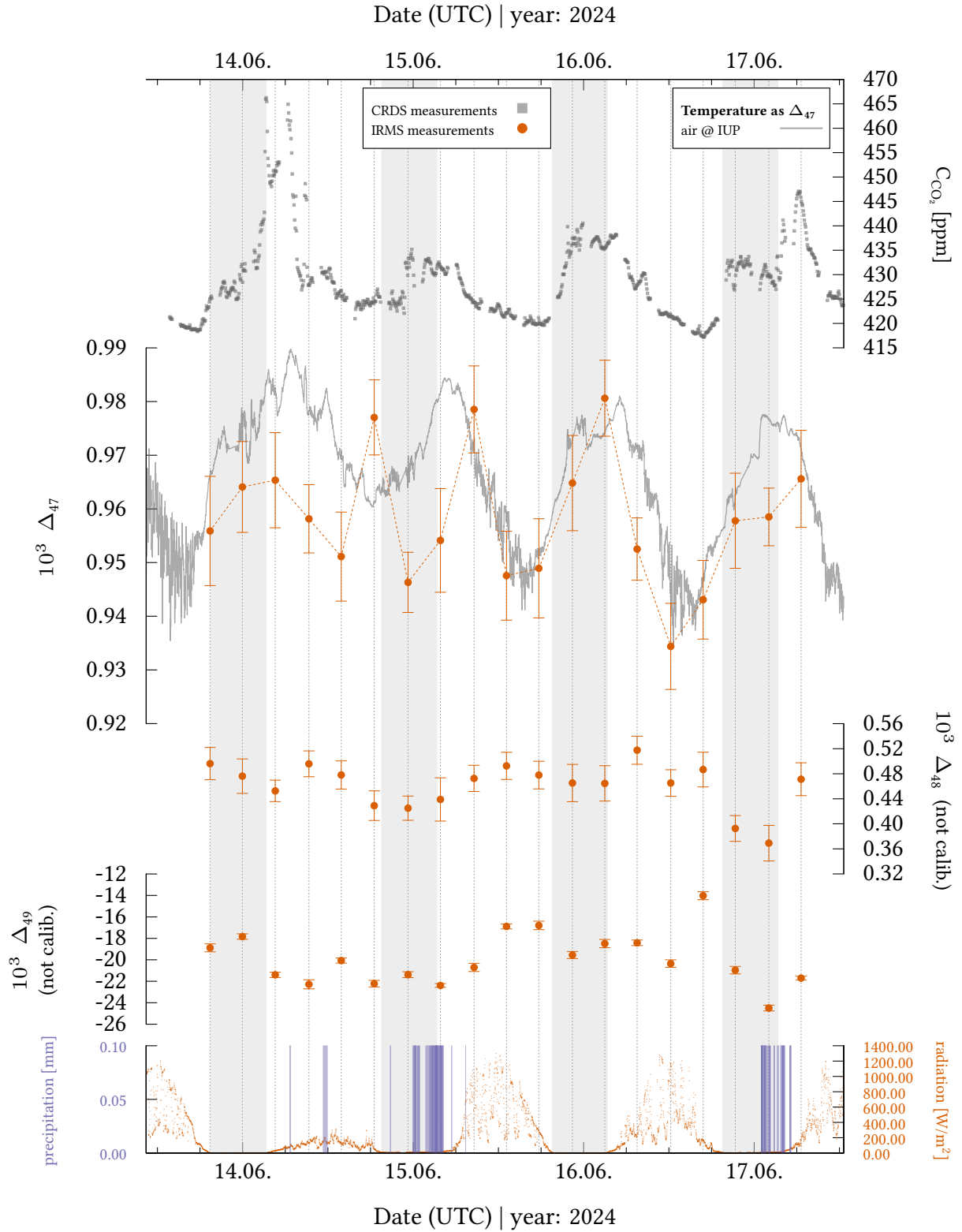
**Figure D.1.:** Extended period for interpretation of  $\delta^{18}\text{O}$  under the heading “Exemplary Periods: May and June – Mean Diurnal Cycle”. CRDS measurements for  $\text{C}_{\text{CO}_2}$  and  $\delta^{13}\text{C}$  are shown in gray. IRMS measurements are shown in orange. Weather data is from IUP’s roof weather station. Green circles in  $\delta^{13}\text{C}$  and  $\delta^{18}\text{O}$  subplots indicate data used for Keeling plots. There was no precipitation for about a week before the May 14–15 measurements were taken, except for a brief rain event on May 13.



**Figure D.2.:** Corresponding graphic to Figure 5.12, but with uncalibrated  $\Delta_{48}$  and  $\Delta_{49}$ .  $\Delta_{48}$  and  $\Delta_{49}$  show no unusual enhancements when  $\Delta_{47}$  is high in the morning. Therefore, potential contamination is an unlikely cause for the increased  $\Delta_{47}$  signals.

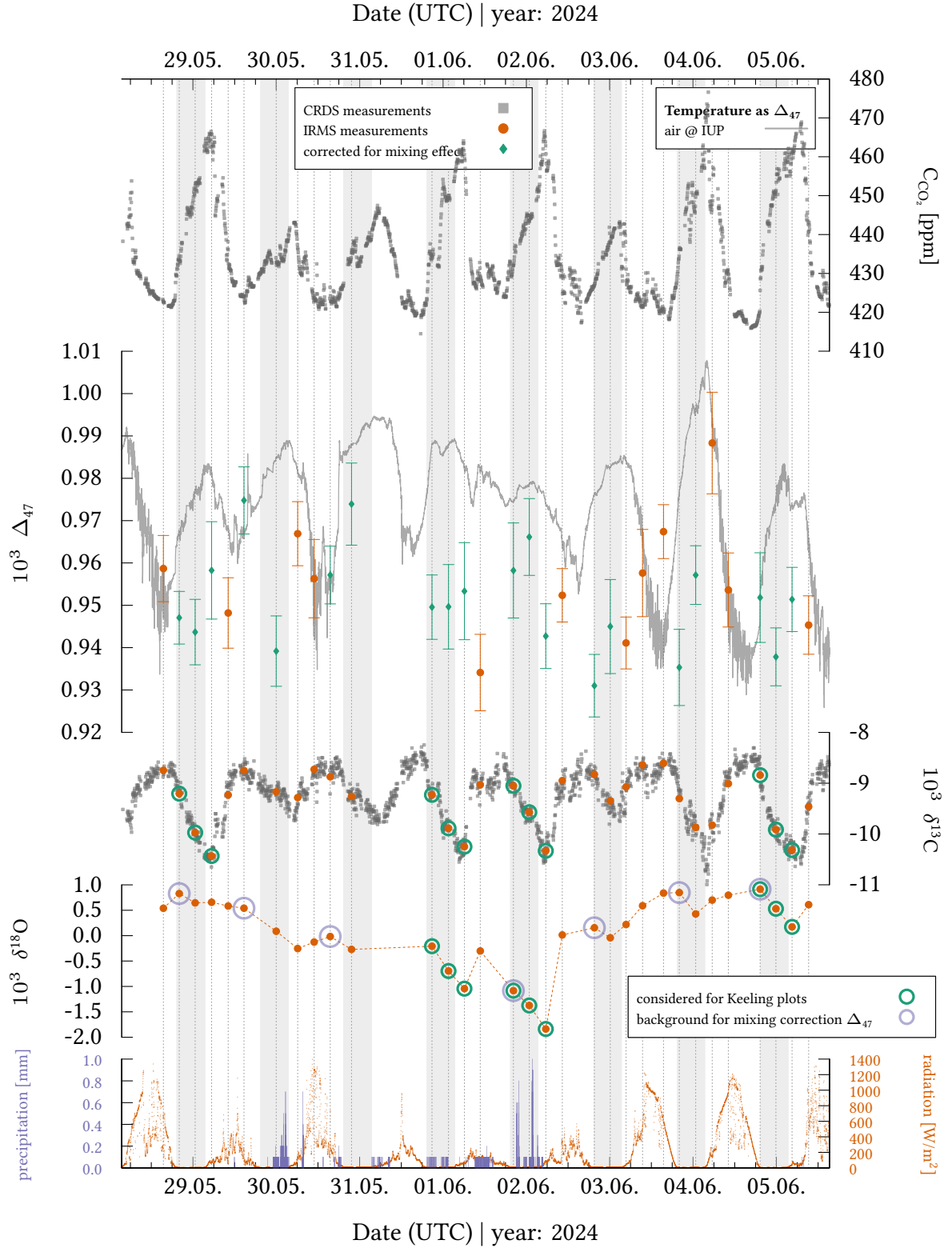


**Figure D.3.:** Corresponding graphic to Figure 5.13, but with uncalibrated  $\Delta_{48}$  and  $\Delta_{49}$ .  $\Delta_{48}$  and  $\Delta_{49}$  show no unusual enhancements when  $\Delta_{47}$  is high. Therefore, potential contamination is an unlikely cause for increased  $\Delta_{47}$  signals.

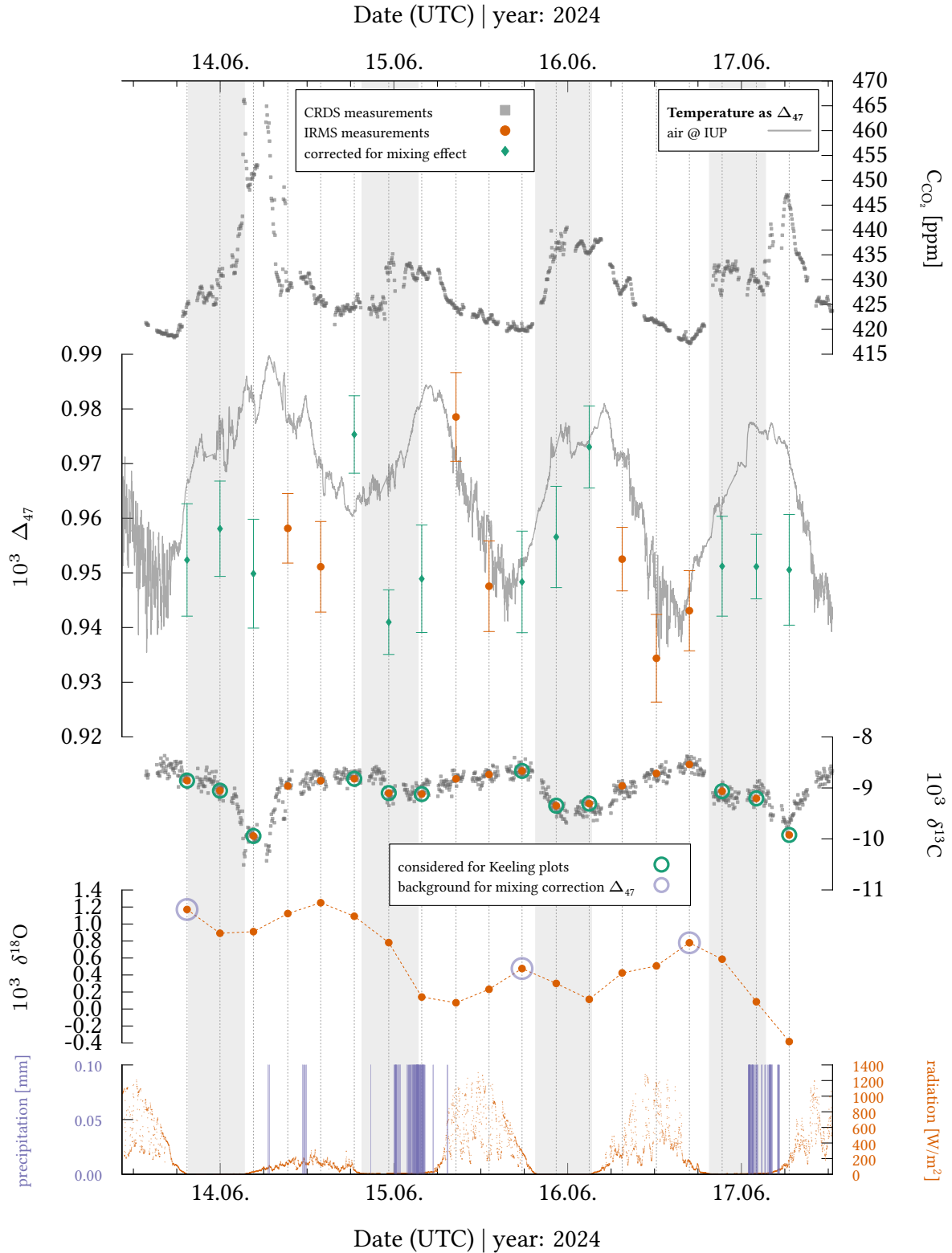


**Figure D.4.:** Corresponding graphic to Figure 5.14, but with uncalibrated  $\Delta_{48}$  and  $\Delta_{49}$ .  $\Delta_{48}$  and  $\Delta_{49}$  show no unusual enhancements when  $\Delta_{47}$  is high. Therefore, potential contamination is an unlikely cause for increased  $\Delta_{47}$  signals.

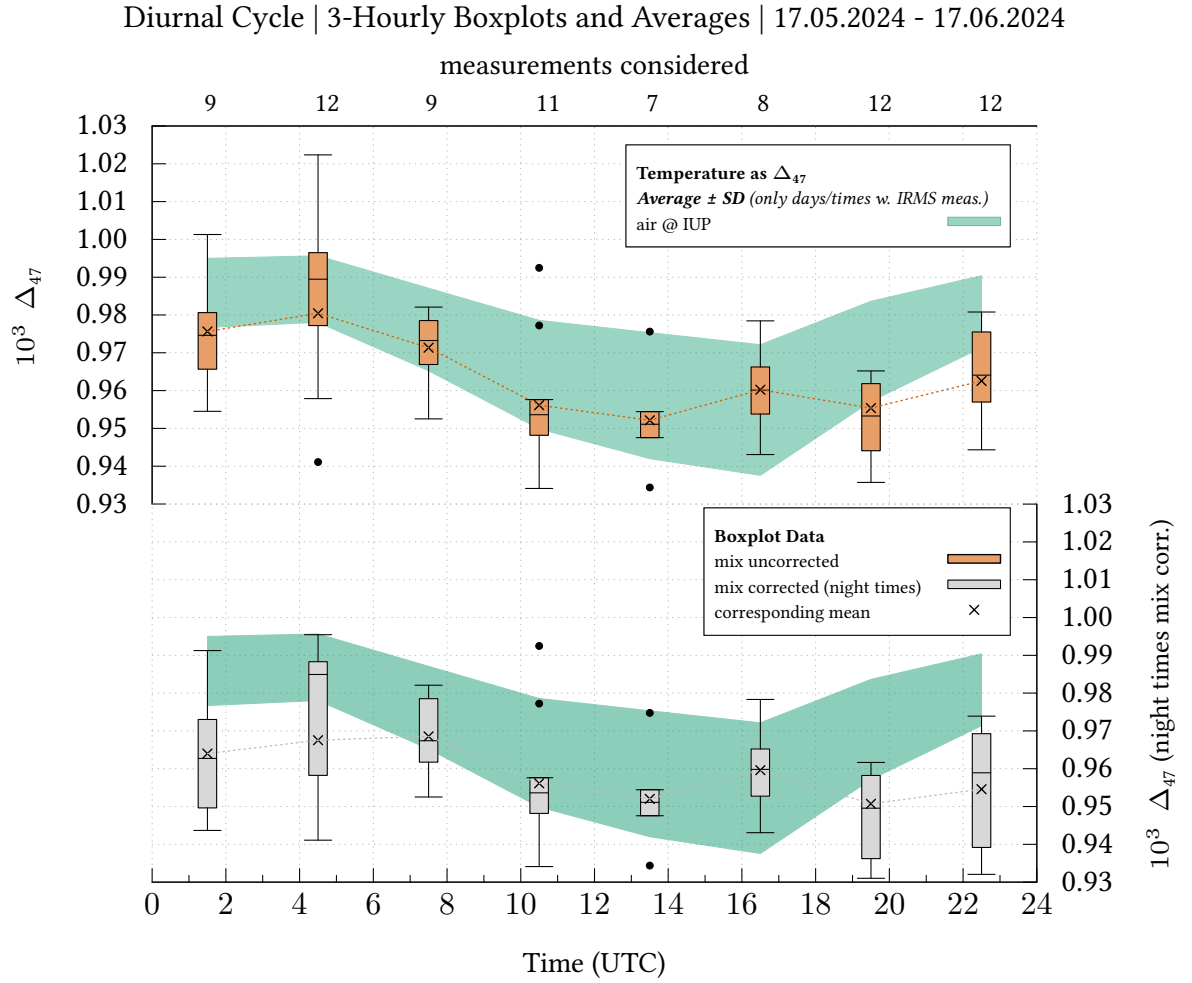




**Figure D.5.:** This graphic corresponds to Figure 5.13, but has been modified to include mixing-effect corrected  $\Delta_{47}$  data at nights (green), using Equations (5.4) & (5.5). Additionally, blue circles in the subplot of  $\delta^{18}\text{O}$  represent data used as  $\delta^{18}\text{O}_{\text{background}}$  in the correction. For some days, including May 31,  $\delta^{18}\text{O}_{\text{background}}$  was estimated by extrapolation. The values used for  $\delta^{18}\text{O}_{\text{source}}$ ,  $\delta^{13}\text{C}_{\text{source}}$ ,  $\delta^{13}\text{C}_{\text{background}}$ , and  $f_{\text{background}}$  are discussed in the text. The corrected data should be viewed as a rough estimate, as the prerequisites for an accurate correction may be flawed.



**Figure D.6.:** This graphic corresponds to Figure 5.14, but has been modified to include mixing-effect corrected  $\Delta_{47}$  data at nights (green), using Equations (5.4) & (5.5). Additionally, blue circles in the subplot of  $\delta^{18}O$  represent data used as  $\delta^{18}O_{background}$  in the correction. For some days, including June 14,  $\delta^{18}O_{background}$  was estimated by extrapolation. The values used for  $\delta^{18}O_{source}$ ,  $\delta^{13}C_{source}$ ,  $\delta^{13}C_{background}$ , and  $f_{background}$  are discussed in the text. The corrected data should be viewed as a rough estimate, as the prerequisites for an accurate correction may be flawed.



**Figure D.7.:** Diurnal cycle for mixing-effect uncorrected and corrected  $\Delta_{47}$ , determined similarly to those in Figure 5.16. However, the day was divided into 3-hour slices, resulting in more corresponding data per time interval. This results in smoothing, but a midday change between 12-15 UTC and 15-18 UTC remains noticeable.



# List of Figures

2.1.	Perturbation of global carbon cycle . . . . .	6
2.2.	Systematic uncertainty due to assumption $\Delta^{17}\text{O} = 0$ . . . . .	9
2.3.	Typical $\delta^{13}\text{C}$ & $\delta^{18}\text{O}$ values . . . . .	10
2.4.	Dependence $\Delta_{45}$ to $\Delta_{49}$ on temperature . . . . .	16
2.5.	$\Delta_{47}$ results from <i>Laskar</i> and <i>Liang</i> , 2016 for different environments and sources . . . . .	17
2.6.	Schematic illustration from <i>Adnew</i> et al., 2021 on altering $\Delta_{47}$ during air-leaf exchange . . . . .	18
2.7.	Location Heidelberg and Institute of Environmental Physics (IUP) . . . . .	19
2.8.	Setup of cavity ring-down spectrometer . . . . .	20
2.9.	Image of MAT 253+ . . . . .	22
2.10.	Schematics of MAT 253+ . . . . .	22
2.11.	Schematic of Dual Inlet setup . . . . .	23
3.1.	Concept for the automatic preparation line . . . . .	30
3.2.	Overall view of the automatic preparation line . . . . .	31
3.3.	Schematic representation of the automatic preparation line . . . . .	32
3.4.	Images of outside of GC . . . . .	36
3.5.	Image of inside of GC oven . . . . .	37
3.6.	Image of sample outlet area of GC . . . . .	37
3.7.	Close-up of GC section from Air Trap schematics . . . . .	38
3.8.	Tests on the method of the GC step . . . . .	41
3.9.	Effect additional evacuation step at GC step . . . . .	42
4.1.	$\text{N}_2\text{O}$ correction for $\Delta_{47}$ . . . . .	53
4.2.	Comparison of $^{30}R^{\text{CO}_2}$ & $^{30}\Lambda^{\text{CO}_2}$ . . . . .	57
4.3.	Temporal development of $\frac{10^3 C_{\text{N}_2\text{O}}}{C_{\text{CO}_2}}/\delta 30$ . . . . .	58
4.4.	Comparison $\delta^{13}\text{C}$ measurements of “Pic_8_1” and “D484276” between Heidelberg and MPI-BGC Jena . . . . .	60

## List of Figures

4.5. Comparison $\delta^{18}\text{O}$ measurements of “Pic_8_1” and “D484276” between Heidelberg and MPI-BGC Jena . . . . .	61
4.6. Calibration of $\Delta_{47}$ and correction regarding $^{47}\delta$ . . . . .	67
4.7. Drift of $\Delta_{47}$ of equilibrated $\text{CO}_2$ standards . . . . .	69
4.8. Reproducibility of the finally corrected and calibrated $\delta^{13}\text{C}$ , $\delta^{18}\text{O}$ , and $\Delta_{47}$ . . . . .	73
5.1. Sketch: Mixing of gases with different bulk isotopic compositions . . . . .	76
5.2. Visualization of correction function for two-component mixtures . . . . .	79
5.3. Theoretical example of three-component mixture and effect on $\Delta_{47}$ . . . . .	79
5.4. Two-component mixture experiment on $\Delta_{47}$ . . . . .	83
5.5. Setup for sampling human breath . . . . .	84
5.6. Underground parking garage sampling sites . . . . .	86
5.7. Overview of IRMS ambient air measurements 2024 . . . . .	96
5.8. Annual trend of ambient air measurements 2024 . . . . .	97
5.9. Keeling plots using nighttime measurements October 22–23, 2024 . . . . .	102
5.10. Measurement results at nighttime inversion October 22–23, 2024 . . . . .	103
5.11. Diurnal cycle for May 17 to June 17, 2024 . . . . .	107
5.12. Measurement results for period 14.05.-26.05. . . . .	108
5.13. Measurement results for period 28.05.-05.06. . . . .	109
5.14. Measurement results for period 13.06.-17.06. . . . .	111
5.15. Measurement results for period 14.05.-26.05. (including mixing-corrected $\Delta_{47}$ ) . . . . .	115
5.16. Comparison of diurnal cycles (17.05.-17.06.) of mixing-effect uncorrected and corrected $\Delta_{47}$ . . . . .	117
A.1. Dependence of $\Delta_{47}$ on bulk isotopic composition . . . . .	126
A.2. Intake for ambient air on roof IUP . . . . .	127
A.3. Comparison of $\Delta_{47}$ calculations . . . . .	128
A.4. Comparison of different background corrections . . . . .	134
A.5. Effect of imbalance at $m/z$ 44 on $^{49}\delta$ . . . . .	136
A.6. Measurement of “EG50_LW” with almost no imbalance at $m/z$ 44 . . . . .	138
A.7. Measurement of “Oberlahnstein” with almost no imbalance at $m/z$ 44 . . . . .	139
A.8. Measurement of “EG50_LW” with strong imbalance at $m/z$ 44 . . . . .	140
B.1. Picture of exemplary structure of Air Trap . . . . .	141
B.2. Picture of pneumatically actuated gold stamp diaphragm valve . . . . .	142
B.3. Picture of pneumatically actuated globe valve . . . . .	142
B.4. Picture of valves AT S1 & AT S2 . . . . .	143

B.5. Picture of Air Trap pumps . . . . .	144
B.6. Picture of H <sub>2</sub> O, CO <sub>2</sub> , GC & SB trap . . . . .	145
B.7. Image of Multifunction Device and Pfeiffer pressure sensor control unit . . . . .	147
B.8. Pictures of control devices, mass flow controller & silver wool trap . . . . .	149
B.10. Picture of multiposition valve and ambient air connection . . . . .	151
B.11. Picture of flask and gas cylinder connections . . . . .	152
B.12. Image of sample inlet via syringe & needle valve . . . . .	153
B.13. Images of valve blocks & standards . . . . .	154
B.14. GUI of automatic preparation line . . . . .	159
B.15. User interface for measurements and preparations . . . . .	161
B.16. Schematic of Dual Inlet system including added parts for reference refill . . . . .	163
B.17. Mechanism for bellow adjustment . . . . .	166
B.18. Drift of $\delta^{13}\text{C}_{\text{norm}}$ and $\delta^{18}\text{O}_{\text{norm}}$ with refill number . . . . .	170
B.19. Results on experiment using reference gas multiple times . . . . .	175
B.20. Basic structure of preparation line at pick-up in France . . . . .	178
B.21. Parts added to the original Dual Inlet system . . . . .	179
B.22. MAT252 including AirTrap extension . . . . .	180
B.23. Cleaning of diaphragm valves . . . . .	181
B.24. Image of AT S3 & AT S4 . . . . .	182
B.25. Image of workstations for Li7000 and mass spectrometer . . . . .	183
B.26. Image of the Dual Inlet system of the IRMS MAT253+ . . . . .	185
B.27. Original GUI Dual Inlet system . . . . .	186
B.28. Results of experiment on sample quantity (GC step) . . . . .	187
C.1. Temperature-regulated water bath and glass cylinder used for production of standards . . . . .	192
C.2. Manual preparation line for production of pure CO <sub>2</sub> standards . . . . .	193
C.3. Calibration of $\Delta_{48}$ and correction regarding $^{48}\delta$ . . . . .	195
C.4. Calibration of $\Delta_{49}$ and correction regarding $^{49}\delta$ . . . . .	196
C.5. Calibrated $\Delta_{47}$ for measurements of “Pic_8_1” and “D484276” . . . . .	197
C.6. Drift of $\Delta_{47}^{\text{LF}}$ of temperature-equilibrated standards . . . . .	198
C.7. $\delta^{18}\text{O}$ of temperature-equilibrated standards over time . . . . .	199
C.8. $\delta^{13}\text{C}$ of temperature-equilibrated standards over time . . . . .	200
C.9. Reproducibility of $\delta^{13}\text{C}$ , $\delta^{18}\text{O}$ , and $\Delta_{47}^{\text{LF}}$ ( $\delta^{13}\text{C}$ & $\delta^{18}\text{O}$ drift corrected) . . . . .	201
D.1. Extended period for interpretation of $\delta^{18}\text{O}$ under heading “Exemplary Periods: May and June – Mean Diurnal Cycle” . . . . .	205
D.2. Uncalibrated $\Delta_{48}$ and $\Delta_{49}$ for period 14.05.-26.05. . . . .	206

## *List of Figures*

D.3. Uncalibrated $\Delta_{48}$ and $\Delta_{49}$ for period 28.05.-05.06. . . . .	207
D.4. Uncalibrated $\Delta_{48}$ and $\Delta_{49}$ for period 13.06.-17.06. . . . .	208
D.5. Measurement results for period 28.05.-05.06. (including mixing-corrected $\Delta_{47}$ ) . . . . .	209
D.6. Measurement results for period 13.06.-17.06. (including mixing-corrected $\Delta_{47}$ ) . . . . .	210
D.7. Diurnal cycles under 3-hour time intervals (17.05.-17.06.) of mixing-effect uncorrected and corrected $\Delta_{47}$ . . . . .	211



# List of Tables

2.1.	International measurement standards . . . . .	8
2.2.	Naturally occurring stable CO <sub>2</sub> isotopologues under stochastic distribution	11
3.1.	Effect of GC preparation . . . . .	44
4.1.	Stable CO <sub>2</sub> isotopologues compared to those of N <sub>2</sub> O . . . . .	48
4.2.	Example N <sub>2</sub> O correction values . . . . .	52
5.1.	Measurement results parking garage experiment . . . . .	88
5.2.	Car exhaust literature values & Keeling plot results of parking garage measurement . . . . .	90
A.1.	Zero point energies, normal mode wave numbers, symmetry numbers for CO <sub>2</sub> isotopologues . . . . .	125
A.2.	Differences old and new measurement protocol . . . . .	130
B.1.	List of standards and there isotope deltas & $\Delta_{47}$ values . . . . .	155
B.2.	Overview on baking of columns . . . . .	184
C.1.	Equilibration temperatures and reference frame data of temperature- equilibrated standards . . . . .	194
C.2.	Mean measurement results for temperature-equilibrated standards . . . .	194
D.1.	Measurement results for temperature-equilibrated CO <sub>2</sub> standards at rele- vant time periods of $\Delta_{47}$ mixing experiments . . . . .	203
D.2.	Results of $\Delta_{47}$ mixing experiments . . . . .	203
D.3.	Overview of some results for exemplarily period May/June, 2024 . . . . .	204



# Bibliography - Author-Related Contributions

- Eckhardt, H.* (2019). “Messung von Mehrfach Substituierten CO<sub>2</sub>-Isotopologen in Der Atmosphäre — Bestimmung von Atmosphärischem  $\Delta_{47}$ .” MA thesis. Institute of Environmental Physics: Heidelberg.
- Eckhardt, H., M. Schmidt, and V. Schmid* (2022). “Poster: Atmospheric CO<sub>2</sub> Sources with Specific  $\Delta_{47}$  Signals under Mixing Conditions.” In: 10th ISI and 12th Isotopes Conference. Zürich.
- Hoheisel, A., C. Yeman, F. Dinger, H. Eckhardt, and M. Schmidt* (2019). “An Improved Method for Mobile Characterisation of  $\delta^{13}\text{CH}_4$  Source Signatures and Its Application in Germany.” In: *Atmospheric Measurement Techniques* 12.2, pp. 1123–1139. ISSN: 1867-1381. DOI: 10.5194/amt-12-1123-2019.
- Kalb, M. et al.* (2020). “CO<sub>2, Gas</sub>-H<sub>2</sub>O<sub>liquid</sub> Isotope Exchange Rates up to 150 °C – Experimental Study and Application to Hydrothermal CO<sub>2</sub>.” In: *Geochimica et Cosmochimica Acta* 269, pp. 167–183. ISSN: 0016-7037. DOI: 10.1016/j.gca.2019.10.023.



# Bibliography

- Adnew, G. A., E. Workman, C. Janssen, and T. Röckmann (2022). “Temperature Dependence of Isotopic Fractionation in the CO<sub>2</sub> - O<sub>2</sub> Isotope Exchange Reaction.” In: *Rapid Communications in Mass Spectrometry* 36.12, e9301. ISSN: 0951-4198, 1097-0231. DOI: 10.1002/rcm.9301.
- Adnew, G. A. et al. (2021). “Leaf Scale Quantification of the Effect of Photosynthetic Gas Exchange on  $\Delta_{47}$  of CO<sub>2</sub>.” In: *Scientific Reports* 11.1 (1), p. 14023. ISSN: 2045-2322. DOI: 10.1038/s41598-021-93092-0.
- Affek, H. P. (2013). “Clumped Isotopic Equilibrium and the Rate of Isotope Exchange between CO<sub>2</sub> and Water.” In: *American Journal of Science* 313.4, pp. 309–325. ISSN: 0002-9599. DOI: 10.2475/04.2013.02.
- Affek, H. P. and D. Yakir (2014). “The Stable Isotopic Composition of Atmospheric CO<sub>2</sub>.” In: *Treatise on Geochemistry*. Elsevier, pp. 179–212. ISBN: 978-0-08-098300-4. DOI: 10.1016/B978-0-08-095975-7.00407-1.
- Affek, H. P. and J. M. Eiler (2006). “Abundance of Mass 47 CO<sub>2</sub> in Urban Air, Car Exhaust, and Human Breath.” In: *Geochimica et Cosmochimica Acta* 70.1, pp. 1–12. ISSN: 0016-7037. DOI: 10.1016/j.gca.2005.08.021.
- Affek, H. P., X. Xu, and J. M. Eiler (2007). “Seasonal and Diurnal Variations of <sup>13</sup>C<sup>18</sup>O<sup>16</sup>O in Air: Initial Observations from Pasadena, CA.” In: *Geochimica et Cosmochimica Acta* 71.21, pp. 5033–5043. ISSN: 0016-7037. DOI: 10.1016/j.gca.2007.08.014.
- Agilent Technologies (2000). *Agilent 6890 Series Gas Chromatograph - Operating Manual Volume 1. General Information*. Manual. USA, p. 286.
- Amt für Stadtentwicklung und Statistik (2022). *Statistische Jahrbuch*. Stadt Heidelberg. URL: <https://ckan.datenplattform.heidelberg.de/de/organization/statistics> (visited on 20.7.2025).
- Andres, R. J., G. Marland, T. Boden, and S. Bischof (1994). *Carbon Dioxide Emissions from Fossil Fuel Consumption and Cement Manufacture, 1751-1991; and an Estimate of Their Isotopic Composition and Latitudinal Distribution*. CONF-9307181-4. Oak Ridge National Lab., TN (United States); Oak Ridge Inst. for Science and Education, TN (United States). URL: <https://www.osti.gov/biblio/10185357> (visited on 10.6.2025).

## Bibliography

- Aoki, N., S. Ishidoya, S. Murayama, and N. Matsumoto (2022). "Influence of CO<sub>2</sub> Adsorption on Cylinders and Fractionation of CO<sub>2</sub> and Air during the Preparation of a Standard Mixture." In: *Atmospheric Measurement Techniques* 15.20, pp. 5969–5983. ISSN: 1867-1381. DOI: 10.5194/amt-15-5969-2022.
- Assonov, S. S. and C. a. M. Brenninkmeijer (2006). "On the N<sub>2</sub>O Correction Used for Mass Spectrometric Analysis of Atmospheric CO<sub>2</sub>." In: *Rapid Communications in Mass Spectrometry* 20.11, pp. 1809–1819. ISSN: 1097-0231. DOI: 10.1002/rcm.2516.
- Assonov, S. S., C. a. M. Brenninkmeijer, C. Koepfel, and T. Röckmann (2009). "CO<sub>2</sub> Isotope Analyses Using Large Air Samples Collected on Intercontinental Flights by the CARIBIC Boeing 767." In: *Rapid Communications in Mass Spectrometry* 23.6, pp. 822–830. ISSN: 1097-0231. DOI: 10.1002/rcm.3946.
- Assonov, S. S. and C. A. M. Brenninkmeijer (2003). "A Redetermination of Absolute Values for 17RVPDB-CO<sub>2</sub> and 17RVSMOW." In: *Rapid Communications in Mass Spectrometry* 17.10, pp. 1017–1029. ISSN: 1097-0231. DOI: 10.1002/rcm.1011.
- Baertschi, P. (1976). "Absolute 18O Content of Standard Mean Ocean Water." In: *Earth and Planetary Science Letters* 31.3, pp. 341–344. ISSN: 0012-821X. DOI: 10.1016/0012-821X(76)90115-1.
- Barkan, E. and B. Luz (2005). "High Precision Measurements of <sup>17</sup>O/<sup>16</sup>O and <sup>18</sup>O/<sup>16</sup>O Ratios in H<sub>2</sub>O." In: *Rapid Communications in Mass Spectrometry* 19.24, pp. 3737–3742. ISSN: 1097-0231. DOI: 10.1002/rcm.2250.
- Bauska, T. K., E. J. Brook, A. C. Mix, and A. Ross (2014). "High-Precision Dual-Inlet IRMS Measurements of the Stable Isotopes of CO<sub>2</sub> and the N<sub>2</sub>O / CO<sub>2</sub> Ratio from Polar Ice Core Samples." In: *Atmospheric Measurement Techniques* 7.11, pp. 3825–3837. ISSN: 1867-1381. DOI: 10.5194/amt-7-3825-2014.
- Bernasconi, S. M. et al. (2021). "InterCarb: A Community Effort to Improve Interlaboratory Standardization of the Carbonate Clumped Isotope Thermometer Using Carbonate Standards." In: *Geochemistry, Geophysics, Geosystems* 22.5, e2020GC009588. ISSN: 1525-2027. DOI: 10.1029/2020GC009588.
- Bernasconi, S. M. et al. (2013). "Background Effects on Faraday Collectors in Gas-Source Mass Spectrometry and Implications for Clumped Isotope Measurements." In: *Rapid Communications in Mass Spectrometry* 27.5, pp. 603–612. ISSN: 1097-0231. DOI: 10.1002/rcm.6490.
- Bernecker, M. et al. (2023). "A Robust Methodology for Triple ( $\Delta_{47}$ ,  $\Delta_{48}$ ,  $\Delta_{49}$ ) Clumped Isotope Analysis of Carbonates." In: *Chemical Geology* 642, p. 121803. ISSN: 0009-2541. DOI: 10.1016/j.chemgeo.2023.121803.

- Blonder, B. and S. T. Michaletz (2018). “A Model for Leaf Temperature Decoupling from Air Temperature.” In: *Agricultural and Forest Meteorology* 262, pp. 354–360. ISSN: 0168-1923. DOI: 10.1016/j.agrformet.2018.07.012.
- Bowler, D. E., L. Buyung-Ali, T. M. Knight, and A. S. Pullin (2010). “Urban Greening to Cool Towns and Cities: A Systematic Review of the Empirical Evidence.” In: *Landscape and Urban Planning* 97.3, pp. 147–155. ISSN: 0169-2046. DOI: 10.1016/j.landurbplan.2010.05.006.
- Brand, W. A., S. S. Assonov, and T. B. Coplen (2010). “Correction for the  $^{17}\text{O}$  Interference in  $\delta(^{13}\text{C})$  Measurements When Analyzing  $\text{CO}_2$  with Stable Isotope Mass Spectrometry (IUPAC Technical Report).” In: *Pure and Applied Chemistry* 82.8, pp. 1719–1733. ISSN: 0033-4545, 1365-3075. DOI: 10.1351/PAC-REP-09-01-05.
- Brenninkmeijer, C. A. M., P. Kraft, and W. G. Mook (1983). “Oxygen Isotope Fractionation between  $\text{CO}_2$  and  $\text{H}_2\text{O}$ .” In: *Chemical Geology* 41, pp. 181–190. ISSN: 0009-2541. DOI: 10.1016/S0009-2541(83)80015-1.
- Canadell, J. G. et al. (2021). “Global Carbon and Other Biogeochemical Cycles and Feedbacks.” In: *Climate Change 2021 – The Physical Science Basis: Working Group I Contribution to the Sixth Assessment Report of the Intergovernmental Panel on Climate Change*. Ed. by Intergovernmental Panel on Climate Change (IPCC). Cambridge, United Kingdom and New York, NY, USA: Cambridge University Press, pp. 673–816. DOI: 10.1017/9781009157896.007.
- Cao, X. and Y. Liu (2012). “Theoretical Estimation of the Equilibrium Distribution of Clumped Isotopes in Nature.” In: *Geochimica et Cosmochimica Acta* 77, pp. 292–303. ISSN: 0016-7037. DOI: 10.1016/j.gca.2011.11.021.
- Carlstad, J. M. and K. A. Boering (2023). “Isotope Effects and the Atmosphere.” In: *Annual Review of Physical Chemistry* 74.1, pp. 439–465. ISSN: 0066-426X, 1545-1593. DOI: 10.1146/annurev-physchem-061020-053429.
- Chang, T. and W. Li (1990). “A Calibrated Measurement of the Atomic-Weight of Carbon.” In: *Chin Sci Bull* 35, p. 290.
- Ciais, P., P. P. Tans, M. Trolier, J. W. C. White, and R. J. Francey (1995). “A Large Northern Hemisphere Terrestrial  $\text{CO}_2$  Sink Indicated by the  $^{13}\text{C}/^{12}\text{C}$  Ratio of Atmospheric  $\text{CO}_2$ .” In: *Science* 269.5227, pp. 1098–1102. DOI: 10.1126/science.269.5227.1098.
- Ciais, P. et al. (1997). “A Three-Dimensional Synthesis Study of  $\delta^{18}\text{O}$  in Atmospheric  $\text{CO}_2$ : 1. Surface Fluxes.” In: *Journal of Geophysical Research: Atmospheres* 102.D5, pp. 5857–5872. ISSN: 2156-2202. DOI: 10.1029/96JD02360.
- Ciais, P. et al. (2014). “Carbon and Other Biogeochemical Cycles.” In: *Climate Change 2013: The Physical Science Basis. Contribution of Working Group I to the Fifth Assessment*

## Bibliography

- Report of the Intergovernmental Panel on Climate Change*. Cambridge University Press, pp. 465–570.
- Clog, M., D. Stolper, and J. M. Eiler (2015). “Kinetics of CO<sub>2</sub>(g)–H<sub>2</sub>O(1) Isotopic Exchange, Including Mass 47 Isotopologues.” In: *Chemical Geology* 395, pp. 1–10. ISSN: 0009-2541. DOI: 10.1016/j.chemgeo.2014.11.023.
- Copernicus (2025). *Copernicus Sentinel-2 Mosaic (Jan - Mar 2025)*. Copernicus Browser. URL: <https://browser.dataspace.copernicus.eu/> (visited on 19.7.2025).
- Coplen, T. B. (2002). *Compilation of Minimum and Maximum Isotope Ratios of Selected Elements in Naturally Occurring Terrestrial Materials and Reagents*. 2001–4222. US Department of the Interior, US Geological Survey.
- Coplen, T. B. (2011). “Guidelines and Recommended Terms for Expression of Stable-Isotope-Ratio and Gas-Ratio Measurement Results.” In: *Rapid Communications in Mass Spectrometry* 25.17, pp. 2538–2560. ISSN: 1097-0231. DOI: 10.1002/rcm.5129.
- Craig, H. (1957). “Isotopic Standards for Carbon and Oxygen and Correction Factors for Mass-Spectrometric Analysis of Carbon Dioxide.” In: *Geochimica et Cosmochimica Acta* 12.1, pp. 133–149. ISSN: 0016-7037. DOI: 10.1016/0016-7037(57)90024-8.
- Craig, H. and C. D. Keeling (1963). “The Effects of Atmospheric NO<sub>2</sub> on the Measured Isotopic Composition of Atmospheric CO<sub>2</sub>.” In: *Geochimica et Cosmochimica Acta* 27.5, pp. 549–551. ISSN: 0016-7037. DOI: 10.1016/0016-7037(63)90088-7.
- Cranton, W. G. K. (2023). “Evaluation of Nine Years of Continuous  $\delta^{13}\text{CO}_2$  Measurements in Heidelberg, Germany.” Year in Europe Thesis. Heidelberg: Heidelberg University.
- Crutzen, P. J. (2002). “Geology of Mankind.” In: *Nature* 415.6867, pp. 23–23. ISSN: 1476-4687. DOI: 10.1038/415023a.
- Cuntz, M. et al. (2003). “A Comprehensive Global Three-Dimensional Model of  $\delta^{18}\text{O}$  in Atmospheric CO<sub>2</sub>: 2. Mapping the Atmospheric Signal.” In: *Journal of Geophysical Research: Atmospheres* 108.D17. ISSN: 2156-2202. DOI: 10.1029/2002JD003154.
- Daëron, M., D. Blamart, M. Peral, and H. P. Affek (2016). “Absolute Isotopic Abundance Ratios and the Accuracy of  $\Delta_{47}$  Measurements.” In: *Chemical Geology* 442, pp. 83–96. ISSN: 0009-2541. DOI: 10.1016/j.chemgeo.2016.08.014.
- Das, S. and M. Pal (2020). “Review—Non-Invasive Monitoring of Human Health by Exhaled Breath Analysis: A Comprehensive Review.” In: *Journal of The Electrochemical Society* 167.3, p. 037562. ISSN: 1945-7111. DOI: 10.1149/1945-7111/ab67a6.
- Davies, A. J. and C. M. John (2017). “Reducing Contamination Parameters for Clumped Isotope Analysis: The Effect of Lowering Porapak™ Q Trap Temperature to below –50°C.” In: *Rapid Communications in Mass Spectrometry* 31.16, pp. 1313–1323. ISSN: 1097-0231. DOI: 10.1002/rcm.7902.



- De Laeter, J. R. et al. (2003). "Atomic Weights of the Elements:: Review 2000 - (IUPAC Technical Report)." In: *PURE AND APPLIED CHEMISTRY* 75.6, pp. 683–800. ISSN: 0033-4545, 1365-3075. DOI: 10.1351/pac200375060683.
- De Vos, J. M., L. N. Joppa, J. L. Gittleman, P. R. Stephens, and S. L. Pimm (2015). "Estimating the normal background rate of species extinction." In: *Conservation Biology* 29.2, pp. 452–462. ISSN: 1523-1739. DOI: 10.1111/cobi.12380.
- Defliese, W. F. and K. C. Lohmann (2015). "Non-Linear Mixing Effects on Mass-47 CO<sub>2</sub> Clumped Isotope Thermometry: Patterns and Implications." In: *Rapid Communications in Mass Spectrometry* 29.9, pp. 901–909.
- DeNiro, M. J. and S. Epstein (1978). "Influence of Diet on the Distribution of Carbon Isotopes in Animals." In: *Geochimica et Cosmochimica Acta* 42.5, pp. 495–506. ISSN: 0016-7037. DOI: 10.1016/0016-7037(78)90199-0.
- Dennis, K. J., H. P. Affek, B. H. Passey, D. P. Schrag, and J. M. Eiler (2011). "Defining an Absolute Reference Frame for 'Clumped' Isotope Studies of CO<sub>2</sub>." In: *Geochimica et Cosmochimica Acta* 75.22, pp. 7117–7131. ISSN: 0016-7037. DOI: 10.1016/j.gca.2011.09.025.
- Deutscher Wetterdienst (DWD) (2023). *Lufttemperatur: Vieljährige Mittelwerte 1991 - 2020 | StationsID: 2080 (Heidelberg)*. URL: [https://www.dwd.de/DE/leistungen/klimadatendeutschland/mittelwerte/temp\\_9120\\_SV\\_html.html?view=nasPublication&nn=16102](https://www.dwd.de/DE/leistungen/klimadatendeutschland/mittelwerte/temp_9120_SV_html.html?view=nasPublication&nn=16102) (visited on 20.7.2025).
- Deva, C. R., M. O. Urban, A. J. Challinor, P. Falloon, and L. Svitáková (2020). "Enhanced Leaf Cooling Is a Pathway to Heat Tolerance in Common Bean." In: *Frontiers in Plant Science* 11. ISSN: 1664-462X. DOI: 10.3389/fpls.2020.00019.
- Dierkes, J. et al. (2023). "Stable Isotope Ratios of Nitrogen and Carbon as Biomarkers of a Vegan Diet." In: *European Journal of Nutrition* 62.1, pp. 433–441. ISSN: 1436-6215. DOI: 10.1007/s00394-022-02992-y.
- Dinger, F. (2014). "Characterisation of a Cavity Ring-Down Spectrometer for Measuring CO<sub>2</sub>, CH<sub>4</sub>,  $\delta^{13}\text{CO}_2$ , and  $\delta^{13}\text{CH}_4$  in Ambient Air." MA thesis. Heidelberg: Heidelberg University.
- Eagle, R. A. et al. (2010). "Body Temperatures of Modern and Extinct Vertebrates from <sup>13</sup>C-<sup>18</sup>O Bond Abundances in Bioapatite." In: *Proceedings of the National Academy of Sciences* 107.23, pp. 10377–10382. DOI: 10.1073/pnas.0911115107.
- Eiler, J. M. (2007). "'Clumped-isotope' Geochemistry—The Study of Naturally-Occurring, Multiply-Substituted Isotopologues." In: *Earth and planetary science letters* 262.3–4, pp. 309–327.
- Eiler, J. M. and E. Schauble (2004). "<sup>18</sup>O<sup>13</sup>C<sup>16</sup>O in Earth's Atmosphere." In: *Geochimica et Cosmochimica Acta* 68.23, pp. 4767–4777. ISSN: 0016-7037. DOI: 10.1016/j.gca.2004.05.035.

## Bibliography

- Ellegård, L. et al. (2019). “Distinguishing Vegan-, Vegetarian-, and Omnivorous Diets by Hair Isotopic Analysis.” In: *Clinical Nutrition* 38.6, pp. 2949–2951. ISSN: 0261-5614. DOI: 10.1016/j.clnu.2018.12.016.
- Eobaldt, E. (2019). “Isotope exchange rates of pure CO<sub>2</sub>.” BA thesis. Heidelberg: Heidelberg University.
- Epstein, S. and L. Zeiri (1988). “Oxygen and Carbon Isotopic Compositions of Gases Respired by Humans.” In: *Proceedings of the National Academy of Sciences of the United States of America* 85.6, pp. 1727–1731. ISSN: 0027-8424. DOI: 10.1073/pnas.85.6.1727. PMID: 3162303.
- Farquhar, G. D., J. R. Ehleringer, and K. T. Hubick (1989). “Carbon Isotope Discrimination and Photosynthesis.” In: *Annual Review of Plant Biology* 40 (Volume 40, 1989), pp. 503–537. ISSN: 1543-5008, 1545-2123. DOI: 10.1146/annurev.pp.40.060189.002443.
- Farquhar, G. D. et al. (1993). “Vegetation Effects on the Isotope Composition of Oxygen in Atmospheric CO<sub>2</sub>.” In: *Nature* 363.6428 (6428), pp. 439–443. ISSN: 1476-4687. DOI: 10.1038/363439a0.
- Fauset, S. et al. (2018). “Differences in Leaf Thermoregulation and Water Use Strategies between Three Co-occurring Atlantic Forest Tree Species.” In: *Plant, Cell & Environment* 41.7, pp. 1618–1631. ISSN: 0140-7791, 1365-3040. DOI: 10.1111/pce.13208.
- Fiebig, J. et al. (2016). “Slight Pressure Imbalances Can Affect Accuracy and Precision of Dual Inlet-Based Clumped Isotope Analysis.” In: *Isotopes in Environmental and Health Studies* 52.1–2, pp. 12–28. ISSN: 1025-6016, 1477-2639. DOI: 10.1080/10256016.2015.1010531.
- Fiebig, J. et al. (2019). “Combined High-Precision  $\Delta_{48}$  and  $\Delta_{47}$  Analysis of Carbonates.” In: *Chemical Geology* 522, pp. 186–191. ISSN: 0009-2541. DOI: 10.1016/j.chemgeo.2019.05.019.
- Fiebig, J. et al. (2021). “Calibration of the Dual Clumped Isotope Thermometer for Carbonates.” In: *Geochimica et Cosmochimica Acta* 312, pp. 235–256. ISSN: 0016-7037. DOI: 10.1016/j.gca.2021.07.012.
- Fiebig, J. et al. (2024). “Carbonate Clumped Isotope Values Compromised by Nitrate-Derived NO<sub>2</sub> Interferent.” In: *Chemical Geology* 670, p. 122382. ISSN: 0009-2541. DOI: 10.1016/j.chemgeo.2024.122382.
- Francey, R. J. et al. (1995). “Changes in Oceanic and Terrestrial Carbon Uptake since 1982.” In: *Nature* 373.6512, pp. 326–330. ISSN: 1476-4687. DOI: 10.1038/373326a0.
- Friedli, H. and U. Siegenthaler (1988). “Influence of N<sub>2</sub>O on Isotope Analyses in CO<sub>2</sub> and Mass-Spectrometric Determination of N<sub>2</sub>O in Air Samples.” In: *Tellus B* 40B.2, pp. 129–133. ISSN: 1600-0889. DOI: 10.1111/j.1600-0889.1988.tb00216.x.

- Friedlingstein, P. et al. (2025). “Global Carbon Budget 2024.” In: *Earth System Science Data* 17.3, pp. 965–1039. ISSN: 1866-3516. DOI: 10.5194/essd-17-965-2025.
- GEO-NET Umweltconsulting GmbH (2023). *Stadtklimaanalyse 2023; Figure: Bodennahe Lufttemperatur (14 Uhr)*. URL: [https://www.heidelberg.de/site/Heidelberg2021/get/documents\\_E470624834/heidelberg/Objektdatenbank/31/PDF/Stadtklima/31\\_pdf\\_02\\_Bodennahe\\_Lufttemperatur\\_14Uhr.pdf](https://www.heidelberg.de/site/Heidelberg2021/get/documents_E470624834/heidelberg/Objektdatenbank/31/PDF/Stadtklima/31_pdf_02_Bodennahe_Lufttemperatur_14Uhr.pdf) (visited on 19.7.2025).
- Ghasemifard, H. et al. (2019). “Atmospheric CO<sub>2</sub> and  $\delta^{13}\text{C}$  Measurements from 2012 to 2014 at the Environmental Research Station Schneefernerhaus, Germany: Technical Corrections, Temporal Variations and Trajectory Clustering.” In: *Aerosol and Air Quality Research* 19.3, pp. 657–670. ISSN: 2071-1409. DOI: 10.4209/aaqr.2018.01.0010.
- Ghosh, P. and W. A. Brand (2004). “The Effect of N<sub>2</sub>O on the Isotopic Composition of Air-CO<sub>2</sub> Samples.” In: *Rapid Communications in Mass Spectrometry* 18.16, pp. 1830–1838. ISSN: 1097-0231. DOI: 10.1002/rcm.1560.
- Ghosh, P., M. Patecki, M. Rothe, and W. A. Brand (2005). “Calcite-CO<sub>2</sub> Mixed into CO<sub>2</sub>-free Air: A New CO<sub>2</sub>-in-air Stable Isotope Reference Material for the VPDB Scale.” In: *Rapid Communications in Mass Spectrometry* 19.8, pp. 1097–1119. ISSN: 1097-0231. DOI: 10.1002/rcm.1886.
- Ghosh, P. et al. (2006). “<sup>13</sup>C–<sup>18</sup>O Bonds in Carbonate Minerals: A New Kind of Paleothermometer.” In: *Geochimica et Cosmochimica Acta* 70.6, pp. 1439–1456. ISSN: 0016-7037. DOI: 10.1016/j.gca.2005.11.014.
- Godwin, H. (1962). “Half-Life of Radiocarbon.” In: *Nature* 195.4845, pp. 984–984. ISSN: 1476-4687. DOI: 10.1038/195984a0.
- Grandke, S. (2022). “Characterisation of a Cavity Ring-Down Spectrometer for Measurements of CH<sub>4</sub>,  $\delta^{13}\text{CH}_4$ , CO<sub>2</sub> and  $\delta^{13}\text{CO}_2$  in Ambient Air and Natural Gas Samples.” BA thesis.
- Graven, H., R. F. Keeling, and J. Rogelj (2020). “Changes to Carbon Isotopes in Atmospheric CO<sub>2</sub> Over the Industrial Era and Into the Future.” In: *Global Biogeochemical Cycles* 34.11, e2019GB006170. ISSN: 1944-9224. DOI: 10.1029/2019GB006170.
- Großmann, J. (2022). “Characterising CH<sub>4</sub> Traffic Emissions via Mobile Tunnel Air Measurements in Baden-Württemberg, Germany.” BA thesis. Heidelberg: Heidelberg University.
- Haun, M. (2017). “CO<sub>2</sub> Clumped Isotopes in Der IRMS - Optimierung Der Auswertemethode Und Beispielhafte Anwendung Auf Ein Spieläothem Aus Dem MIS11.” BA thesis. Institute of Environmental Physics: Heidelberg.
- He, B., G. A. Olack, and A. S. Colman (2012). “Pressure Baseline Correction and High-Precision CO<sub>2</sub> Clumped-Isotope ( $\Delta_{47}$ ) Measurements in Bellows and Micro-Volume

## Bibliography

- Modes.” In: *Rapid Communications in Mass Spectrometry* 26.24, pp. 2837–2853. ISSN: 1097-0231. DOI: 10.1002/rcm.6436.
- Hetherington, A. M. and F. I. Woodward (2003). “The Role of Stomata in Sensing and Driving Environmental Change.” In: *Nature* 424.6951, pp. 901–908. ISSN: 1476-4687. DOI: 10.1038/nature01843.
- Hoheisel, A. (2021). “Evaluation of Greenhouse Gas Time Series to Characterise Local and Regional Emissions.” PhD thesis. Heidelberg University.
- Hoheisel, A., C. Couret, B. Hellack, and M. Schmidt (2023). “Comparison of Atmospheric CO, CO<sub>2</sub> and CH<sub>4</sub> Measurements at the Schneefernerhaus and the Mountain Ridge at Zugspitze.” In: *Atmospheric Measurement Techniques* 16.9, pp. 2399–2413. ISSN: 1867-1381. DOI: 10.5194/amt-16-2399-2023.
- Horváth, B., M. E. G. Hofmann, and A. Pack (2012). “On the Triple Oxygen Isotope Composition of Carbon Dioxide from Some Combustion Processes.” In: *Geochimica et Cosmochimica Acta* 95, pp. 160–168. ISSN: 0016-7037. DOI: 10.1016/j.gca.2012.07.021.
- Huntington, K. W. et al. (2009). “Methods and Limitations of ‘Clumped’ CO<sub>2</sub> Isotope ( $\Delta_{47}$ ) Analysis by Gas-Source Isotope Ratio Mass Spectrometry.” In: *Journal of Mass Spectrometry* 44.9, pp. 1318–1329. ISSN: 1096-9888. DOI: 10.1002/jms.1614.
- Huntington, K. W. and S. V. Petersen (2023). “Frontiers of Carbonate Clumped Isotope Thermometry.” In: *Annual Review of Earth and Planetary Sciences* 51.1, pp. 611–641. ISSN: 0084-6597, 1545-4495. DOI: 10.1146/annurev-earth-031621-085949.
- IUPAC (1994). “Atomic Weights of the Elements 1993.” In: *PURE AND APPLIED CHEMISTRY* 66.12, pp. 2423–2444. ISSN: 0033-4545.
- Junk, G. and H. J. Svec (1958). “The Absolute Abundance of the Nitrogen Isotopes in the Atmosphere and Compressed Gas from Various Sources.” In: *Geochimica et Cosmochimica Acta* 14.3, pp. 234–243. ISSN: 0016-7037. DOI: 10.1016/0016-7037(58)90082-6.
- Kaiser, J. (2002). “Stable Isotope Investigations of Atmospheric Nitrous Oxide.” PhD thesis. Mainz: Johannes Gutenberg-Universität.
- Kaiser, J., T. Röckmann, and C. A. M. Brenninkmeijer (2003). “Complete and Accurate Mass Spectrometric Isotope Analysis of Tropospheric Nitrous Oxide.” In: *Journal of Geophysical Research: Atmospheres* 108.D15. ISSN: 2156-2202. DOI: 10.1029/2003JD003613.
- Kalb, M. (2015). “Automated Calibration of CO<sub>2</sub> and Carbonate Clumped Isotopes.” BA thesis. Institute of Environmental Physics: Heidelberg.
- Kapiluto, Y., D. Yakir, P. Tans, and B. Berkowitz (2007). “Experimental and Numerical Studies of the <sup>18</sup>O Exchange between CO<sub>2</sub> and Water in the Atmosphere–Soil Invasion

- Flux.” In: *Geochimica et Cosmochimica Acta* 71.11, pp. 2657–2671. ISSN: 0016-7037. DOI: 10.1016/j.gca.2007.03.016.
- Keeling, C. D. (1958). “The Concentration and Isotopic Abundances of Atmospheric Carbon Dioxide in Rural Areas.” In: *Geochimica et Cosmochimica Acta* 13.4, pp. 322–334. ISSN: 0016-7037. DOI: 10.1016/0016-7037(58)90033-4.
- Keeling, C. D. et al. (2001). “Exchanges of Atmospheric CO<sub>2</sub> and <sup>13</sup>CO<sub>2</sub> with the Terrestrial Biosphere and Oceans from 1978 to 2000. I. Global Aspects.” In.
- Keeling, R. F., S. C. Piper, and M. Heimann (1996). “Global and Hemispheric CO<sub>2</sub> Sinks Deduced from Changes in Atmospheric O<sub>2</sub> Concentration.” In: *Nature* 381.6579, pp. 218–221. ISSN: 1476-4687. DOI: 10.1038/381218a0.
- Kraftfahrt-Bundesamt (2025a). *Jahresbilanz 2024*. URL: [https://www.kba.de/DE/Statistik/Fahrzeuge/Bestand/Jahresbilanz\\_Bestand/fz\\_b\\_jahresbilanz\\_node.html](https://www.kba.de/DE/Statistik/Fahrzeuge/Bestand/Jahresbilanz_Bestand/fz_b_jahresbilanz_node.html) (visited on 10.6.2025).
- Kraftfahrt-Bundesamt (2025b). *Pressemitteilungen - Der Fahrzeugbestand Am 1. Januar 2025*. URL: [https://www.kba.de/DE/Presse/Pressemitteilungen/Fahrzeugbestand/2025/pm10\\_fz\\_bestand\\_pm\\_komplett.html](https://www.kba.de/DE/Presse/Pressemitteilungen/Fahrzeugbestand/2025/pm10_fz_bestand_pm_komplett.html) (visited on 10.6.2025).
- Kubistin, D. et al. (2025). *ICOS ATC FastTrack NRT GHG Data Product from Karlsruhe (30.0 m) | ICOS*. Atmosphere Thematic Centre. HDL: 11676/BHWKP15u0DkhWEY0BI tqH0hy. URL: <https://hdl.handle.net/11676/BHWKP15u0DkhWEY0BI tqH0hy> (visited on 26.7.2025).
- Kuderer, M., S. Hammer, and I. Levin (2018). “The Influence of <sup>14</sup>CO<sub>2</sub> Releases from Regional Nuclear Facilities at the Heidelberg <sup>14</sup>CO<sub>2</sub> Sampling Site (1986–2014).” In: *Atmospheric Chemistry and Physics* 18.11, pp. 7951–7959. ISSN: 1680-7316. DOI: 10.5194/acp-18-7951-2018.
- Lan, X., P. Tans, and K. W. Thoning (2025). *Trends in Globally-Averaged CO<sub>2</sub> Determined from NOAA Global Monitoring Laboratory Measurements. Version Friday, 14-Mar-2025 11:33:44 MDT*. URL: <https://gml.noaa.gov/ccgg/trends/global.html> (visited on 29.3.2025).
- Lan, X., K. Thoning, and E. Dlugokencky (2025). “Trends in Globally-Averaged CH<sub>4</sub>, N<sub>2</sub>O, and SF<sub>6</sub> Determined from NOAA Global Monitoring Laboratory Measurements. Version 2025-05.” In: DOI: 10.15138/P8XG-AA10.
- Landesanstalt für Umwelt Baden-Württemberg (LUBW) (2022). *Tabelle: Kreisebene - Daten- und Kartendienst der LUBW*. URL: [https://udo.lubw.baden-wuerttemberg.de/public/processingChain?repositoryItemGlobalId=emission.ekat%3Aekat\\_kreis.sel&conditionValuesSetHash=2C0BD00&selector=emission.ekat%3Aekat\\_kreis.sel&sourceOrderAsc=false&offset=0&limit=2147483647](https://udo.lubw.baden-wuerttemberg.de/public/processingChain?repositoryItemGlobalId=emission.ekat%3Aekat_kreis.sel&conditionValuesSetHash=2C0BD00&selector=emission.ekat%3Aekat_kreis.sel&sourceOrderAsc=false&offset=0&limit=2147483647) (visited on 20.7.2025).

## Bibliography

- Laskar, A. H., S. Mahata, S. K. Bhattacharya, and M.-C. Liang (2019). "Triple Oxygen and Clumped Isotope Compositions of CO<sub>2</sub> in the Middle Troposphere." In: *Earth and Space Science* 6.7, pp. 1205–1219. ISSN: 2333-5084. DOI: 10.1029/2019EA000573.
- Laskar, A. H., S. Mahata, and M.-C. Liang (2016). "Identification of Anthropogenic CO<sub>2</sub> Using Triple Oxygen and Clumped Isotopes." In: *Environmental Science & Technology* 50.21, pp. 11806–11814. ISSN: 0013-936X. DOI: 10.1021/acs.est.6b02989.
- Laskar, A. H., M. Y. Soesanto, and M.-C. Liang (2021). "Role of Vehicular Catalytic Converter Temperature in Emission of Pollutants: An Assessment Based on Isotopic Analysis of CO<sub>2</sub> and N<sub>2</sub>O." In: *Environmental Science & Technology* 55.8, pp. 4378–4388. ISSN: 0013-936X. DOI: 10.1021/acs.est.0c07430.
- Laskar, A. H., T.-F. Yui, and M.-C. Liang (2016). "Clumped Isotope Composition of Marbles from the Backbone Range of Taiwan." In: *Terra Nova* 28.4, pp. 265–270. ISSN: 1365-3121. DOI: 10.1111/ter.12217.
- Laskar, A. H. and M.-C. Liang (2016). "Clumped Isotopes in Near-Surface Atmospheric CO<sub>2</sub> over Land, Coast and Ocean in Taiwan and Its Vicinity." In: *Biogeosciences* 13.18, pp. 5297–5314. ISSN: 1726-4170. DOI: 10.5194/bg-13-5297-2016.
- Lee, H., H. Mayer, and L. Chen (2016). "Contribution of Trees and Grasslands to the Mitigation of Human Heat Stress in a Residential District of Freiburg, Southwest Germany." In: *Landscape and Urban Planning* 148, pp. 37–50. ISSN: 0169-2046. DOI: 10.1016/j.landurbplan.2015.12.004.
- Leuenberger, M. C., M. F. Schibig, and P. Nyfeler (2015). "Gas Adsorption and Desorption Effects on Cylinders and Their Importance for Long-Term Gas Records." In: *Atmospheric Measurement Techniques* 8.12, pp. 5289–5299. ISSN: 1867-8548. DOI: 10.5194/amt-8-5289-2015.
- Levin, I., S. Hammer, B. Kromer, and F. Meinhardt (2008). "Radiocarbon Observations in Atmospheric CO<sub>2</sub>: Determining Fossil Fuel CO<sub>2</sub> over Europe Using Jungfraujoch Observations as Background." In: *Science of The Total Environment*. Research at Jungfraujoch - Contributions to the International Conference in Celebration of the 75th Anniversary of the High Altitude Research Station Jungfraujoch at Interlaken, Switzerland (11-13 September, 2006) 391.2, pp. 211–216. ISSN: 0048-9697. DOI: 10.1016/j.scitotenv.2007.10.019.
- Levin, I., B. Kromer, M. Schmidt, and H. Sartorius (2003). "A Novel Approach for Independent Budgeting of Fossil Fuel CO<sub>2</sub> over Europe by <sup>14</sup>CO<sub>2</sub> Observations." In: *Geophysical Research Letters* 30.23. ISSN: 1944-8007. DOI: 10.1029/2003GL018477.
- LGL-BW (2024a). "WMS LGL-BW ATKIS digitale orthophotos in farbe 20 cm bodenauflösung" | datenlizenz deutschland - namensnennung - version 2.0 | www.lgl-bw.de. URL: https://w

- www.geoportal-bw.de/?permalinkId=7b536fd9-2240-4479-83c1-f20ff3110ff7#/(sidenav:karten) (visited on 19.7.2025).
- LGL-BW (2024b). "WMS LGL-BW HIST Digitale Orthophotos in Farbe 2010-2019" + "WMS LGL-BW ATKIS Digitales Geländemodell Schummerung 25cm" | datenlizenz deutschland - namensnennung - version 2.0 | www.lgl-bw.de. URL: [https://www.geoportal-bw.de/?permalinkId=545a8ea3-c82e-4374-bfe7-d35953cb25b8#/\(sidenav:karten\)](https://www.geoportal-bw.de/?permalinkId=545a8ea3-c82e-4374-bfe7-d35953cb25b8#/(sidenav:karten)) (visited on 19.7.2025).
- Li, W. (1988). "Measurement of the Absolute Abundance of Oxygen-17 in V-SMOW." In: *Chin. Sci. Bull.* 33, pp. 1610–1613.
- Liang, M.-C. and S. Mahata (2015). "Oxygen Anomaly in near Surface Carbon Dioxide Reveals Deep Stratospheric Intrusion." In: *Scientific Reports* 5.1, p. 11352. ISSN: 2045-2322. DOI: 10.1038/srep11352.
- Lin, J. C. et al. (2003). "A Near-Field Tool for Simulating the Upstream Influence of Atmospheric Observations: The Stochastic Time-Inverted Lagrangian Transport (STILT) Model." In: *Journal of Geophysical Research: Atmospheres* 108.D16. ISSN: 2156-2202. DOI: 10.1029/2002JD003161.
- Lollar, B. S. et al. (2008). "Isotopic Signatures of CH<sub>4</sub> and Higher Hydrocarbon Gases from Precambrian Shield Sites: A Model for Abiogenic Polymerization of Hydrocarbons." In: *Geochimica et Cosmochimica Acta* 72.19, pp. 4778–4795. ISSN: 0016-7037. DOI: 10.1016/j.gca.2008.07.004.
- LUBW (2025). *Land unter: Hochwasser und Starkregen prägten das Jahr | Eine klimatische Einordnung des Jahres 2024 für Baden-Württemberg*. Landesanstalt für Umwelt Baden-Württemberg. URL: <https://pudi.lubw.de/detailseite/-/publication/10731> (visited on 9.7.2025).
- Lucarelli, J. K. et al. (2023). "Equilibrated Gas and Carbonate Standard-Derived Dual ( $\Delta_{47}$  and  $\Delta_{48}$ ) Clumped Isotope Values." In: *Geochemistry, Geophysics, Geosystems* 24.2, e2022GC010458. ISSN: 1525-2027. DOI: 10.1029/2022GC010458.
- Mahadevan, P. et al. (2008). "A Satellite-Based Biosphere Parameterization for Net Ecosystem CO<sub>2</sub> Exchange: Vegetation Photosynthesis and Respiration Model (VPRM)." In: *Global Biogeochemical Cycles* 22.2. ISSN: 1944-9224. DOI: 10.1029/2006GB002735.
- Matos, M. P. V. and G. P. Jackson (2020). "Compound-Specific Isotope Analysis of Human Hair: Predicting Behaviors and Biometrics beyond Dietary Factors." In: *Analytical Chemistry* 92.4, pp. 3014–3022. ISSN: 0003-2700, 1520-6882. DOI: 10.1021/acs.analchem.9b04085.
- Meckler, A. N., M. Ziegler, M. I. Millán, S. F. M. Breitenbach, and S. M. Bernasconi (2014). "Long-Term Performance of the Kiel Carbonate Device with a New Correction Scheme

## Bibliography

- for Clumped Isotope Measurements.” In: *Rapid Communications in Mass Spectrometry* 28.15, pp. 1705–1715. ISSN: 1097-0231. DOI: 10.1002/rcm.6949.
- Merck KGaA (Sigma-Aldrich) (2020). *Certificate of Analysis Supel-Q™ Plot Capillary Column 30 m x 0.53 Mm Catalog No. 25462 (Column No. 260326-04)*. URL: <https://www.sigmaaldrich.com/DE/en/coa/SUPELCO/2.5462/260326-04> (visited on 15.4.2025).
- Merck KGaA (Sigma-Aldrich) (2025). *GC Analysis of Permanent Gases and Light Hydrocarbons on Supel-Q PLOT Suitable for GC | Sigma-Aldrich*. URL: <https://www.sigmaaldrich.com/DE/en/technical-documents/chromatograms/gas-chromatography/gc-analysis-of-permanent-gases-and-light-hydrocarbons/supelco/794-0619> (visited on 15.4.2025).
- Merritt, D. A. and J. M. Hayes (1994). “Factors Controlling Precision and Accuracy in Isotope-Ratio-Monitoring Mass Spectrometry.” In: *Analytical Chemistry* 66.14, pp. 2336–2347. ISSN: 0003-2700. DOI: 10.1021/ac00086a020.
- Michaletz, S. T. et al. (2015). “Plant Thermoregulation: Energetics, Trait–Environment Interactions, and Carbon Economics.” In: *Trends in Ecology & Evolution* 30.12, pp. 714–724. ISSN: 0169-5347. DOI: 10.1016/j.tree.2015.09.006.
- Mills, G. A. and H. C. Urey (1940). “The Kinetics of Isotopic Exchange between Carbon Dioxide, Bicarbonate Ion, Carbonate Ion and Water.” In: *Journal of the American Chemical Society* 62.5, pp. 1019–1026. ISSN: 0002-7863. DOI: 10.1021/ja01862a010.
- Mook, W. G. (1986). “<sup>13</sup>C in Atmospheric CO<sub>2</sub>.” In: *Netherlands Journal of Sea Research* 20.2, pp. 211–223. ISSN: 0077-7579. DOI: 10.1016/0077-7579(86)90043-8.
- Mook, W. G., S. Van der Hoek, W. G. Mook, and S. Van der Hoek (1983). “The N<sub>2</sub>O Correction in the Carbon and Oxygen Isotopic Analysis of Atmospheric CO<sub>2</sub>.” In: *Chemical Geology* 41, pp. 237–242. ISSN: 0009-2541. DOI: 10.1016/S0009-2541(83)80021-7.
- Mook, W. G. (2000). *Introduction: Theory, Methods, Review*. Ed. by W. G. Mook. Vol. 1. 6 vols. Environmental Isotopes in the Hydrological Cycle - Principles and Applications. Groningen: UNESCO/IAEA Series. 280 pp.
- Moore, H. (1974). “Isotopic Measurement of Atmospheric Nitrogen Compounds.” In: *Tellus* 26.1–2, pp. 169–174. ISSN: 2153-3490. DOI: 10.1111/j.2153-3490.1974.tb01963.x.
- Müller, I. A. et al. (2017). “Carbonate Clumped Isotope Analyses with the Long-Integration Dual-Inlet (LIDI) Workflow: Scratching at the Lower Sample Weight Boundaries.” In: *Rapid Communications in Mass Spectrometry* 31.12, pp. 1057–1066. ISSN: 1097-0231. DOI: 10.1002/rcm.7878.
- Neubert, R. (1998). “Messung Der Stablen Isotopomere Des Atmosphärischen Kohlendioxids.” PhD thesis. Heidelberg.
- Newman, S., X. Xu, H. P. Affek, E. Stolper, and S. Epstein (2008). “Changes in Mixing Ratio and Isotopic Composition of CO<sub>2</sub> in Urban Air from the Los Angeles Basin, California,



- between 1972 and 2003.” In: *Journal of Geophysical Research: Atmospheres* 113.D23. ISSN: 2156-2202. DOI: 10.1029/2008JD009999.
- Nier, A. O. (1950). “A Redetermination of the Relative Abundances of the Isotopes of Carbon, Nitrogen, Oxygen, Argon, and Potassium.” In: *Physical Review* 77.6, pp. 789–793. ISSN: 0031-899X. DOI: 10.1103/PhysRev.77.789.
- O’Brien, D. M., K. R. Niles, J. Black, and D. A. Schoeller (2021). “The Breath Carbon Isotope Ratio Reflects Short-term Added-Sugar Intake in a Dose-Response, Crossover Feeding Study of 12 Healthy Adults.” In: *The Journal of Nutrition* 151.3, pp. 628–635. ISSN: 0022-3166. DOI: 10.1093/jn/nxaa352.
- Olack, G. and A. S. Colman (2019). “Modeling the Measurement:  $\Delta_{47}$ , Corrections, and Absolute Ratios for Reference Materials.” In: *Geochemistry, Geophysics, Geosystems* 20.7, pp. 3569–3587. ISSN: 1525-2027. DOI: 10.1029/2018GC008166.
- Pan, L. et al. (2024). “Site-Specific Apparent Optimum Air Temperature for Vegetation Photosynthesis across the Globe.” In: *Scientific Data* 11.1, p. 758. ISSN: 2052-4463. DOI: 10.1038/s41597-024-03603-7.
- Pantelev, N., F. Péronnet, C. Hillaire-Marcel, C. Lavoie, and D. Massicotte (1999). “Carbon Isotope Fractionation between Blood and Expired CO<sub>2</sub> at Rest and Exercise.” In: *Respiration Physiology* 116.1, pp. 77–83. ISSN: 0034-5687. DOI: 10.1016/S0034-5687(99)00027-4.
- Peters, R. L. et al. (2025). “Uniform Regulation of Stomatal Closure across Temperate Tree Species to Sustain Nocturnal Turgor and Growth.” In: *Nature Plants* 11.4, pp. 725–730. ISSN: 2055-0278. DOI: 10.1038/s41477-025-01957-3.
- Petersen, S. V., I. Z. Winkelstern, K. C. Lohmann, and K. W. Meyer (2016). “The Effects of Porapak™ Trap Temperature on  $\delta^{18}\text{O}$ ,  $\delta^{13}\text{C}$ , and  $\Delta_{47}$  Values in Preparing Samples for Clumped Isotope Analysis.” In: *Rapid Communications in Mass Spectrometry* 30.1, pp. 199–208. ISSN: 1097-0231. DOI: 10.1002/rcm.7438.
- Petzke, K. J., H. Boeing, and C. C. Metges (2005). “Choice of Dietary Protein of Vegetarians and Omnivores Is Reflected in Their Hair Protein  $^{13}\text{C}$  and  $^{15}\text{N}$  Abundance.” In: *Rapid Communications in Mass Spectrometry* 19.11, pp. 1392–1400. ISSN: 1097-0231. DOI: 10.1002/rcm.1925.
- Peylin, P. et al. (1999). “A 3-Dimensional Study of  $\delta^{18}\text{O}$  in Atmospheric CO<sub>2</sub>: Contribution of Different Land Ecosystems.” In: *Tellus B: Chemical and Physical Meteorology* 51.3, pp. 642–667. ISSN: null. DOI: 10.3402/tellusb.v51i3.16452.
- Pfeiffer Vacuum GmbH (2024). *OPERATING INSTRUCTIONS RPT 200/RPT 201 Digital Piezo/Pirani Gauge*.
- Pieber, S. M. et al. (2022). “Analysis of Regional CO<sub>2</sub> Contributions at the High Alpine Observatory Jungfraujoch by Means of Atmospheric Transport Simulations and  $\delta^{13}\text{C}$ .”

## Bibliography

- In: *Atmospheric Chemistry and Physics* 22.16, pp. 10721–10749. ISSN: 1680-7316. DOI: 10.5194/acp-22-10721-2022.
- Popa, M. E. et al. (2014). “Vehicle Emissions of Greenhouse Gases and Related Tracers from a Tunnel Study: CO:CO<sub>2</sub>, N<sub>2</sub>O:CO<sub>2</sub>, CH<sub>4</sub>:CO<sub>2</sub>, O<sub>2</sub>:CO<sub>2</sub> Ratios, and the Stable Isotopes <sup>13</sup>C and <sup>18</sup>O in CO<sub>2</sub> and CO.” In: *Atmospheric Chemistry and Physics* 14.4, pp. 2105–2123. ISSN: 1680-7324. DOI: 10.5194/acp-14-2105-2014.
- Price, J. T. and R. Warren (2016). *Literature Review of the Potential of “Blue Carbon” Activities to Reduce Emissions*.
- Pugliese, S. C., J. G. Murphy, F. Vogel, and D. Worthy (2017). “Characterization of the  $\delta^{13}\text{C}$  Signatures of Anthropogenic CO<sub>2</sub> Emissions in the Greater Toronto Area, Canada.” In: *Applied Geochemistry*. Urban Geochemistry 83, pp. 171–180. ISSN: 0883-2927. DOI: 10.1016/j.apgeochem.2016.11.003.
- Riley, W. J., C. J. Still, B. R. Helliker, M. Ribas-Carbo, and J. A. Berry (2003). “<sup>18</sup>O Composition of CO<sub>2</sub> and H<sub>2</sub>O Ecosystem Pools and Fluxes in a Tallgrass Prairie: Simulations and Comparisons to Measurements.” In: *Global Change Biology* 9.11, pp. 1567–1581. ISSN: 1365-2486. DOI: 10.1046/j.1365-2486.2003.00680.x.
- Saenger, C. P., A. J. Schauer, E. O. Heitmann, K. W. Huntington, and E. J. Steig (2021). “How <sup>17</sup>O Excess in Clumped Isotope Reference-Frame Materials and ETH Standards Affects Reconstructed Temperature.” In: *Chemical Geology* 563, p. 120059. ISSN: 0009-2541. DOI: 10.1016/j.chemgeo.2021.120059.
- Santrock, Jeffrey., S. A. Studley, and J. M. Hayes (1985). “Isotopic Analyses Based on the Mass Spectra of Carbon Dioxide.” In: *Analytical Chemistry* 57.7, pp. 1444–1448. ISSN: 0003-2700. DOI: 10.1021/ac00284a060.
- Schibig, M. F., D. Kitzis, and P. P. Tans (2018). “Experiments with CO<sub>2</sub>-in-Air Reference Gases in High-Pressure Aluminum Cylinders.” In: *Atmospheric Measurement Techniques* 11.10, pp. 5565–5586. ISSN: 1867-1381. DOI: 10.5194/amt-11-5565-2018.
- Schmid, V. (2023). “Theoretical Analysis of  $\Delta_{47}$  under Mixing Conditions in Atmospheric CO<sub>2</sub>.” BA thesis. Institute of Environmental Physics: Heidelberg.
- Schmidt, M., R. Graul, H. Sartorius, and I. Levin (2003). “The Schauinsland CO<sub>2</sub> Record: 30 Years of Continental Observations and Their Implications for the Variability of the European CO<sub>2</sub> Budget.” In: *Journal of Geophysical Research: Atmospheres* 108.D19. ISSN: 2156-2202. DOI: 10.1029/2002JD003085.
- Schmiede, S. C., M. Heskell, Y. Fan, and D. A. Way (2023). “It’s Only Natural: Plant Respiration in Unmanaged Systems.” In: *Plant Physiology* 192.2, pp. 710–727. ISSN: 0032-0889. DOI: 10.1093/plphys/kiad167.

- Schumacher, M. et al. (2011). "Oxygen Isotopic Signature of CO<sub>2</sub> from Combustion Processes." In: *Atmospheric Chemistry and Physics* 11.4, pp. 1473–1490. ISSN: 1680-7316. DOI: 10.5194/acp-11-1473-2011.
- Seibt, U., L. Wingate, J. Lloyd, and J. A. Berry (2006). "Diurnally Variable  $\delta^{18}\text{O}$  Signatures of Soil CO<sub>2</sub> Fluxes Indicate Carbonic Anhydrase Activity in a Forest Soil." In: *Journal of Geophysical Research: Biogeosciences* 111.G4. ISSN: 2156-2202. DOI: 10.1029/2006JG000177.
- Sirignano, C., R. E. M. Neubert, and H. A. J. Meijer (2004). "N<sub>2</sub>O Influence on Isotopic Measurements of Atmospheric CO<sub>2</sub>." In: *Rapid Communications in Mass Spectrometry* 18.16, pp. 1839–1846. ISSN: 1097-0231. DOI: 10.1002/rcm.1559.
- Stadt Heidelberg (2024). *Pressemitteilung | 02.06.2024 Hochwasser: Neckarpegel steigt weiter an, Scheitelpunkt in der Nacht auf Montag erwartet*. URL: [https://heidelberg.de/HD/Presse/02\\_06\\_2024+hochwasser\\_+neckarpegel+steigt+weiter+an\\_+scheidelpunkt+in+der+nacht+auf+montag+erwartet.html](https://heidelberg.de/HD/Presse/02_06_2024+hochwasser_+neckarpegel+steigt+weiter+an_+scheidelpunkt+in+der+nacht+auf+montag+erwartet.html) (visited on 13.7.2025).
- Stadt Heidelberg (2025). *Stadtklima Heidelberg*. URL: <https://heidelberg.de/HD/Leben/Stadtklima+Heidelberg.html> (visited on 19.7.2025).
- Statistisches Bundesamt (2023). *Erdölimporte aus Russland im Januar 2023 auf 3 500 Tonnen gesunken*. URL: [https://www.destatis.de/DE/Presse/Pressemitteilungen/2023/03/PD23\\_098\\_51.html](https://www.destatis.de/DE/Presse/Pressemitteilungen/2023/03/PD23_098_51.html) (visited on 11.6.2025).
- Still, C. J. et al. (2022). "No Evidence of Canopy-Scale Leaf Thermoregulation to Cool Leaves below Air Temperature across a Range of Forest Ecosystems." In: *Proceedings of the National Academy of Sciences* 119.38, e2205682119. DOI: 10.1073/pnas.2205682119.
- Swart, P. K. et al. (2021). "A Calibration Equation between  $\Delta_{48}$  Values of Carbonate and Temperature." In: *Rapid Communications in Mass Spectrometry* 35.17, e9147. ISSN: 1097-0231. DOI: 10.1002/rcm.9147.
- Taha, H., H. Akbari, A. Rosenfeld, and J. Huang (1988). "Residential Cooling Loads and the Urban Heat Island—the Effects of Albedo." In: *Building and Environment* 23.4, pp. 271–283. ISSN: 0360-1323. DOI: 10.1016/0360-1323(88)90033-9.
- Tans, P. (1981). "<sup>13</sup>C/<sup>12</sup>C of Industrial CO<sub>2</sub>, Carbon Cycle Modelling." In: *Scope* 16, pp. 127–129.
- Tans, P. P. (1998). "Oxygen Isotopic Equilibrium between Carbon Dioxide and Water in Soils." In: *Tellus B: Chemical and Physical Meteorology* 50.2. ISSN: 0280-6509. DOI: 10.3402/tellusb.v50i2.16094.
- Tans, P. P., I. Y. Fung, and T. Takahashi (1990). "Observational Constrains on the Global Atmospheric CO<sub>2</sub> Budget." In: *Science* 247.4949, pp. 1431–1438. DOI: 10.1126/science.247.4949.1431.

## Bibliography

- Thermo Fisher Scientific (2016). *253 Plus 10 kV Isotope Ratio MS Operating Manual*.
- Trajan Scientific Australia Pty Ltd (2017). *Manual - Instructions for Pneumatic on/off Valves MOVPT and MOVPT*. Version MN-0078-A\_RevI.
- United Nations (2015). "Paris Agreement." In: *Report of the Conference of the Parties to the United Nations Framework Convention on Climate Change (21st Session, 2015: Paris)*. Retrived December.
- Urban, J., M. W. Ingwers, M. A. McGuire, and R. O. Teskey (2017). "Increase in Leaf Temperature Opens Stomata and Decouples Net Photosynthesis from Stomatal Conductance in Pinus Taeda and Populus Deltoides x Nigra." In: *Journal of Experimental Botany* 68.7, pp. 1757–1767. ISSN: 0022-0957. DOI: 10.1093/jxb/erx052.
- Urey, H. C. (1947). "The Thermodynamic Properties of Isotopic Substances." In: *Journal of the Chemical Society (Resumed)*, pp. 562–581.
- Vardag, S. N., S. Hammer, M. Sabasch, D. W. T. Griffith, and I. Levin (2015). "First Continuous Measurements of  $\delta^{18}\text{O}\text{-CO}_2$  in Air with a Fourier Transform Infrared Spectrometer." In: *Atmospheric Measurement Techniques* 8.2, pp. 579–592. ISSN: 1867-8548. DOI: 10.5194/amt-8-579-2015.
- Vardag, S. N., S. Hammer, and I. Levin (2016). "Evaluation of 4 Years of Continuous  $\delta^{13}\text{C}(\text{CO}_2)$  Data Using a Moving Keeling Plot Method." In: *Biogeosciences* 13.14, pp. 4237–4251. ISSN: 1726-4170. DOI: 10.5194/bg-13-4237-2016.
- Wang, Z., E. A. Schauble, and J. M. Eiler (2004). "Equilibrium Thermodynamics of Multiply Substituted Isotopologues of Molecular Gases." In: *Geochimica et Cosmochimica Acta* 68.23, pp. 4779–4797. ISSN: 0016-7037. DOI: 10.1016/j.gca.2004.05.039.
- Weise, A. and T. Kluge (2020). "Isotope Exchange Rates in Dissolved Inorganic Carbon between 40 °C and 90 °C." In: *Geochimica et Cosmochimica Acta* 268, pp. 56–72. ISSN: 0016-7037. DOI: 10.1016/j.gca.2019.09.032.
- Werner, R. A., M. Rothe, and W. A. Brand (2001). "Extraction of  $\text{CO}_2$  from Air Samples for Isotopic Analysis and Limits to Ultra High Precision  $\delta^{18}\text{O}$  Determination in  $\text{CO}_2$  Gas." In: *Rapid Communications in Mass Spectrometry* 15.22 (22), pp. 2152–2167. ISSN: 1097-0231. DOI: 10.1002/rcm.487.
- WMO/IAEA (2016). "19th WMO/IAEA Meeting on Carbon Dioxide, Other Greenhouse Gases and Related Tracers Measurement Techniques (GGMT-2017) Rep." In.
- World Meteorological Organization (2014). "17th WMO/IAEA Meeting on Carbon Dioxide, Other Greenhouse Gases and Related Tracers Measurement Techniques (GGMT-2013)." In: *GAW Report No. 123*. Ed. by P. Tans and C. Zellweger.
- Worthy, D. E. J. et al. (2023). "Results of a Long-Term International Comparison of Greenhouse Gas and Isotope Measurements at the Global Atmosphere Watch (GAW) Ob-

- servatory in Alert, Nunavut, Canada.” In: *Atmospheric Measurement Techniques* 16.23, pp. 5909–5935. ISSN: 1867-1381. DOI: 10.5194/amt-16-5909-2023.
- Yakir, D. and X.-F. Wang (1996). “Fluxes of CO<sub>2</sub> and Water between Terrestrial Vegetation and the Atmosphere Estimated from Isotope Measurements.” In: *Nature* 380.6574, pp. 515–517. ISSN: 1476-4687. DOI: 10.1038/380515a0.
- Yan, H., Y. Peng, and H. Bao (2022). “Isotope Fractionation during Capillary Leaking in an Isotope Ratio Mass Spectrometer.” In: *Rapid Communications in Mass Spectrometry* 36.11, e9290. ISSN: 1097-0231. DOI: 10.1002/rcm.9290.
- Yanes, Y. and C. J. Yapp (2010). “Indoor and Outdoor Urban Atmospheric CO<sub>2</sub>: Stable Carbon Isotope Constraints on Mixing and Mass Balance.” In: *Applied Geochemistry* 25.9, pp. 1339–1349. ISSN: 0883-2927. DOI: 10.1016/j.apgeochem.2010.06.004.
- Yeung, L. Y. et al. (2009). “Large and Unexpected Enrichment in Stratospheric <sup>16</sup>O<sup>13</sup>C<sup>18</sup>O and Its Meridional Variation.” In: *Proceedings of the National Academy of Sciences* 106.28, pp. 11496–11501. DOI: 10.1073/pnas.0902930106.
- York, D., N. M. Evensen, M. L. Martínez, and J. De Basabe Delgado (2004). “Unified Equations for the Slope, Intercept, and Standard Errors of the Best Straight Line.” In: *American Journal of Physics* 72.3, pp. 367–375. ISSN: 0002-9505. DOI: 10.1119/1.1632486.
- Zhang, Q. L., T. L. Chang, and W. J. Li (1990). “A Calibrated Measurement of the Atomic-Weight of Carbon.” In: *Chin Sci Bull* 35, p. 290.
- Zhao, C. L. and P. P. Tans (2006). “Estimating Uncertainty of the WMO Mole Fraction Scale for Carbon Dioxide in Air.” In: *Journal of Geophysical Research: Atmospheres* 111.D8. ISSN: 2156-2202. DOI: 10.1029/2005JD006003.
- Zhou, Y. et al. (2023). “Leaf Thermal Regulation Strategies of Canopy Species across Four Vegetation Types along a Temperature and Precipitation Gradient.” In: *Agricultural and Forest Meteorology* 343, p. 109766. ISSN: 0168-1923. DOI: 10.1016/j.agrformet.2023.109766.
- Zúñiga, J., A. Bastida, M. Alacid, and A. Requena (2001). “Variational Calculations of Rovibrational Energies for CO<sub>2</sub>.” In: *Journal of Molecular Spectroscopy* 205.1, pp. 62–72. ISSN: 0022-2852. DOI: 10.1006/jmsp.2000.8237.



# Danksagung

Insbesondere in der Endphase und während der intensiven Messungen im ersten Halbjahr 2024 hat mir diese Arbeit sehr viel abverlangt. Umso dankbarer bin ich, dass ich auf die Unterstützung vieler Menschen zählen durfte. Dabei ist mir bewusst, dass die Diskussionen und Gespräche mit mir nicht immer leicht waren. Umso dankbarer bin ich, dass ich dennoch diese Unterstützung erfahren durfte, die es mir ermöglicht hat, diese Dissertation fertigzustellen.

Zunächst danke ich Dr. Martina Schmidt für die langjährige Betreuung und dafür, dass sie mir diese Dissertation ermöglicht hat. An dieser Stelle danke ich auch Prof. Dr. Norbert Frank, der mich als Doktorand angenommen und als Erstgutachter für diese Arbeit fungiert. Ich danke beiden insbesondere auch dafür, dass sie eine langjährige Finanzierung ermöglicht haben, und für die vielen wertvollen Anmerkungen und Verbesserungsvorschläge.

Ebenso danke ich Prof. Dr. Werner Aeschbach, der sich bereit erklärt hat, das Zweitgutachten zu übernehmen. Ich danke den beiden Gutachtern sowie den Mitarbeiter:innen des Sekretariats der HGSFP insbesondere für ihr Entgegenkommen während der stressigen Abgabephase. Des Weiteren danke ich Prof. Dr. Björn Malte Schäfer und Prof. Dr. Rüdiger Klingeler dafür, dass sie sich bereit erklärt haben, Teil meines Prüfungskomitees zu sein.

Ich danke Dr. Tobias Kluge dafür, dass er mich im Rahmen meiner damaligen Masterarbeit in die Messung mit dem Massenspektrometer MAT 253+ sowie in die manuelle Aufbereitung von Proben für die  $\Delta_{47}$ -Messung eingearbeitet hat und für die zahlreichen wertvollen Diskussionen.

Ebenso danke ich Herrn Prof. Dr. Thomas Röckmann für die Übernahme der außeruniversitären Drittbetreuung im Rahmen des HGSFP-Programms und konstruktive Gespräche.

Ein besonderer Dank gilt Michael Sabasch, der mich im Labor tatkräftig unterstützt hat, insbesondere beim Bereitstellen von Gasflaschen, dem Wiederbefüllen von Kühlfallen und bei Messungen.

## *Danksagung*

In diesem Zusammenhang möchte ich auch der gesamten Werkstatt des IUP in Form von Ralph Pfeiffer, Heribert Sommer, Alexandra Mertens, Sebastian Gehrig und dem inzwischen ausgeschiedenen Udo Weller danken. Sie haben durch die Konstruktion zahlreicher Elemente und wertvolle Anregungen die Umsetzung des im Rahmen dieser Arbeit konstruierten automatischen Aufbereitungssystems ermöglicht. Ebenso gebührt Ursula Scheurich aus der Glastechnikwerkstatt Dank für ihre Arbeit bezüglich der Glasbauteile. Daneben möchte ich mich auch bei allen anderen Beteiligten des IUP bedanken, insbesondere bei den Mitarbeitenden des Sekretariats, die sich um die buchhalterische Abwicklung der zahlreichen notwendigen Bestellungen gekümmert haben.

Ich danke Dr. Julia Wietzel für das Korrekturlesen einzelner Teile meiner Arbeit sowie allen anderen Mitgliedern meiner Gruppe GGWI für ihre Unterstützung. In diesem Zusammenhang möchte ich mich insbesondere bei Till Gonser für das Erstellen von Fotografien der Aufbereitungsanlage bedanken, welche im Rahmen der Arbeit Verwendung fanden. Mein Dank gilt auch William Cranton und Valentin Schmid. Die Mitbetreuung ihrer großartigen Arbeiten sowie die zahlreichen Diskussionen haben mir große Freude bereitet und waren sehr bereichernd.

Ich möchte mich außerdem bei Dr. Markus Erritt bedanken, der mir zu Beginn meiner Arbeit zahlreiche Tipps zu Isodat und ISL gegeben hat. Ebenso danke ich Dr. Markus Greule für die Unterstützung bei der Reinigung der Quelle des Massenspektrometers sowie für die Bereitstellung einer Ersatzkathode.

Zuletzt möchte ich Verena und Philipp danken, die mir während dieser Arbeit, die sich doch etwas länger als erhofft hingezogen hat, stets zur Seite standen und mir die oft notwendige emotionale Unterstützung gaben. Selbiges gilt auch für meine Familie, insbesondere für meine Eltern Sonja und Peter.

Ich danke auch meinen Mitbewohner:innen sowie allen Freund:innen und Unterstützer:innen, die ich nicht namentlich erwähnt habe, mich in verschiedenen Phasen dieser Arbeit aber unterstützt haben.

Lieben Dank!